The thermal and non-thermal radio emission from the galaxy

Alison Broadbent

The thermal and non-thermal radio emission from the Galaxy

by

Alison Broadbent

A thesis submitted to the University of Durham
for the Degree of Doctor of Philosophy

August, 1989

Abstract

It is shown that a detailed correlation exists between IRAS 60 μm band emission from the galactic disc and radio continuum emission measured at a similar angular resolution at 11 and 6 cm. The emission at these short radio wavelengths is predominantly from thermal bremsstrahlung in regions of ionized gas and so the strong correlation, which holds for the diffuse, extended emission as well as the discrete, compact sources, indicates that an important contribution to the 60 μm emission is associated with HII regions. Isolation of this component of the 60 μm infrared emission has involved the estimation of the zodiacal light contamination and detailed modelling of the HI-associated dust emission. The residual 60 μm emission can then be used as a tracer of radio thermal emission. On the small scale this enabled a search for new supernova remnant candidates in the 11 cm survey of Reich *et al.* and the 6 cm survey of Haynes *et al.* close to the inner Galactic Plane. On the large scale we have separated the thermal and non-thermal emission of the 408 MHz all-sky survey of Haslam *et al.* from the whole of the Galactic Plane and within $\sim 8°$ of the plane. From the thermal galactic emission we have been able to estimate the average infrared excess, the total 60 μm luminosity and total mass of HII in the Galaxy. The clearer picture obtained of the non-thermal emission of the Galaxy has allowed us to improve upon previous attempts at modelling the synchrotron emission in terms of the cosmic ray electron distribution and magnetic field variation modulated by the galactic spiral structure.

Preface

The studies reported in this thesis were carried out between 1986 and 1989 while the author was a research student under the supervision of Dr. J.L. Osborne, in the Physics Department at the University of Durham. None of the material has been submitted previously for a degree at this or any other university. Although the initial conception of the project was by Dr. J.L. Osborne and Dr. C.G.T. Haslam, its development and execution has been performed almost entirely by the author. Some of the results presented here have also been published in the following papers:

Broadbent, A., Osborne, J.L. & Haslam, C.G.T., 1988. In: *Comets to Cosmology, 3rd IRAS Symp.*, p.109, ed. Lawrence, A., Spinger-Verlag, Berlin.

Broadbent, A., Haslam, C.G.T. & Osborne, J.L., 1989. *Mon. Not. R. astr. Soc.*, 237, 381.

Broadbent, A., Haslam, C.G.T. & Osborne, J.L., 1989. In: *Galactic and Intergalactic Magnetic Fields, IAU Symp. No. 140.*, in press.

Contents

Chapter 1

Introduction

In 1987, Haslam and Osborne published a short paper pointing out the remarkably detailed correlation, both spatial and in intensity, between emission from the inner Galactic Plane detected by the Infrared Astronomical Satellite (IRAS) at 60 μm and that from high frequency radio surveys at a similar resolution. Close to the plane of the Galaxy at frequencies of about 2 GHz and above, the radio emission is dominated by that produced via the thermal bremsstrahlung (or free-free) mechanism from electrons accelerated in the electrostatic field of protons and ions. Thus, thermal radio continuum emission is a tracer of the ionized gas. One location of ionized gas is in the immediate vicinity of O stars which are young massive stars formed in dense clouds of molecular hydrogen. Photons emitted from these stars are of sufficiently high energy not only to dissociate the H_2 molecules but also to ionize the hydrogen atoms thus produced. Other elements such as helium and those present in much smaller quantities are also ionized. These localized sources of thermal radio continuum are usually referred to as compact radio HII regions and typically have radii of only a few parsecs and electron density as high as $\sim 10^4\,\mathrm{cm}^{-3}$ (Schraml and Mezger, 1969). In addition to these discrete sources the thermal radio continuum shows evidence for much more diffuse and extended volumes of ionized gas (*e.g.* Westerhout, 1958; Mathewson *et al.*, 1962) which have typical electron densities of 5–10 cm^{-3} and linear extent $\sim$ 100 pc (Mezger, 1978). These extended, low density (ELD) HII regions are believed to be maintained by O stars each of which having left its progenitor gas cloud and whose surrounding sphere of ionization has merged with those of other O stars.

Before the advent of IRAS it was well established that IR emission from the Galaxy was concentrated close to the Galactic Plane and was composed of bright discrete sources superimposed on a diffuse component (*e.g.* Low *et al.*, 1977). It was generally accepted that the origin of far infrared ($\sim$ 40 μm–submm) radiation was dust heated by starlight and that the discrete sources could be identified readily with compact radio HII regions. The precise location of the dust grains responsible for the diffuse far infrared (FIR) emission and that of the stars heating them was much less clear. Two main theories had been proposed. The first was that the diffuse IR emission was from dust mixed in with the ionized gas of the ELD HII regions where it assumed temperatures of 30–40 K (*e.g.* Mezger, 1978). The second proposal was that the diffuse IR was from dust grains which existed in molecular clouds

where they were heated by as yet unobservable O stars (*e.g.* Ryter and Puget, 1977). If the latter proposal was correct then one would expect that the spatial distribution of the FIR emission would be preferentially correlated with the ^{12}CO line emission in the Galaxy which is the hall-mark of molecular gas clouds. If the former argument was true then the FIR would be better matched to thermal radio continuum emission. Unfortunately, because HII regions tend to be associated with molecular clouds anyway, the resolution of the Galactic Plane surveys had been too poor to validate either model. However, with the much higher angular resolution of IRAS ($\sim 4'$) it became clearer where the fundamental correlation lay.

The fact that Haslam and Osborne found such a close correspondence between the morphology of the 60 μm IRAS band emission and the 11 cm brightness temperatures of the $4.3'$ resolution survey by Reich *et al.* (1984) of the northern inner Galactic Plane naturally led them to the conclusion that the thermal radio continuum emission and a substantial fraction of the FIR emission has a common origin *i.e.* that FIR is produced by dust mixed in with the ELD and compact radio HII regions. Only a few bright radio sources have no corresponding IR emission and most are identified with catalogued supernova remnants (SNRs).

Fig. 1.1 shows a grey-scale representation of a short section along the Galactic Plane for the galactic longitude range 35° (left) $\geq l \geq$ 23° (right) and latitudes $|b| \leq 1.5°$. The top and bottom panels show the 100 and 60 μm band IRAS intensities respectively and the middle strip shows the 11 cm radio brightness temperatures. This is the same as the figure presented by Haslam and Osborne to illustrate the striking resemblance of the FIR, especially at 60 μm, to the 11 cm emission. The bright blobs of radio emission at $l = 34.7°$ and 27.8° are both well known SNRs and have no apparent IR emission. Haslam and Osborne realized that this property of known SNRs could be exploited. By studying the 60 μm and 11 cm radio surveys simultaneously it should be possible to pick out new SNR candidates by their lack of IR emission and absence from the catalogues. The radio emission from SNRs is non-thermal in nature being the synchrotron radiation of relativistic electrons which are accelerated by magnetic fields. The standard indications that a source is a SNR is a steep spectral index at radio frequencies, polarized radio emission and lack of recombination line emission which is more usually found in HII regions. Although these methods of SNR identification have proved quite successful, some SNRs have been identified which have unusually flat spectral indices and other sources lying along the same line of sight in densely crowded regions of the sky can cause confusion. The complete absence of a radio bright source in the IR provides a more clear-cut criterion.

Although this new method of SNR identification was very useful in itself Haslam and Osborne found the large scale correspondence of 60 μm IR and thermal radio emission an even more interesting result as it could potentially provide a new independent method of separating the thermal and non-thermal radio continuum emission on a Galactic scale. If the correlation were quantified then it would be possible to subtract from radio continuum surveys the thermal contribution to the emission in the form of the appropriately scaled IR intensities. Free-free emission has a flat spectrum and constant spectral index over a frequency range from $\sim$ 100 MHz to tens of GHz. Therefore once the scaling factor between IR and thermal radio has been established at one, fairly high frequency where thermal

Figure 1.1: Overleaf are shown grey-scale representations of the distributions of far infrared and radio continuum emission in the Galactic Plane. The central galactic longitude is 29° and each panel covers the range from 35°(left) down to 23°(right). The extent in galactic latitude of each strip is from $-1.5°$(bottom) to $+1.5°$(top). The top and bottom panels show 100 and 60 μm IRAS intensities respectively and the centre panel shows 11 cm radio continuum brightness temperatures from the Effelsberg survey (Reich *et al.*, 1984). This figure originally appeared in Haslam and Osborne (1987).

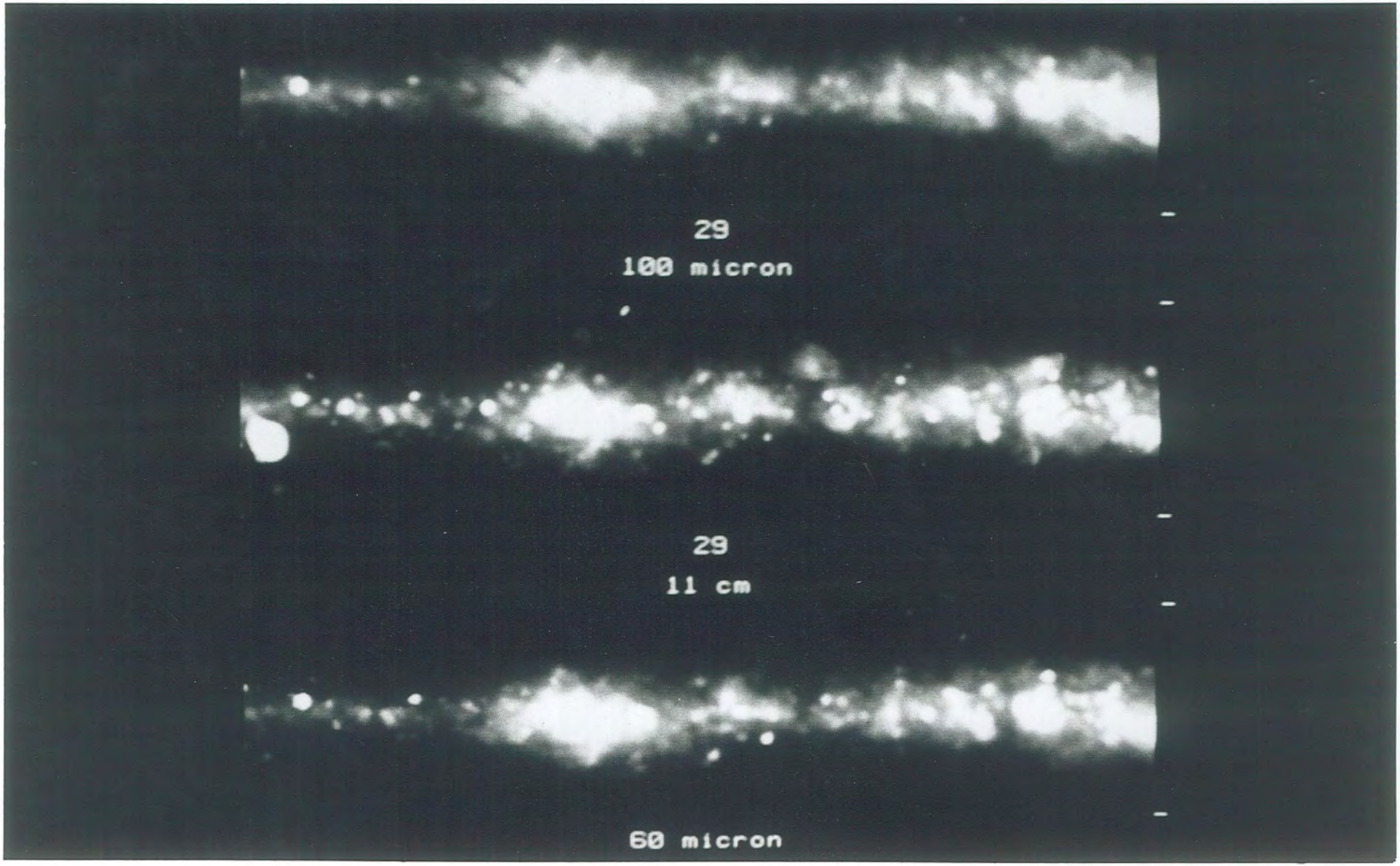
29
100 micron
29
11 cm
60 micron

emission dominates over non-thermal radio emission close to the Galactic Plane, it will be possible to determine the thermal component at lower frequencies where non-thermal emission becomes more dominant.

Synchrotron emission on the large scale is produced by relativistic cosmic ray electrons accelerated in the general Galactic magnetic field and so the study of the non-thermal component of the radio continuum emission of the Galaxy is one way of obtaining information about the magnitude and distribution of both field and electrons. For example, along the Galactic Plane the radio brightness temperature increases towards the Galactic Centre in quite distinct steps. This has been assumed to be a consequence of the spiral structure of the Galaxy. However, to obtain a clearer picture of the extent of the modulation of field and electron distributions across the spiral arms of the Galaxy, the thermal component, which tends also to be concentrated in the arms, should be subtracted.

The usual method employed to separate the two components involves two radio continuum surveys one typically at a frequency of a few hundred MHz and the other at a few GHz. The spectral index of the thermal and non-thermal components between these two frequencies are assumed to be constant for the whole Galaxy and must be chosen beforehand. While this is reasonable for the thermal component, there is evidence that the non-thermal spectral index varies with position (Lawson *et al.*, 1987) and even its mean value is not well established. Other problems encountered with the spectral index separation method is the sensitivity to errors in base level and absolute temperature scale calibration of the radio surveys. These problems could be circumvented by using the FIR emission as a tracer of the thermal emission instead.

In this thesis an account is given of the development and execution of a new technique of separating the thermal and non-thermal components of the radio continuum emission from the Galaxy using the 60 μm band IRAS survey. By doing this the main objective was to obtain a view of the synchrotron emission of the Galaxy, uncluttered by thermal emission, which we could then attempt to model. It was hoped that a clearer idea of the distribution and behaviour of the magnetic field and the relativistic cosmic ray electrons could be gleaned from an improved picture of the non-thermal brightness temperatures. The pursuit of this main programme of research has inevitably encountered a number of unforeseen problems but has also provided the opportunity to investigate a number of topics related to the far infrared and thermal radio continuum emission of the Galaxy.

In Chapter 2 we give a short description of the IRAS survey and then proceed to give an account of the preparatory work required on the 60 μm band Galactic Plane survey before it can be used to determine the thermal component of radio continuum emission. There are two contributions to the 60 μm band emission which we have modelled and subtracted. The first is the foreground contamination due to dust lying in the Solar System and this we estimated empirically. The second is that from dust associated with neutral atomic hydrogen within the Galaxy.

Neutral atomic hydrogen (HI) is a major ingredient of the interstellar medium and can be detected by the characteristic 21 cm line emission which is due to a hyper-fine transition between parallel and antiparallel spin states of the constituent electron and proton of the atom. Because the energy of the transition is so small the atom is easily excited into the

parallel spin state by atomic collisions in the interstellar medium (ISM). Decay back to the ground state is predominantly caused by collisions rather than being spontaneous since the transition is 'forbidden'. This fact also implies that self absorption of the decay photons is rare. Also, dust grains cause little attenuation at these wavelengths. Although it is not safe to assume that sources are always optically thin, the measurement of the 21 cm line is still a powerful tool for mapping the HI gas situated throughout the Galaxy and in other galaxies. Along any line of sight emission from neutral hydrogen is detected over a range of frequencies about 1420 MHz ($\equiv$21 cm) because gas in different parts of the Galaxy moves at different velocities with respect to the observer and the received emission is thus Doppler shifted accordingly. In principle therefore, a knowledge of the variation of the gas velocity with position in the Galaxy enables the translation of observed 21 cm velocity profiles into a picture of the distribution of atomic gas.

Throughout this work we have supposed that the dust-to-gas mass ratio is everywhere proportional to the metallicity (the abundance of oxygen relative to hydrogen) which varies with galactocentric distance. The dust-to-gas mass ratio has a value of ~ 0.01 in the solar neighbourhood and increases with decreasing galactocentric radius. We also assume that the grain composition and size distribution is the same over the whole of the Galaxy. Thus the distribution of the atomic gas can be used as a tracer of the embedded dust also. It is highly unlikely however that the dust composition, size distribution or the dust-to-gas ratio vary in such a regular way in reality. In the centre of quiescent molecular clouds for instance, the grains are believed to be coated with a layer of ice unlike the bare grains in the diffuse ISM. However, we would not expect much infrared at 60 μm from these grains as they are too cold and instead most of their emission would be at longer wavelengths (sub-mm). The number of grains per hydrogen atom is also likely to vary from place to place in the Galaxy. The formation of dust grains is believed to occur in the cool circumstellar shells of late spectral-type stars and in the expanding shells of novae and planetary nebulae. Hence these objects and their immediate vicinity will probably be rich in dust in comparison to the average dust content of the ISM. At the other extreme, in the proximity of the ionizing star of a compact HII region some grains will be destroyed due to exposure to an intense radiation field. There is evidence however (Panagia, 1978) that in the more extended and more evolved HII regions this depletion of grains does not occur. These cases of grain enhancement or depletion are in localized regions however and it seems reasonable to adopt for the general ISM, the assumptions made by others (*e.g.* Mezger *et al.*, 1982), that the dust to gas mass ratio follows the metallicity and that increases in the ratio imply an increase in numbers rather than sizes of grains.

Another factor affecting the emission from dust grains apart from their size distribution, composition and number density is the intensity of the heating source which, for the case of the HI-associated dust, is the general interstellar radiation field. All these factors have been considered and in Chapter 2 we examine the relative merits of three models of the HI-associated emission at 60 μm. By predicting the 100 μm emission from HI-associated dust as well for a part of the Galactic Plane, we have been able also to study the IRAS colour temperatures between 60 and 100 μm, suggesting an alternative to the popular explanation of its apparently large and nearly constant value over a wide range of environments within

the Galaxy and other galaxies.

In Chapter 3 we first reinforce the opinion of Haslam and Osborne that the residual 60 μm emission from the Galactic Plane is primarily from HII regions rather than molecular gas using a more quantitative approach. We then proceed to determine the relationship between this residual 60 μm and the thermal radio continuum emission for the inner Galactic Plane and within $1\frac{1}{2}^\circ$ above or below the plane. For the northern side of the Galaxy we use the 11 cm survey of Reich *et al.* (1984) and for the southern side the 6 cm survey of Haynes *et al.* (1978) which again has an angular resolution of $\sim 4'$. As a by-product of deducing the linear relationship between 60 μm and thermal radio emission we are able to estimate global properties of the Galaxy such as the infrared excess and the total luminosity and mass of the ionized gas. At the end of Chapter 3 we include a discussion of the vexed problem of the tight correlation observed between the total far infrared luminosity and radio power of other galaxies and compare the ratio of these quantities which we derive here for our Galaxy with that of other galaxies of a similar type.

At the beginning of Chapter 4 we report on the successes of a search for new SNR candidates from the 11 and 6 cm surveys by comparing their radio fluxes with those at 60 μm. In addition to producing a list of such candidates we examine a number of sources whose nature has not been conclusively deduced from other measurements and using the radio–IR comparison method try to decide whether they are thermal or non-thermal. In Section 4.2 we return to the main theme of this thesis by proceeding with the separation of the thermal and non-thermal components of the radio continuum emission at 408 MHz for the whole of the Galactic Plane and within $\sim 8^\circ$ of it. The radio survey used here is the 408 MHz all-sky survey of Haslam *et al.* (1982) which has $51'$ resolution. The thermal component was estimated by scaling the residual 60 μm band emission appropriately. It was found that for a few very bright HII regions a correction to the scaled 60 μm emission would have to be made to avoid over-estimation of the peak radio temperatures. After subtraction of the thermal emission from the 408 MHz data we further isolate the large scale non-thermal Galactic emission by estimating and subtracting the emission from catalogued SNRs situated within 2° of the Galactic Plane. Finally in Chapter 4 we compare our new method of separation with the spectral index approach and illustrate some of the problems faced by the latter method by looking in more detail at specific cases where it has been employed.

Chapter 5 deals with the modelling of the non-thermal or synchrotron emission of the Galaxy using the end product of the new separation technique described in previous chapters. We first describe earlier attempts to use radio continuum surveys to learn about the structure of the Galactic magnetic field and cosmic ray electron distribution. In particular we discuss the unfolding method used by Phillipps *et al.* 1981a and 1981b and the modelling method which was employed by French (1977) and Kearsey (1983). It is this latter technique that we have followed and our work is a continuation of the work of Kearsey and French. With the advantage of a more realistic estimation of the thermal component of the 408 MHz radio continuum and also the benefit of the results of several more years of research appearing in the literature regarding parameters which are input into our model, we hope that we have been able to improve on the models of these authors. The mod-

elling involves a consideration of the spiral arm pattern of the synchrotron emission, the variation of emissivity with galactocentric radius and height above the plane and the compression variation across an arm. For convenience of calculation we have assumed that the synchrotron emissivity variation with radius can be attributed entirely to a variation in magnetic field strength and changes with height above the plane to changes in the electron flux density. We appreciate that this is an over-simplification but it is easy from the results presented to see for instance how the variation of magnetic field would be modified if one wanted to include any given variation of cosmic ray electron density with radius. We also compare models whose local magnetic field strength are different but still within the range of reported measurements. Recent radio observations of the spiral galaxies M81 and M51 suggest that the magnetic field is more uniform in interarm regions than in the arm regions. This is contrary to the assumption made for our Galaxy and we make preliminary investigations of this by introducing an expression into our model calculations which mimics the behaviour of the field in M81 between arms and interarms.

At the end of Chapter 5 we present a short list of aspects of the model which could be investigated more thoroughly in future. The final chapter in this thesis summarizes the main results and conclusions of the whole thesis and makes suggestions for further research related to the work presented here.

Chapter 2

Infrared emission

2.1 The IRAS survey

In January 1983, the Infrared Astronomical Satellite was launched and it remained operational until November of the same year when the liquid helium used to cool the telescope was exhausted. Within this period IRAS made observations of 96% of the sky in four wavebands centred at 12, 25, 60 and 100 μm. The IRAS survey is of unprecedented completeness and reliability at these wavelengths and has proved an invaluable asset to the astronomical community. The results are presented in the form of a catalogue of point sources, a catalogue of sources which are extended but less than $8'$ in size, a catalogue of low-resolution spectra and an atlas of sky brightness images.

Reobservations of the same regions of sky on different timescales enabled differentiation between various types of infrared (IR) sources. Very local, fast moving objects and particle irradiation of the telescope detectors could be eliminated by observing again after a period of seconds. Slower moving local sources such as man-made satellites were recognised by making two observations separated by 103 minutes to 36 hours while asteroids, comets and planets were identified from reobservations after weeks or months. One 'hours confirmed' coverage (HCON) of the sky consists of two sets of observations separated by a few hours. During the working lifetime of the satellite, two nearly complete hours confirmed all-sky surveys were performed and a third was in progress when the program was terminated.

The sky brightness images give an overall view of the sky at an effective resolution of 4–$6'$. From these images a set of maps covering the whole of the Galactic Plane and extending out to $\pm 10°$ in latitude were produced. It is these Galactic Plane maps that we use in the present work and so a brief description of the processing and calibration procedures performed at the Jet Propulsion Laboratories (JPL) to attain their published form is in order.

The data were collected by making scans along meridians of ecliptic longitude the directions of which were determined by a combination of information from Sun sensors and gyros on the satellite and by observations of bright stars. Photons incident on the detectors created a current source whose magnitude was assumed to be proportional to the incident flux. This current was input to an amplifier and the output voltage was converted to a

digital signal which was transmitted to Earth. With a knowledge of the telescope transfer function the size of the current at the detector could be recovered. At the beginning and end of each scan in the survey the detectors were exposed to an internal source. Each detector's response to the external emission was thus known relative to the response to this reference source.

The absolute calibration of the internal reference source was performed by taking the results of a ground based calibration at 10 μm of α Tau by Rieke *et al.* (1984). The 12, 25 and 60 μm band fluxes were deduced from stellar models. The 100 μm band calibration involved finding the colour temperature between 25 and 60 μm of asteroids and assuming the same temperature between 60 and 100 μm. Because the effective width of the four bands is so large it was necessary to assume a spectral energy distribution for sources to derive the quoted fluxes. The distribution chosen is a constant flux per logarithmic frequency interval and so if the source energy spectrum differs from this then a 'colour correction' must be applied to obtain the true flux. An estimation of the uncertainties in the IRAS intensities at 60 and 100 μm are $\sim$ 15% and 20% respectively which include consideration of systematic errors in the colour corrections, calibration and frequency response of detectors.

Having completed the calibration, images of extended emission had to be created from the time-ordered data. The whole survey program was co-ordinated to avoid stray light from the Earth and Sun and no data were used for the images which were from within 1° of Jupiter or 30° of the Moon. This latter restriction means that lune-shaped areas with no data appear on images in all three of the hours-confirmed coverages. The calibrated data from the detectors were compressed in time in such a way that, in the projected images, samples were at 2′ intervals. A procedure involving adjustment of individual detector baselines and responsivities was used to remove most of the striping in the images and weighted averages of multiple observations of the same regions of sky were calculated to produce a single image. Between successive HCON coverages the orbital position of the Earth changed and so for a given line of sight the path through the interplanetary dust will also have changed. Hence, the contribution to the total will be different in each of the coverages. For this reason the three coverages were presented separately and consequently no weeks confirmation of the extended survey was performed. It was left to the user to compare different hours confirmed coverages in order to pick out small sources whose positions move between coverages, many of which are presumed to be asteroids. To facilitate subtraction of the zodiacal contribution from the images , the Zodiacal Observation History File was created which has time-ordered data samples at 30′ intervals together with information such as Sun-referenced observation angles and time as well as celestial co-ordinates.

The final data were converted to brightness intensities expressed in Jy sr^{-1}. The Galactic Plane maps were created by re-mapping the sky brightness images into 24 16.7° × 20° fields per band each centred on zero galactic latitude and at 15° intervals of galactic longitude. The effective resolution is 4′–6′ and the pixel size is 2′ × 2′. A cylindrical projection of the celestial sphere is used which preserves area unlike the gnomonic projection used for the sky brightness images. The Zodiacal Observation History File was used to produce two low resolution all-sky maps for each HCON coverage and each waveband. The projection used is the Aitoff equal area projection, one map being centred on the Galactic Centre and the

other on the anticentre. The resolution is $\sim \frac{1}{2}^\circ$ with data samples in $\frac{1}{2}^\circ \times \frac{1}{2}^\circ$ pixels. Both the Galactic Plane maps and all-sky maps are in machine readable form.

One of the most serious problems of the IRAS survey as far as the extended emission is concerned is that of photon induced responsivity enhancement which was only discovered well into the mission. When the telescope scanned across bright IR sources such as Saturn and more importantly the Galactic Plane, the 100 μm band detectors and to a lesser extent the 60 μm band detectors have increased responsivity. The enhancement on crossing the Galactic Plane can be as much as 15% in the 100 μm band and although it does decrease again the time constant involved is unknown. For the first two HCON coverages the scans crossed the Galactic Plane in the same sense but the third coverage was generally in the opposite direction. Had the third coverage been complete it may have been possible to eliminate the problem but as it is no attempt at correcting the surface brightness of the extended emission survey has been made.

The reader is referred to the IRAS Explanatory Supplement (1985) for a more detailed discussion of all aspects of the survey.

Before any analysis of the IRAS Galactic Plane maps was performed, further processing of the published form was necessary using existing software written specifically for IRAS extended emission images and which is available on the Starlink computer network. Each image array was reoriented such that the first pixel is at the southernmost galactic latitude and the highest galactic longitude of the map. The data points were then regridded such that at the origin of the map the pixel size is $2.5' \times 2.5'$. For the analysis described in the next few sections we have assumed that the data points are on a $2.5'$ rectangular grid rather than a cylindrical projection. The discrepancy incurred is small amounting to ~ 1.2 pixels at the middle of the top edge of a Galactic Plane map. Therefore, since the majority of the work described in subsequent chapters is concentrated within 2° of the Galactic Plane, the above approximation is adequate. We used HCON1 data only, except over a few small areas on the Galactic Plane maps which were not covered in the first hours confirmed coverage but were in the second.

2.2 Zodiacal light emission

In the introductory chapter it was shown that there appears to be a detailed correlation between the IRAS 60 μm band emission from the Galactic disc and the thermal component of the radio continuum emission at 11 and 6 cm. Thus it would seem that a substantial proportion of the 60 μm band emission is from dust associated with the compact HII regions and the extended low density (ELD) HII regions. Before a more quantitative relation between the thermal radio emission and 60 μm emission from HII regions can be deduced, other contributions to the total IRAS 60 μm emission must be estimated and removed from the Galactic Plane maps. The first of such components considered is the zodiacal light contamination which at far infrared (FIR) wavelengths is foreground emission of interplanetary dust particles.

The proximity of the zodiacal dust to the Sun means that its temperature is generally higher than that of the dust in the general interstellar medium (ISM). Thus in the shorter

wavelength (12 and 25 μm) IRAS bands the emission is dominated by the zodiacal light whereas at 60 and 100 μm the Galactic disc emission is more prominent. In Fig. 2.1 are low resolution all-sky grey-scale maps in galactic co-ordinates of the 60 and 100 μm IRAS band emission. The emission from the Galactic disc can be seen in both wavebands as a bright, structured band concentrated along the Galactic Plane in the centre of the photograph. At 100 μm more diffuse filamentary structure is seen away from the plane which is the so-called infrared cirrus (Low *et al.* , 1984). At 60 μm and less clearly at 100 μm , an almost sinusoidal band of emission can be seen. This is the zodiacal light and the maximum intensities roughly follow the ecliptic plane with emission falling off smoothly on either side of this line.

Both of the photographs are from the first hours confirmed survey (HCON1). The zodiacal light contribution to the equivalent HCON3 maps would be different due to the changed position of the Earth in its orbit as was explained in the previous section. A more detailed examination of the 60 μm band zodiacal light emission reveals that a saw-tooth pattern of intensities runs along the ecliptic plane. This is due to changes at regular intervals of the orientation of the satellite relative to the Sun. Apart from this however, as was shown by Burton *et al.* (1986), the ecliptic latitude profile of the 60 μm zodiacal light emission varies little with ecliptic longitude.

Models of varying complexity have been used to subtract the zodiacal emission from IRAS images (*e.g.* Burton *et al.* 1986; Hauser *et al.* 1984; Tereby and Fich, 1986; Boulanger and Pérault, 1988), the more accurate ones referring to the Zodiacal Observation History File (see Section 2.1). The present study is concentrated in the direction of the Galactic Plane where the zodiacal light contamination is only a small fraction of the total emission and so an approximate model seems sufficient. The relative importance of the zodiacal emission increases towards the anticentre direction and at high galactic latitudes.

In the model of zodiacal light subtraction adopted here we assume that at galactic latitudes $|b| \geq 20°$ the 60 and 100 μm band intensity is dominated by emission from two dust components, one associated with the Solar System and the other with neutral atomic hydrogen (HI) in the solar neighbourhood. That HI-associated dust does contribute a major proportion of the emission at high galactic latitudes has been demonstrated by many authors who have found a strong correlation between many of the IR cirrus features, seen most clearly at 100 μm and the HI column density (*e.g.* Low *et al.*, 1984; Boulanger *et al.*, 1985; Tereby and Fich, 1986; Boulanger and Pérault, 1988). Other sources of IR emission at high galactic latitudes may contribute to the 60 and 100 μm band emission but we assume that they are small compared with the zodiacal light and HI-associated dust emission.

One such minor contributor is from dust associated with molecular gas. Magnani *et al.* (1985) reported that they had detected 57 molecular clouds at $|b| \geq 25°$ from ^{12}CO observations. The clouds covered angles ranging from a fraction of a square degree to several square degrees. They found that for all the detections of CO there was an associated HI feature and many of the CO clouds had size and morphology similar to that of the IR cirrus. It was pointed out that for a dust temperature between 25 and 40 K in the molecular clouds the flux expected at 100 μm would be of the same order as that observed at high latitudes. Thus it would seem that the emission from dust associated with molecular gas may be important. However, from an estimation of the total sky coverage of these clouds Magnani

Figure 2.1: Overleaf are grey-scale representations of the IRAS low resolution all-sky maps at (*a*) 60 μm and (*b*) 100 μm. The images were projected onto a $1^\circ \times 1^\circ$ rectangular grid by M.L. Parkinson and are centred on the Galactic Centre. Note the band of emission from the Galactic disc running across the centre of each image which is broader in the 100 μm band. The filamentary cirrus features are also clearly seen on the 100 μm image at high galactic latitudes. The zodiacal light can be seen as an almost sinusoidal band of emission passing through the Galactic Centre and is brighter at 60 μm. The levels of grey on each image run from 0 (black) to 30 MJysr^{-1} (white) which is approximately the maximum intensity of the 60 μm zodiacal light contribution and is very much less than the maximum Galactic intensities.

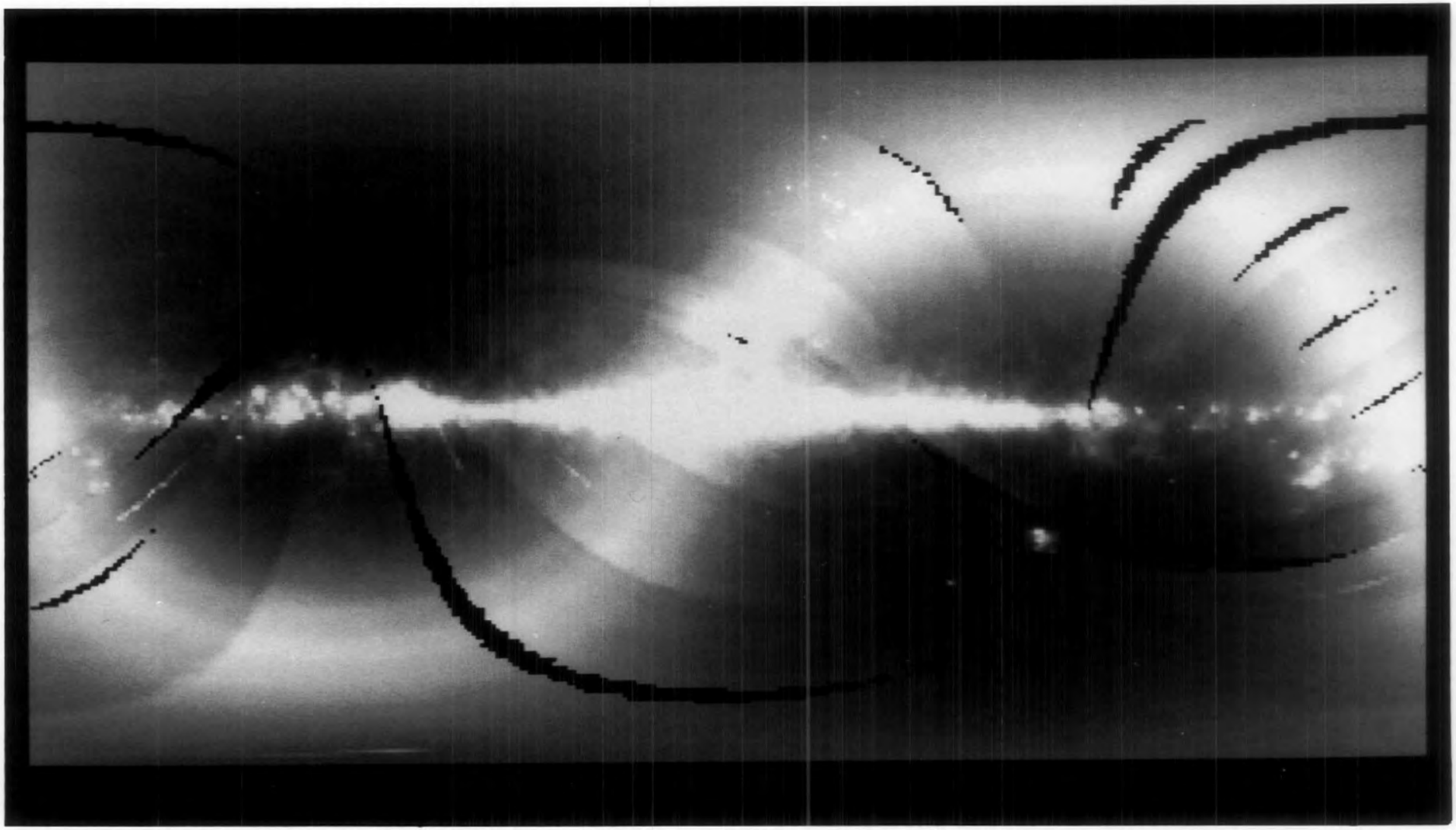

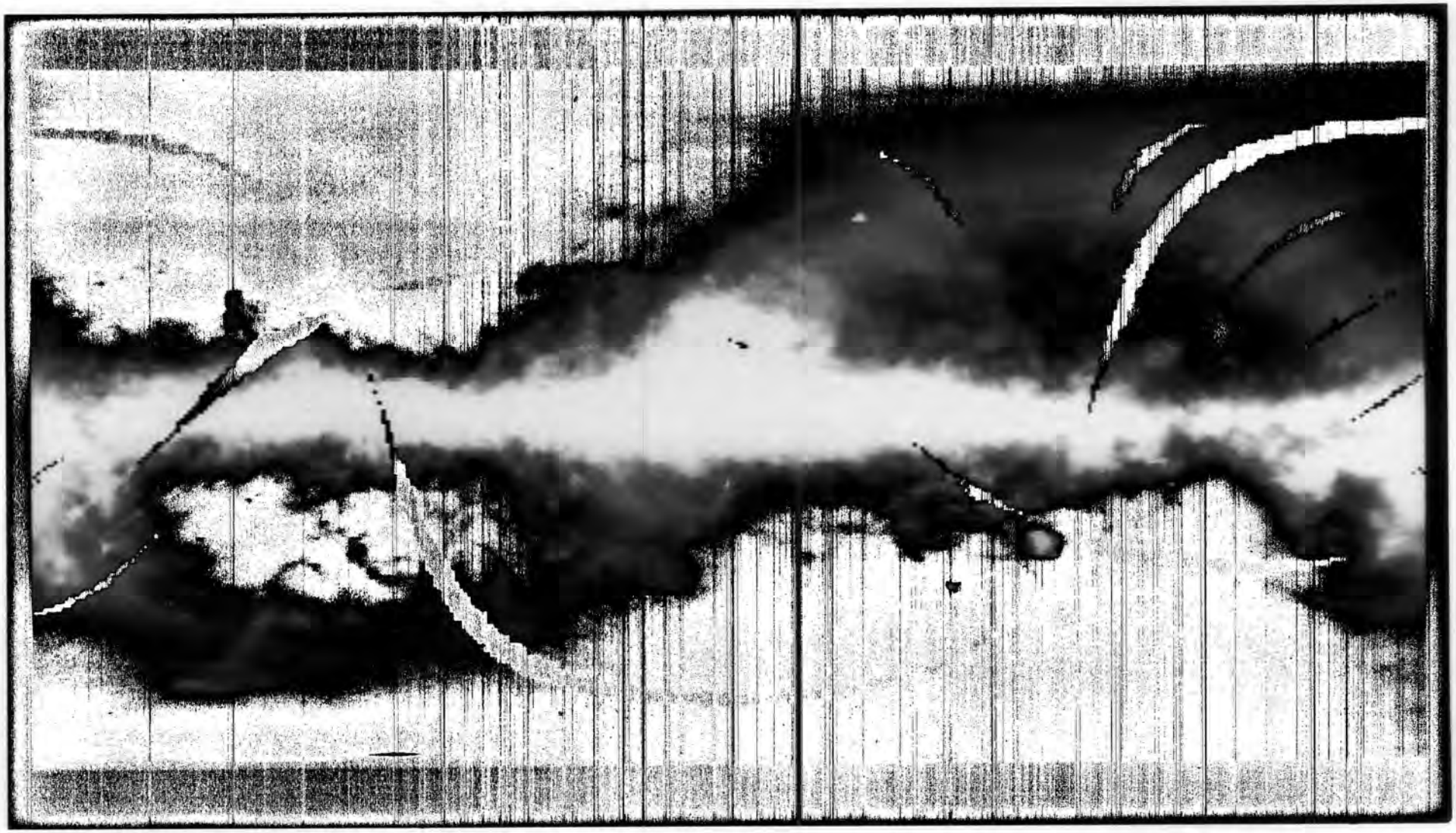

et al. deduced that only about $\frac{1}{4}\%$ of all random observations at $|b| \geq 25°$ would result in a positive detection of CO. This suggests that although these local molecular clouds could produce a significant flux in the 60 and 100 μm bands, their occurrence is rare enough that it can be ignored for the purposes of our rough estimation of the zodiacal light component. Also, in the assumptions we will make in following sections, we would consider between 25 and 40 K to be rather high for a molecular cloud.

Another source of emission in the 60 and 100 μm bands at high galactic latitudes could be from dust associated with ionized gas. The only compact HII regions which lie above $|b| \gtrsim 20°$ are associated with the Orion Nebula. The average half-power width of the thermal component of the radio continuum emission is only of the order of 1.5° as was shown by the 1390 MHz survey of Westerhout (1958). Thus it would seem reasonable to suppose that dust associated with the ELD HII regions is negligible at high latitudes. Exterior to the compact and fully ionized gas regions there exists a very diffuse ionized component both in the plane and at high galactic latitudes whose presence has been detected by its very low intensity optical recombination lines (Reynolds, 1984; 1985) and by pulsar dispersion measures (Harding and Harding, 1982). The temperature and electron density of this component is about 8000 K (Kulkarni and Heiles, 1986) and 0.17 cm^{-3} (Mathis, 1986) respectively. Here the density is the rms density within the region. The corresponding quantities for the ELD HII regions are believed to be $\sim$ 7000 and $\sim$ 5–10 cm^{-3} respectively (Mezger, 1978). Thus if the dust-to-gas ratio is the same for all components of the ISM, then we would expect the IR emissivity to be much smaller in the very diffuse ionized gas than in the ELD HII gas. Boulanger and Pérault (1988) predicted that the emission at high latitudes from the ionized gas should be about 20% of the total at 100 μm. However, when they then tried to estimate the HII contribution at 100 μm for $|b| \geq 20°$ using HI column densities they found that the discrepancy between the total 100 μm band and their predicted HI 100 μm emission is substantially less than 20%.

There is also emission at high latitudes which has an extragalactic origin. The Large Magellanic Cloud is an obvious bright extended source on the all-sky maps. It has been suggested that there may be a diffuse IR background of extragalactic origin (Rowan-Robinson, 1986). If there is indeed an isotropic background then by the method described below it will be subtracted with the zodiacal light contamination.

We assume that for both the zodiacal light and HI-associated emission there is a constant ratio between their contributions to the 60 and 100 μm band intensities for $|b| \geq 20°$. Also a linear relationship between the HI-associated dust emission in either band and the HI column density is assumed. Thus at high galactic latitudes, for a particular direction the intensities in the 60 and 100 μm bands, I_{60} and I_{100} respectively can be expressed as:

$$\begin{aligned} I_{60} &= I_{ZL} + \gamma N_H \\ I_{100} &= \alpha I_{ZL} + \gamma/\beta N_H. \end{aligned} \tag{2.1}$$

Here I_{ZL} is the 60 μm band zodiacal light component and N_H is the column density in the same line of sight. α, β and γ are constants with both α and β expected to be less than unity. In order to estimate the value of α, the ratio between the 100 and 60 μm band emission from the zodiacal dust, we made the use of the low resolution all-sky maps for both

wavebands from the HCON1 survey projected onto a 1° rectangular grid. A corresponding map of HI column densities was also required and this was compiled from the Berkeley 21 cm survey (Weaver and Williams, 1973) and the Durham-Parkes survey (Strong *et al.*, 1982) for the area within 10° of the Galactic Plane. The data for higher latitudes were from Heiles and Cleary (1979) and Heiles and Habing (1974). From this map of N_H, for each galactic latitude in the range $40° > |b| > 70°$, two points were chosen whose HI column densities were within $10^{19}\,\mathrm{cm}^{-2}$ of each other. The selection was such that one of the pair was near the position of maximum zodiacal light and the other near the minimum. This ensured that the differences in the 60 and 100 μm intensities between the two points was as large as possible to minimize the percentage uncertainty. Pairs were typically between 120° and 200° apart in galactic longitude.

If $I_\lambda(1)$, $I_\lambda(2)$ are the intensities of the points in the pair at either $\lambda = 100$ or 60 μm, then, eliminating N_H from the Equations 2.1, an expression for α can be deduced:

$$\alpha = \frac{I_{100}(1) - I_{100}(2)}{I_{60}(1) - I_{60}(2)} \tag{2.2}$$

For some of the pairs chosen one of the points happened to lie in a region where there was no data. In all, α was evaluated for 52 directions with average and standard deviation 0.37 ± 0.05. Fig. 2.2 is a histogram plot of the distribution of values of α deduced.

The ratio between 60 and 100 μm band HI-associated dust emission, β, was not derived empirically but rather selected from theoretical considerations consistent with the model we adopt in the next section for estimating the HI-associated dust emission in the Galactic disc. In the model of Cox *et al.* (1986) the temperature of this dust component in the solar neighbourhood is about 20 K and over the range of wavelengths encompassed by the 60 and 100 μm bands we assume that the dust grains follow an inverse-square wavelength emissivity dependence. The Cox *et al.* model will be discussed in detail later but at the present it is sufficient to state that according to this model $\beta \simeq 0.1$.

Elimination of I_{ZL} between Equations 2.1 leads to an expression for γ, the 60 μm HI-associated intensity to HI column density ratio:

$$\gamma = \frac{I_{100} - \alpha I_{60}}{1/\beta - \alpha} \tag{2.3}$$

Therefore, for each galactic longitude at latitudes above $|b| = 20°$ a value of γ can be determined using the three 1° rectangular grids of 60 μm intensities, 100 μm intensities and HI column densities. A weighted average, $\overline{\gamma}$, was calculated using the formula:

$$\overline{\gamma} = \frac{\sum_b \overline{\gamma}(b)\cos(b)}{\sum_b \cos(b)} \qquad |b| > 20° \tag{2.4}$$

where $\overline{\gamma}(b)$ is the mean γ at a particular galactic latitude. This weighting takes into account the actual number of data points at each latitude. The resulting value of $\overline{\gamma}$ is $0.14\,\mathrm{MJy\,sr^{-1}(10^{20}cm^{-2})^{-1}}$. Fig. 2.3 is a histogram of the distribution of $\overline{\gamma}(b)$ values obtained. The scatter in $\overline{\gamma}(b)$ may reflect small variations in the values of α, β or γ across

the sky or could be due to the presence of molecular or ionized material. However, both Fig. 2.2 and Fig. 2.3 show that the assumptions of constant 60 to 100 μm intensity ratio of the zodiacal and HI-associated dust emission and the IR intensity to HI column density ratio are reasonable approximations at high galactic latitudes.

Having established $\overline{\gamma}$ it was possible to subtract the emission from HI-associated dust from the 60 μm band 1° rectangular grid all-sky map. The residual map was then transformed to ecliptic co-ordinates and an average profile along the ecliptic was obtained avoiding the area with galactic latitude $< 20°$ and removing spikes caused by the Large Magellanic Cloud and the Orion Nebula. This profile is shown in Fig. 2.4 and can be used to map the 60 μm band zodiacal emission. In subtracting this from the Galactic Plane maps we should also eliminate any isotropic extragalactic background and so hopefully have only diffuse emission from the Galactic disc exterior to the Solar System remaining. In Fig. 2.5 the cut across the Galactic Plane at $l = 10°$ illustrates that the zodiacal light contamination in the 60 μm band is only a small contribution to the total emission along the Galactic Plane in the inner part of the Galaxy ($\sim 3\%$ at $l = 10°$, $b = 0°$) and justifies the use of such an approximate method of removal here. Obviously, as shown by the cross-cut at $l = 240°$, in the outer plane the zodiacal emission is a substantial fraction ($\sim 90\%$ at $l = 240°$, $b = 0°$) of the total 60 μm intensity and errors in the approximation of this contribution are more important.

As mentioned before, the value of $\beta = 0.1$ used to obtain the above results ensured that the assumptions involved in estimating the zodiacal light contamination were consistent with the model of Cox *et al.* (1986) for dust emission associated with neutral atomic hydrogen in the Galactic disc. This model assumes that the grain size distribution follows that of Mathis *et al.* (1977). However, various authors (*e.g.* Low *et al.*, 1984; Boulanger and Pérault, 1988) have discovered that the observed IRAS 60 to 100 μm ratio of intensities at high galactic latitude, after removal of the zodiacal emission, is more like 0.2. Explanations of this have invoked an additional population of grains with very small size (Draine and Anderson, 1985). A fuller discussion of this will be given in the next section when we deal with the HI-associated dust emission in the Galactic disc but now it is instructive to compare the results obtained when $\beta = 0.2$ is used instead of $\beta = 0.1$ to calculate the zodiacal emission contribution to the 60 μm band Galactic Plane maps. Henceforth our main result, using $\beta = 0.1$, and which we use to subtract the zodiacal emission from the Galactic Plane maps will be referred to as the 'standard grain' results. Those obtained using $\beta = 0.2$ will be called the 'small grain' results.

By following the same procedure as described above $\overline{\gamma}$, the mean ratio of 60 μm HI-associated dust intensity to HI column density, becomes $0.285\,\mathrm{MJy\,sr^{-1}(10^{20}cm^{-2})^{-1}}$. The ecliptic latitude profile for the small grain model, shown as the solid line in Fig. 2.6, is obtained. The dashed line in the same figure is the standard grain profile. The small grain profile is a few tenths of a $\mathrm{MJy\,sr^{-1}}$ below the previous estimation. This difference is negligible when examining regions close to the Galactic Plane but could be more important at higher latitudes.

It is interesting to compare our predictions of the zodiacal dust emission using both

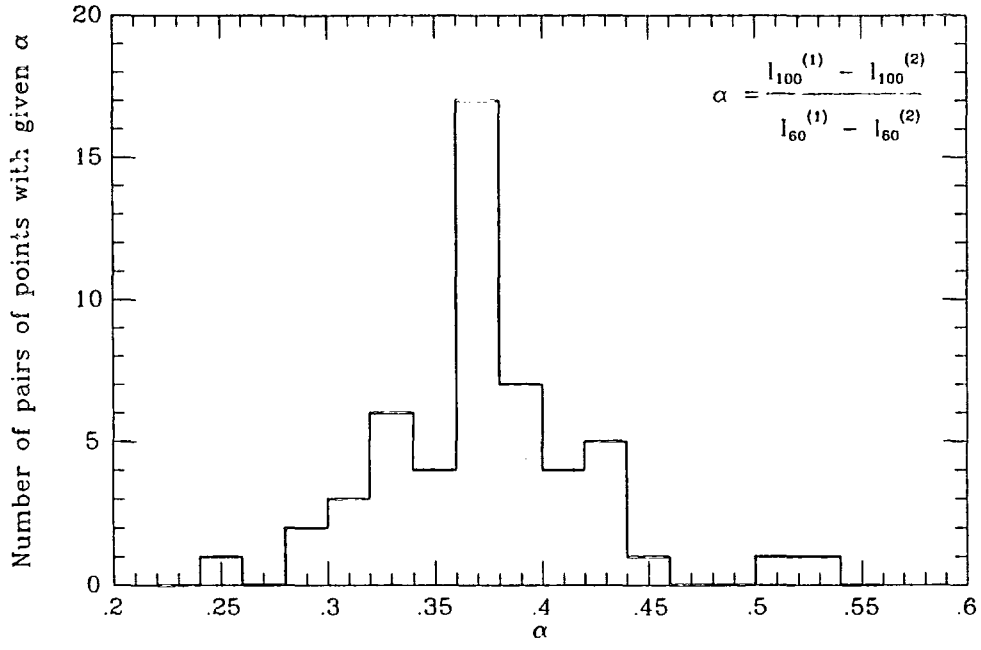

Figure 2.2: Histogram of the distribution of α, the ratio between 100 and 60 μm band emission from zodiacal dust for 52 pairs of points in the latitude range $40° > |b| > 70°$.

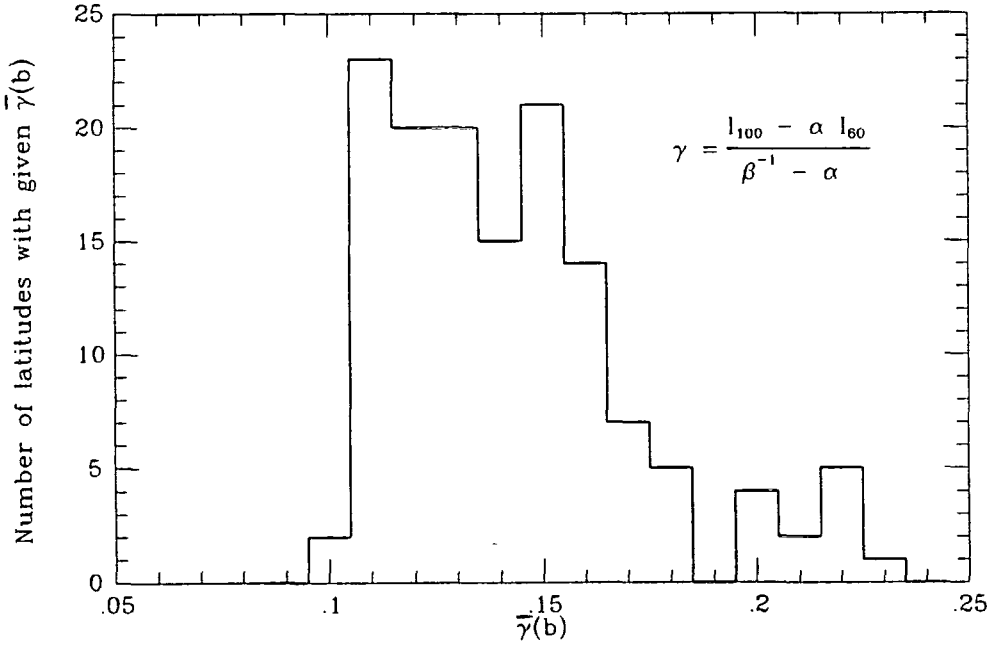

Figure 2.3: Histogram of the distribution of $\bar{\gamma}(b)$, the average 60 μm HI-associated intensity to HI column density ratio at galactic latitude b lying in the range $|b| > 20°$.

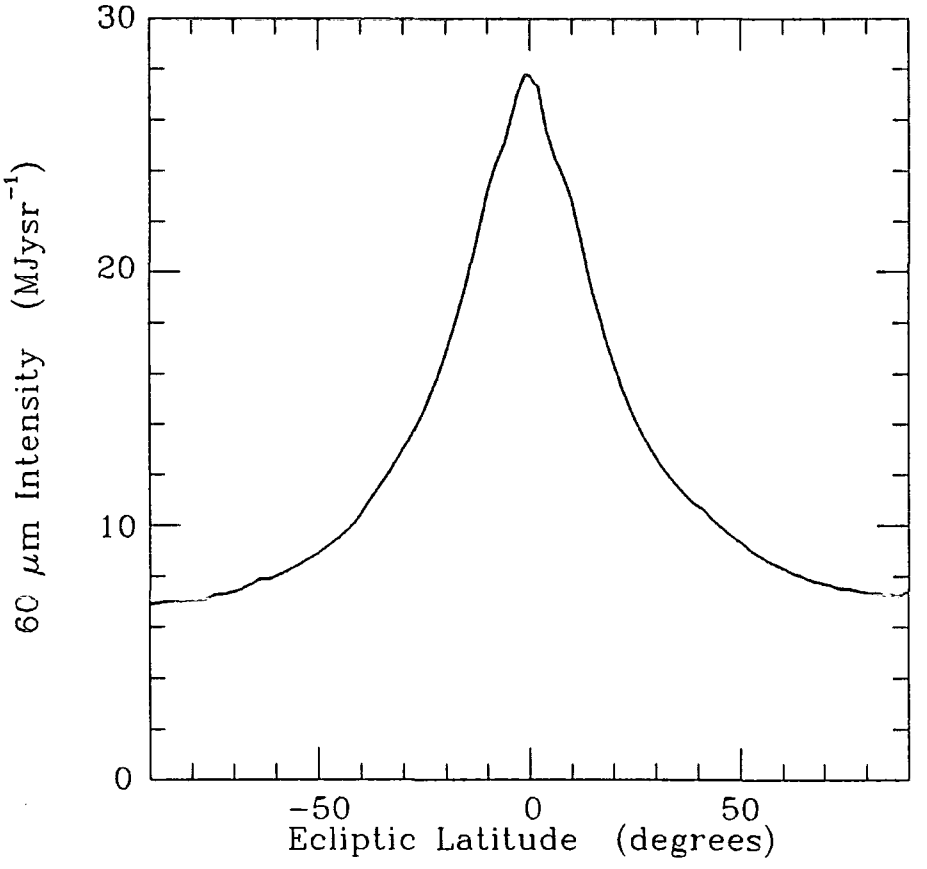

Figure 2.4: The variation of zodiacal light intensity at 60 μm with ecliptic latitude. This is the mean variation averaged over all ecliptic longitudes. As a first-order approximation, sufficiently accurate when working close to the Galactic Plane, the same variation has been used at all ecliptic longitudes.

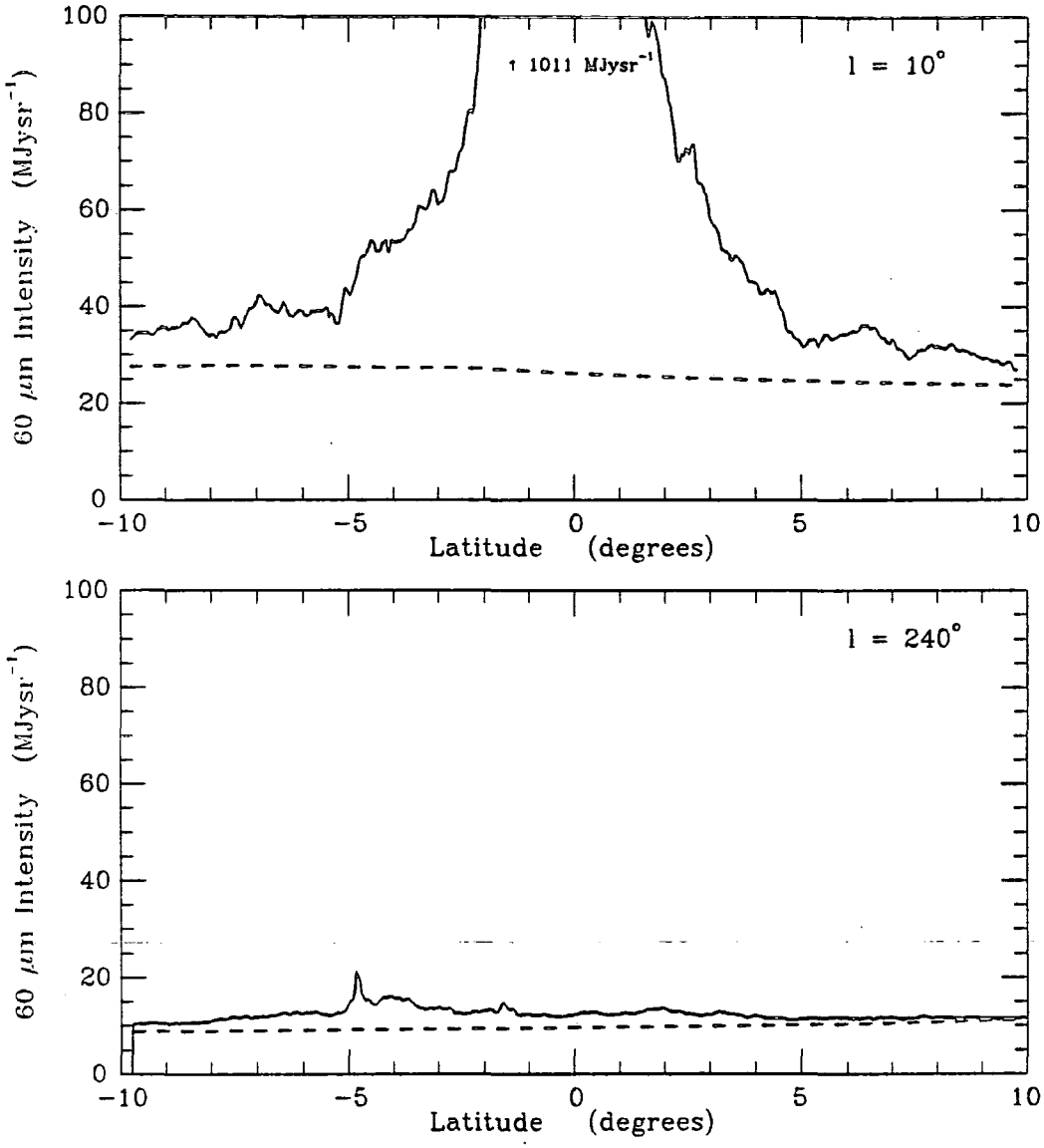

Figure 2.5: Cuts across the Galactic Plane showing the total observed 60 μm intensities (solid lines) and the modelled zodiacal light (dashed lines). The upper plot at $l = 10°$ has the zodiacal light close to its maximum value. It is a minor component however within a few degrees of the Galactic Plane. The lower plot at $l = 240°$ shows that part of the plane where the total emission is at a minimum and the zodiacal light has its greatest relative contribution.

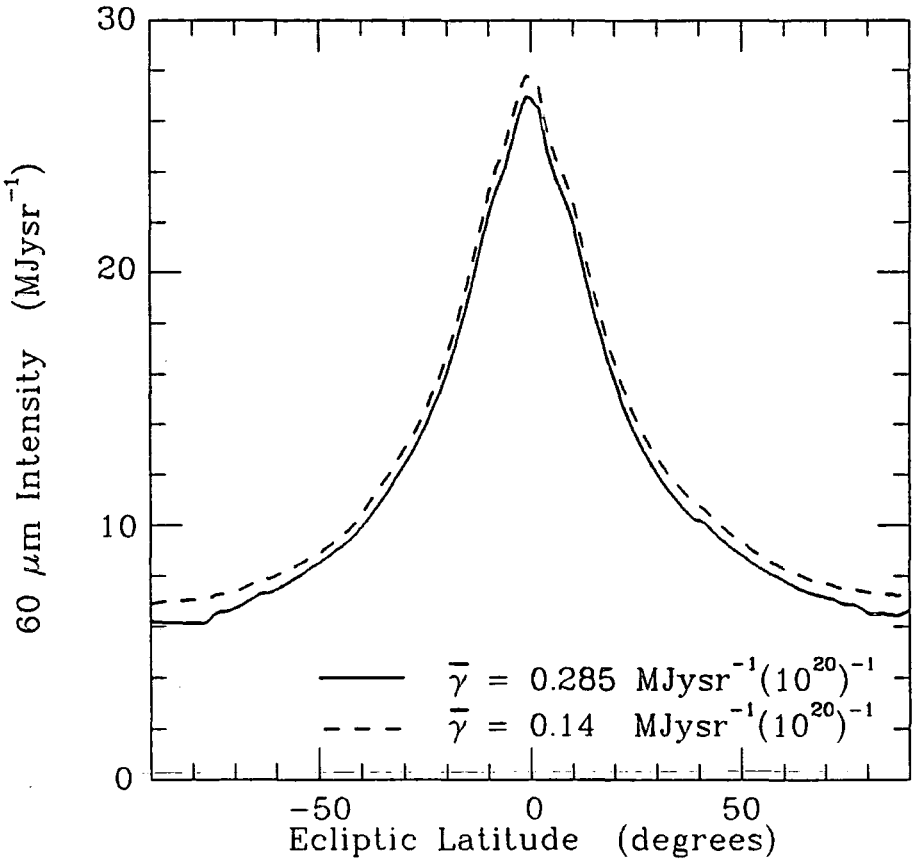

Figure 2.6: The variation of zodiacal light intensity at 60 μm with ecliptic latitude. The dashed curve is the same as that in Fig. 2.4 and is for 'standard grains' ($\beta = 0.1$). The solid line is for 'small grains' ($\beta = 0.2$). The two curves thus show the sensitivity to the assumed ratio of 60:100 μm intensities for Galactic emission at high galactic latitudes.

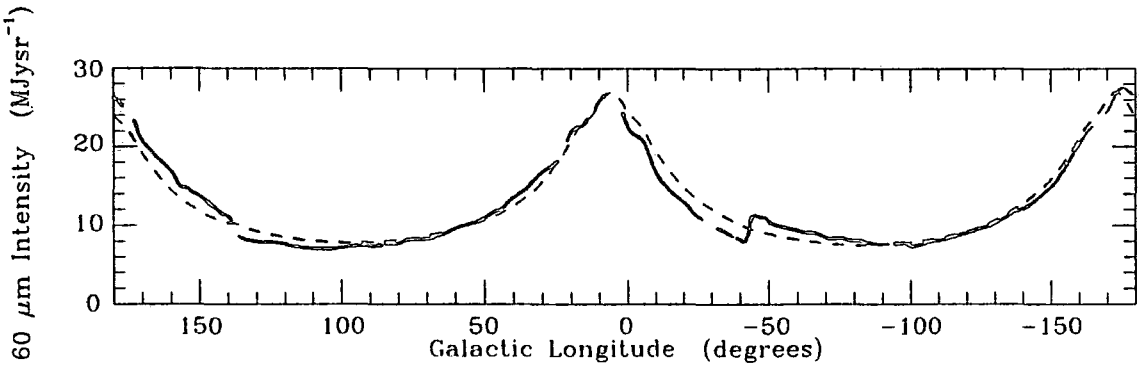

Figure 2.7: The variation along the Galactic Plane of the zodiacal light contribution to the 60 μm band intensity. The dashed line is derived from the ecliptic latitude variation for the 'small grain' model (solid line of Fig. 2.6). The solid line is taken from Sodroski *et al.* (1987).

values of β with the results of more accurate analyses performed by other authors. Sodroski *et al.* (1987) used a model which employs the Zodiacal Observation History File and they present a profile along the Galactic Plane of the zodiacal light contribution to the 60 μm band intensity. We can compare this directly with our results by deriving a similar Galactic Plane profile from the ecliptic latitude variation (Figs. 2.4 and 2.6). Fig. 2.7 shows the profile thus obtained for the small grain model. Superposed upon this is the profile taken from Sodroski *et al.* (1987). There are obvious differences between the two, most notably between galactic longitudes 310° and 330° where there is a discontinuity in the Sodroski *et al.* curve reflecting a change in orientation of the satellite's orbit with respect to the Sun. The maximum discrepancy between the two curves is of the order of 2.2 MJy sr^{-1}. Nevertheless, there are appreciable ranges of galactic longitude where the two curves are almost identical. The standard grain profile will lie a few tenths of a MJy sr^{-1} above the small grain profile of Fig. 2.7. For more detailed comparisons of the standard grain and small grain predictions for the HI-associated dust emission described in the next section we chose to study in particular galactic longitudes within the ranges $270° \geq l \geq 220°$ and $90° \geq l \geq 40°$, the directions over which our estimation of the zodiacal emission at 60 μm in the Galactic Plane are in accord with Sodroski *et al.*

Hauser *et al.* (1984) made one of the first studies of the diffuse IR emission observed by IRAS. He deduced that above ecliptic latitudes of 40° the zodiacal emission brightness depends on the cosecant of the ecliptic latitude. Tereby and Fich (1986) utilise this to eliminate the zodiacal emission from two regions in the outer Galaxy at 60 and 100 μm. Their results indicate that the ratio between the 60 and 100 μm zodiacal emission ($1/\alpha$) for the two regions are 2.2 and 1.9. They compare these values with those of Jongeneelen *et al.* (1986) and Hauser (1986) who find 60 to 100 μm zodiacal emission ratios of 1.9 ± 0.2 and 2.7 respectively.

Authors	$1/\alpha = I_{60\,ZL}/I_{100\,ZL}$[a]
Boulanger and Pérault (1988)	2.7
Boulanger *et al.* (1985)	2.8
Tereby and Fich (1986)	2.2 1.9
Jongeneelen *et al.* (1986)[b]	1.9 ± 0.2
Hauser (1986)[c]	2.7
Present work	2.7 ± 0.4

Table 2.1: Compilation of values determined for the ratio of 60 to 100 μm intensities of zodiacal light.

[a] $I_{60\,ZL}$ and $I_{100\,ZL}$ are intensity contributions at 60 and 100 μm from the zodiacal dust along a given line of sight.
[b] Preprint referred to by Tereby and Fich (1986).
[c] Private communication to Tereby and Fich (1986).

Boulanger *et al.* (1985) also made use of the Hauser *et al.* (1984) cosecant law at high ecliptic latitudes when studying a region at high galactic latitudes. To subtract the zodiacal emission from the 60 and 100 μm IRAS maps they use a value of $1/\alpha = 2.8$ which is deduced by extrapolation of the Hauser *et al.* spectra of zodiacal emission. Boulanger and Pérault (1988) assume, without obvious justification, a value of $\alpha = 0.371$ ($1/\alpha = 2.7$). All of these values are summarized in Table 2.1 together with our value of $1/\alpha = 2.7$. In passing, it is worth noting that Boulanger *et al.* (1985) found a value of the HI-associated dust intensity in the 100 μm band to HI column density ratio (γ/β in our notation) of $1.4 \pm 0.3\,\mathrm{MJy\,sr^{-1}}(10^{20}\mathrm{cm^{-2}})^{-1}$. This is the same as the value we obtain using either $\beta = 0.1$ or 0.2. The insensitivity of γ/β to β can be understood by considering Equation 2.3, noting that $\alpha\beta \ll 1$.

2.3 HI-associated dust emission

2.3.1 Introduction

The prediction of the emission from dust associated with neutral atomic hydrogen at FIR wavelengths in the Galactic disc was approached using three different models each of which is described in this section. The first model described assumes a constant interstellar radiation field (ISRF) over the whole Galaxy, the second considers the dust size distribution of Mathis *et al.* (1977) modified by Draine and Lee (1984) situated in an ISRF which varies with galactocentric radius and the third model is the same as the second except that an additional

population of very small grains is assumed. In all three models it is assumed that the HI-associated dust grains are heated only by the ISRF from which the dust grains absorb energy and re-radiate in the IR. For the purposes of the radio continuum separation programme we have used the predictions of the second model to subtract from the Galactic 60 μm band emission.

2.3.2 Model A: constant ISRF

By consideration of the best estimates available at the time of the variation with galactocentric distance of the surface brightness due to stellar illumination and the opacity of the Galactic disk, Mezger *et al.* (1982) deduced that the ISRF was nearly constant over the whole Galaxy. From this they deduced that the temperature of dust associated with neutral hydrogen also would be the same everywhere. Graphite grains would have a temperature of about 19 K. Working on this basis our first approach to predicting HI-associated FIR emission was to use a local value of the 60 μm HI-associated intensity to HI column density ratio ($I_{60\,\mathrm{HI}}/N_H$) and apply it to the whole of the Galactic disc. We found in the last section that for a 60 to 100 μm intensity ratio of 0.1 for the HI-associated dust emission at $|b| > 20°$ then the average $I_{60\,\mathrm{HI}}/N_H = 0.14\,\mathrm{MJy\,sr^{-1}}(10^{20}\mathrm{cm^{-2}})^{-1}$. Thus, multiplication of this solar neighbourhood value by the HI column densities along all lines of sight should yield the 60 μm HI-associated emission over the whole Galaxy.

The HI column densities used are from the Berkeley survey and the Durham-Parkes survey for the northern and southern sides of the Galactic Plane respectively and cover $|b| \leq 10°$. In Fig. 2.8 the upper profile is the total observed 60 μm emission from the inner part of the Galactic Plane with the Model A prediction for the HI-associated dust below. The intensities are averaged over $-0.5° \leq b \leq +0.5°$. Fig. 2.9 shows cross cuts across the Galactic Plane at various galactic longitudes for $-10° \leq b \leq +10°$ showing the total Galactic emission and Model A prediction for the HI-associated dust emission at 60 μm. Both Figs. 2.8 and 2.9 illustrate that in this model the HI-associated dust emission is only a very small contribution to the total ($\sim$ 1% at $l = 30°$, $b = 0°$) along the inner Galactic Plane. An estimate of the percentage of the total 60 μm emission due to HI-associated dust in the Galactic disc within $|b| \leq 1°$ and $79.5° \geq l \geq 280°$ is about 10% using this constant ISRF assumption. This was the model assumed in Haslam and Osborne (1987).

2.3.3 Model B: standard grains in a varying ISRF

In a paper by Cox, Krügel and Mezger (1986) a model of the emission of dust grains heated by the ISRF is presented which is an improvement on the Mezger *et al.* (1982) model following the recalculation of the ISRF in the light of new observations and new investigations of the optical properties of dust grains. The re-evaluated ISRF of Mathis *et al.* (1983), unlike that of Mezger (1982), decreases with increasing galactocentric radius which means that the dust temperatures also vary in a similar manner. The dust model assumed by Cox *et al.* is basically that of Mathis *et al.* (1977). The dust grains are of silicate and graphite and the particle size distribution of each species follows the form $f(a) \propto a^{-3.5}$ where $f(a)da$ is the number density of grains with radii between a and $a + da$. The size

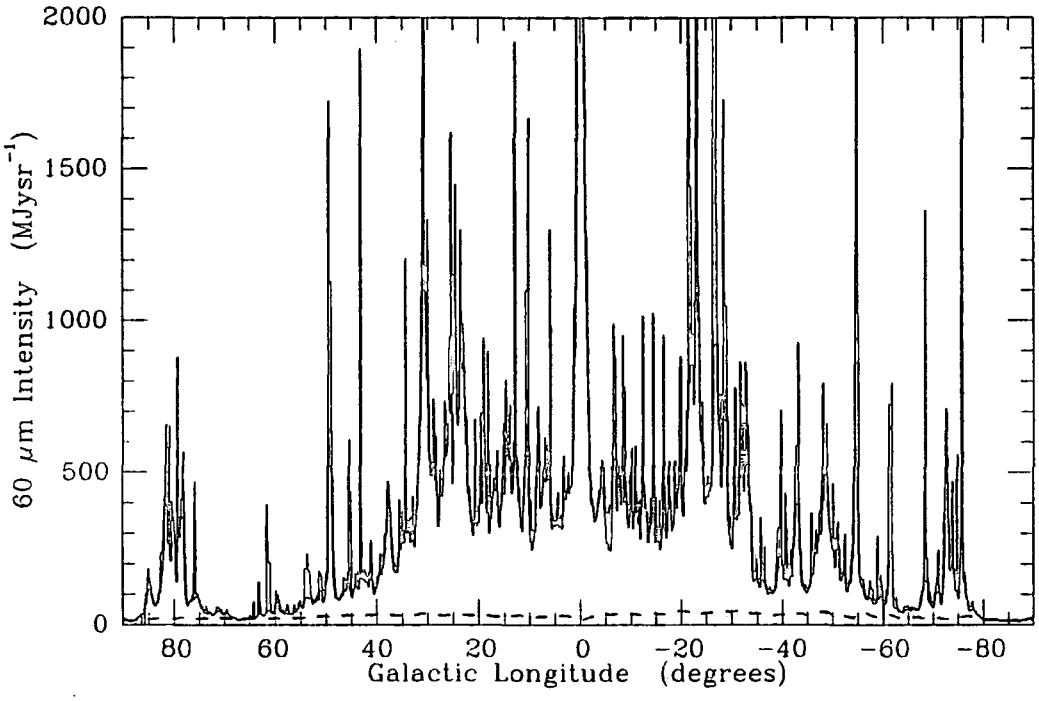

Figure 2.8: Profiles of the total observed 60 μm emission for the inner part of the Galactic Plane averaged over $|b| \leq 0.5°$ (solid line) and the Model A prediction for the HI-associated dust assuming a constant ISRF (dashed line).

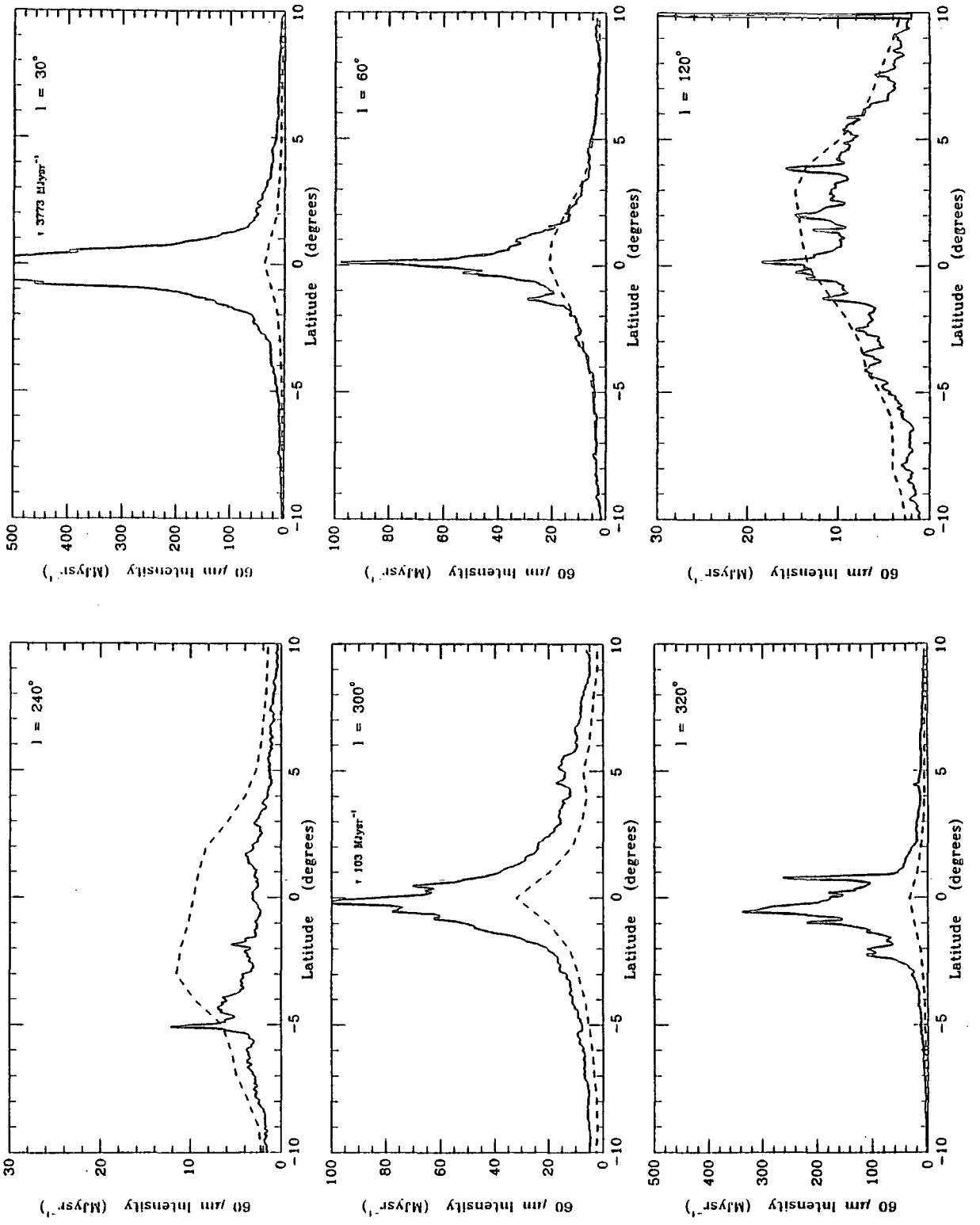

Figure 2.9: Six cuts across the Galactic Plane showing the HI-associated 60 μm emission predicted using Model A which assumes a constant ISRF and a HI-associated 60 μm intensity to HI column density ratio of $0.14\,\mathrm{MJy\,sr^{-1}}(10^{20}\,\mathrm{cm^{-2}})^{-1}$ (dashed line). Also shown is the total Galactic emission (solid line). In the outer Galaxy, predicted HI-associated emission tends to exceed the total while in the inner Galaxy close to the plane it is only a very small fraction of the total emission.

Wavelength	Absorption cross-section (cm^2/H-atom)		
	silicate	graphite	total
$60\,\mu m$	7.4×10^{-25}	1.1×10^{-24}	1.8×10^{-24}
$100\,\mu m$	2.5×10^{-25}	4.1×10^{-25}	6.6×10^{-25}

Table 2.2: Absorption cross-sections in cm^2/H-atom taken from Fig. 17 of Cox *et al.* (1986).

range for graphite grains in Mathis *et al.* is $\sim 1\,\mu m$ down to 50 Å. Using this model it is possible to fit the observed interstellar extinction curve between wavelengths of $0.11\,\mu m$ and $1\,\mu m$, including the $0.2\,\mu m$ feature attributed to graphite, assuming the optical constants of Tosatti and Bassini (1970).

Draine and Lee (1984) re-investigated the dielectric functions of graphite and silicates and using their results, together with the grain size distribution of Mathis *et al.* (1983), they evaluated the theoretical extinction curve in the UV, visible and IR. The fit to the observations was optimized in the visible and UV by adjusting the abundances of the two types of grains and appears to be in good agreement generally over the whole range of wavelengths studied. The absorptivity of the silicate grains in the FIR that Draine and Lee deduced was much smaller than that assumed by Mezger *et al.* (1982).

Cox *et al.* adopted the absorption coefficients of Draine and Lee in the FIR and recalculated the temperatures of the silicate grains exposed to the ISRF. The other modification made by Cox *et al.* to the Mathis *et al.* (1977) model was to extend the range of radii of the grains down to ~5 Å which increases the dust emission at mid IR (MIR) wavelengths. The temperature variation with galactocentric radius of graphite and silicate grains heated by the ISRF is shown in Fig. 2.10 and is taken from Fig. 5 of Cox *et al.* (1986).

We use the temperature variation shown in Fig. 2.10 together with an estimation of the absorption cross-section in our second model for the HI-associated dust emission at FIR wavelengths. The absorption cross-sections per hydrogen atom of graphite and silicate grains in the local solar neighbourhood are taken from Cox *et al.* and the variation with galactocentric radius is assumed to follow the metallicity gradient. Table 2.2 shows the adopted absorption cross-sections per H-atom in the solar vicinity at 60 and $100\,\mu m$ for silicate and graphite grains. Equation 1 of Cox *et al.* expresses the volume emissivity of dust grains in terms of the hydrogen number density, the metallicity and temperature of the dust grains. From this we deduce that an element along a given line of sight at a galactocentric radius R contributes ΔI_λ to the total brightness intensity in that direction in the IRAS waveband centred at λ where ΔI_λ is given by:

$$\Delta I_\lambda = \Delta N_H \left(\frac{z}{z_\odot}\right) \sum_i \sigma_{\nu i} B_\nu(T_i) K_i \qquad (2.5)$$

- ΔN_H is the contribution of the element to the HI column density along the line of sight.

- $z/z_\odot$ is the metallicity gradient assumed to be the same as that for the [O/H] abundance given by Güsten and Mezger (1983). It has the form:

$$\frac{z}{z_\odot} = \exp(-0.12\left(\frac{R}{\text{kpc}} - 10\right)) \tag{2.6}$$

- $\sigma_{\nu i}$ is the absorption cross-section at the effective frequency of the IRAS band for the dust species i, i being either silicate or graphite.

- $B_\nu(T_i)$ is the Planck function at the effective frequency of the IRAS band and temperature T_i of the dust species i.

- K_i is the colour correction factor and its inclusion in Equation 2.5 means that intensities are directly comparable with those quoted in the IRAS survey. It takes into account the relative system response over the IRAS passbands and also the spectral energy distribution intrinsic to the source. Here the emission spectrum of the dust is assumed to follow a modified Planck curve, $\nu^2 B_\nu$, in accordance with the λ^{-2} emissivity law which was imposed on the basis of observations by Draine and Lee when calculating their absorption cross-sections of silicate grains for $\lambda > 20\mu$m. Over the range of temperatures of the dust grains considered here the value of K varies between 0.93 and 2.8 for the 60 μm band and 0.95 and 1.1 for the 100 μm band. Details of the colour correction are given in the IRAS Explanatory Supplement.

Fig. 2.11 shows $\Delta I_\lambda / \Delta N_H$ as a function of galactocentric radius for the 60 and 100 μm bands. The graphite grains are the dominant contributors to the total ratio at these wavelengths. Note that there is a very steep increase of emissivity per hydrogen atom with decreasing galactocentric radius of about 2 and 3 orders of magnitude for the 100 and 60 μm bands respectively. This sharp rise is largely due to the temperature variation of the grains as can be seen by the flattening off of the curve at 12 kpc beyond which the dust temperatures are assumed constant.

To calculate the total intensity of the HI-associated dust emission along any line of sight within 10° of the Galactic Plane we used this radial dependence of $\Delta I_\lambda / \Delta N_H$ in combination with the three dimensional information contained in the Durham-Parkes and Berkeley 21 cm surveys. For each direction sampled in the surveys, brightness temperature profiles in line of sight velocity space are available. In the approximation of circular rotation about the axis through the centre of the Galaxy and perpendicular to the Galactic Plane, a tangential velocity, V, is associated with a galactocentric radius, R, with $V_\odot$ and $R_\odot$ being the values for the solar circle. Referring to Fig. 2.12, the line of sight velocity $v - v_\odot = \Delta v$ is given by the equation:

$$\left(\frac{\Delta v}{\sin l} + V_\odot\right) \frac{1}{R_\odot} = \frac{V}{R} \tag{2.7}$$

where l is the galactic longitude. Thus for each velocity channel the ratio V/R can be calculated. To assign a galactocentric radius to each value of V/R we used the rotation curve of Burton and Gordon (1978) who assume $V_\odot = 250\,\text{km s}^{-1}$ and $R_\odot = 10\,\text{kpc}$. For all R between $R = 0.1$ and 20 kpc there is a unique value of V/R.

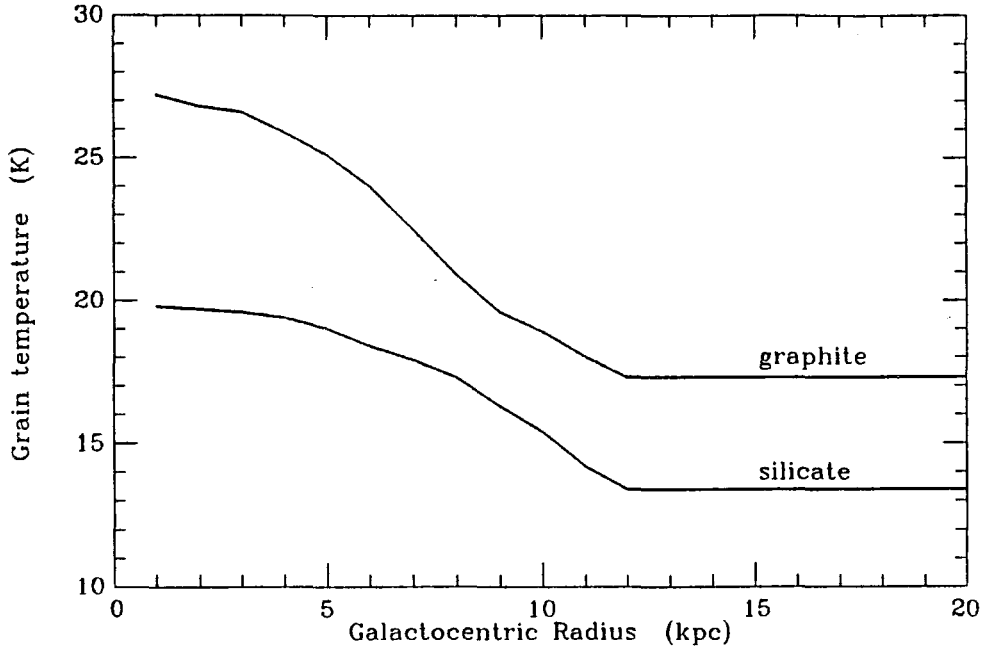

Figure 2.10: The temperature variation of graphite and silicate grains heated by the general ISRF which varies with galactocentric radius. Taken from Cox *et al.* (1986).

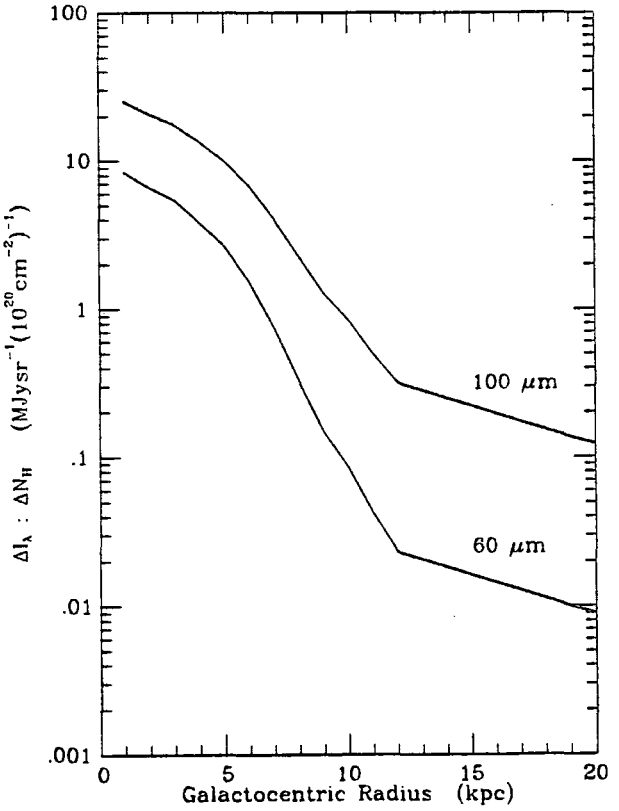

Figure 2.11: The variation with galactocentric radius of 60 and 100 μm band HI-associated dust intensity per 10^{20}cm^{-2} in HI column density calculated using Equation 2.5.

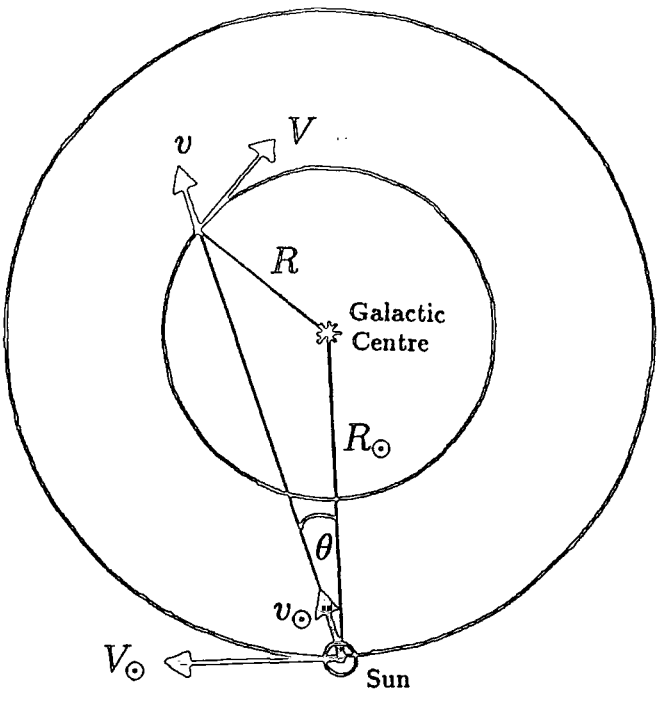

Figure 2.12: Diagram illustrating the terms in Equation 2.7

For a given velocity channel corresponding to velocity V and having brightness temperature $T_b(V)$, the optical depth is:

$$\tau(V) = -\ln\left(1 - \frac{T_b(V)}{T_s}\right) \tag{2.8}$$

where T_s is the gas spin temperature. The HI column density along a particular line of sight is given by:

$$N_H(l,b) = 1.823 \times 10^{18} \int_0^\infty T_s \tau(V)\, dV \text{ cm}^{-2} \tag{2.9}$$

(from Burton, 1976). Thus if:

$$\frac{\Delta I_\lambda}{\Delta N_H}(V) = \frac{\Delta I_\lambda}{\Delta N_H}(R)$$

where V is the circular velocity associated with galactocentric radius R, then the total HI-associated dust intensity in that direction, I_λ, in the IRAS band centred at wavelength λ, can be calculated from the velocity profiles and Equation 2.5 using the expression:

$$I_\lambda(l,b) = 1.823 \times 10^{18} T_s \sum \frac{\Delta I_\lambda}{\Delta N_H}(V)\tau(V)\, \Delta V \text{ Jy sr}^{-1} \tag{2.10}$$

The sum is over the velocity channels of the profile and ΔV is the channel width. We assume that the spin temperature is 135 K everywhere.

Obviously in the Galactic Centre and anticentre directions the assumption of circular rotation in obtaining the distance of the emitting HI regions breaks down since all line of sight velocities should be zero. The fact that there are non-zero temperatures for velocity

channels other than the $V = 0$ channel in the anticentre direction illustrates that there are deviations from the circular rotation approximation. Deviations from the average rotation velocities of the HI exist on large scales in the vicinity of spiral arms as well as on smaller scales. Burton (1970) estimated that the magnitude of large scale streaming motion of HI in the Galactic Plane amounts to between 3 and 8 $\mathrm{km\,s^{-1}}$. Suppose that in our calculations of the 60 μm HI-associated emission along a particular line of sight gas situated at $R = 7\,\mathrm{kpc}$ say has a velocity of 5 $\mathrm{km\,s^{-1}}$ higher (lower) than that of the average rotation curve. This gas would then be assigned a kinematic galactocentric radius of 8.2 (6.4) kpc and therefore a 60 μm intensity per H-atom of 0.28 (1.28) instead of 0.75 $\mathrm{MJy\,sr^{-1}(10^{20}cm^{-2})^{-1}}$. In this example of the magnitude of the deviations incurred we have chosen a radius at which the ratio $\Delta I_{60}/\Delta N_H$ is varying most rapidly. Since there is no straightforward solution to this problem we will not try to correct for it but merely acknowledge that it exists. We point out however that the integration along each line of sight will reduce its effect on our calculations of the 60 μm HI-associated emission.

In the Galactic Centre direction an estimation for the HI-associated emission was not even attempted because there is the additional problem that the emission in this direction becomes optically thick. The Galactic Centre is a special region and therefore we accept that our procedure for separating the radio continuum emission from the Galactic disc will probably not apply here.

We note that both the Berkeley and Durham-Parkes surveys are at a lower resolution (35.5′ and 15′ respectively) than the 4′– 6′ of the IRAS Galactic Plane survey. In addition, the Durham-Parkes survey is undersampled. Rather than lose the important information on the detailed correlation between the radio continuum and IR emission we did not convolve the IRAS data to the lower resolutions before subtracting the HI-associated emission. Study of the correlation is mainly concentrated within 1.5° of the inner Galactic Plane where the HI-associated emission is not generally the major component. The subtraction of estimates made at lower resolution will add some noise to the correlation. Fig. 2.13 shows the profile, averaged over $|b| \leq 0.5°$ for (*a*) the inner and (*b*) the outer Galactic Plane, of the 60 μm band intensity with the zodiacal light contamination removed, together with the corresponding profile for the predicted HI-associated dust intensity. The averaging should help to reduce the discrepancies introduced because of the different resolutions of the HI and IRAS surveys.

Fig. 2.14 shows six typical cuts across the Galactic Plane taken at longitudes in all four quadrants. Again, the IRAS 60 μm intensity with zodiacal light removed is shown together with the predicted contribution from HI-associated dust. It should be noted that at higher latitudes, where we would expect there to be little ionized hydrogen, the two curves converge remarkably well considering that at these latitudes the estimated zodiacal light contamination is several times larger than the residual emission. This can be seen by comparing the cuts for $l = 240°$ in Figs. 2.5 and 2.14. Also, it can be seen that within $1\frac{1}{2}°$ of the Galactic Plane the HI-associated emission in general does not dominate but rather the residual which we would suggest is emission from the HII-associated dust.

The 60 μm band HI-associated dust emission was predicted for all galactic longitudes within the latitude range $|b| \leq 10°$. Also, 100 μm band predictions were made by using the $\Delta I_{100}/\Delta N_H$ values shown in Fig. 2.11 but only for a limited range of longitudes

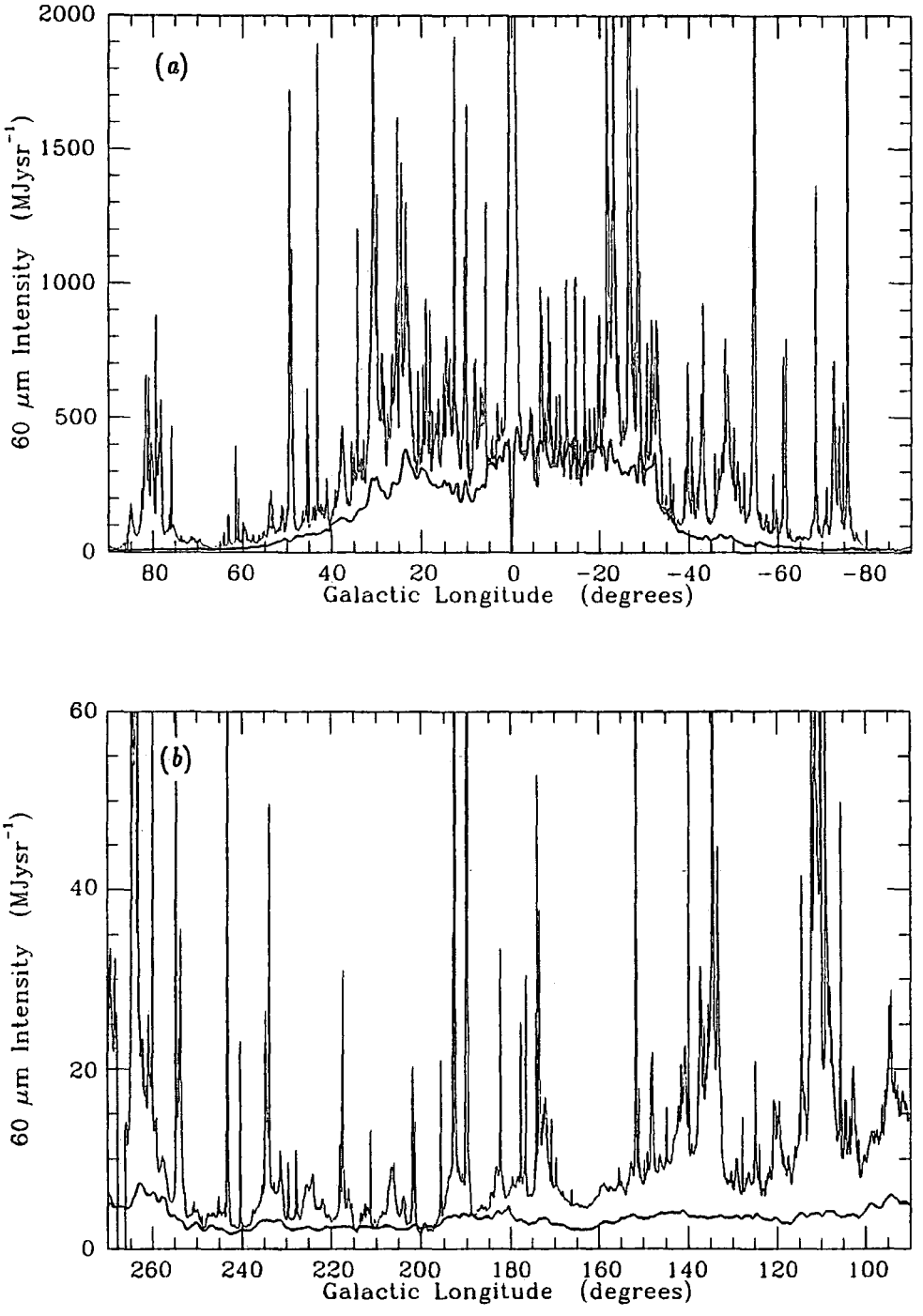

Figure 2.13: Profiles of the total observed 60 μm band emission for (a) the inner and (b) the outer parts of the Galactic Plane averaged over $|b| \leq 0.5°$(upper line)and the corresponding Model B predictions for the HI-associated dust (lower lines). Model B assumes a 'standard grain' distribution heated by a ISRF which varies with galactocentric radius. The local minimum at $l = 0°$ is an artefact of the modelling.

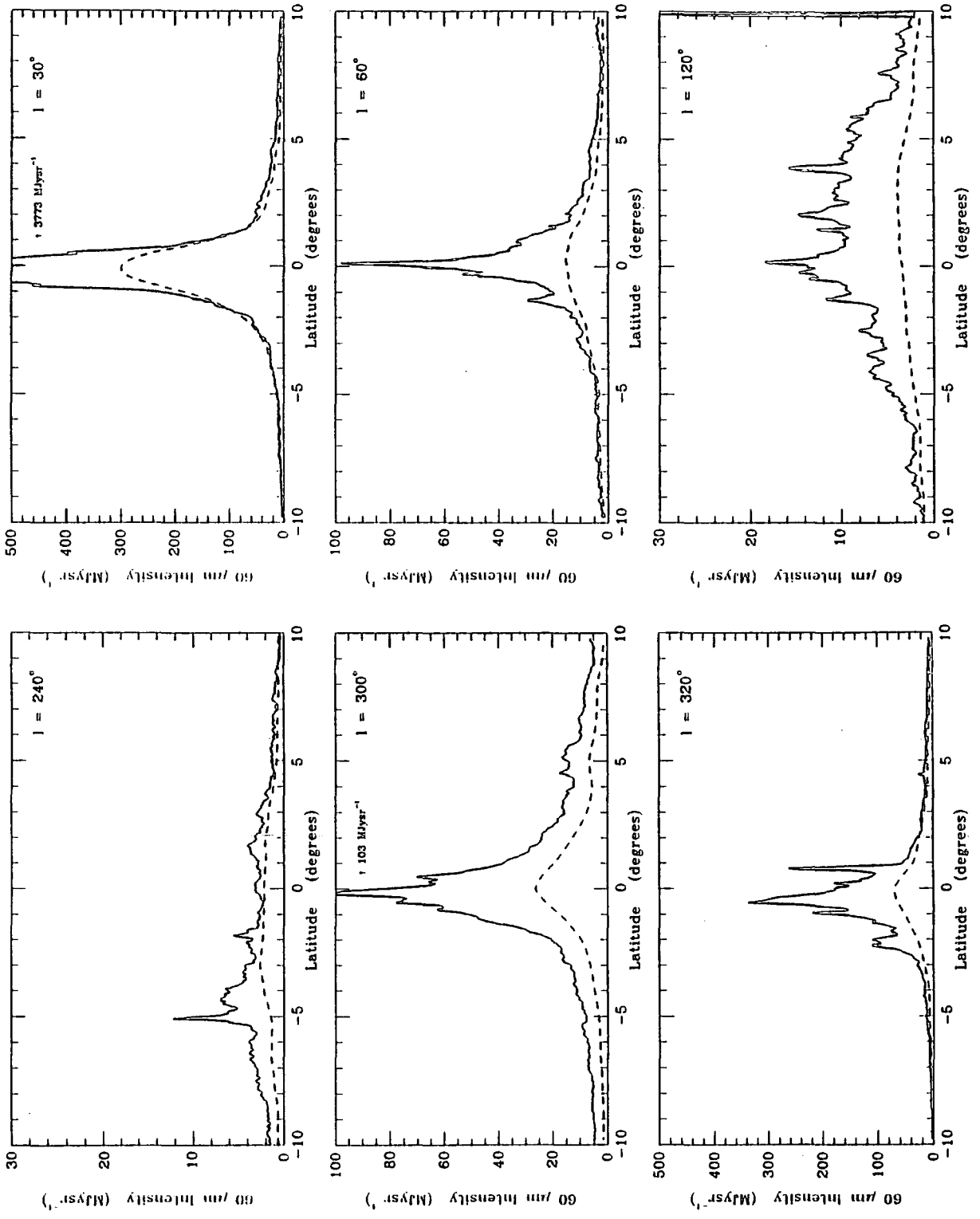

Figure 2.14: Six cuts across the Galactic Plane showing the Model B predicted HI-associated component (dashed line) relative to the total Galactic emission (solid line) at 60 μm. This component fits the observations well at latitudes $\gtrsim 5°$ for most longitudes and it is the predictions made by this model which we use to estimate the HI component of the 60 μm band emission in the radio continuum separation method.

($79.5° \geq l \geq 10°$) in the first quadrant. This region was covered by the Berkeley 21 cm survey which has a resolution of $35\frac{1}{2}'$. For this limited area of sky the IRAS data at both 60 and 100 μm were convolved to the lower resolution of the HI survey assuming that the effective telescope beams are gaussian. Fig. 2.15 shows profiles for (a) the 60 μm and (b) the 100 μm band for $79.5° \geq l \geq 10°$. Each line represents an average over $\pm 0.5°$ in galactic latitude. The upper profile in each plot is the IR emission after removal of the zodiacal light contamination. The lower solid line is the predicted HI-associated dust contribution from Model B. The dotted line is the HI-associated dust contribution which is predicted by Model A. Comparison of the profiles predicted at 60 μm by Model A and Model B shows that at higher longitudes the two are not too far removed from each other as might be expected but closer towards the Galactic Centre direction the predictions for Model B become as much as an order of magnitude larger than those for Model A. From the convolved data we deduce for Model B over $79.5° \geq l \geq 10°$ and $|b| \leq 0.5°$ that HI-associated dust contributes $\sim 42\%$ of the total emission in the 60 μm band and $\sim 53\%$ in the 100 μm band. Fig. 2.16 shows two cuts across the Galactic Plane at $l = 60°$ and 30° for the 100 μm band which correspond to the 60 μm band cross-cuts shown in Fig. 2.14 apart from the different resolution of the total emission.

2.3.4 Colour temperatures

Over the area for which both 60 and 100 μm HI-associated dust contributions have been predicted and for which the IRAS Galactic Plane maps with zodiacal emission subtracted have been convolved to the resolution of the HI surveys, the ratio of the 60 to 100 μm intensities could be found for the various components. In Fig. 2.17 are shown profiles of the ratio of 60 to 100 μm intensities of (a) the total emission less zodiacal light, (b) the predicted HI-associated dust emission and (c) the residual emission having subtracted (b) from (a). The profiles are averages over $|b| \leq \frac{1}{2}°$. Assuming that the dust grain emissivity follows an inverse-square wavelength variation and applying the necessary colour corrections, effective colour temperatures along the line of sight can be assigned to the 60 to 100 μm ratios. These temperatures are marked on the profiles also.

The total intensity ratios shown in profile (a) of Fig. 2.17 appears fairly constant over the whole range of longitude at a value of about 0.22 corresponding to a temperature of about 23 K. This confirms the findings of other authors (*e.g.* Sodroski *et al.*, 1987; Cox and Mezger, 1987). The excursions above the mean level occur at the positions of large HII complexes which are seen on the 11 cm survey of Reich *et al.* (1984). In profile (b), the colour temperature of HI-associated dust emission increases monotonically with decreasing galactic longitude from a temperature of about 18 K at $l = 79\frac{1}{2}°$ to 24 K at $l = 10°$. This reflects the 17 to 25 K temperature variation with galactocentric distance of the graphite grains which dominate the emission at 60 and 100 μm in Model B.

Since the observed total intensity ratio is fairly constant and the predicted HI intensity ratios for this standard grain model increases towards the Galactic Centre, the ratios of the residual emission necessarily decreases towards the lower longitudes as is shown in profile (c) of Fig. 2.17. The colour temperature remains fairly constant at ~ 28 K between $l = 79.5°$

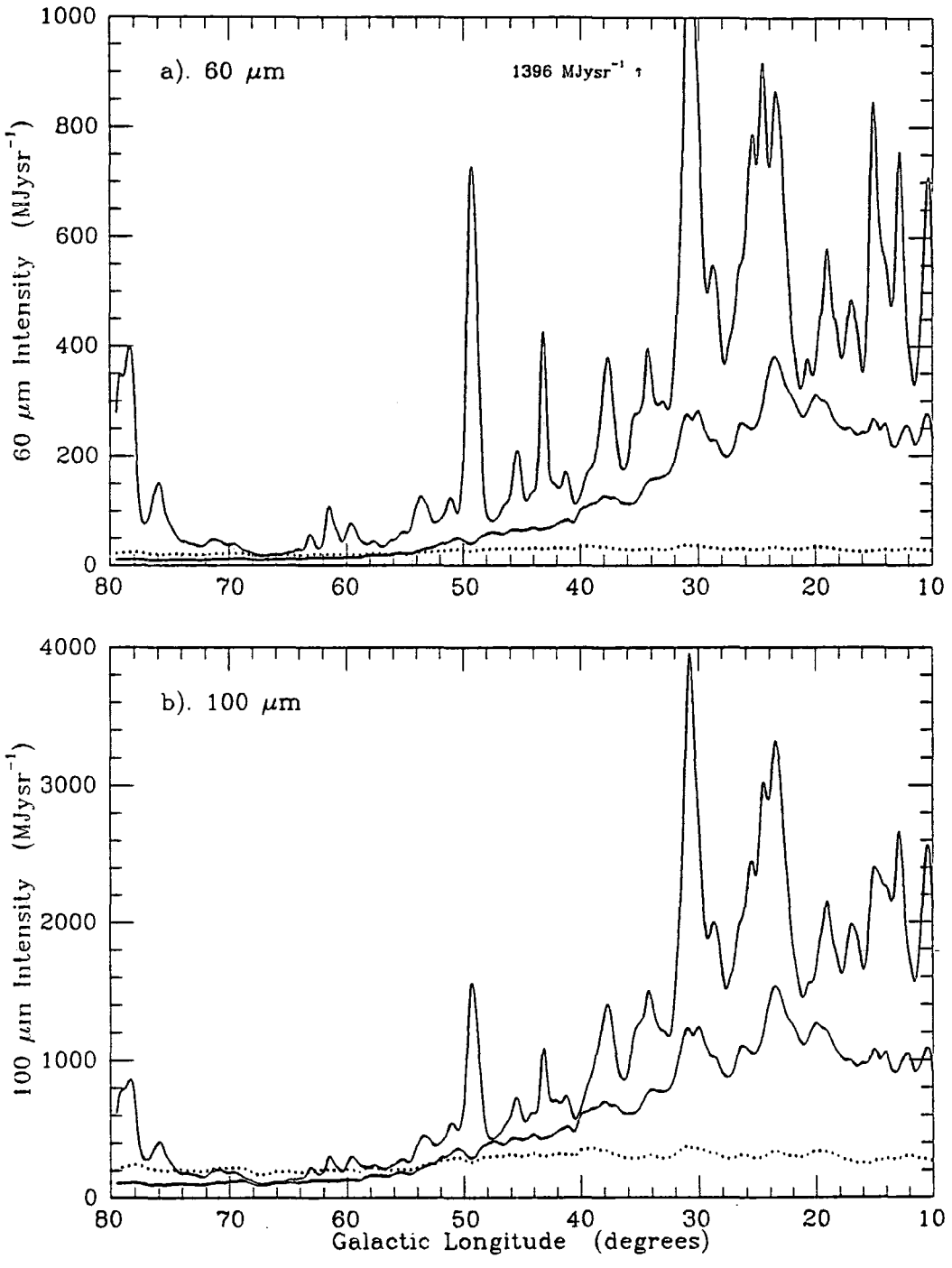

Figure 2.15: Profiles for (*a*) the 60 μm and (*b*) the 100 μm band for the longitude range $79\frac{1}{2}^\circ \geq l \geq 10^\circ$. In each the top solid line is the total Galactic emission, the lower solid line is the predicted HI-associated component when the dust temperature variation with galactocentric radius follows the model of Cox *et al.* (Model B), and the dotted line is the HI contribution predicted assuming a constant ISRF (Model A). Each line represents an average over $-0.5^\circ \leq b \leq +0.5^\circ$ and the total Galactic emission has been convolved to the same resolution as the HI surveys.

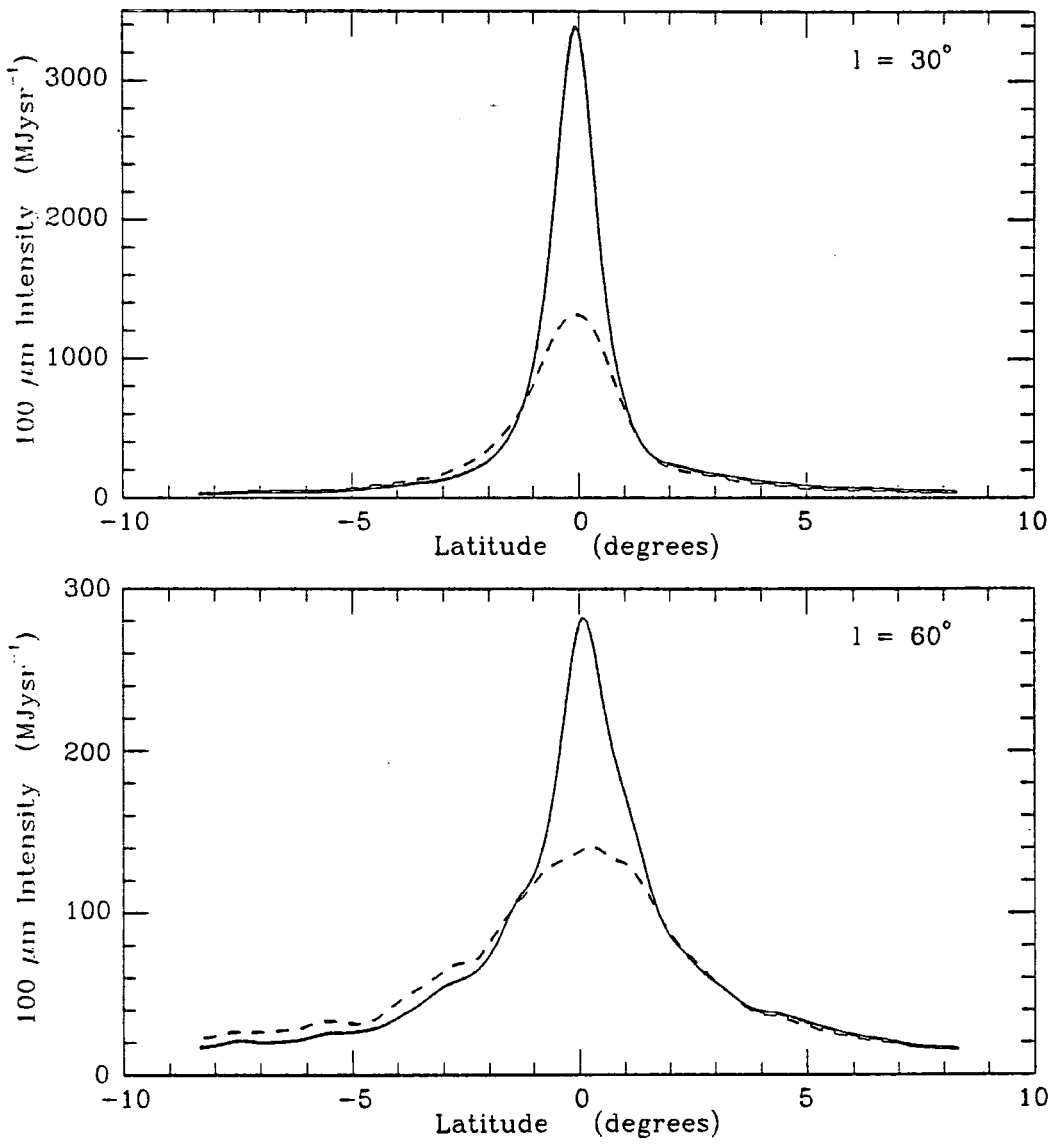

Figure 2.16: Two cuts across the Galactic Plane of the total Galactic emission at 100 μm (solid line) and the HI-associated dust emission at 100 μm assuming a dust temperature variation with galactocentric radius following the model of Cox *et al.* (Model B) (dashed line).

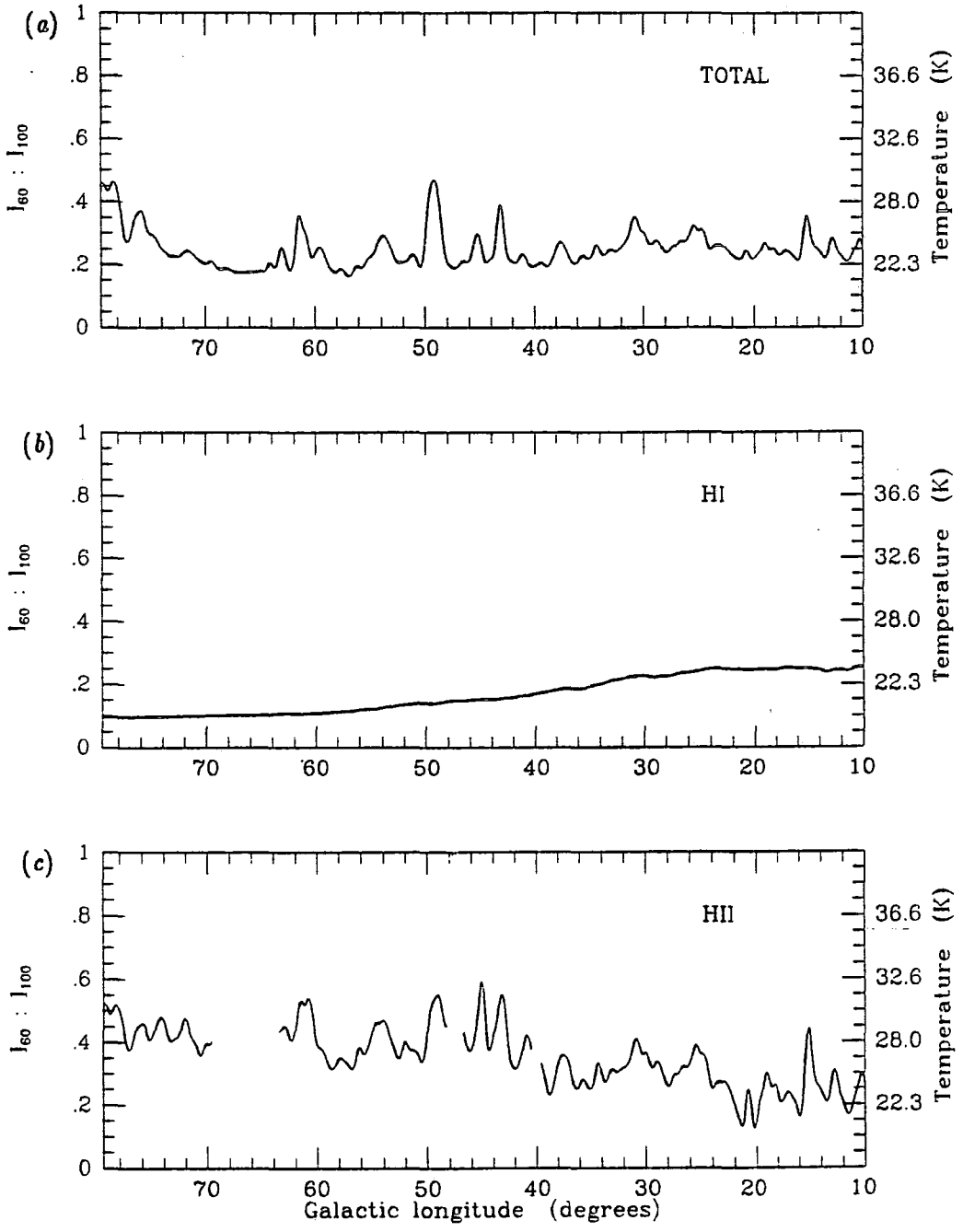

Figure 2.17: Profiles of the ratio of 60:100 μm intensity along the Galactic Plane. The top line, (*a*), represents the observed values. The middle line, (*b*), is the predicted ratio for HI-associated emission (Model B). The bottom line, (*c*), shows the ratio of the residuals when the HI-associated emission is subtracted from the observed values. Blank regions appear where the residual 100 μm emission is very small and the error in the ratio would be very large. The implied colour temperatures are shown on the right hand side. The lines represent averages over $|b| \leq 0.5°$.

and 40° but drops steadily to $\sim 23\,\mathrm{K}$ at $l = 10°$.

In the next chapter we will attempt to provide more arguments that this residual emission does emanate from HII-associated dust. For the present however, if one accepts that this is the case and that the Model B predictions for HI-associated dust emission also are correct then we are faced with the problem of explaining the decrease in colour temperature with decreasing galactic longitude of the HII-associated component whilst the total observed 60 to 100 μm ratios remain reasonably constant.

Harwit *et al.* (1986) suggested that some of the diffuse IRAS emission from cirrus clouds could be due to fine-structure line emission. In low density ionized regions the line at 88.35 μm due to doubly ionized oxygen would contribute to the 100 μm IRAS band but hardly at all to the 60 μm band. We suggest therefore that if this 88 μm line contributes an appreciable amount to the 100 μm band intensities from compact and ELD HII regions close to the Galactic Plane then a decrease in the apparent 60 to 100 μm colour temperature could be explained in terms of an increased [OIII/O] abundance ratio towards the Galactic Centre since the dust-to-gas mass ratio was assumed to follow the [O/H] gradient.

Unfortunately, due to insufficient measurements of the OIII line in the Galactic Plane, testing this hypothesis has proved difficult. A necessarily rough estimate using line measurements of Watson *et al.* (1981) suggests that for the HII region M17 at least the contribution to the 100 μm band flux by the 88 μm line could be about 6%. Attempts to establish the behaviour of $[O^{++}/O]$ with galactocentric radius have been thwarted by a lack of data for HII regions within 6 kpc of the Galactic Centre.

An alternative explanation of the colour temperatures in Fig. 2.17 is that the ratios of the 60 to 100 μm intensities for the HI-associated dust emission predicted by Model B are at fault and that in reality the ratios for both the HI- and HII-associated dust are constant with galactic longitude. It was with this in mind that we explored a third model for the HI-associated dust emission despite the fact that the cross-cuts of the predictions from the second, standard grain model and of the observations agree impressively well in the wings without any normalization. The third model, the small grain model, is discussed below.

2.3.5 Model C: small grains

The constancy of the 60 to 100 μm intensity ratio (I_{60}/I_{100}) on large scales along the Galactic Plane at a value of ~0.2 which we demonstrate in Fig. 2.17, has been noted by many authors (*e.g.* Cox and Mezger, 1987; Pérault *et al.*, 1988; Sodroski *et al.*, 1987). It is also seen in the discs of other spiral galaxies (Beck and Golla, 1988). Sodroski *et al.* (1987) deduced that the effective line of sight dust temperature is about 24 K for much of the inner Galactic Plane with a slight decrease of 1 K in the outer Galaxy whereas the IR luminosity per H-atom decreases 4 or 5 fold. A similar behaviour has been noted in M31 by Walterbos and Schwering (1987) who found that although the ISRF varies with distance from the centre of the Andromeda Galaxy and the 100 μm emission to HI column density ratio (I_{100}/N_H) varies by a factor of 2, the 60 to 100 μm ratio only changes from 0.14 to 0.22 over 80% of the disc. This corresponds to a dust temperature variation of 20 to 23 K assuming a λ^{-2} emissivity law for the grains.

Tereby and Fich (1986) made a study of the strong correlation of the IR emission and atomic hydrogen in two regions in the outer Galaxy near the plane. From their analysis of the two $\sim 20° \times 20°$ fields they deduced that the I_{60}/N_H ratios are not the same even within the quoted errors but the values of I_{60}/I_{100} obtained by a least squares fit for each region agree remarkably well.

Studies also have been made of the IR radiation emitted locally. Low *et al.* (1984) looked at emission at high galactic latitudes and in particular they discuss four IR cirrus features which have associated local maxima in HI column density. The I_{60}/I_{100} values vary between 0.15 and 0.3 having a mean value of 0.21. In the comparison of the HI and IR emission from a field $20° \times 18°$ in extent at high galactic latitude, Boulanger *et al.* (1985) find a strong correlation between HI column densities and IR emission in all four IRAS wavebands. Their study of the spectrum of one cirrus feature close to this area indicates a I_{60}/I_{100} ratio of 0.21. Other small regions of sky at high galactic latitude were investigated by Boulanger and Pérault (1988) by considering the 60 and 100 μm emission as well as the HI column densities. Again, although they found a linear relationship of the IR emission to HI column densities within each area, there were variations of I_λ/N_H between areas whilst the I_{60}/I_{100} ratio only changed between 0.19 and 0.22 over the fields. The average I_{60}/I_{100} ratio for three high latitude molecular clouds situated centrally in IRAS cirrus features and which were studied by Weiland *et al.* (1986) each have the slightly lower value of 0.17. All of these observed I_{60}/I_{100} values are compiled in Table 2.3 together with the IR intensity to HI column density ratios when available. For comparison the corresponding theoretical values are given for IR cirrus calculated by Draine and Lee (1984). The temperature variation of grains with galactocentric radius and the absorption cross-sections presented in Cox *et al.* (1986) were derived using optical properties of grains calculated by Draine and Lee. Hence our values of $\Delta I_\lambda/\Delta N_H$ for the solar vicinity in Model B (standard grain model) are the same as the Draine and Lee values as can be verified by referring back to Fig. 2.11.

All of the data summarized in the table raise some problems which are difficult to explain in terms of the 'classical' grain theories (Mathis *et al.*, 1977; Draine and Lee, 1984). Firstly, the I_{60}/I_{100} ratio appears to be fairly constant on large scales not only along the Galactic Plane but from all diffuse regions of the Galaxy despite their widely different environments. Secondly, the value of this ratio is about 0.2 which would suggest temperatures of grains in thermal equilibrium of above 20 K. By contrast, the models of standard grains would predict an I_{60}/I_{100} ratio of ~ 0.1 in the solar vicinity corresponding to dust temperatures less than 20 K.

There have been studies of the IRAS colour temperature variations as a function of radiation field also, which again have led to surprising results that are difficult to explain in terms of the standard grain models. By looking at various angles from the star ξ Per in the California Nebula, Boulanger *et al.* (1987) deduced the variation of IRAS colour ratios with energy density of starlight. They found that the I_{60}/I_{100} ratio increased steadily from 0.18 to 1.05 as the energy density increased from 0.7 to 325 eVcm^{-3}. Although this kind of behaviour would be predicted by standard grain models, the increase in the 60 to 100 μm ratio would be expected to be much more rapid. The I_{12}/I_{25} ratio is constant for moderate radiation energy densities but drops rapidly above energy densities of a few eVcm^{-3}. The

Author	Co-ordinates /object	I_{60}/I_{100}	I_{60}/N_H	I_{100}/N_H
			$MJysr^{-1}(10^{20}cm^{-2})^{-1}$	
Cox and Mezger (1987)	diffuse emission in the Galactic Plane	0.22		
Pérault *et al.* (1988)	diffuse emission in the Galactic Plane	~ 0.2		
Tereby and Fich (1986)	l=125° $\|b\| < 10°$	0.207 ± 0.022	0.13	0.64 ± 0.11
	l=215° $\|b\| < 10°$	0.205 ± 0.026	0.086	0.42 ± 0.08
Low *et al.* (1984)	Cloud A $l = 129.7°$ $b = -69.4°$	0.30	0.49	1.63
	Cloud B $l = 273.0°$ $b = 74.7°$	0.18	0.16	0.83
	Cloud C $l = 272.7°$ $b = 81.7°$	0.15	0.051	0.33
	Cloud D $l = 252.9°$ $b = 61.4°$	0.20	0.20	0.98
Boulanger *et al.* (1985)	20° × 18° field centred at $l = 116.6°$ $b = 72.3°$	0.21 ± 0.03 (for one cirrus feature near field only)	0.29	1.4 ± 0.3
Boulanger and Pérault (1988)	Auriga $150° < l < 170°$ $15° < b < 30°$	0.19	0.09	0.47
	Lupus $330° < l < 345°$ $10° < b < 20°$	0.22	0.46	2.1
	Orion $200° < l < 230°$ $-30° < b < -20°$	0.19	0.21	1.1
	NGC $b > 50°$	0.20	0.20	0.81
	SGC $b < -50°$	0.22	0.16	0.74
Weiland *et al.* (1986)	(molecular clouds)			
	Cloud 16 $l \sim 171°$ $b \sim -37°$	0.17		
	Cloud 20 $l \sim 211°$ $b \sim -37°$	0.17		
	Cloud 30 $l \sim 143°$ $b \sim 38°$	0.17		
Present work	$\|b\| > 20°$	0.1 (assumed)	0.14	1.4
		0.2 (assumed)	0.285	1.4
Draine and Lee (1984)	theoretical values for IR cirrus using standard grain model	0.1	0.081	0.83

Table 2.3: Compilation of 60 to 100 μm intensity ratios and IR intensity to HI column density ratios observed in various directions within the Galaxy.

I_{25}/I_{60} ratio drops to its minimum value at about $10\,\mathrm{eVcm^{-3}}$ but then increases again at higher energy densities. Ryter *et al.* (1987) made a similar investigation of the colour ratios in the ρ Oph region. Again they deduced that the 60 to 100 μm ratio increases slowly with energy density of starlight and that at high energy densities of $\sim 100\,\mathrm{eVcm^{-3}}$ the 12 to 100 μm ratio is depressed. Instead of examining the emission around stars as Boulanger *et al.* and Ryter *et al.* have done, Laureijs *et al.* (1988) investigated the variations of I_{60}/I_{100} and I_{12}/I_{100} in three diffuse clouds and one dark cloud which are all at high galactic latitudes, appear nearly spherical and have no strong heating source. Approaching the centre of a cloud or equivalently a decrease in the radiation energy density causes an increase in the 60 to 100 μm ratio. The opposite behaviour is seen for the I_{12}/I_{100} ratio in the one cloud where the 12 μm brightness could be determined.

In their calculation of the general ISRF, Mathis *et al.* (1983) deduced that the total energy density increases seven-fold between galactocentric distances of 10 and 5 kpc, the local energy density being $\sim 0.45\,\mathrm{eVcm^{-3}}$. Thus it would appear that for these modest variations in the general ISRF on large scales the ratio of 60 to 100 μm intensity remains fairly constant. However for much larger radiation fields found around stars, the 60 to 100 μm intensity ratio does increase but not by the amount predicted by standard grain models.

The above observations of I_{60}/I_{100} throughout the Galaxy on large and small scales have been interpreted in terms of the presence of small grains which are mixed uniformly with the large grain population of Mathis *et al.* (1977). Small grains were first invoked to explain the secondary peak at $\lambda \sim 10\,\mu$m in the observed IR emission spectrum of diffuse emission from the Galactic Plane. The major peak is at about 100 μm and the large grain model of Cox *et al.* (1986) fits the spectrum longward of $\lambda \sim 70\,\mu$m very well. The smaller peak at shorter wavelengths was discovered by Price (1981) from measurements of the diffuse emission at 4, 10 and 20 μm and has since been confirmed by the IRAS observations in the 12 and 25 μm wavebands (*e.g.* Cox and Mezger, 1987). As Pajot *et al.* (1986) point out, this feature requires dust temperatures of a few hundred kelvin. Such temperatures are not attainable by large grains in thermal equilibrium heated by the general ISRF. Suggestions have been made that the source of the MIR emission could be dust grains in the vicinity of stars (Cox *et al.*, 1986, de Muizon and Rouan, 1985) but the energy emitted would fall short of that observed in the Galactic Plane. Also, the MIR excess has been detected in high latitude cirrus where there are no stars (Boulanger *et al.*, 1985). The introduction of an ubiquitous grain population whose radii extend down to a few Å can explain some of the observations which the larger grains of Mathis *et al.* (1977) of radii $\gtrsim 0.01\,\mu$m, fail to do. As is discussed by various authors (*e.g.* Duley, 1973, Greenberg and Hong, 1974, Purcell, 1976), when very small grains absorb a UV photon from the ISRF, since the energy of the photon is comparable to the internal energy of the grain, large temperature fluctuations are experienced by the grain. The grains can attain temperatures of a few 100 K for a length of time which is short compared to the time between photon collisions and so the dependence of the emission from the grains on the strength of the ISRF is small.

Draine and Anderson (1985) studied in detail the IR emission spectra of graphite and

silicate grains heated by the ISRF and whose grain size distribution took the form:

$$f(a) \propto \begin{cases} a^{-3.5} & a_b < a < a_{max} \\ a_b^{0.5} a^{-4.0} & a_{min} < a < a_b \end{cases} \tag{2.11}$$

The notation used is the same as in Section 2.3.3, $f(a)da$ is the number density of grains with radius between a and $a + da$. This distribution is the same as the Mathis *et al.* (1977) distribution down to radius a_b, below which there is an enhancement in grain numbers. Both a_b and a_{min} were varied with a_{min} being taken as low as 3 Å. Taking temperature fluctuations of grains into account, Draine and Anderson produced a table of IRAS intensity ratios and I_{100}/N_H ratios predicted for various values of a_{min} with and without the enhancement and also for variations in the intensity of the ISRF of between one half and three times the local value. The extension and enhancement at small radii of the standard, large grain model not only considerably increases the predicted I_{12}/I_{100} and I_{25}/I_{100} ratios in the solar vicinity thereby explaining some of the observed MIR excess but also increases the I_{60}/I_{100} ratios. For a grain distribution extending down to 10 Å and enhanced below radii of 100 Å the I_{60}/I_{100} ratio predicted from the local IR cirrus is 0.22 and varies from 0.204 to 0.274 with an increase in the ISRF of 0.5 to 3 times the local intensity. This is small compared with the predicted I_{100}/N_H variation of 0.457 to 3.70 which reflects the increasing ISRF strength. To provide a better fit to the MIR emission of diffuse Galactic clouds, Puget *et al.* (1985) postulated that for grains of size $\lesssim$ 15 Å the bulk optical properties are no longer appropriate and instead the grains exist in the form of polycyclic aromatic hydrocarbon (PAH) molecules which emit discrete lines in the 3 to 10 μm wavelength range.

Ryter *et al.* (1987) and Boulanger *et al.* (1987) interpreted their observations that the 12 to 100 μm intensity ratio decreases at very high ISRF strength in terms of the destruction of the smallest grains when exposed to such intense radiation. Likewise, the slow increase of the 60 to 100 μm intensities would be expected if small grains experiencing temperature fluctuations on absorption of a single photon were responsible for some of the 60 μm emission. Laureijs *et al.* (1988) also explained their observations of brightness intensity ratio variation with decreasing radiation field in interstellar clouds in terms of two populations of grains. Only the large grains contribute to the 100 μm intensities but the 60 μm intensities have contributions from both populations. A decreasing ISRF causes the emission of the standard grains to reduce faster than that from the small grains and hence the observed increase in 60 to 100 μm brightness intensity ratio. Approaching the centre of the cloud the opacity to UV photons is greater than to near infrared (NIR) photons. Small grains absorb most of their energy from the former and larger grains from the latter. Hence the decline in the 12 to 100 μm intensity ratio in the cloud is observed.

Although the presence of small grains could explain many observations there are still problems. Walterbos and Schwering (1987) noted that models involving small grains predict a suppressed increase of the I_{60}/I_{100} ratio with ISRF with respect to the predictions of large grain models but they do not predict the almost constant ratio observed for diffuse emission from the disc of M31 and along the Galactic Plane. Also Boulanger and Pérault (1988) have pointed out that the model of Draine and Anderson (1985) requires a percentage of

the carbon abundance in grains less than 50 Å in radius which is unacceptable in terms of the observed local extinction curve.

Recently, Chlewicki and Laureijs (1988) have suggested that the excess 60 μm flux observed could be explained if there exists a population of grains of size $0.01 > a \gtrsim 0.005\,\mu$m composed of a conducting material, the most likely candidate being iron. The iron would have no effect on the observed interstellar extinction curve and in addition to providing the observed excess emission at 60 μm would make the 60 to 100 μm flux ratio almost independent of opacity of a cloud. At the shorter wavelengths they still explain the emission with PAHs but with only $\sim$ 10% of the cosmic carbon instead of 19% required by the model of Draine and Anderson (1985).

In order to remodel properly the emission in the 60 μm IRAS band due to HI-associated dust including the effects of small grains we would need to calculate the emission of small grains in a ISRF which is varying with galactocentric radius. Given the uncertainties of the nature of the grains and that in the current models (*e.g.* Draine and Anderson) their properties have been chosen mainly in order to attempt to reproduce the observed constancy of the I_{60}/I_{100} ratio at $\sim$ 0.2 we decided to adopt a simpler approach which we hope will still provide an adequate estimation of the effect. Since it is generally agreed that small grains will contribute negligibly to the 100 μm band emission (*e.g.* Cox *et al.*, 1986, Draine and Anderson, 1985), we use our predictions from Model B of the HI-associated dust emission in the 100 μm band scaled by a factor of 0.2 as the Model C 60 μm band emission. The choice of a constant factor 0.2 was made by consideration of Fig. 2.17(*a*) and the observed I_{60}/I_{100} ratios for high latitude cirrus compiled in Table 2.3.

As mentioned in Section 2.2 we compared the two Models B and C (standard and small grains) in directions where our predictions of the zodiacal emission were closest to those obtained by Sodroski *et al.* (1987) *i.e.* in the ranges $270° \geq l \geq 220°$ and $90° \geq l \geq 40°$. For consistency we resubtracted the zodiacal light contribution to the total 60 μm Galactic Plane maps covering these regions, this time using the profile of the zodiacal light across the ecliptic plane which was derived assuming β, the I_{60}/I_{100} ratio for HI-associated dust is 0.2 (see section 2.2 and Fig. 2.6 therein). Fig. 2.18 shows examples of two cuts across the Galactic Plane. The solid line represents the observed 60 μm band emission with the zodiacal emission subtracted and the dashed line is the predicted 100 μm band HI-associated dust emission from the standard grains of Model B scaled by 0.2 to simulate the 60 μm band HI-associated dust emission including that from small grains. These two Model C profiles can be compared with the corresponding Model B ones in Fig. 2.14. In general the new estimation of the HI-associated dust emission is a fairly good fit in the wings ($|b| \gtrsim 5°$) but tends to be higher than the observed total Galactic emission at intermediate latitudes ($2° \lesssim |b| \lesssim 5°$).

In Table 2.4 is given the percentage HI-associated dust contribution to the total 60 μm band emission for all three models in the latitude range $79.5° \geq l \geq 10°$ and for both $|b| \leq 1.5°$ and $|b| \leq 0.5°$. This table shows again that in Model A the HI contribution is very small especially very close to the Galactic Plane. It is clear also that the overall differences between Model B and C are small. It is interesting to note that the two models attribute the same percentage of the emission to HI-associated dust within $1\frac{1}{2}°$ of the plane

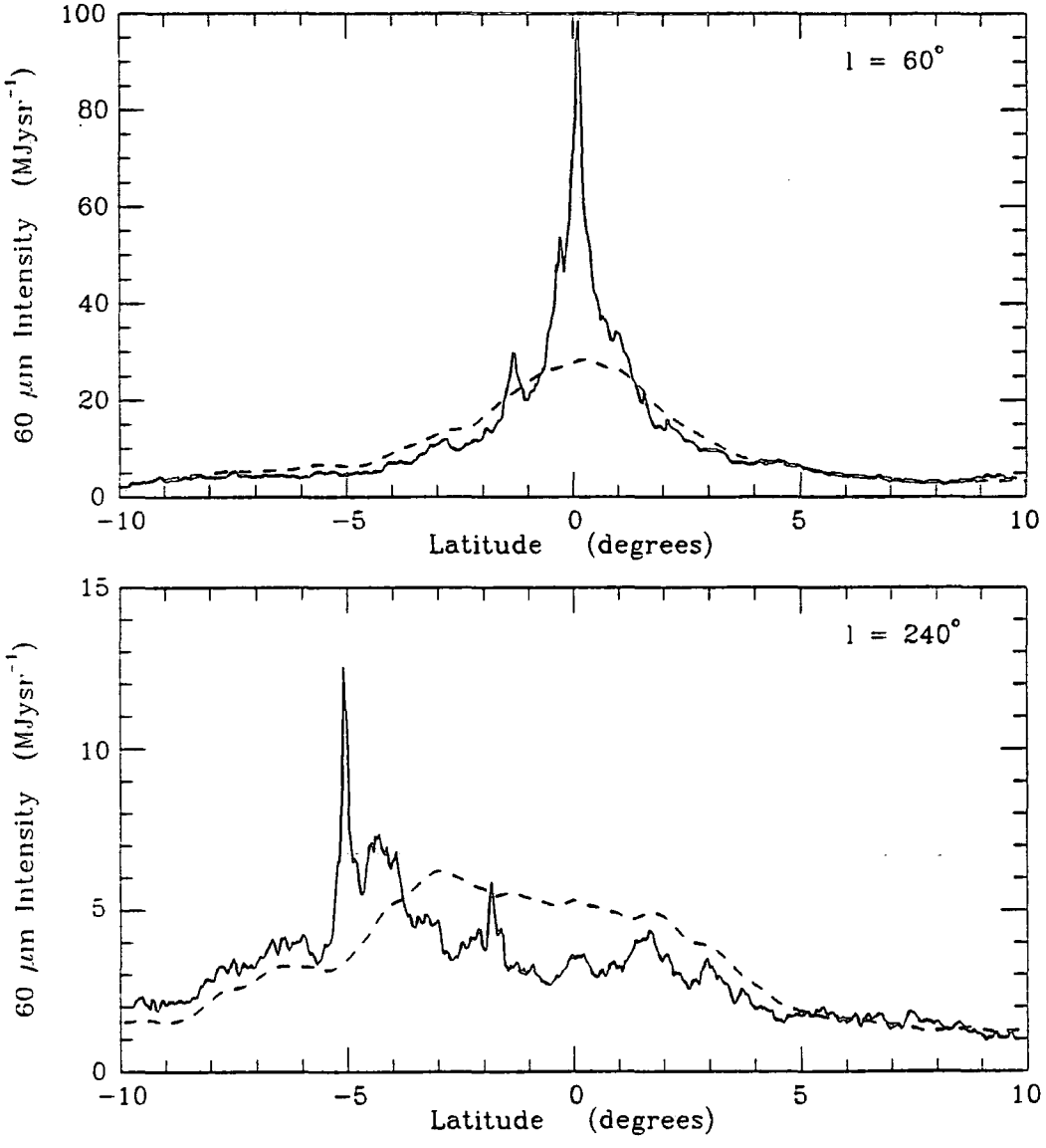

Figure 2.18: Two cuts across the Galactic Plane showing the predicted HI-associated component at 60 μm for the 'small grain' variant (Model C: dashed line) relative to the total emission (solid line). These are to be compared with Fig. 2.14 which shows the 'standard grain' variant (Model B).

Model	percentage emission from HI-associated dust	
	$\|b\| \leq 1.5°$	$\|b\| \leq 0.5°$
A: constant ISRF	13%	10%
B: varying ISRF standard grains	48%	42%
C: varying ISRF small grains	48%	40%

Table 2.4: Percentage contributions of HI-associated dust emission to the total 60 μm band emission from the Galactic Plane over the longitude range $79.5° \geq l \geq 10°$ for two latitude ranges and for all three models of the HI dust emission.

but within $\frac{1}{2}°$ of the plane the small grain model predicts a slightly lower percentage than the standard grain model. This can be understood as follows. Away from the Galactic Plane the fraction of the emission from the local neighbourhood is large and the Model B predictions are roughly only half those of Model C. However, in the Galactic Plane at $l \leq 34°$ the predictions of the large grain model are larger than that of the small grain model (see Fig. 2.19). Thus over the larger region of sky the two effects tend to compensate for each other and the integrated emission from the small and standard grain model predictions of HI-associated dust are roughly the same. However for the area only extending $\pm\frac{1}{2}°$ from the plane a smaller amount of local emission is incorporated resulting in an overall decrease in the small grain model predictions relative to those of the standard grain model.

It was mentioned earlier that we decided to use the results of the calculations of the HI-associated dust emission of Model B for the purposes of the radio thermal and non-thermal separation. Should more concrete evidence for the existence of small grains and a clearer picture of their behaviour become available in future then it will be possible to use this knowledge to produce a refined model of the HI-associated dust emission. The differences between the HI-associated dust emission predicted from Models B and C give an estimate of the uncertainty of the calculations.

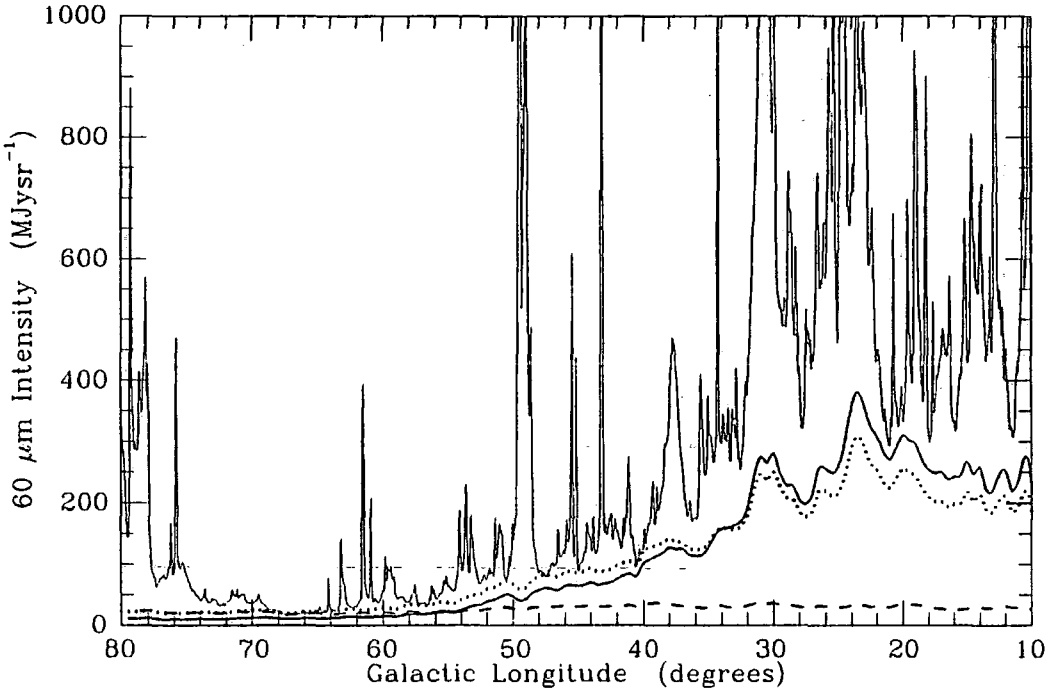

Figure 2.19: Profiles along part of the Galactic Plane showing the total Galactic 60 μm emission (thin solid line) and the HI-associated dust intensities for Model A (dashed line), Model B (thick solid line) and Model C (dotted line). The profiles represent averages over $|b| \leq 0.5°$.

Chapter 3

Galactic thermal emission

3.1 Correlations of the far infrared with HII and molecular clouds.

Analysis of the low resolution survey of Westerhout (1958) along the Galactic Plane at 1.39 GHz first revealed that in addition to the free-free continuum emission from compact HII complexes there appeared to be an underlying diffuse background. Also, a diffuse FIR emission was discovered by Pipher (1973) when he observed the Galactic Plane at $l = 2\frac{1}{2}^\circ$ in the 85–115 μm waveband. The survey of the plane by Low *et al.* (1977) over longitudes between 348° and $35\frac{1}{2}^\circ$ in the 118–196 μm band confirmed the presence of a diffuse FIR emission upon which emission from bright compact sources is superimposed. This led Mezger (1978) to propose that the diffuse radio emission is from extended low density (ELD) HII regions which have evolved beyond the compact radio phase but whose gas is still fully ionized. In an earlier paper Mezger and Smith (1975) had concluded that only about 10–20% of all OB stars are situated in the compact HII regions and so Mezger suggested that the remaining 80–90% are located in the ELD HII regions causing ionization of the gas and also providing some heating for dust. Another source of dust heating would be from Lyman-α photons emitted by the ionized gas. Energy absorbed by grains embedded in both the compact and ELD HII regions would be re-emitted in the FIR. Since this original work a series of papers have been produced (Mezger *et al.*, 1982; Mathis *et al.*, 1983; Cox *et al.*, 1986; Cox and Mezger, 1987) investigating and refining in the light of new observations the model of the origin of the FIR/sub-mm emission. The basic idea is that the diffuse FIR emission is from dust associated with the ELD HII regions and atomic hydrogen with the dust in quiescent molecular clouds (MCs) making a negligible contribution. The bright FIR sources, concentrated along the Galactic Plane, are associated with molecular cloud/HII complexes.

An alternative model of the origin of the FIR emission from the Galaxy was proposed by Ryter and Puget (1977). They studied nine large molecular clouds in the Galactic Plane which are associated with well-known HII regions and for which both FIR and ^{13}CO measurements were available. They calculated the IR luminosity per H-atom of these clouds

and found this to be comparable with that measured for the diffuse FIR emission along the Galactic Plane. Hence they suggested that most of the FIR emission is produced by dust in star-forming molecular clouds which have as yet unobservable young stars as heat sources.

Contrary to this model, Drapatz (1979) calculated the expected FIR emission along the Galactic Plane using data on the known distribution of stars and interstellar matter and found reasonable agreement with observations available at the time without invoking an unobservable population of stars.

The Galactic FIR emission surveys made before IRAS tended to lead to conflicting conclusions about the origin of the emission when compared with 5 GHz radio continuum and ^{12}CO surveys. This was mainly due to the poor resolution of the FIR observations which made it difficult to distinguish the true source of the FIR emission particularly since there is a general spatial correlation between giant molecular clouds (GMCs) and HII regions as both are associated with star formation. Few of the groups performing these earlier surveys compared their results with 21 cm data to investigate the possibility of FIR emission from neutral hydrogen clouds. Table 3.1 summarizes the conclusions drawn from a selection of FIR surveys made before the IRAS survey regarding the origin of the majority of the FIR emission.

In the last chapter we described the derivation of the emission in the 60 μm band from dust associated with neutral hydrogen using three different approaches. For reasons explained then we have decided to use our estimates deduced using the three-dimensional distribution of HI and following closely the model of Cox *et al.* (1986) for the emission of dust grains heated by the ISRF whose intensity varies with galactocentric radius. These predictions were made for all galactic longitudes and within 10° of the plane and were subtracted from the 60 μm band IRAS Galactic Plane maps from which we had already removed the zodiacal light contamination. The top photograph in Fig. 3.1 shows the residual emission for the longitude range $55° \geq l \geq 18°$ and $-1.5° \leq b \leq +1.5°$. Most of the diffuse emission beyond $b \sim \pm 1°$ has now been subtracted as it is associated with the HI. The residual emission is confined very close to the Galactic Plane and although the bright sources are most prominent there is still some underlying diffuse emission. This is also demonstrated in Fig. 3.2 which is a profile along $b = 0°$ of the residual 60 μm emission for the same longitude range as the photograph. Comparison of the top panel of the photograph showing the residual 60 μm emission and the lower panel showing the 11 cm radio continuum emission over the same area taken from the survey of Reich *et al.* (1984), reveals that there is a remarkable similarity both spatially and in intensity discerned by the eye. This was noted by Haslam and Osborne (1987) even before any estimated HI contribution had been subtracted from the 60 μm emission and led these authors to propose that the source of a large portion of the emission lies in compact and ELD HII regions. However, before we accept that the residual 60 μm emission is indeed from dust associated with HII we must first explore in a more quantitative fashion the possibility that the source of emission is in molecular clouds as suggested by Ryter and Puget (1977) and that the apparent correlation of the residual 60 μm with high frequency radio continuum emission is a secondary effect caused by the general association of HII regions with molecular clouds.

For our investigations we utilize the Massachusetts–Stony Brook survey (Sanders *et*

Author	Waveband /effective wave-length (μm)	Beam size	Galactic longitude range studied l_{high}–l_{low}	Conclusions
Gispert *et al.* (1982)	73–94 114–196	0.4° 0.37°	51°–358° & Cygnus 90°–358°	Most of unresolved component of FIR associated with extended MCs. ELD contribution small. FIR sources associated with MC/HII complexes.
Hauser *et al.* (1984)	150 250 300	$10' \times 10'$	62°–355°	FIR most likely from dust in MCs.
Low *et al.* (1977)	60–300 150–300	$15'$	$32\frac{1}{2}$°–348°	Positions of FIR sources and compact radio HII regions agree well but correlation of diffuse FIR and ELD not as good.
Maihara *et al.* (1979)	150	0.7° × 1°	$32\frac{1}{2}$°–340°	Many sources seem associated with radio HII regions but origin of diffuse FIR unclear.
Nishimura *et al.* (1980)	100–300	$30'$	42°–352°	Most sources of FIR have associated radio continuum and CO emission but a few just have one or the other.
Caux *et al.* (1984)	114–196	0.2° × 0.2°	20°–250°	Diffuse FIR probably from of unresolved weaker sources rather than ELD medium.
Caux *et al.* (1985)	114–196	0.2° × 0.2°	20°–250°	Many FIR sources show better correlation with MC/HII complexes than HII regions alone.
Myers *et al.* (1986)	Using data of Hauser *et al.* (1984) (see above)		60°–12°	Positional corrn. between peaks in FIR and radio continuum appears better than between radio/FIR and CO peaks.

Table 3.1: Summary of pre-IRAS FIR Galactic surveys.

Figure 3.1: Overleaf are grey-scale representations illustrating the detailed correlation between the residual 60 μm and the 11 cm radio continuum emission. A section of the Galactic Plane is shown extending from $l = 55°$ on the left down to $l = 18°$ on the right and between $\pm 1\frac{1}{2}°$ in galactic latitude. The top panel is the IRAS 60 μm band emission after removal of the zodiacal light and the modelled HI-associated contribution. The bottom panel shows the 11 cm brightness temperatures of Reich *et al.* (1984). The infrared map has been scaled by a factor $6.4 \times 10^{-6}\,\mathrm{mK\,(Jy\,sr^{-1})^{-1}}$ which is the 11 cm thermal radio to net 60 μm ratio deduced (see Section 3.3). Note the supernova remnants which appear on the lower panel at $l = 49.2°$, $b = -0.7°$ (W51), $l = 34.7°$, $b = -0.4°$ (W44), and $l = 27.8°$, $b = +0.6°$.

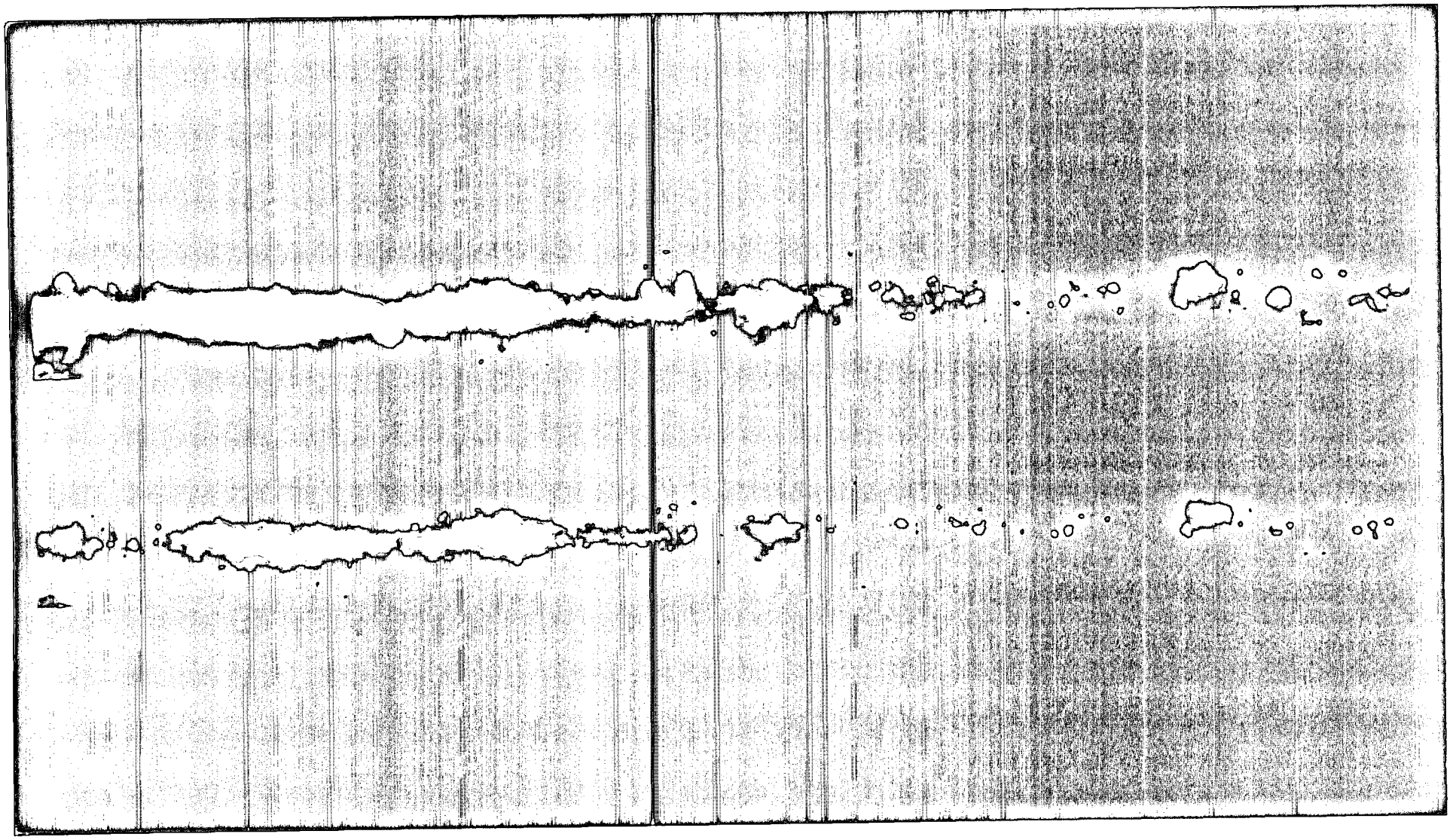

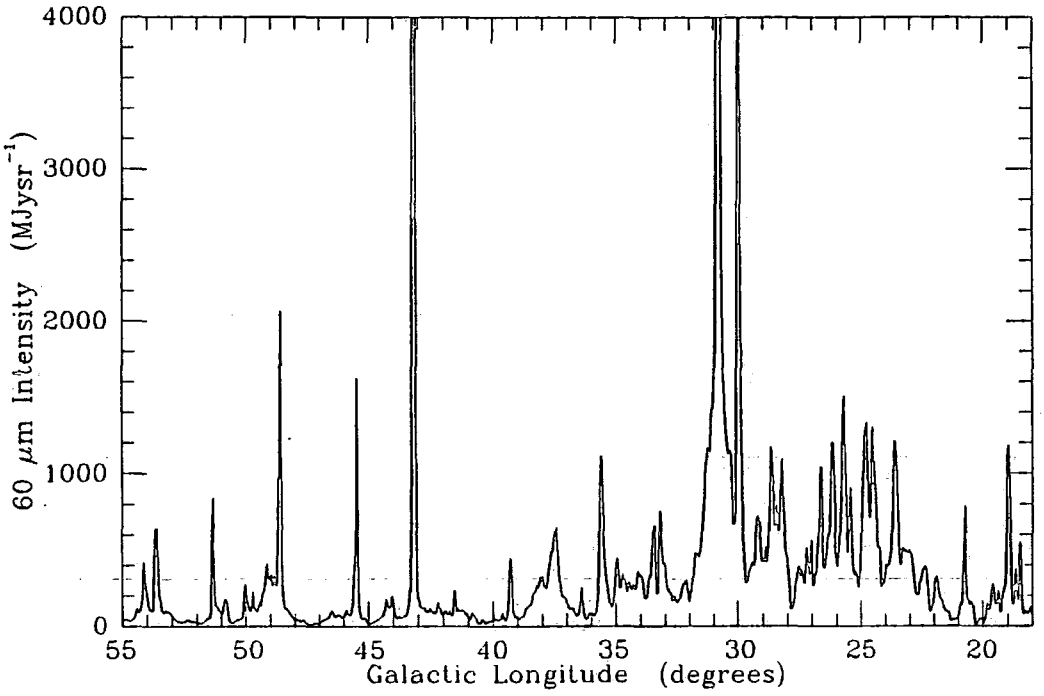

Figure 3.2: Profile of the residual 60 μm emission along the Galactic Plane between longitudes $l = 55°$ and 18° *i.e.* the same range as for the grey-scale representation in Fig. 3.1.

al., 1986) of the 2.6 mm wavelength ^{12}CO $J = 1$–0 transition. For the area $55° \geq l \geq 18°$, $-1.05° \leq b \leq +1.0°$ data samples were taken on a $3'$ grid with a telescope beamwidth $45''$. The survey covered other longitudes outside of this range but with a sampling interval twice as large. The velocity resolution was smoothed to $1\,\mathrm{km\,s^{-1}}$ and the full range of velocities covered at each position of l and b was $300\,\mathrm{km\,s^{-1}}$. Although the survey is spatially grossly undersampled, Sanders *et al.* believe that it is adequate to resolve the individual clouds. For each position on the $3'$ grid we summed the velocity channels in order to gain a measure of the CO and hence the molecular hydrogen column density along the line of sight, making the usual assumption that the molecular hydrogen column density is proportional to the total integrated ^{12}CO emission. The profile in Fig. 3.3(*c*) is a longitude profile between $l = 55°$ and 18° obtained from the velocity integrated data. In an attempt to compensate for the undersampling we have averaged over $|b| < 0.5°$. A similarly averaged profile of 11 cm brightness temperature was produced using the Reich *et al.* (1984) survey and is shown in Fig. 3.3(*b*). We will discuss the 11 cm survey, together with other radio data used, in Section 3.2 . A comparison of these two profiles with that of the 60 μm emission with zodiacal light and HI-associated dust contribution subtracted (Fig. 3.3(*a*)) reveals that the shape of all three are similar, for example, there are broad peaks in all three profiles around $l = 24°$ and $l = 30°$. However we see a much tighter correlation between the 11 cm and IR than between the CO and IR profiles. For all the 60 μm emission peaks there is a corresponding peak on the 11 cm profiles. In addition, the changes in the level of the underlying IR and 11 cm background appear to follow each other closely. All the peaks on the 11 cm profile with no IR counterpart which are marked by arrows in Fig. 3.3(*b*) are due to catalogued supernova remnants, *i.e.* the emission is produced by a non-thermal mechanism.

A quantitative test of the relative correlation was performed by dividing the $3'$ grid of integrated velocity profiles into smaller sections about 6° wide in galactic longitude. After extraction of the same areas from the residual 60 μm band Galactic Plane maps and regridding from $2.5'$ to $3'$ spacings, a pixel by pixel plot of integrated CO emission against IR brightness intensity was created for each area and a least squares fit was performed. Similarly, for these same intervals of longitude, least squares fits were made to the 11 cm brightness temperature *versus* residual 60 μm brightness intensity plots. Fig. 3.4 shows the two plots for the longitude range between 29° and 35° with $-1.05° \leq b \leq +1.0°$ for the CO-IR plot and $|b| \leq 1.5°$ for the 11 cm-IR plot. The fitted line is shown also in each case. For the CO *vs.* 60 μm plot the correlation coefficient is 54% to be compared with 82% for the 11 cm *vs.* 60 μm plot. Table 3.2 shows the correlation coefficients found for the other areas. The 11 cm-60 μm coefficient for the plot in Fig. 3.4 would in fact be even higher if the points close to the vertical axis, which are due to the bright SNR W44, had been eliminated. Although there will be an indeterminate amount of noise introduced into the CO measurements due to undersampling, the results suggest that the primary correlation of the residual 60 μm is with the radio continuum emission and that the poorer correlation with CO is through the general spatial coincidence of molecular clouds and HII regions.

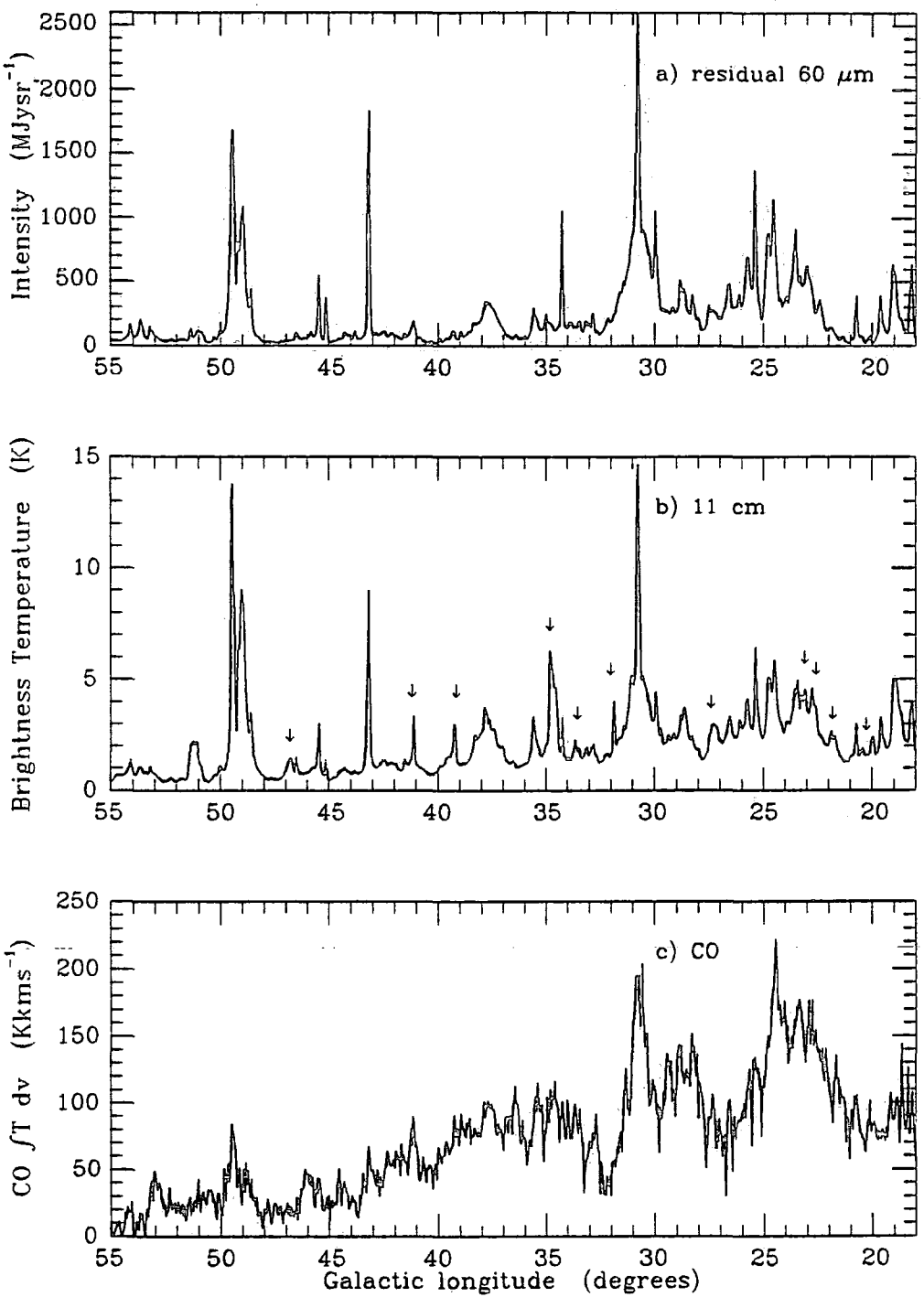

Figure 3.3: Comparison of profiles along the Galactic Plane of (*a*) the 60 μm band IRAS emission after subtraction of the modelled HI-associated component, (*b*) the 11 cm radio continuum emission from Reich *et al.* (1984), with peaks due to known SNRs marked by arrows, and (*c*) ^{12}CO column densities from the Massachusetts–Stony Brook survey. All are averaged over $-0.5° < b < +0.5°$.

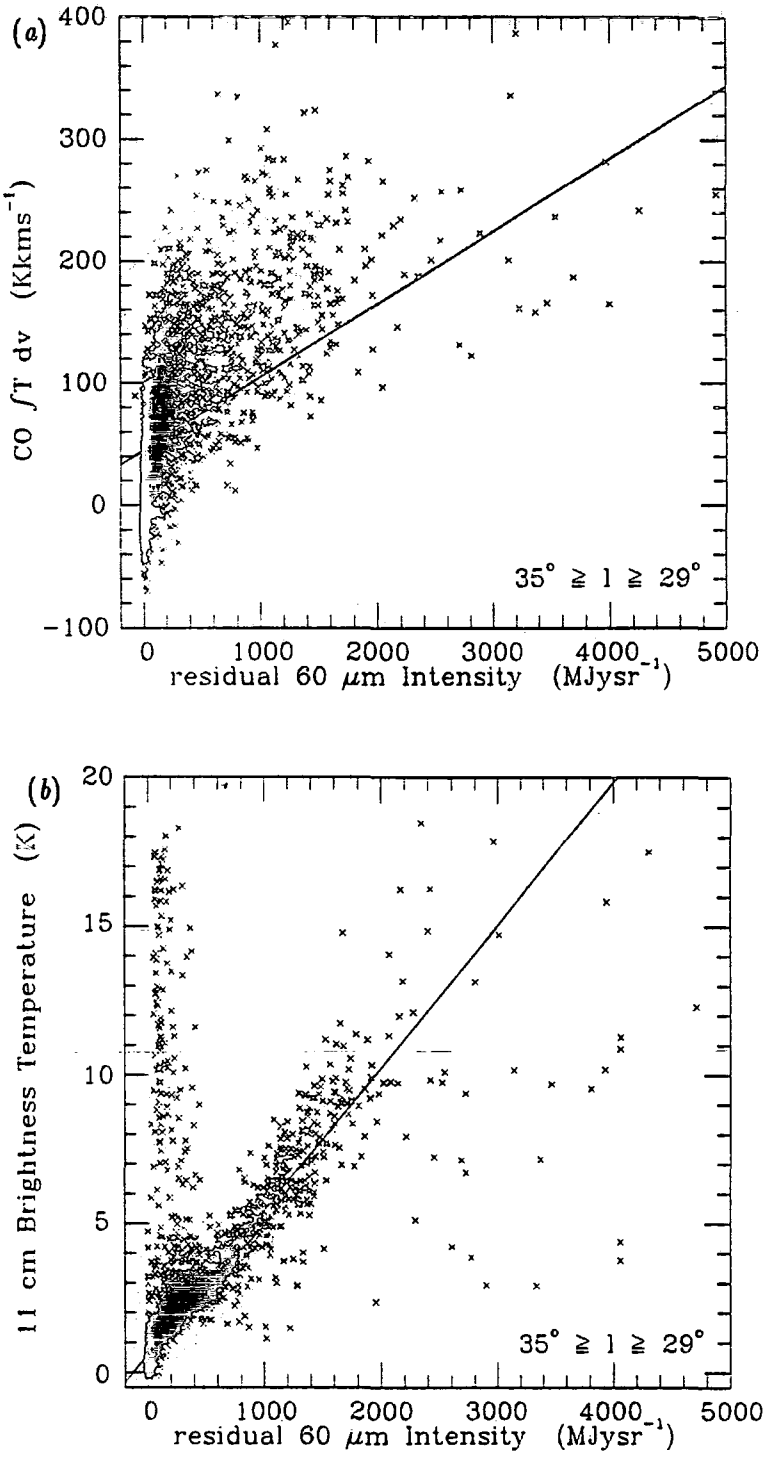

Figure 3.4: Plots of (*a*) ^{12}CO column densities against 60 μm intensities and (*b*) 11 cm brightness temperatures against 60 μm intensities. The correlation coefficients are 54% and 82% respectively, but the latter is reduced by points close to the vertical axis due to the bright SNR W44. The least squares fit to the points is drawn on each plot. The longitude range covered is $35° \geq l \geq 29°$ and the latitude range is $-1.05° \leq b \leq +1.0°$ for (*a*) and $-1.5° \leq b \leq 1.5°$ for (*b*). The modelled HI-associated component of the 60 μm intensities has been subtracted.

CO				11 cm			
l range	b range	Slope	r	l range	b range	Slope	r
23°–18°	−1.05°–+1.0°	0.11	0.47	23°–17°	−1.5°–+1.5°	5.0	0.81
29°–23°	−1.05°–+1.0°	0.11	0.62	29°–23°	−1.5°–+1.5°	4.6	0.87
35°–29°	−1.05°–+1.0°	0.06	0.54	35°–29°	−1.5°–+1.5°	4.8	0.82
41°–35°	−1.05°–+1.0°	0.18	0.49	41°–35°	−1.5°–+1.5°	8.1	0.82
47°–41°	−1.05°–+1.0°	0.02	0.20	47°–41°	−1.5°–+1.5°	4.2	0.82
53°–47°	−1.05°–+1.0°	0.02	0.39	53°–47°	−1.5°–+1.5°	7.2	0.91
55°–53°	−1.05°–+1.0°	0.10	0.33	59°–53°	−1.5°–+1.5°	5.6	0.77

Table 3.2: Results of least squares fits to the plots for integrated ^{12}CO emission *vs.* residual 60 μm intensity and 11 cm brightness temperature *vs.* residual 60 μm intensity. The slopes are in units of K km s^{-1}(MJy sr^{-1})$^{-1}$ and mK (MJy sr^{-1})$^{-1}$ respectively. r is the correlation coefficient.

3.2 The radio continuum surveys

3.2.1 Introduction

The radio continuum emission from the Galactic Plane has a thermal and non-thermal component. The thermal emission is produced by the bremsstrahlung mechanism and the theoretical thermal brightness temperature spectral index, α_{th}, is 2.1 ($T_b(\nu) \propto \nu^{-\alpha}$). On the other hand, the non-thermal or synchrotron emission from relativistic electrons accelerated in magnetic fields has a steeper spectrum. For example the brightness temperature spectral indices, α_{nth}, of SNRs typically have values between 2.3 and 2.8. Thus at higher frequencies the thermal component of the emission dominates over the non-thermal emission close to the Galactic Plane and this is why in the next section we use surveys at 11 cm ($\equiv$ 2.7 GHz) and 6 cm ($\equiv$ 5 GHz) to investigate and quantify the correlation between the IR and thermal radio emission from the inner Galactic Plane. For the first quadrant the 11 cm survey of Reich *et al.* (1984) is used and for the fourth quadrant the 6 cm Haynes *et al.* (1978) survey. The two surveys have a similar resolution to that of the IRAS survey. Having established this relationship the residual IRAS 60 μm emission can be scaled to any radio frequency, in particular to lower frequencies where the non-thermal emission dominates. We give a full account of this in Chapter 4 where we separate the emission from the Galactic Plane at 408 MHz. The radio data used was the all-sky map of Haslam *et al.* (1982) and so a short description of this survey as well as the 11 and 6 cm surveys will be presented in this section.

3.2.2 The 11 cm survey (Reich *et al.*, 1984)

This survey was made using the Effelsberg 100 m telescope and has angular resolution of about 4.3′. So far, the area covered is $357.4° \leq l \leq 76°$, $|b| \leq 1.5°$ which avoids the Cygnus complex at $l \sim 79°$. The latitude range is in the process of being extended to $|b| \leq 5°$. On completion of this extension an absolute calibration will be possible using the lower resolution survey made with the Stockert 25 m telescope covering the range $|b| \leq 20°$. The zero contour level of the Effelsberg survey published to date is set at approximately $|b| = 1\frac{1}{2}°$ except in source affected regions in which case extended scans were made. We have attempted to determine the absolute temperatures by noting the temperatures of the Altenhoff *et al.* (1970) 11 cm survey at $|b| = 1\frac{1}{2}°$ for longitudes where the zero level on the Effelsberg survey (Reich *et al.*) is at or very close to $|b| = 1\frac{1}{2}°$. Interpolating across longitudes where strong sources lie we thus obtained from the Altenhoff *et al.* data a smoothly varying profile which varies from 0.5 K at $l \simeq 65°$ to 1.5 K at $l \simeq 0°$. The Altenhoff *et al.* survey extends over $|b| \leq 2°$ but the base level was set by assuming a zero level at $|b| = 5°$. By looking at the 408 MHz all-sky survey of Haslam *et al.* (1982) and assuming a spectral index of -2.8 at this latitude we deduced that a further 0.2 to 0.6 K should be added to the 11 cm survey to obtain absolute brightness temperatures. Reference to Fig. 3.3(b) shows that a total addition of between 0.7 and 2.1 K is very significant in terms of the absolute level of the Effelsberg survey. However, the method we employ to deduce the thermal radio emission described in the next section is not sensitive to a smoothly varying background provided that we divide the survey into small longitude ranges and study each separately.

3.2.3 The 6 cm survey (Haynes *et al.*, 1978)

The 6 cm survey was made using the Parkes 64 m telescope. The region $40° \geq l \geq -170°$ $(+190°)$, $|b| \leq 2°$ was mapped at an angular resolution of 4.4′ although we only use the longitudes down to $-79°$ $(281°)$ which incorporates the Carina Nebula. The brightness temperatures on the published maps were believed to be accurate to within 10%. The zero level is defined at $|b| \sim 2.5°$ but then a constant base level was added to the digitized data. By looking at the temperatures in the wings of several cross-cuts over the whole range of longitude we deduced that this constant was 1.0 ± 0.1 K. By extrapolating from the 408 MHz data at $|b| = 2.5°$ we inferred that the absolute temperatures at these latitudes were of the order of the error in the determination of the constant base level. We therefore subtract 1 K from the 6 cm data to obtain a best estimate of the absolute brightness temperatures. There is an overlap of 42.6° in longitude between the 11 and 6 cm surveys.

3.2.4 The 408 MHz all-sky survey (Haslam *et al.*, 1982)

The 408 MHz survey of the whole sky was done using four different telescopes, the Mark I Jodrell Bank Telescope, the Effelsberg 100 m Telescope, the Parkes 64 m Telescope and the Jodrell Bank Mark IA Telescope. After the four parts had been combined, the data were convolved to a common resolution of 51′. An absolute calibration of the 408 MHz

observations was made using the 408 MHz survey of Pauliny-Toth and Shakeshaft (1962). The zero level and temperature scale errors are believed to be ±3 K and less than 10% respectively.

Lawson *et al.* (1987), in their study of the variations of the spectral index of the Galactic radio continuum emission, estimated that the extragalactic background contributed a total of 5.89 K isotropically to the 408 MHz observations. This is composed of two smooth components which are the 2.7 K cosmic background radiation and 3.19 K due to unresolved extragalactic sources. This background, although small in absolute terms, should be subtracted from the survey for the purposes of studying the Galactic non-thermal component at 408 MHz (see Chapter 5). The extragalactic unresolved sources should have a spectral index similar to that of the Galactic non-thermal emission and hence at 11 and 6 cm will be very small. The best estimates of the 11 and 6 cm absolute temperatures do not include the 2.7 K cosmic background.

3.3 Determining the relation between the thermal radio continuum and residual 60 μm emission

In Section 3.1 it was established that the residual 60 μm emission from the Galactic Plane after removal of the zodiacal light and the modelled HI-associated dust emission was better correlated with the radio continuum than the CO column density. This was illustrated by plotting diagrams of radio continuum or integrated CO emission against the residual 60 μm band emission (see Fig. 3.4). We used such plots in order to quantify the relationship between high frequency thermal radio continuum brightness temperature and residual 60 μm band brightness intensity.

The longitude range covered by the 11 and 6 cm surveys was divided into small areas each 6° wide in galactic longitude and extending to ±1.5° in latitude. The study of such small areas avoids problems caused by the base levels of the radio surveys which vary gradually with galactic longitude (see Section 3.2). For each area the radio brightness temperature against net IR intensity is plotted pixel by pixel. Since the pixel size is $2.5' \times 2.5'$ there are over ten thousand points per plot. Fig. 3.5 shows more representative plots both with 11 and 6 cm data in addition to that in Fig. 3.4.

Before describing the technique employed to find the net 60 μm–radio continuum relationship it is worth examining the plots more closely. Each plot has a well defined lower envelope above which a band containing several thousands of points is positioned. Since the radio brightness temperature from any direction is the sum of a thermal and non-thermal component, the former being correlated with the IR intensity, then points on this lower envelope will represent directions in which the non-thermal emission is negligible above a constant background level. By fitting a straight line to this lower envelope, therefore, we may determine a linear relationship between 60 μm and thermal radio continuum emission.

The points which lie well above the lower envelope and close to the ordinate axis are from directions where there are SNRs or radio galaxies along the line of sight. In a few of the plots a small number of points have very low radio brightness temperatures but quite

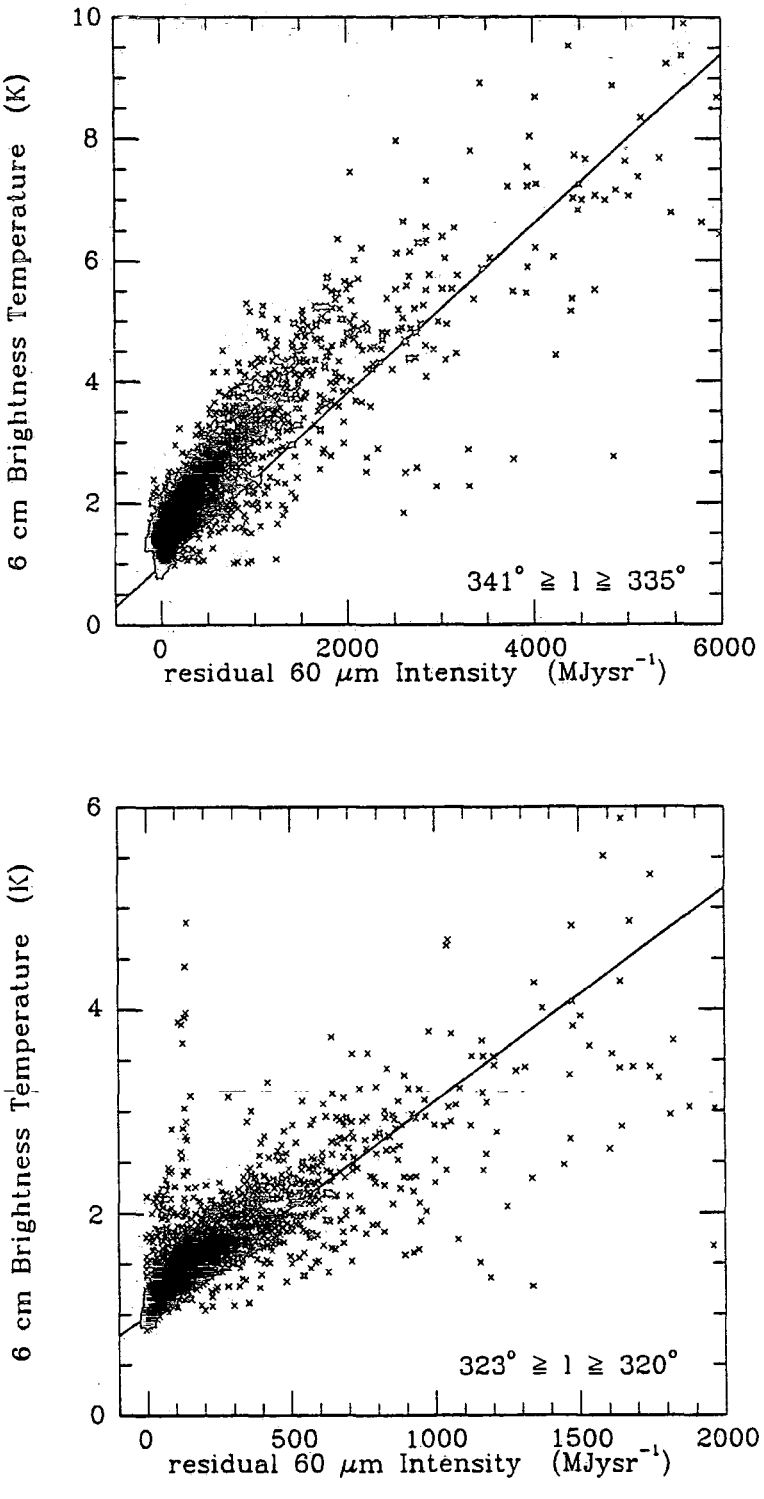

Figure 3.5: Six more plots of 11 or 6 cm brightness temperatures against residual 60 μm intensities in addition to the one shown in Fig. 3.4. Each plot contains points covering 6° in longitude and ranging between $\pm 1\frac{1}{2}^\circ$ in latitude. The line drawn on each plot represents the lower envelope which we have fitted to each plot separately by a method described in Section 3.3. (Continued on next page.)

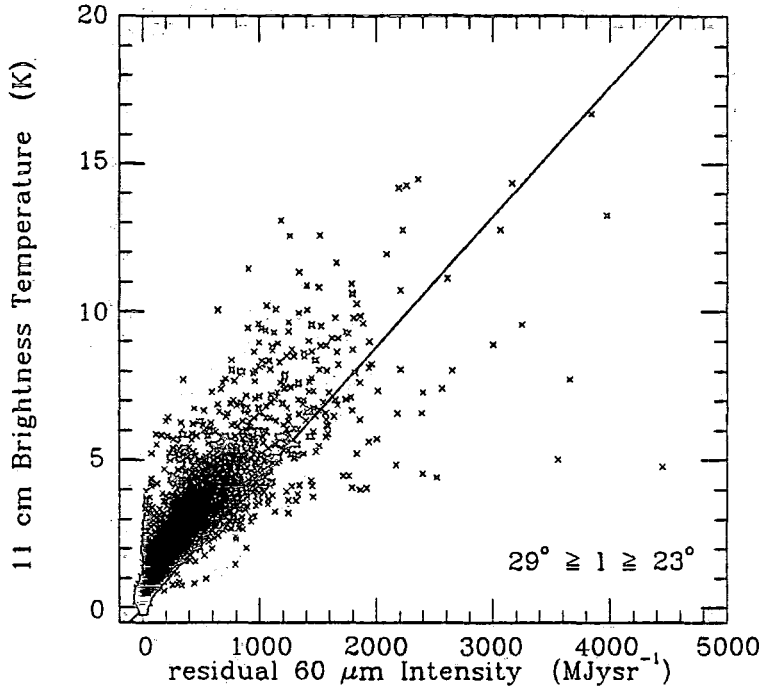

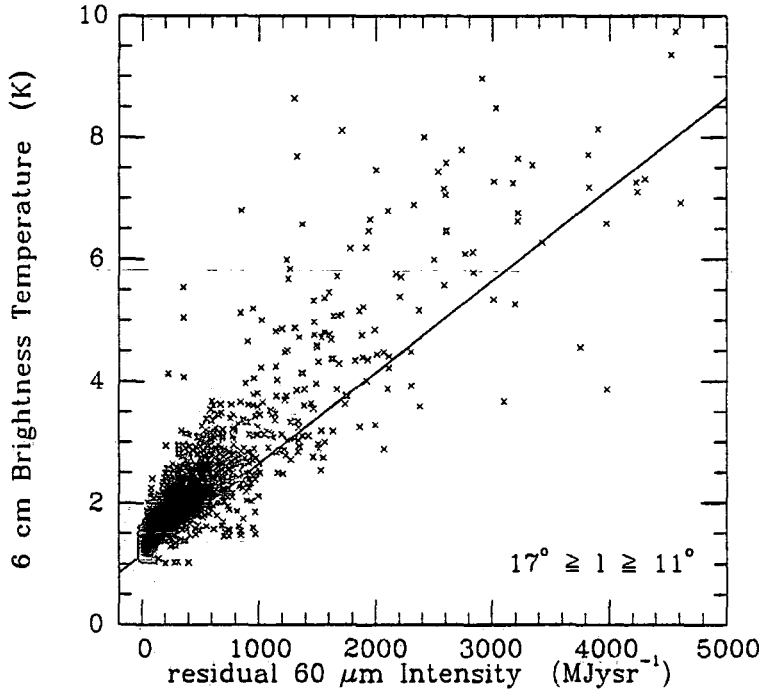

Figure 3.5: ***contd.*** **(Continued on next page.)**

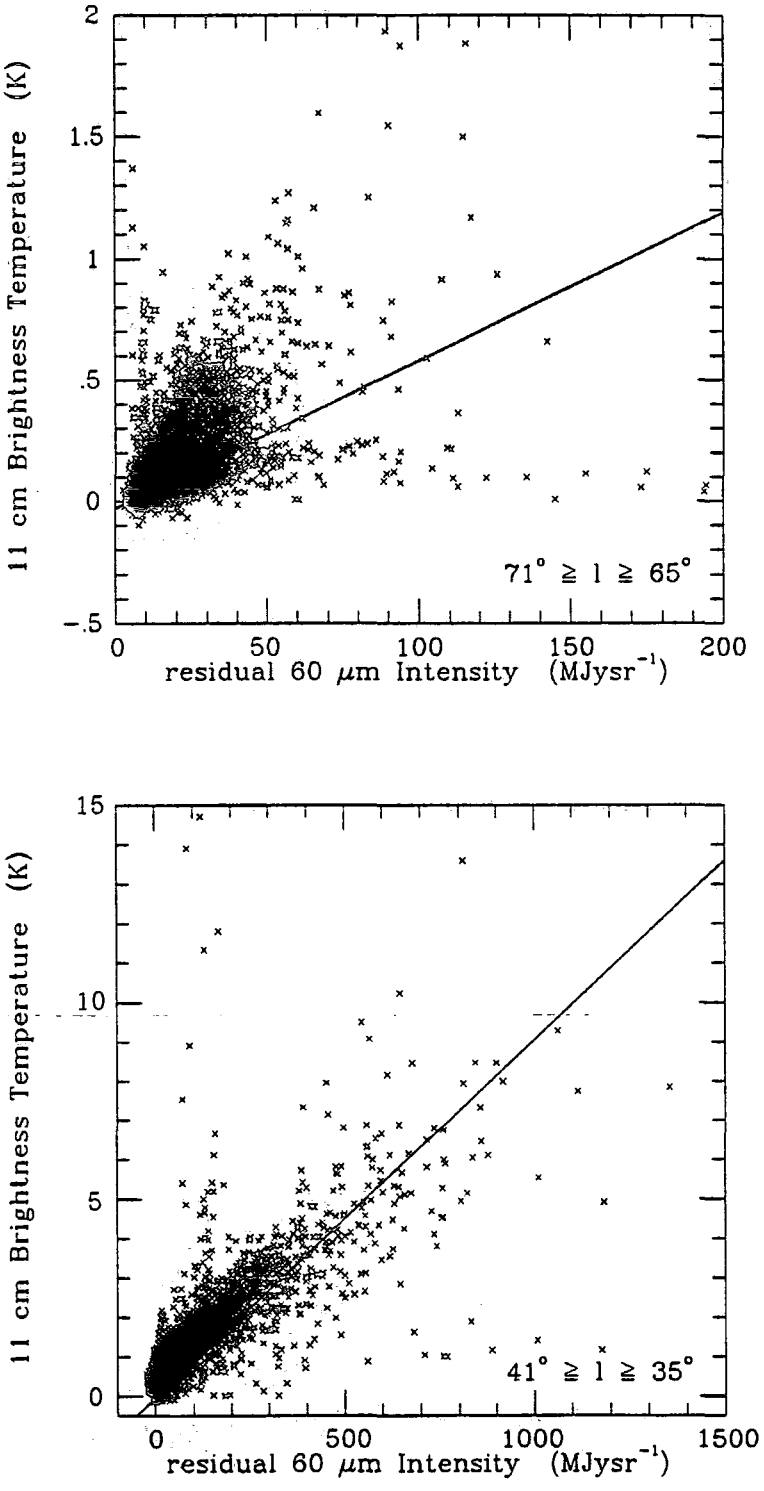

Figure 3.5: ***contd.***

high IR intensities. These are from positions where there is a bright IR source with no radio counterpart. The occurrence of these objects is rare; there are less than 30 bright 60 μm sources with no obvious 11 cm radio continuum emission within the area $76° \geq l \geq -1°$, $|b| \leq 1.5°$. In the plot for the range $l = 71°$ to $65°$ (Fig. 3.5) the points lying well below the lower envelope are from two 60 μm sources at $l \sim 69.5°$, $b \sim -1.0°$ and $l \sim 69.5°$, $b \sim +0.5°$. The former is unresolved and is listed in the IRAS Point Source Catalogue. The flux density of this source is given for all four IRAS bands in this catalogue and it is brightest in the 100 μm band. The latter source is slightly extended having an angular diameter $\sim 10'$–$15'$. A rough estimate of the flux densities shows that it is strongest in the 60 μm band. The two sources appear in the same positions in both the HCON1 and HCON2 sky coverages. This eliminates the possibility that they are asteroids since in the weeks between the two sets of observations such objects would have moved their positions on the sky. We can only suggest therefore that these objects are stellar, and surrounded by cool neutral gas clouds.

Determination of the lower envelope of a plot objectively is quite difficult. The method adopted here is as follows. Initially, a line is drawn by eye which seems to be the best representation of the lower envelope. A search is then made by computer over a range of slopes and y-intercepts about those values for the line chosen by eye. If y and x represent the radio brightness temperature in mK and residual 60 μm intensity in Jy sr^{-1} respectively for any point on the plot, then for a line $y = Ax + B$ the range and increments of A and B searched are:

$$\left.\begin{aligned}(A_\circ - 12 \times 10^{-7}) < A < (A_\circ + 12 \times 10^{-7}) \\ dA = 2 \times 10^{-7}\end{aligned}\right\} \quad \text{mK (Jy sr}^{-1})^{-1}$$

$$\left.\begin{aligned}(B_\circ - 1000) < B < (B_\circ + 1000) \\ dB = 50\end{aligned}\right\} \quad \text{mK} \qquad (3.1)$$

where $A_\circ$ and $B_\circ$ are the values of A and B of the line drawn by eye. For each combination of A and B the number of points, $N_a(A, B)$ satisfying the condition:

$$0 < y - (Ax + B) \leq 100\,\text{mK} \qquad (3.2)$$

and the number of points, $N_b(A, B)$, satisfying:

$$0 > y - (Ax + B) \geq -100\,\text{mK} \qquad (3.3)$$

are determined. If the line with the maximum $N_a - N_b$ does not have either A or B at the extremes of the search ranges and provided that $N_b \leq 100$ then this line is taken to be the lower envelope of the plot. Although this approach may seem rather arbitrary it is more systematic and less subjective than an estimation by eye. The lower envelopes determined by this method are marked on each plot in Fig. 3.5.

Out of all 33 plots which cover the areas of both surveys, there were four for which it was not possible to determine a lower envelope by this technique without ignoring points having slightly negative residual 60 μm intensities due to over-estimation of the zodiacal

Central longitude of area	Computed lower envelope		$\frac{I_{60\,\mu m}}{I_{11\,cm}}$	$\frac{I_{60\,\mu m}}{I_{6\,cm}}$
	Gradient 10^{-6}mK (Jy sr^{-1})$^{-1}$	Intercept mK		
11 cm vs. 60 μm				
2°	6.6	0	676	
8°	5.2	−100	858	
14°	4.7	−250	949	
*20°	5.9	0	756	
26°	4.4	0	1014	
32°	4.0	0	1115	
38°	9.1	−50	490	
44°	5.5	0	811	
50°	6.5	0	686	
56°	7.4	−50	603	
62°	9.0	−50	496	
68°	6.1	−30	731	
$73\frac{1}{2}$°	8.8	−100	507	
6 cm vs. 60 μm				
284°	0.8	1050		1625
290°	1.3	1000		1000
296°	1.9	900		684
302°	2.0	950		650
308°	1.3	1000		1000
314°	2.1	900		619
320°	2.1	1000		619
* 326°	2.7	1000		481
* 332°	2.0	950		650
338°	1.4	1000		929
* 344°	2.3	1000		565
350°	1.6	1150		813
356°	1.1	1250		1182
†2°	1.5	1000		867
8°	1.1	1200		1182
14°	1.5	1150		867
20°	1.3	1250		867
26°	1.2	1050		1083
32°	1.5	950		867
38°	1.8	1100		722

Table 3.3: Results of lower envelope fitting. * — determined excluding points with net 60 μm< 0, † — estimated by eye only.

Central longitude of area	Gradient of lower envelope 10^{-6}mK (Jy sr^{-1})$^{-1}$		α_{th} [a]
	11 cm:60 μm	6 cm:60 μm	
2°	6.6	1.5	2.4
8°	5.2	1.1	2.5
14°	4.7	1.5	1.9
20°	5.9	1.3	2.5
26°	4.4	1.2	2.1
32°	4.0	1.5	1.6
38°	9.1	1.8	2.6

Table 3.4: Thermal spectral indices between 11 and 6 cm for the areas covered by both surveys.

[a] $$\alpha_{th} = -\frac{\ln\left(\frac{6\,\mathrm{cm\,gradient}}{11\,\mathrm{cm\,gradient}}\right)}{\ln\left(\frac{5}{2.7}\right)}$$

light or HI-associated dust emission. At 6 cm, for the area including the Galactic Centre the lower envelope fitting procedure failed completely and only an estimation by eye could be made. Table 3.3 gives a list of the gradients and intercepts for all of the areas. The average slope from the thirteen plots of 11 cm brightness temperature against residual 60 μm intensity is $(6.4 \pm 1.7) \times 10^{-6}$ mK (Jy sr^{-1})$^{-1}$ and for the twenty plots of 6 cm brightness temperature against 60 μm intensity the average slope and intercept are $(1.6 \pm 0.5) \times 10^{-6}$ mK (Jy sr^{-1})$^{-1}$ and 1040 ± 100 mK respectively. We find no systematic variation of slope with galactic longitude. Converting the radio brightness temperature, T_b, to intensity, I, in Jysr^{-1} using the relation:

$$T_b/K = 3.25 \times 10^{-5} \frac{I/\mathrm{Jy\,sr^{-1}}}{(\nu/\mathrm{GHz})^2} \tag{3.4}$$

the corresponding 60 μm:11 cm and 60 μm:6 cm intensity ratios are 700 ± 200 and 810 ± 250 respectively.

There are seven areas between 41° and 359° in galactic longitude for which the 6 and 11 cm surveys overlap. Hence for each of the areas a value for the 11 to 6 cm thermal spectral index can be calculated from the slopes of the lower envelopes. These are listed in Table 3.4. The average spectral index α_{th}, where $T_b \propto \nu^{-\alpha_{th}}$, is 2.2 ± 0.4 compared with 2.1 predicted theoretically by the thermal bremsstrahlung mechanism (*e.g.* Mezger and Henderson, 1967). This gives some support to our method of fitting the lower envelope.

3.4 The infrared excess

Gas in both ELD and compact HII regions is ionized by Lyman continuum photons (Lyc) from the O stars situated within. Eventually, most Lyc photons are degraded into Lyman-α

photons (Lyα) which can be absorbed subsequently by dust grains. Mezger (1978) defined the infrared excess (IRE) of a HII region as the ratio between the total IR luminosity and the power input into Lyα photons. If dust grains absorbed all Lyα photons available and this was the only source of heating then the IRE would be unity. In general however observations show that the IRE is greater than 1 implying that the dust is heated also by photons of different energies and not necessarily all the Lyα photons are absorbed.

From our determination of the constant ratio between the 60 μm emission due to dust associated with the HII regions and 11 cm radio continuum emission it is possible to estimate a value of the IRE as follows. Mezger (1978) derives an expression relating the integrated IR flux (F_{IR}) of the Galactic Plane to the thermal component of the radio flux at a given frequency (S_{radio}) in terms of IRE and T_e, the electron temperature:

$$(\mathrm{IRE})^{-1}\left[\frac{F_{IR}}{\mathrm{Wcm^{-2}}}\right] = 6.54\times10^{-14}\left[\frac{T_e}{\mathrm{K}}\right]^{-0.45}\left[\frac{\nu}{\mathrm{GHz}}\right]^{0.1}\left[\frac{S_{radio}}{\mathrm{Jy}}\right] \qquad (3.5)$$

The flux in the IRAS 60 μm band S_{IRAS} will be given by $S_{IRAS} = KfF_{IR}$ where f is the conversion factor from the total IR flux to the flux density per hertz at 60 μm and K is the colour correction (see Section 2.3.3) which depends on the response function of the whole IRAS system and the spectrum of the source. Since the radio continuum and IRAS surveys are at roughly the same resolution we can equate the ratio of the thermal radio to IR fluxes to the ratio of the intensities ($I_{60\,\mu\mathrm{m}}/I_{11\,\mathrm{cm}}$) which we deduced in the last section. Hence:

$$\mathrm{IRE} = \frac{I_{60\,\mu\mathrm{m}}}{I_{11\,\mathrm{cm}}}\,\frac{1.53\times10^{-17}}{Kf{T_e}^{-0.45}\nu^{0.1}} \qquad (3.6)$$

We take 7000 K for T_e as deduced by Mezger (1978) for the ELD HII regions. The value of IRE is not very sensitive to the value of T_e assumed. To calculate K and f we need to assume certain properties of the emitting dust grains. We assume that the grain temperature is 30 K in accord with the temperature of the warm dust component in the model of Cox *et al.* (1986) which is mainly associated with ionized gas in the ELD HII regions. Also, the dust is assumed to follow a λ^{-2} emissivity law over the range of wavelengths in the IRAS 60 μm band as was imposed by Draine and Lee (1984) on the basis of observational data in their calculations of the optical properties of silicate grains. Making these two assumptions, the values of f and K are $1.44\times10^{-13}\mathrm{Hz}^{-1}$ and 0.90 respectively. The average value of $I_{60\,\mu\mathrm{m}}/I_{11\,\mathrm{cm}}$ (see Table 3.3) is 700 ± 200 giving a value of IRE of 4 ± 2. The estimate of the uncertainty in this value was made by taking into account the scatter in the slopes of the lower envelopes. Also the effect of varying the grain temperature between 20 and 35 K and the power of the emissivity law between 1 and 3 were considered.

The value of the IRE we have derived here is in accord with the value Mezger considered reasonable on theoretical grounds for the ELD HII regions. However, it is only about half of the value he obtained using the IR intensities of Low *et al.* (1977) and the diffuse free-free continuum at 1.39 GHz deduced from the Westerhout (1958) and Matthewson *et al.* (1962) thermal–non-thermal separations of the Galactic emission. Sodroski *et al.* (1987) found a mean value of 7 for the IRE of emission from the Galactic Plane. Caux *et al.* (1985) use

the results of their IR survey of the inner Galactic Plane to derive values of the IRE both for the diffuse component and the sources. They calculate the IRE from the IR luminosity in the 114–196 μm channel of their balloon-borne experiment and from 5 GHz observations of Haynes *et al.* (1978) and Altenhoff *et al.* (1970, 1979). For the unresolved component in the north side, south side and centre regions of the Galactic Plane they find average values for the IRE of > 8, > 13 and > 14 respectively. The corresponding figures for the sources deduced are 3, 4 and 12. They argue however that the IRE of the unresolved component could be of the order of 25 because a significant proportion of the 5 GHz diffuse emission will be non-thermal in origin leading to an underestimate of the IRE.

In these studies of Mezger, Sodroski *et al.* and Caux *et al.* no subtraction of the HI-associated emission from the IR luminosity had been performed and therefore these large values of the IRE might be expected. The original definition of the IRE was applied only to the compact HII regions and ELD ionized regions in which the O stars are situated rather than to a combination of these regions with regions of neutral gas whose associated dust is heated mainly by the general ISRF.

Myers *et al.* (1986) calculated a median value of 6 for the IRE of 25 FIR sources which have associated radio HII regions. Unlike Gispert *et al.* (1982) and Caux *et al.* (1985), Myers *et al.* found no evidence for the longitude dependence of the IRE. This observation is consistent with our use of a constant value for the ratio between 60 μm and radio continuum emission although on smaller scales the IRE probably does vary.

3.5 The luminosity of the Galaxy at 60 μm

Having estimated the contribution of the HII-associated dust in the Galaxy to the IRAS 60 μm band-intensity we can attempt to construct a picture of the Galactic radial variation of the emission from this component as would be discerned by an external observer. The unfolding procedure we employ is that described by Strong (1975) and Worrall (1977) which was developed in order to calculate γ-ray emissivities in the Galaxy.

It is assumed that there is cylindrical symmetry about the Galactic Centre for both the north and south sides of the Galaxy separately. The distance of the Sun from the centre of the Galaxy, $R_\odot$, is taken to be 10 kpc for the purposes of the calculations but derived quantities can easily be scaled by the relevant power of $r = R_\odot/10$. Thus, the HII regions are assumed to be in a disc of total thickness $260\,r$ kpc. This value corresponds to the boundary of the ELD HII region which was adopted by Mezger (1978). The residual 60 μm intensities on the maps of the inner Galactic Plane are converted to line intensities expressed in Jy r^{-1} by summing the emission over the latitude range $|b| \leq 1.5°$ and binning into longitude intervals of 2°. The resulting line intensities are shown in Fig. 3.6. On the north side they extend as far as $l = 76°$ which avoids the local Cygnus complex. On the south side the line intensities extend down to 282° (−78°) thus encompassing the Carina Nebula. As we will show later the total emission from beyond these ranges is only a small fraction of that from within and for the purposes of the unfolding procedure we will assume that the emissivity is zero in the outer Galaxy.

The above assumptions are somewhat crude but should enable the observed longitude

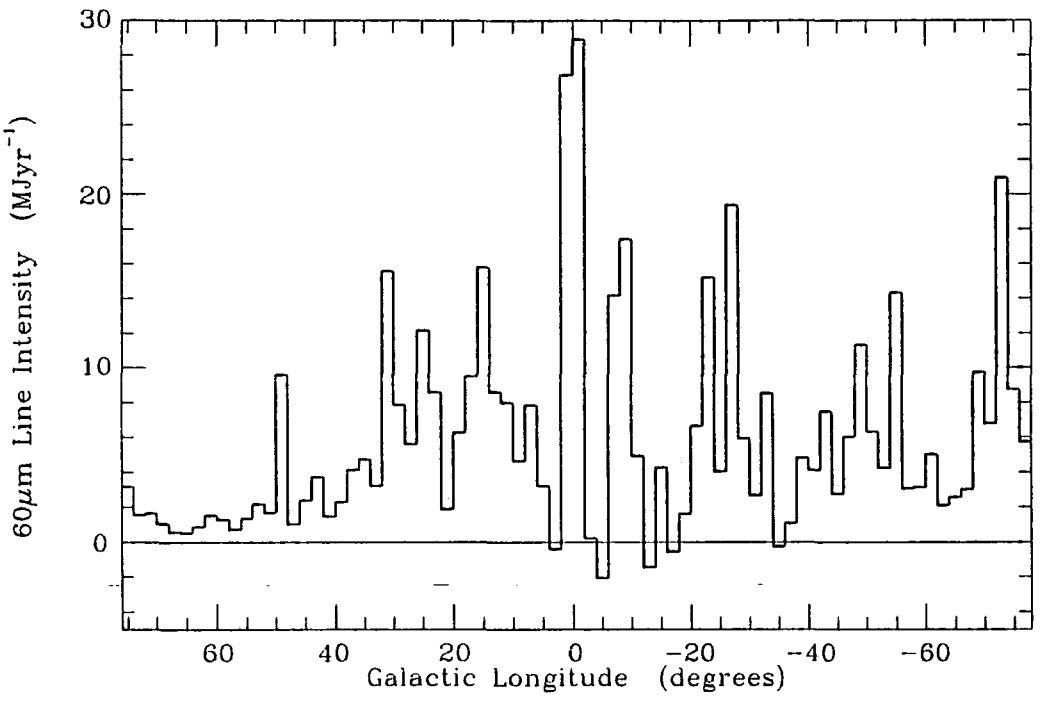

Figure 3.6: Line intensities of the residual 60 μm band emission for the inner Galactic Plane calculated by summing the emission over the latitude range $|b| \leq 1\frac{1}{2}^\circ$ and binning into longitude intervals of 2°.

variation of the 60 μm intensity to be converted to an emissivity variation with galactocentric radius, R, with sufficient accuracy to determine the total luminosity of the whole Galaxy. The assumption of circular symmetry of the emission about the Galactic Centre will clearly not be the case in reality considering for example the work by Georgelin and Georgelin (1976) and Downes *et al.* (1980) on the spatial distribution of HII regions in the Galaxy. However as will be discussed in Chapter 5 there is no general consensus as yet for the exact spiral structure of the Galaxy (see also Liszt, 1985). Georgelin and Georgelin concluded that the distribution of HII regions is consistent with there being four spiral arms. Lockman (1979), studying the central 100° of the Galactic Plane deduced that the most luminous HII regions lies along two narrow trailing arms.

The 2° longitude bins into which the line intensities are arranged define rings about the Galactic Centre as shown in Fig. 3.7. The inner and outer radius of the i^{th} ring is $R_\odot \sin 2(i-1)°$ and $R_\odot \sin 2i°$ respectively and the volume emissivity of the i^{th} ring is denoted w_i. The outermost ring is the N^{th} ring and as mentioned before it is assumed that $w_N = 0$.

The line intensity of the i^{th} longitude bin has two contributions from each ring exterior to the i^{th} ring and can be expressed as:

$$J_i = \sum Q_{ik} w_k \tag{3.7}$$

where $Q_{ik} w_k$ is the contribution of the k^{th} ring to the i^{th} longitude bin. Inversion of the above equation enables the determination of w_i for $i < N$:

$$w_i = \frac{J_i - \sum_{k=i+1}^{N} Q_{ik} w_k}{Q_{ii}} \tag{3.8}$$

The quantities Q_{ik} depend on the line of sight distance through the k_{th} ring. Because of the finite width of the assumed slab model of the disc, there will be a dilution effect for distances beyond about $5\,r$ kpc as shown in Fig. 3.8. At this distance the disc subtends an angle of 3° at the Sun, the latitude range over which the intensities were integrated to obtain the J_is. This dilution effect must be taken into account when calculating Q_{ik} also.

Equations 3.8 are solved in order of decreasing i, each w_i requiring knowledge of the emissivities of the rings exterior to itself for its solution. The estimated radial emissivities at 60 μm deduced from this unfolding procedure are shown in Fig. 3.9. The emissivities have been binned into r kpc wide intervals in radius and are expressed in units of $\mathrm{Wm^{-3}Hz^{-1}}$. The negative values are indicative of the fact that the emissivity does not increase steadily with decreasing galactocentric radius and the assumption of azimuthal symmetry is only approximately true. There is also an obvious asymmetry between the two sides of the Galaxy but both sides have a peak at about $5\,r$ kpc.

An estimate of the luminosity outside the solar circle was made by assuming that all of the HII-associated emission between $l = 76°$ and 282° and $|b| \leq 1.5°$ is emitted uniformly over a volume between $10\,r$ and $13\,r$ kpc from the Galactic Centre. This is a very crude model and in reality most of the emission is from the Cygnus complex. From this estimate however we conclude that the luminosity outside of the solar circle is about $1.1 \times 10^{22}\, r^2$ W $\mathrm{Hz^{-1}}$.

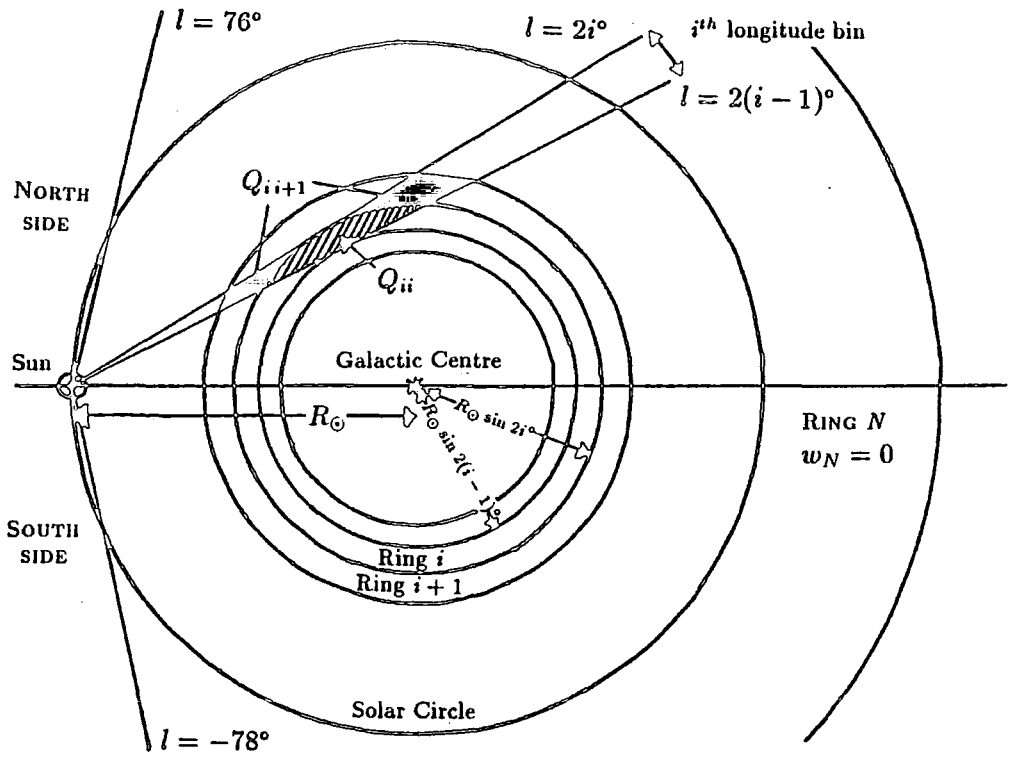

Figure 3.7: The division of the Galaxy into annuli for the unfolding procedure. The N^{th} ring extends from $R = 10\,r$ to $13\,r$ kpc. The diagram is not to scale.

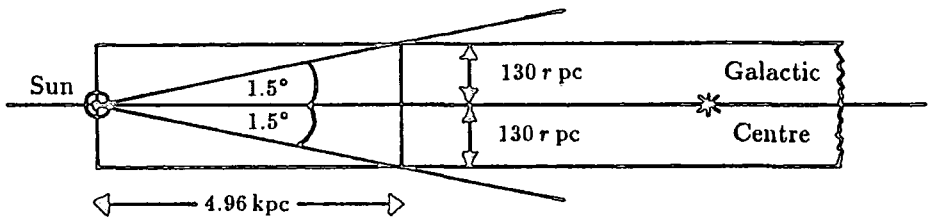

Figure 3.8: Illustration of the distance from the Sun at which the model Galactic disc subtends an angle of 3° in the latitude direction. At distances greater than this the summation of the emission over $|b| < 1.5°$ includes regions outside the disc and the resulting emission is diluted.

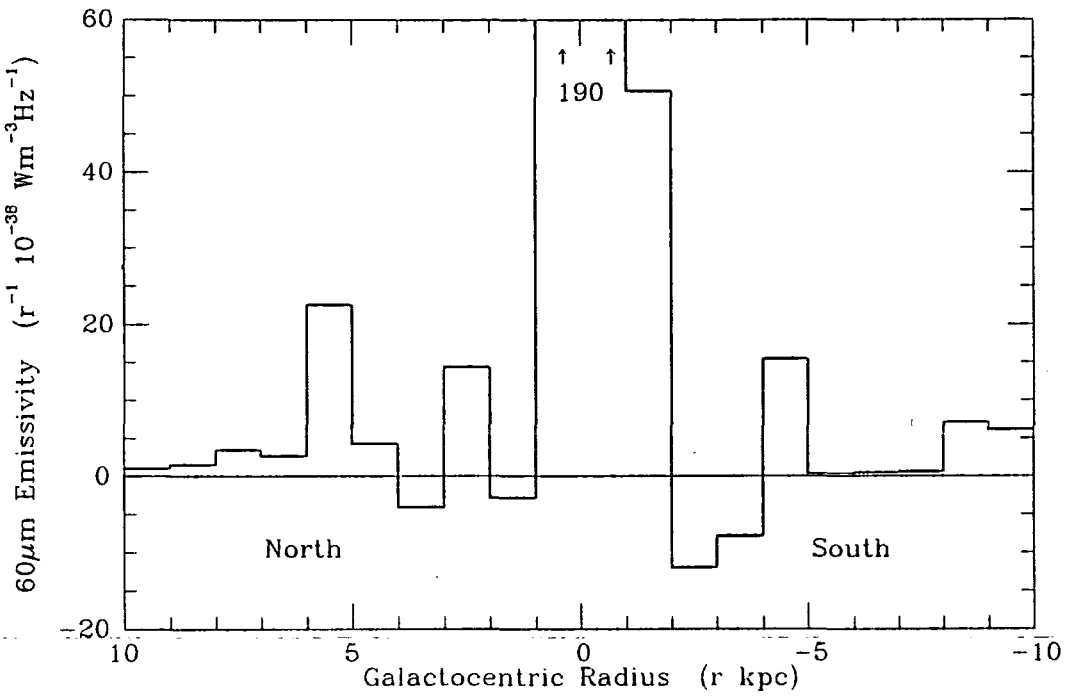

Figure 3.9: The distribution with galactocentric radius of the HII-associated 60 μm emissivity. The unfolding assumes azimuthal symmetry but the presence of some negative emissivities indicate that this is only approximately true. The north and south sides of the Galaxy are treated separately.

Range (kpc)	IRAS 60 μm Luminosity ($\mathrm{WHz^{-1}}$)	
	HI-associated	HII-associated
whole Galaxy	$1.6 \times 10^{23} r^2$	$1.6 \times 10^{23} r^2$
$R < 10r$	$1.5 \times 10^{23} r^2$	$1.5 \times 10^{23} r^2$
$r < R < 10r$	$1.5 \times 10^{23} r^2$	$1.1 \times 10^{23} r^2$
$R > 10r$	$1.2 \times 10^{22} r^2$	$1.1 \times 10^{22} r^2$

Table 3.5: Estimations of the HI- and HII-associated luminosity of the Galaxy in the 60 μm IRAS band for various ranges of galactocentric radii.

The luminosity from within the solar circle estimated from the unfolding procedure is $1.5 \times 10^{23} r^2$ W Hz^{-1} or $1.1 \times 10^{23} r^2$ W Hz^{-1} if we exclude the central r kpc. It is apparent therefore that the emission due to HII-associated dust from the outer Galaxy is small in comparison to that from within. This justifies our rough estimation of the 60 μm luminosity of the outer Galaxy and also the assumption that $w_N = 0$.

For a comparison of these luminosities with the HI-associated dust luminosity of the Galaxy at 60 μm we refer to Li *et al.* (1983) who present a plot of the surface density of HI as a function of galactocentric radius. Using this in conjunction with the variation of dust emissivity per H-atom (see Section 2.3.3), the total luminosity in the 60 μm band of HI-associated dust in the Galactic disc can be calculated. The results are summarized in Table 3.5. Thus we deduce that for the inner Galaxy excluding the Galactic Centre region about 58% of the 60 μm band emission is HI-associated and 42% is HII-associated.

In the calculation of IRE (Section 3.4) we estimated a conversion factor from the total IR flux to flux density at 60 μm given by the IRAS survey of 1.3×10^{-13} Hz^{-1} for HII regions. Hence for the range $2r \leq R(\mathrm{kpc}) \leq 10r$ the total IR flux of HII-associated dust is $\sim 1.7 \times 10^9 r^2$ L$_\odot$. Cox and Mezger (1987) calculate that for their 'warm dust' component of the interstellar medium the total integrated luminosity within the same range of R is $2.7 \times 10^9 r^2$ L$_\odot$. This is somewhat larger than that estimated here but considering the large uncertainties involved in our derived values of the luminosity at 60 μm and the fraction of the total IR this represents, the two are in fairly good agreement.

3.6 The mass of ionized gas

In the last section the method and results of an unfolding procedure were described for the 60 μm band HII-associated dust emission from the Galactic disc. Since we have established a relation between the HII-associated 60 μm and thermal radio continuum emission (see Section 3.3), we effectively have found also the variation with galactocentric radius of the thermal radio emissivity of the ionized gas in HII regions at a given frequency. We can use this to derive rms electron density as a function of galactocentric radius and therefore the mass of ionized gas in the HII regions.

By scaling the 60 μm emissivities $w(R)$ by a factor 1.4×10^{-3}, we obtain the thermal

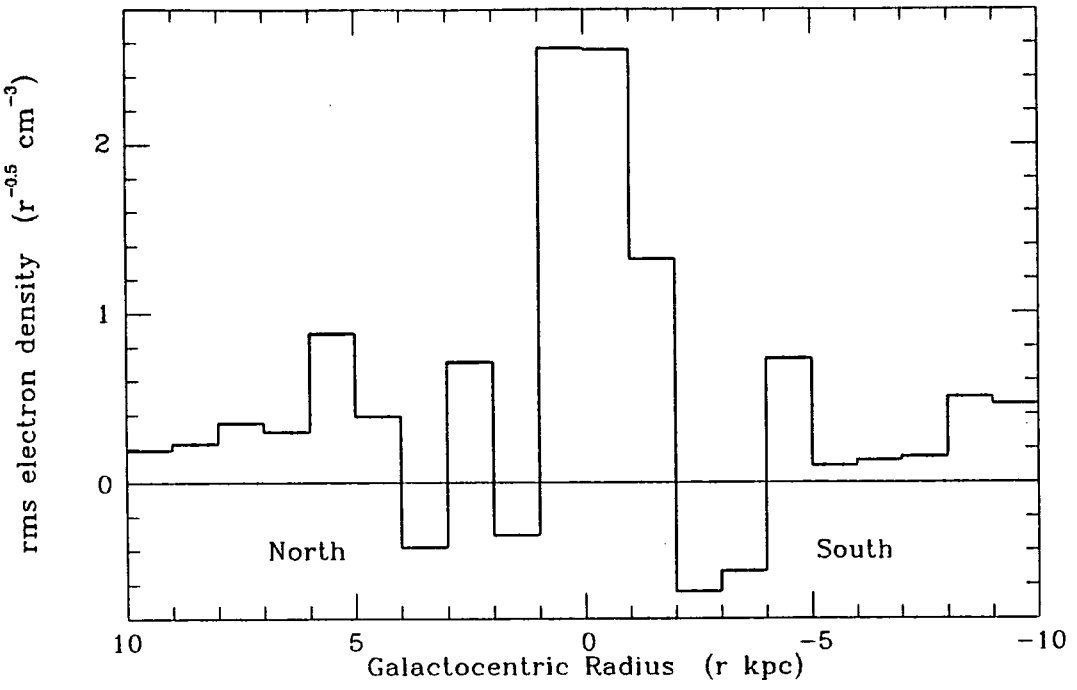

Figure 3.10: The distribution with galactocentric radius of the rms thermal electron density derived from the distribution of HII-associated 60 μm emissivity (Fig. 3.9) and the residual 60 μm–thermal 11 cm relationship derived in Section 3.3.

radio-emissivity at 11 cm. Assuming that this emission is due to thermal bremsstrahlung one can derive a rms electron density $n_e(R)$ for each r kpc wide annulus about the Galactic Centre using the relation:

$$\left[\frac{n_e(R)}{\mathrm{cm}^{-3}}\right] = 1.86 \times 10^{18} \left[\frac{w(R)}{\mathrm{Wm}^{-3}\mathrm{Hz}^{-1}}\right]^{\frac{1}{2}} \tag{3.9}$$

which was derived assuming that the electron temperature is 7000 K. The values of n_e are plotted as a function of galactocentric radius in Fig. 3.10 for both north and south sides of the Galaxy. The negative values reflect the negative values of emissivity which arose from the simplifying assumptions of the unfolding procedure described in the last section. These rms electron densities must be multiplied by the square root of the clumping factor, C, in order to obtain the actual density within the HII regions. Since the unfolding procedure only extends out to $\sim 10\,r$ kpc we must make an estimate of the electron density exterior to the solar circle. To do this we take the rough estimate of the emissivity which was calculated in the previous section assuming that the emission emanates uniformly from the annulus of internal and external radius $10\,r$ and $13\,r$ kpc between galactic longitudes 76° and 282°.

To calculate the total mass of ionized hydrogen in the HII regions of the Galaxy, we assume a constant scale height of $130\,r$ pc as in the last section. The total mass of ionized

R range (r kpc)	M_{ion} $C^{-1/2}r^2\,M_\odot$
0 – 10	8.5×10^8
1 – 10	7.8×10^8
10 – 13	2.1×10^8

Table 3.6: Estimated mass of ionized gas in the Galactic compact and ELD HII regions.

gas M_{ion} is found by multiplying by a factor 1.4 to account for the ionized helium. Hence:

$$M_{ion} = \sum_R 1.4 C^{-\frac{1}{2}} r^2 m_H V(R) n_e(R) \tag{3.10}$$

where V(R) is the volume of the annulus whose mean galactocentric radius is R. The results are summarized in Table 3.6. For the whole Galaxy excluding the central r kpc we estimated that the mass of the ionized gas within compact and ELD HII regions is $9.9 \times 10^8\, C^{-\frac{1}{2}} r^2\, M_\odot$. Again, for reasons described in the previous section these results are only a rough estimate. More refined approaches would consider the spiral structure of the Galaxy but is really beyond the scope of this work. We can compare our estimation with that of Mezger (1978). Excluding the Galactic Centre he estimates that the total mass of ionized gas is $1.3 \times 10^9\, C^{-\frac{1}{2}} r^2\, M_\odot$ which is higher but still in reasonable agreement with our own estimation. Kulkarni and Heiles (1987) estimate the mass of the diffuse ionized gas in our Galaxy to be in the order of $10^9\, M_\odot$ which is to be compared with $4.8 \times 10^9\, M_\odot$ of neutral hydrogen.

3.7 The radio–FIR correlation of spiral galaxies

In Section 3.5 we presented estimates of the luminosity of the Galaxy in the 60 μm waveband both from HI-associated and HII-associated dust emission. We can use the latter to derive a value for the thermal part of the total luminosity of the Galaxy at radio frequencies (L_ν^{th}) knowing the relationship between 60 μm HII-associated emission and 11 cm thermal radio continuum which we found in Section 3.3:

$$L_\nu^{th} = \frac{L_{60\,\mu m}^{HII}}{700} \left(\frac{\nu}{2.7\mathrm{GHz}}\right)^{-0.1} \mathrm{W\,Hz^{-1}} \tag{3.11}$$

In Table 3.7 we show the values of the thermal radio luminosity at 408 MHz, 1.49 GHz, 2.7 GHz and 5 GHz. Also in this table are estimates of the non-thermal luminosities at each frequency. A value of the 408 MHz non-thermal luminosity of the Galaxy, 8.5×10^{21} W Hz^{-1}, was calculated by Osborne (private communication) using the emissivity distribution derived by Phillipps *et al.* (1981b) from the same all-sky survey of Haslam *et al.* (1982) via an unfolding technique (see Section 5.2 for further details). The non-thermal emission at

ν (MHz)	Luminosity (r^2 WHz^{-1})		Percentages	
	Thermal	Nonthermal	$\frac{\text{thermal}}{\text{nonthermal}}$	$\frac{\text{thermal}}{\text{total}}$
408	2.1×10^{20}	8.5×10^{21}	2.5	2.4
1490	1.8×10^{20}	$(2.9 \pm 0.6) \times 10^{21}$	6 ± 1	6 ± 1
2700	1.7×10^{20}	$(18 \pm 5) \times 10^{20}$	9 ± 3	9 ± 3
5000	1.6×10^{20}	$(11 \pm 4) \times 10^{20}$	15 ± 5	13 ± 4

Table 3.7: Thermal and non-thermal luminosity of the Galaxy for $R \geq r$ kpc at 408, 1490, 2700 and 5000 MHz.

408 MHz has a much broader distribution about the Plane. In Phillipps *et al.* the emission was divided into two components, one a thick disc of width 1 kpc and the other a non-spherical halo of much lower emissivity extending $\sim$ 10 kpc from the Plane. This is to be compared with the total width of 260 pc for the HII component of the Galaxy which we assumed in Section 3.5 to unfold the residual 60 μm emission along the inner Galactic Plane. Because the emissivity in the Galactic halo is much lower than in the disc, at the higher frequencies of 2.7 and 5 GHz it becomes more difficult to determine the total luminosity of the Galaxy directly. The values in Table 3.7 were derived by scaling from the value at 408 MHz and the error is a measure of the uncertainty in the assumed non-thermal spectral index. In Section 3.2 we discussed the 6 and 11 cm surveys and made an estimate of the zero levels of each. Allowing for the base-level it was possible to estimate an average non-thermal spectral index between 408 MHz and 5 GHz along the Galactic Plane. We can use the 6 cm non-thermal component, whose determination was described in earlier sections of this chapter, and that at 408 MHz which we will discuss in the next chapter. The average non-thermal flux spectral index is $\sim 0.7 (S(\nu) \propto \nu^{-\alpha_{nth}})$. Reich and Reich (1988) however, argue for a much higher value of $\alpha_{nth} \sim 1.0$ between 1420 and 408 MHz.

Thus, we see that at 408 MHz $\sim$ 2.4% of the luminosity of the Galaxy in the range $R \geq r$ kpc is thermal and this rises to $\sim$ 13% at 5 GHz. We can compare this with recent work by Duric *et al.* (1988) who tried to determine the non-thermal spectral indices and the magnitude of the thermal and non-thermal components of the total flux of spiral galaxies using a spectral index technique (see Section 4.3 for a description of the method). They suggested tentatively that their results indicated a correlation between the Luminosity Class of the Galaxy, which is a measure of the development of the spiral structure of a galaxy, and the size of the thermal fraction of the total flux at 5 GHz. They acknowledged however that much more data was required to vindicate, or otherwise, this relationship. The Luminosity Class of our Galaxy is thought to be ~II (Beck and Reich, 1985) and both the range of values of α_{nth} and the percentage thermal emission we have estimated here lie within the rather large scatter found for these quantities in other spiral galaxies of a similar Class.

Duric *et al.* pointed out that if a correlation between Luminosity Class and thermal radio fraction does exist then this would suggest that there exists a three-way relationship between the thermal radio emission, the non-thermal emission and Luminosity Class. This

implies a link between star formation, cosmic-ray production and spiral structure within a galaxy. Therefore, Duric *et al.* cautioned against associating physical properties of spiral galaxies from apparently tight correlations between two measured quantities for example, Hα and radio continuum, optical (blue) and radio continuum and far infrared and radio, as both properties separately could be correlated to a third and not directly to each other. In recent years there has been a great deal of investigation into correlations such as those mentioned above and most especially that between the FIR and radio emission from disc galaxies. In the remainder of this section therefore we will review some of this large body of work which has been performed by many authors. In the process we will use some of the results of the present work to compare our Galaxy with other galaxies for which radio and IR measurements have been made.

The advent of the IRAS all-sky survey yielded for the first time measurements of FIR fluxes of large numbers of galaxies and Dickey and Salpeter (1984) are credited with first noting the strong correlation between the IRAS 60 μm flux and the radio flux of spiral galaxies. They made a study of radio sources at 1.4 GHz in the Hercules Cluster with the VLA and found a ratio of 60 μm to 21 cm fluxes of 80:1 but noted that the relationship did not hold for elliptical galaxies. In 1985, de Jong *et al.* looked at a larger sample of 91 galaxies this time at 4.8 GHz with the 100 m radio telescope at Effelsberg. Again, for the spiral galaxies amongst the sample the 60 μm and also the 100 μm fluxes were closely related to the radio flux. A least squares fit of the log radio *versus* log 60 μm fluxes had equation of slope 0.94 ± 0.06 consistent with a direct proportionality. Sanders and Mirabel (1985) studied the CO emission of bright radio spiral galaxies most of which had a strong excess of IR emission and an energy distribution between optical and radio wavelengths typical of starburst galaxies. They discovered that for this class of mostly peculiar type galaxies the total FIR flux was correlated to the 21 cm radio continuum and was improved after any point-like radio sources of less than $\sim$ 100 pc in diameter had been subtracted from the core of one or two of the Seyfert galaxies amongst the sample.

Thus it would appear that the correlation is not just confined to normal disc galaxies. Helou *et al.* (1985) confirmed this in their study of a sample of 44 spiral galaxies from diverse locations and whose luminosities spanned about three orders of magnitude. The sample of galaxies included 28 field galaxies, 10 from the Virgo cluster and the other 6 were starburst galaxies, *i.e.* galaxies in whose nuclei very active star formation is in progress. Also, the strong correlation between the 1.4 GHz radio continuum and FIR was not degraded by taking the distances of the individual galaxies into account. A linear regression to the corrected fluxes gives a slope for the logarithmic radio against FIR fluxes of 1.1 *i.e.* very close to one.

Gavazzi *et al.* (1986) continued the work by deriving the 2.3 GHz radio continuum and FIR luminosities of a complete sample of $\sim$ 2000 galaxies using redshifts to calculate their distances. The sample included spirals with Hubble Class from SOa to Sd and also irregulars covering $\sim$ 3 orders of magnitude in luminosity. Again, despite an apparent dependence of the FIR and radio luminosity on Hubble Type, there exists a relationship between the two luminosities to which all of the galaxy types conform. The slope of a log–log plot of the FIR against radio luminosities is 0.83 with a very high correlation coefficient of 0.91. Wunderlich

et al. (1987) and Wunderlich and Klein (1988) examined a sample of $\sim$ 100 galaxies at 4.8 GHz and in the FIR whose luminosities varied over 5 orders of magnitude and included normal spirals, blue compact dwarfs (BCDGs) and Seyfert galaxies. They found that the median ratio of the radio to FIR was slightly higher for BCDGs and considerably higher for Seyferts than for the normal spiral galaxies. However, for both low and high luminosity galaxies the power law relationships that they deduced between radio and FIR luminosity were still within one standard deviation of a direct proportionality.

Hummel (1986) and Hummel *et al.* (1988) concentrated on 88 Sbc spiral galaxies and found a slope of 1.1 ± 0.1 for the log–log 1.5 GHz *vs.* 100 μm luminosity plot which again is consistent with unity. However, when studying 65 late-type spiral galaxies in the 6C 151 MHz radio survey Fitt *et al.* (1988) and Cox *et al.* (1988) found that $L_{FIR} \propto L_{151\mathrm{MHz}}^{0.86\pm0.03}$. Also Devereux and Eales (1989), studying a set of 237 optically bright normal spiral galaxies, found the index of $L_{151\mathrm{MHz}}$ in the proportionality to be significantly less than one. A summary of all these results is given in Table 3.8 in roughly chronological order. The last entry in the table is our estimate of the IR to 1.49 GHz radio luminosity ratio for the Galaxy for both the 60 and 100 μm wavebands. These were calculated using the results of the unfolding of the 60 μm emission in Section 3.5 and using the figures for the thermal and non-thermal radio luminosities from Table 3.7. To obtain an estimate of the 100 μm luminosity of the Galaxy we have assumed a mean ratio of 0.22 for the 60 to 100 μm flux of the Galaxy. The luminosities are for the whole Galaxy apart from the central 1 kpc whereas for the other galaxies the luminosities are for the entire galaxy. Because we are taking the ratio of two luminosities we should still be able to compare our ratios with the average found by other authors for samples of galaxies measured at similar radio frequencies. Thus we see that our estimates are not too far removed from the results of Dickey and Salpeter (1984), de Jong *et al.* (1985) and Hummel *et al.* (1988). The last column of the table shows that in several cases authors found that the relationship was not an exact proportionality between the infrared and radio luminosity but rather that γ, defined in Table 3.8, is significantly less than unity.

At all the radio frequencies employed by the authors listed in the Table 3.8 we can see by referring to Table 3.7 that the dominant component is the nonthermal emission which depends on cosmic ray flux and magnetic field strength. The IR emission by contrast is purely thermal. Also, as has been pointed out earlier, the scale heights of the IR and radio emission of galaxies are vastly different. All of these considerations added to the fact that the IR–radio relation holds for such a large range of galaxy types, luminosities and in diverse environments make the extreme tightness of the correlation very surprising indeed. Hummel *et al.* (1988) investigated other correlations that exist for Sbc galaxies between radio continuum, neutral hydrogen, optical and FIR measurements but found that the FIR–radio relation was one of the strongest ones.

Some of the earlier explanations of the FIR–radio correlation for spiral galaxies, such as that by de Jong *et al.* (1985) had assumed that the emission detected by the 60 μm IRAS band was mostly heated by young massive O and B stars in HII regions and that the IR therefore was a signature of star-formation in a galaxy. The minority thermal component of the radio emission also originates from star-formation regions. The origin of the non-

Authors	Galaxy types	Sample size	Wavelength		IR:radio flux (S) or luminosity (L)	γ $L_{IR} \propto L_{radio}^{\gamma}$
			IR (μm)	(frequency) radio		
Dickey and Salpeter (1984)	Hercules cluster spirals	21	60	21 cm (1.4 GHz)	80	–
de Jong *et al.* (1985)	spirals	91	60	21 cm (1.4 GHz)	220 ± 30	1.06 ± 0.07
Helou *et al.* (1985)	spirals	44	42.5–122.5	21 cm (1.4 GHz)	–	0.91
Gavazzi *et al.* (1986)	spirals	~ 2000	42.5–.5 122.5	13 cm (2.3 GHz)	– –	0.83
Hummel *et al.* (1988)	Sbc spirals	88	100	20 cm (1.49 GHz)	500	0.91 ± 0.08
Wunderlich and Klein (1988)	normal spirals BCDGs Seyferts	71 21 36	42.5–122.5	6.3 cm (4.8 GHz)	–	1.0 ± 0.4 $L_{FIR} < 3.5 \times 10^{36}$ W 0.8 ± 0.3 $L_{FIR} \geq 3.5 \times 10^{36}$ W
Fitt *et al.* Cox *et al.* (1988)	late-type spirals	65	42.5–122.5	2 m (151 MHz)	–	0.86 ± 0.03
Devereux and Eales (1989)	normal spirals	237	42.5–122.5	20 cm (1.49 GHz)	–	0.78 ± 0.05
Our Galaxy	Sbc		60 100	20 cm (1.49 GHz)	~ 90 ~ 410	–

Table 3.8: The far infrared–radio correlation for disc galaxies.

thermal radio emission had been a point of contention for some time but the extremely tight correlation between the IR and non-thermal radio emission suggested that the non-thermal too was associated with the young massive star population rather than the old disc population. A source of relativistic electrons then would be SN explosions of young massive stars. Helou *et al.* (1985) also confirmed the not too surprising result that the combined emission from SNRs alone is insufficient to explain the total non-thermal radio luminosity. The emission from cosmic rays in the general interstellar galactic magnetic field which have diffused away from their sources is required also. Hummel (1986) examined the distribution of deviations of Sbc galaxies from the strong correlation. The magnetic field strength, B, was calculated for each galaxy by assuming that the minimum energy condition between CRs and magnetic field was valid, and it was discovered that the frequency distribution of $B^{1.9}$ was the same as that of the deviations from the IR–radio correlation. Hummel took this as indicative of the validity of the minimum energy condition in most Sbc galaxies and that the deviations from the IR–radio correlation were due to variations from galaxy to galaxy in the magnetic field strength. The star-formation history of the galaxies must also have remained the same during the past $\sim 10^8$ yr which is the timescales of CR confinement and CR source lifetime.

The supposition that FIR emission is predominantly associated with the young population of stars, is apparently not true either in our Galaxy (*e.g.* Cox and Mezger, 1987; Boulanger and Pérault, 1988, this work) or in other galaxies (Persson and Helou, 1987). In addition to the warm dust component associated with HII regions there is a cool, HI-associated component whose source of heating is the general ISRF from the older population of stars. Persson and Helou estimated that between 50 and 70% of the FIR IRAS flux from a galaxy is associated with this cooler gas and our calculations for the Galaxy (Section 3.5) would support this. Some of the later papers *e.g.* Fitt *et al.* (1988), Cox *et al.* (1988) and Devereux and Eales (1989) have tried to subtract from the FIR luminosity the contribution from the cool dust which they propose is the reason for the non-unity power law between the FIR and radio luminosities which became apparent as more and larger samples of galaxies have been used.

In the model of Devereux and Eales (1989) the two components of the IR are separated by assuming that a constant fraction, f, of the blue luminosity, a good tracer of the old stellar disc population, is equivalent to the contribution of the FIR luminosity from the cool dust component for all the spiral galaxies in the sample. The remaining observed FIR luminosity unaccounted for is assigned to the star-forming regions of the galaxy. The value of f is fixed by stipulating that the FIR star-formation luminosity is directly proportional to the non-thermal radio luminosity at 1.49 GHz. They find that f must have an average value of 0.14 for the sample of galaxies. This implies that for galaxies with observed total FIR luminosities of $\sim 10^9\,L_\odot \sim 50\%$ of it is from dust heated by the general ISRF whereas for total luminosities of $\sim 10^{10}\,L_\odot \sim 14\%$ is from ISRF heated dust.

For their sample of 237 spiral galaxies the relationship between total FIR and total 1.49 GHz luminosity could be expressed as:

$$\log L_{1.49\mathrm{GHz}} = 1.28 \log L_{FIR} + 8.87 \qquad (3.12)$$

where $L_{1.49\mathrm{GHz}}$ is measured in WHz^{-1} and L_{FIR} in solar luminosities ($L_\odot = 3.8 \times 10^{26}\,\mathrm{W}$). On subtracting the cool dust component from the IR then the log of the ratio of the radio to FIR luminosity associated with star-forming regions was found to be 11.33 ± 0.18. We can compare these results with quantities that we have deduced for our Galaxy. The $60\,\mu\mathrm{m}$ band luminosity of the Galaxy beyond r kpc from the Galactic Centre is $2.8 \times 10^{23}\, r^2\ \mathrm{W\,Hz}^{-1}$ (Section 3.5). Now this can be converted to a FIR luminosity using the expression:

$$L_{FIR}(40-120\,\mu\mathrm{m}) = 3.65 \times 10^5 (2.58 \frac{S_{60\mu\mathrm{m}}}{\mathrm{Jy}} + \frac{S_{100\mu\mathrm{m}}}{\mathrm{Jy}}) \frac{D}{\mathrm{Mpc}}^2\ L_\odot \qquad (3.13)$$

(Lonsdale, Good and Rice, 1985). Here $S_{60\mu\mathrm{m}}$ and $S_{100\mu\mathrm{m}}$ is the flux of a galaxy in the 60 and $100\,\mu\mathrm{m}$ wavebands observed from a distance D Mpc. If we assumed that $S_{60\mu\mathrm{m}}/S_{100\mu\mathrm{m}}$ for the Galaxy on average is between 0.22 and 0.25 then the total FIR luminosity is $\sim 6 \times 10^9\, r^2\, L_\odot$. The total radio luminosity at 1.49 GHz we have calculated to be $\sim 3.1 \times 10^{21}\, r^2\ \mathrm{WHz}^{-1}$. Hence:

$$\log \left[\frac{L_{1.49\mathrm{GHz}}}{L_{FIR}^{1.28}} \right]_{\mathrm{Galaxy}} = 8.98$$

which is very close to the fit of Devereux and Eales. Likewise we can estimate a value for the cool and warm dust luminosities separately. Assuming $S_{60\mu\mathrm{m}}/S_{100\mu\mathrm{m}} \simeq 0.2$ for the cool component then its total FIR luminosity is $3.7 \times 10^9\, r^2\, L_\odot$ implying $\sim 2.3 \times 10^9\, r^2\, L_\odot$ is from the HII-associated dust in the Galaxy. Hence $\sim 60\%$ of the luminosity of the Galaxy between 40 and $120\,\mu\mathrm{m}$ is from the HI-associated dust. The ratio of the log of the total luminosity at 1.49 GHz and the warm dust FIR luminosity component is thus:

$$\log \left[\frac{L_{1.49\mathrm{GHz}}}{L_{FIR}^{w}} \right]_{\mathrm{Galaxy}} = 12.13$$

which is quite a bit higher than the 11.33 ± 0.18 intercept of the best line fit to the $\log L_{1.49\mathrm{GHz}}$ *vs.* $\log L_{FIR}^{w}$ plot of Devereux and Eales. The luminosity of the warm component here is estimated at $2.3 \times 10^9\, r^2\, L_\odot$ for 40–120 μm. In Section 3.5 we estimated the total IR luminosity of the HII-associated dust in the Galaxy by integrating over a modified Planck function. For $R \geq r$ kpc this yields a value of $2.4 \times 10^9\, r^2\, \mathrm{L}_\odot$. The two values are in fair agreement considering the uncertainties involved in for example the assumed dust temperature for the cold and warm components.

Völk (1989) has recently proposed a theory to explain the FIR–radio emission correlation for spiral galaxies which supposes that the strengths of the sources of relativistic electrons and ionizing photons are both proportional to the SN rate. The relativistic electrons are held responsible for the non-thermal emission and the ionizing photons are taken as the energy source for the dust grains emitting in the FIR. The timescales over which energy from ionizing photons is converted to FIR is considerably shorter than the timescale for energy loss of CR electrons. However Völk supposed that the electrons of the relevant energy would eventually lose all their energy either by synchrotron emission or the inverse Compton mechanism and therefore would not escape from the galaxy which can thus be

considered as a calorimeter. Under these circumstances the non-thermal radio emission does not depend strongly on the magnetic field strength but rather on the ratio of the average photon and magnetic field energy densities within a galaxy.

This model does not take into account that a large proportion of the dust is heated by the general ISRF from the old disc population. Another problem with the theory may be that it depends quite heavily on the presumption that the frequency of the observed radio emission is much higher than the so called break frequency, corresponding to the energy at which the electron energy spectrum steepens due to energy losses. According to Völk's argument this break frequency is as high as 22 GHz in the solar vicinity but decreases rapidly with increasing distance from the electron sources. Therefore at a height of a few kpc from the galactic plane the break frequency should have fallen below 4.8 GHz which was the observation frequency in the work by de Jong *et al.* (1985). However, a strong correlation has been observed between FIR luminosity and 151 MHz radio emission by Cox *et al.* (1988) and it is difficult to believe that this is still above the break frequency even at very high galactic latitudes.

In this section we have reviewed the observations of the FIR–radio correlation and have found that our calculations for the luminosity of the Galaxy are in reasonable accord with other galaxies of a similar type. We have also described some of the explanations of the tight correlation. A complete, quantitative theory of this phenomenon is still lacking and it is likely that the study of this, perhaps one of the most surprising results revealed by IRAS, will receive much more attention in the next few years.

Chapter 4

Separation of the thermal and non-thermal radio emission

4.1 Supernova remnant candidates from the 11 and 6 cm surveys

In Section 3.3 the empirical relationships between the thermal radio brightness temperatures of the 11 cm (Reich *et al.*, 1984) or 6 cm (Haynes *et al.*, 1978) surveys and the IRAS 60 μm band intensities with zodiacal and HI-associated contributions removed were established. These now can be used to subtract, pixel by pixel, the thermal radio continuum emission from both surveys by scaling the net 60 μm intensities (I_{60}) appropriately, *i.e.* for the thermal 11 cm brightness temperature, $T_{th}(11\,cm)$:

$$\left[\frac{T_{th}(11\,\mathrm{cm})}{\mathrm{mK}}\right] = 6.4 \times 10^{-6} \left[\frac{I_{60}}{\mathrm{Jy\,sr^{-1}}}\right] \tag{4.1}$$

and for the thermal 6 cm brightness temperature, $T_{th}(6\,cm)$:

$$\left[\frac{T_{th}(6\,\mathrm{cm})}{\mathrm{mK}}\right] = 1.6 \times 10^{-6} \left[\frac{I_{60}}{\mathrm{Jy\,sr^{-1}}}\right] + 1040 \tag{4.2}$$

As we have discussed in Section 3.2 when describing the radio continuum data employed, the 11 and 6 cm surveys in their published form are not absolutely calibrated and the large scale structure of the non-thermal emission is not represented accurately. The primary effect of subtraction of the thermal radio component is to enhance bright non-thermal sources most of which can be identified with catalogued SNRs. However, a systematic search by eye of maps of the net radio emission over the area $76° \geq l \geq 359°$, $|b| \leq 1.5°$ for the 11 cm survey and $40° \geq l \geq 281°$, $|b| \lesssim 2°$ for the 6 cm survey in conjunction with the 60 μm emission from the same regions has revealed a number of radio sources which have no 60 μm counterpart and which are not listed in SNR catalogues. A list of these sources is given in Table 4.1 together with the total radio flux and the 60 μm to radio flux ratio.

Position		Flux (Jy)		Flux ratio		
l	b	6 cm	11 cm	60 μm/6 cm	60 μm/11 cm	Comments
280.2	+1.5	0.3		0		
284.3	−1.6	9.1		0		resolved
286.0	−1.1	2.1		0		
286.8	−0.0	12.0		0		resolved
289.1	−2.8	1.1		0		
290.8	+0.8	1.4		23		
299.7	−1.4	0.2		26		
309.7	+1.7	57.0		2		radio galaxy[1]
312.9	−0.1	2.7		0		resolved
313.6	+1.3	0.9		0		
314.0	+1.0	1.1		54		resolved
318.9	−0.5	1.1		52		resolved
319.0	+0.4	3.0		57		resolved
321.5	+1.0	1.2		0		
322.1	+0.0	1.3		0		
322.1	+1.4	1.6		0		
325.5	+1.7	1.3		0		
339.5	−1.3	3.4		0		resolved
341.8	+1.8	1.0		46		resolved
347.7	−1.2	1.8		58		
357.2	−0.2	0.8		0		resolved
2.9	−2.8	2.5		0		
3.7	+0.6	0.6		0		
5.3	−2.5	0.7		0		resolved
5.6	+1.4	0.3		39		
6.3	+1.9	0.4		0		
6.6	+1.4	0.5		0		
8.7	−0.2	14.3	79.0	0		resolved
9.7	−0.1	1.1	1.9	29	17	resolved
15.4	+0.2	0.7	2.6	0	0	resolved
15.5	−0.1	0.7	1.1	0	0	resolved
16.7	+0.1	1.5		73		
19.3	+2.2	1.5		0		
21.0	+2.0	2.7		21		

Table 4.1: Non-thermal sources which are not catalogued SNRs. (Continued on next page)

Position		Flux (Jy)		Flux ratio		
l	b	6 cm	11 cm	60 μm/6 cm	60 μm/11 cm	Comments
21.3	−0.6	1.6	0.8	0	0	
24.9	−1.8	0.5		20		
28.8	−0.5	0.3	0.3	0	0	resolved
29.4	+0.1	1.7		45		resolved
30.1	+1.3	2.3	3.6	20	13	radio galaxy[2]
31.6	−0.6	1.4	1.3	0	0	resolved
32.3	+1.2	0.4		111		
36.5	−0.0	0.5	0.7	0	0	
39.7	−2.2	0.5		8		
40.1	−2.3	0.4		5		
41.5	+0.4		3.3		0	resolved
43.9	−0.5		0.3		0	
57.3	+0.7		1.0		9	
59.6	+0.1		1.2		0	resolved
61.5	+0.3		2.7		0	resolved[3]
62.4	−0.9		0.9		0	radio galaxy[4]
63.8	+1.1		1.3		18	
71.2	−0.1		1.8		0	
72.2	−1.0		1.5		0	radio galaxy[5]
72.4	−0.5		0.5		0	

Table 4.1: *contd.* Non-thermal sources which are not catalogued SNRs.

[1]Shaver and Goss (1970) assume extragalactic.
[2]Presumably a radio galaxy but we have not found confirmation in the literature.
[3]The source is resolved and shows structure but is very near another bright source.
[4]Has been observed at 2.7 GHz by the 5 km Cambridge telescope (Green, 1985).
[5]As for note [3]. A double source.

Co-ordinates		Flux (Jy)		Flux ratio		
l	b	6 cm	11 cm	60 μm/6 cm	60 μm/11 cm	Comments
322.1	+0.6	21		860		compact HII
328.6	−0.5	11		1523		compact HII
333.0	+0.8	6		950		compact HII
350.8	−0.0	2.5		852		compact HII
27.8	+0.6		28		14.3	SNR
34.7	−0.4		147		0	SNR W44
40.5	−0.5		5.4		0	SNR
46.8	−0.3		9.7		0	SNR

Table 4.2: The positions, radio fluxes, 60 μm to radio flux ratios of a few compact HII regions and catalogued SNRs to be compared with the unidentified non-thermal sources listed in Table 4.1.

We have measured the flux of these sources using software provided by the IPMAF team of RAL. The area of the radio source is picked out interactively from the radio contour map and an estimate of the background is obtained from the average intensity in the pixels bounding the chosen area. The flux from exactly the same area is then obtained from the corresponding 60 μm contour map which has had the zodiacal light removed only and the 60 μm band to radio flux ratio is calculated. In all cases the IR flux is low and because of the approximations in determining the background it sometimes has a small negative value. Where this applies we write the 60 μm to radio ratio as zero. All of the sources we picked out have total 11 cm fluxes $\geq$ 0.25 Jy. The 60 μm to 11 cm flux ratios are $<$ 20 and 60 μm to 6 cm flux ratios are $<$ 120. For a comparison, in Table 4.2 is compiled the positions, radio fluxes and total 60 μm to radio flux ratios of a few compact HII regions and catalogued SNRs. In general the 60 μm to 6 cm ratio for HII regions are $\gtrsim$ 500. Also, it may be recalled that the ratio for extended HII regions as derived from the lower envelope of the radio *vs.* net 60 μm plots (Section 3.3) was 700 and 810 for the 60 μm to 11 cm and 60 μm to 6 cm flux ratios respectively.

Of the 44 sources which were found in the 6 cm survey, 25 were unresolved (*i.e.* they have a diameter $<$ 4′) and two were resolved but as explained in the notes to Table 4.1 are probably radio galaxies. The number counts of radio galaxies at 5 GHz (Wall and Cooke, 1975) indicate that there should be approximately 48 radio galaxies with flux $>$ 0.3 Jy over the 524 square degrees of the 6 cm survey studied. A certain fraction of these lying very close to the plane will be obscured by bright Galactic emission and are liable to be missed. The flux–angular size distribution of radio galaxies (Swarup and Subrahmanya, 1976) suggests that approximately 4 should be resolved by the 4.4′ beam. These estimates are consistent with all of the unresolved sources from the 6 cm survey in Table 4.1 being radio galaxies also.

For the search over the 11 cm survey, 17 sources were found, 11 of which are unresolved.

Two of these have been observed (see notes to Table 4.1) and are probably radio galaxies. One of the resolved sources also is most likely extragalactic in origin. The 2.7 GHz number counts of Wall and Cooke imply that there should be about 45 radio galaxies with flux > 0.25 Jy over the 195 square degrees of sky covered by the 11 cm survey. Consideration of the flux–angular size distribution indicates that there is only a 1 in 8 chance of there being a Galaxy which would be resolved with a $4'$ beam.

The remaining 20 resolved sources listed in Table 4.1 are SNR candidates although obviously there is still a chance that some may be radio galaxies. In Fig. 4.1 contour maps of a few of the most likely SNR candidates are presented both for the total 60 μm band emission and either the total 11 cm or total 6 cm emission.

The source at $286.8 - 0.0$ is on the edge of the large HII complex of the Carina Nebula and is surrounded by strong thermal sources and thus would probably be considered as a diffuse extension of these sources if observed in the radio alone. However, the absence of emission in the same area at 60 μm indicates that there is in fact a separate non-thermal source whose 6 cm emission is in close proximity to the thermal emission from the edges of the surrounding sources.

The source centred at $8.7 - 0.2$ is very large having a diameter of about 1°. The strong thermal sources at $8.5 - 0.3$ have probably diverted attention from the surrounding non-thermal emission in previous studies of the Galactic Plane using radio continuum measurements alone.

At $31.6 - 0.6$ there is another large diffuse source on the edge of a complex region of thermal emission. This source was noted by Haslam and Osborne (1987) as being a good SNR candidate.

In addition to the discovery of new SNR candidates the method of comparison of 60 μm to 11 cm flux gives further information concerning sources whose natures are still in question despite polarization and spectral index measurements. We examine three such sources which have been discussed by Reich *et al.* (1985) and Green (1985).

G50.29–0.4 This source was studied by Green with the Cambridge 5 km telescope at 2.7 GHz and was resolved into two objects, a diffuse object and a fainter double source which Green presumed is a radio galaxy. Reich *et al.* found that $G50.29 - 0.4$ has no polarization and a thermal spectral index and concluded therefore that it is probably a HII region but that there was still a slight possibility that it could be a plerionic SNR. The 60 μm to 11 cm flux ratio is of the order of 200 which suggests that the diffuse source is indeed thermal with the nearly coincident radio galaxy being responsible for the lower than average value.

G54.09+0.2 Reich *et al.* (1985) concluded that this object is a plerionic SNR as it has a flat spectral index and a filled centre yet significant polarization. Green (1985) however queried the non-thermal nature of the source on the grounds of its structure and flat spectrum. The absence of substantial 60 μm emission from $G54.09 + 0.26$ (ratio ~ 30) suggests to us that this source is indeed a SNR although we acknowledge that the source lies in a very confused region.

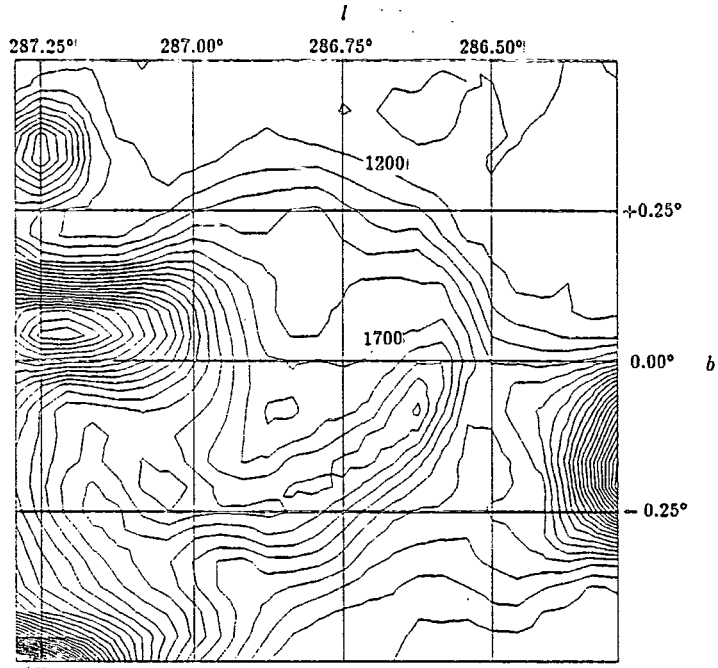

(*i*) 6 cm
Contour levels every 100 mK

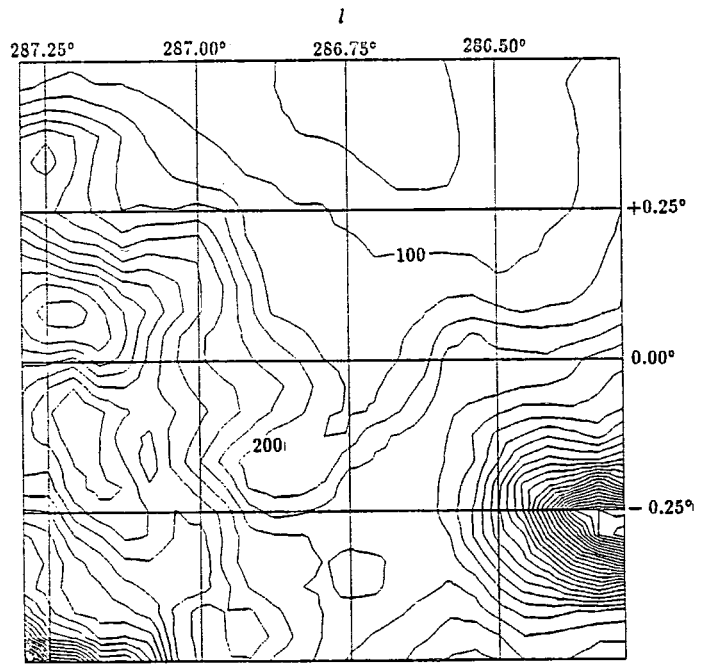

(*ii*) 60 μm
Contour levels every 50 MJy sr^{-1}

Figure 4.1: Contour maps of a few of the most likely candidates found in the search for SNRs. For each source is shown contour levels of equal (*i*) total 6 or 11 cm brightness temperature (mK) and (*ii*) total IRAS 60 μm band brightness intensity (MJy sr^{-1}).

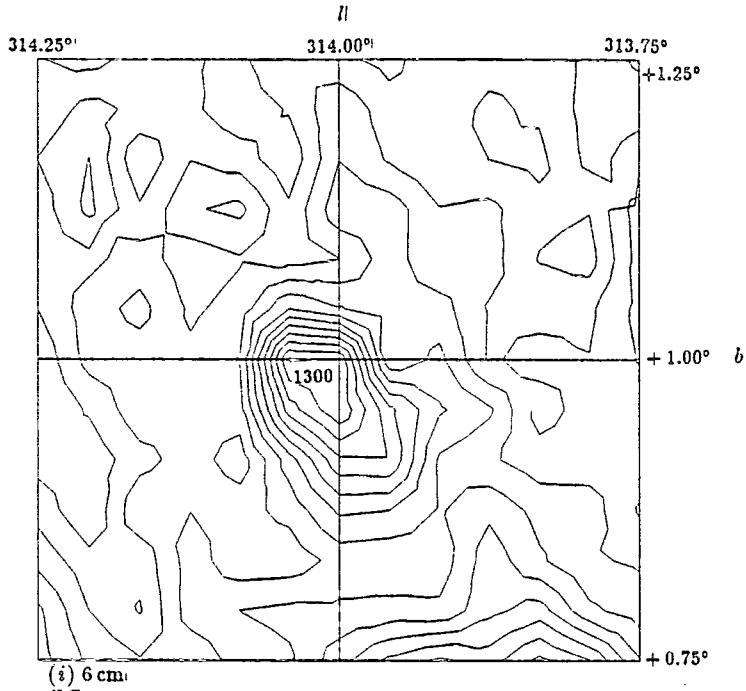

(i) 6 cm
Contour levels every 50 mK

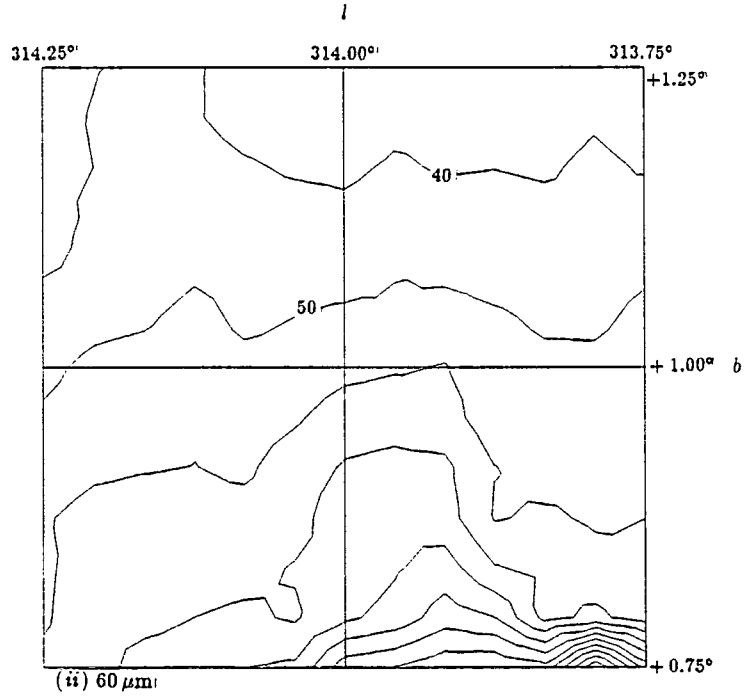

(ii) 60 μm
Contour levels every 10 MJy sr^{-1}

Figure 4.1: *contd.*

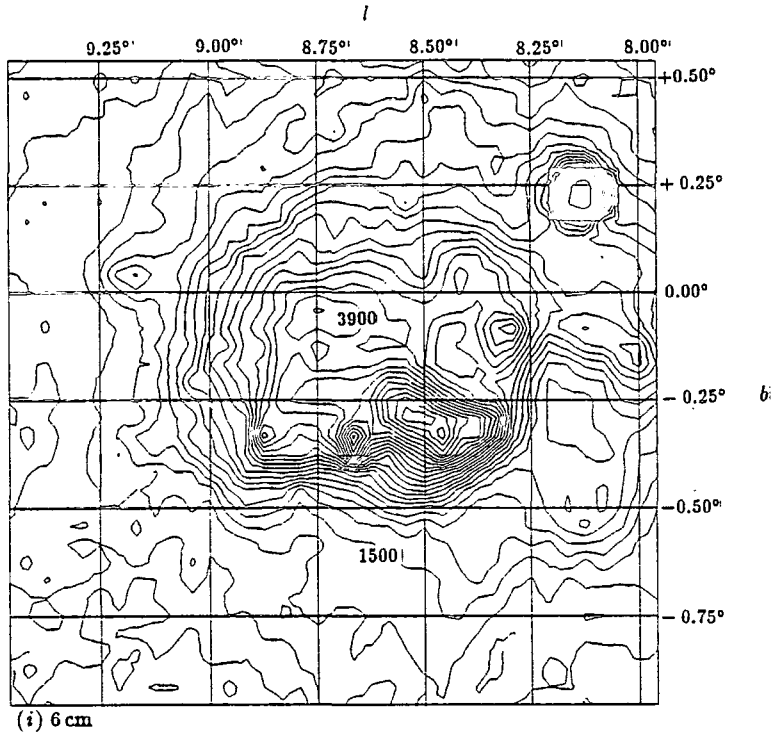

(*i*) 6 cm
Contour levels every 100 mK

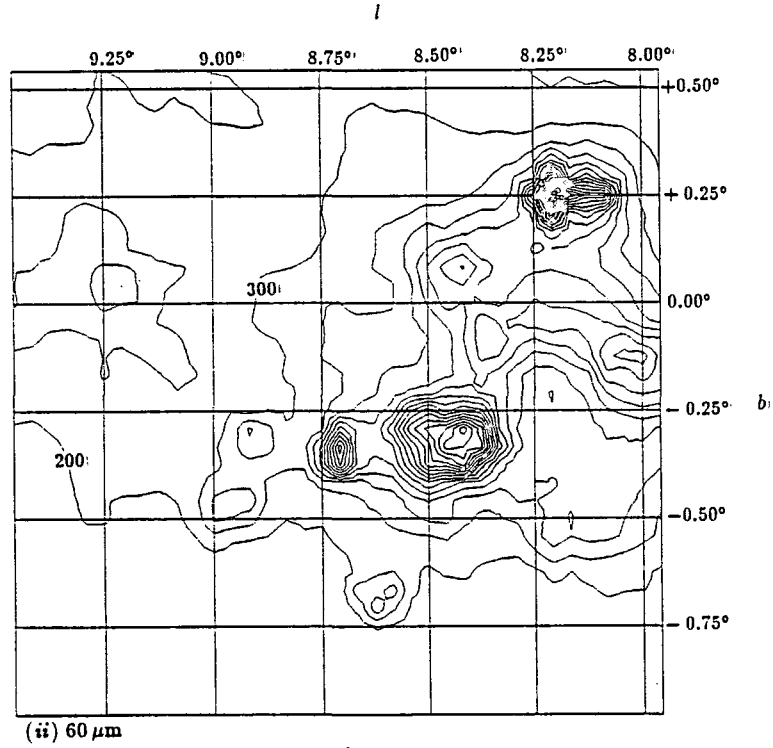

(*ii*) 60 μm
Contour levels every 100 MJy sr^{-1}

Figure 4.1: *contd.*

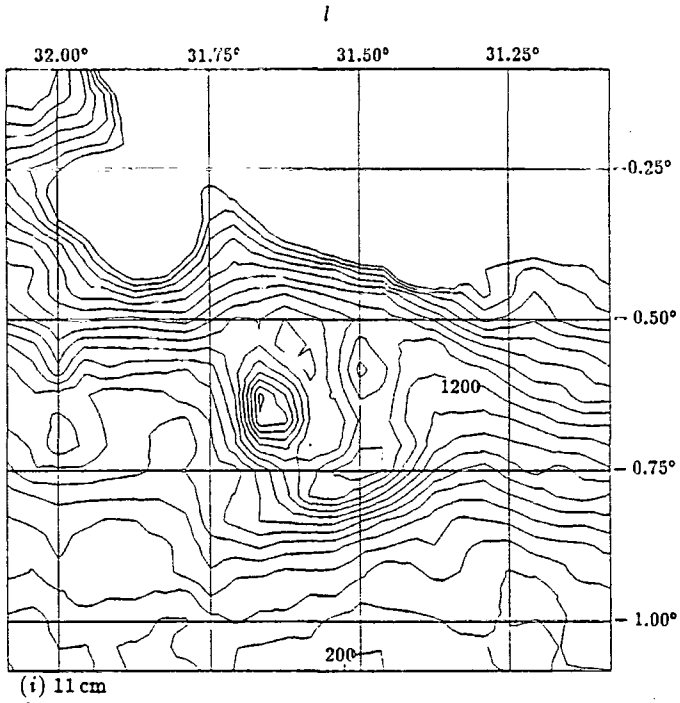

(*i*) 11 cm
Contour levels every 100 mK

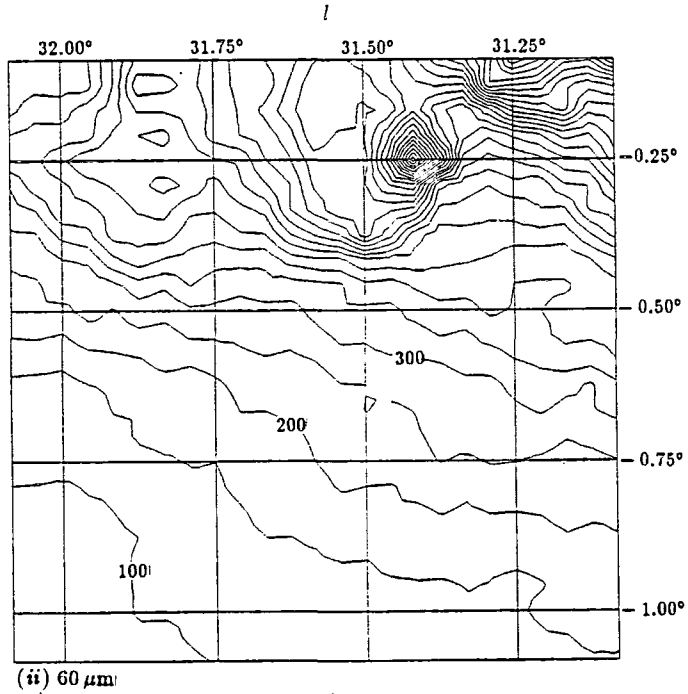

(*ii*) 60 μm
Contour levels every 50 MJy sr^{-1}

Figure 4.1: *contd.*

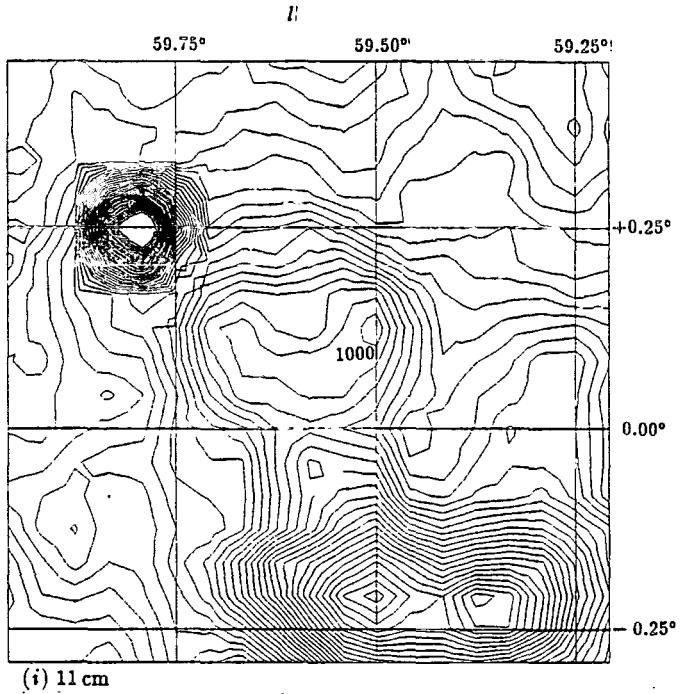

(*i*) 11 cm
Contour levels every 50 mK

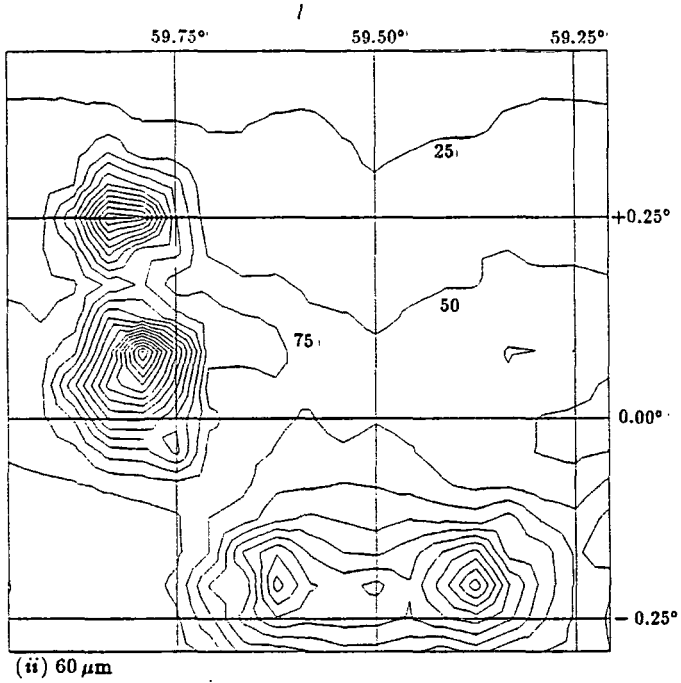

(*ii*) 60 μm
Contour levels every 25 MJy sr^{-1}

Figure 4.1: *contd.*

G70.68+1.20 The map of this source, made with the Cambridge 5 km telescope at 2.7 GHz by Green (1985), reveals its shell structure. However the low polarization and flat spectrum at low frequencies both suggest it is a thermal source. Reich *et al.* however conclude that the object is non-thermal because of the steep spectrum above 2.7 GHz and its SNR-like morphology. The 60 μm:11 cm flux ratio is $\sim$ 350 suggesting that the emission is predominantly thermal.

Fürst *et al.* (1987b) have developed independently a similar procedure based on the 60 μm to radio emission ratio of discrete non-thermal sources in the Galaxy which they are applying to the 11 cm Effelsberg survey. For compact HII regions they find the 60 μm to 11 cm flux ratio clusters around 1000 and that known SNRs have a ratio less than 10.

Some time after we had completed our SNR search over the 6 and 11 cm surveys a revised Catalogue of Galactic SNRs was published by Green (1988). Included in this new list were three of the sources we had picked out as SNR candidates:

G8.7–0.1 has a quoted flux at 1 GHz of 90 Jy and a spectral index 0.25. Scaling to 6 and 11 cm the estimated flux would be 60 and 70 Jy respectively to be compared with our crude estimates of 14 and 79 Jy. This source lies within W30 and Gosachinskiĭ (1985) first suggested that it could be a SNR which was later confirmed by Odegard (1986).

G31.5–0.6 was one of four SNRs identified by Fürst *et al.* (1987a) but because it is near strong thermal sources no spectral index has been obtained.

G57.2+0.8 was listed in Green's new catalogue and was from a list of 33 candidates picked out by Reich *et al.* (1988) from the 11 cm Effelsberg survey. However it is a faint source and its flux and spectral index have not been very well determined.

Green also compiled a list of possible SNRs but which were not included in his catalogue. Two of these are among our list in Table 4.1:

G41.4+0.4 Fürst *et al.* (1987a) investigated this as one component of a complex of features selected from the 11 cm Effelsberg survey and noted that it resembled a filled-centre SNR. Further observations are required at higher resolution to corroborate this.

G284.2–1.8 Milne (1971) suggested this was a SNR and Jones and Findlay (1974) detected it at 29.9 MHz. However the apparent spectrum found by Clark and Caswell (1976) led them to believe that it was a thermal source. On the 6 cm Parkes survey there are two sources at 284.2 – 1.8 and 284.3 – 1.5 and we can find no IR counterpart for either.

Green included a number of other new SNRs in his revised catalogue and on examination of the IR contour maps of these radio sources we would agree that most of them are non-thermal except perhaps those at 16.8 – 1.1 and 20.0 – 0.2. Of the SNRs listed in the catalogue which Green classified as questionable we note that those at 23.6+0.3, 311.5 – 0.3, 338.5 + 0.1 and 299.0+0.2 seem to have associated IR emission.

As we have seen in Table 4.2 the 60 μm emission of SNRs seems to be very small and using our crude method of flux determination we found significant emission above the ambient level for only one of the four listed in the table. Some more careful studies, using all four IRAS wavebands, have been performed by several authors of a few SNRs which were detected at low intensity levels by the survey. Braun and Strom (1986a, 1986b) studied the structure and dynamics of the evolved remnants IC443 and the Cygnus Loop. At 60 μm the intensity levels reach a maximum of only a few tens of MJy sr^{-1}. This is at or below the lowest contour levels which we plotted when studying the 60 μm emission and radio emission close to the Galactic Plane in search of new SNR candidates.

Despite their low levels of emission in the IRAS wavebands, those SNRs that have been studied in the FIR have emission far exceeding that which would be expected from an extrapolation of the radio synchrotron emission. Marsden *et al.* (1984) found that this excess emission in the Crab Nebula could be well fitted by a thermal spectrum from dust at about 80 K for a linear frequency dependence of grain emissivity. They put an upper limit on the mass of dust involved at 0.03 $M_\odot$. Likewise for Cas A, Dwek *et al.* (1987a) found a large excess of IR emission over that expected from the synchrotron mechanism. Most of the excess could be explained in terms of thermal emission from dust of total mass $\sim 3 \times 10^{-3} M_\odot$. Dust grains, being a mixture of silicate and graphite, are swept up in the SN blast wave and are heated mainly by collisions of the grains with the X-ray emitting gas. Dwek *et al.* (1987b) compared the IR flux with the X-ray flux for a number of SNRs both young and old and discovered that the IR dust emission was in fact the dominant cooling mechanism.

Mufson *et al.* (1986) also made a study of IC443 at radio, optical, UV and X-ray wavelengths as well as in the IRAS wavebands. The IR emission appeared to be associated with individual features of the remnant whereas most of the radio continuum emission defined the large scale structure. The IR emission was decomposed into three components; from shock-heated dust, from atomic line emission and from dust heated by UV from the ISRF. It was established that of the three the dominant component at 60 μm is the shock-heated dust but with still quite a large fraction coming from line emission. Only a very small fraction of the IR is from radiation heated dust. In 1987 Braun studied the young SNRs Tycho, Kepler and Cas A mainly in the IRAS wavebands but also at X-ray, optical and radio wavelengths. He deduced that in all cases the IR emission is from shock-heated dust. Of the wavelength regimes studied, the radio emission seemed to be the most uniform over the individual remnants whereas the IR emission tended to originate from the higher density shocked interstellar medium.

4.2 Thermal and non-thermal components at 408 MHz

The theoretical spectral index of Galactic radio continuum emission by the thermal bremsstrahlung mechanism is 2.1 *i.e.* $T_{th}(\nu) \propto \nu^{-2.1}$ where $T_{th}(\nu)$ is the brightness temperature at frequency ν due to thermal emission in a given direction. The non-thermal spectral index on the other hand tends to be steeper and not necessarily constant with frequency or position in the sky (see *e.g.* Lawson *et al.*, 1987, Reich and Reich, 1988). At 2.7 GHz($\equiv$11 cm) and

5 GHz(≡6 cm) the dominant component in the Galactic Plane is the thermal emission and hence, as described in Section 3.3, we found the correlation between 60 μm and thermal radio continuum emission at these higher frequencies. The non-thermal component is dominant out of the plane by virtue of its much larger scale height of emission. However, at lower frequencies the non-thermal component tends to be the greater contributor to the Galactic emission both in and out of the Plane. As was mentioned in Section 3.2 the 408 MHz all-sky survey of Haslam *et al.* (1982) is absolutely calibrated and so provides a suitable data base for the study of the non-thermal emission from the Galaxy on large scales.

Therefore, we have applied the thermal–non-thermal separation technique to the area of the 408 MHz all-sky map within 8° of the Galactic Plane. In Section 3.3 we deduced empirically the relation between $T_{th}(2.7\,\mathrm{GHz})$,the thermal brightness temperature at 11 cm and I_{60}, the 60 μm brightness intensity after removal of zodiacal and HI-associated emission. Hence assuming a thermal spectral index of 2.1 we can scale the residual 60 μm emission to 408 MHz to obtain an estimate of the thermal emission at this frequency:

$$\left[\frac{T_{th}(408\,\mathrm{MHz})}{\mathrm{K}}\right] = \left(\frac{T_{th}(2.7\,\mathrm{GHz})}{I_{60}}\right)\left(\frac{0.408}{2.7}\right)^{-2.1} I_{60} = 3.4\times10^{-7}\left[\frac{I_{60}}{\mathrm{Jy\ sr^{-1}}}\right] \qquad (4.3)$$

Before subtracting this scaled IR emission we convolved all twelve residual 60 μm Galactic Plane maps to the same 51′ resolution of the 408 MHz survey. The spectral index of 2.1 applies provided that the emitting regions are optically thin down to 408 MHz. This is true everywhere except for a few very bright HII regions which could be identified by the local minima resulting from subtraction of the scaled and convolved residual 60 μm emission from the 408 MHz survey. For the inner half of the Galactic Plane 8 obvious minima could be discerned from a greyscale representation and are in the positions of strong HII complexes.

For an optically thin source the flux has spectrum $S^{thin}(\nu) \propto \nu^{-0.1}$. However for a source which is optically thick at a frequency ν, the measured flux $S(\nu)$ is less than $S^{thin}(\nu)$. Therefore the assumption that the source is optically thin will be an overestimate by an amount $S^{corr}(\nu)$. Thus:

$$S^{corr}(408\,\mathrm{MHz}) = \begin{cases} S^{thin}(408\,\mathrm{MHz}) - S(408\,\mathrm{MHz}) \\ S(5\,\mathrm{GHz})\left(\frac{0.408}{5}\right)^{-0.1} - S(408\,\mathrm{MHz}) \end{cases} \qquad (4.4)$$

Most of the optically thick regions that were picked out contain several sources whose fluxes have been measured by Shaver and Goss (1970) at both 408 MHz and 5 GHz. Using these measurements we can calculate $S^{corr}(408\,\mathrm{MHz})$. Each of the sources has size very much smaller than the beam size of 51′ and so a map can be constructed of gaussian temperature distributions in the positions of the optically thick sources and of half-power width 51′. The peak temperature, $T(0)$, of each distribution is given by:

$$\left[\frac{S^{corr}(408\,\mathrm{MHz})}{\mathrm{Jy}}\right] = 2.945\times10^{-3}\left[\frac{\nu}{\mathrm{GHz}}\right]^2\left[\frac{h}{\mathrm{arcmin}}\right]^2\left[\frac{T(0)}{\mathrm{K}}\right] \qquad (4.5)$$

where $\nu = 408$ MHz and $h = 51'$. This is then subtracted from the scaled, convolved residual 60 μm map of the same area to give our best estimate of the brightness temperatures of

thermal emission at 408 MHz. Table 4.3 gives a list of the sources with their fluxes at 408 MHz and 5 GHz measured by Shaver and Goss and the corrections to the optically thin estimate of the 408 MHz peak temperatures.

The middle contour map of Figs. 4.2 and 4.3 show the thermal emission at 408 MHz for the inner half of the Galactic Plane. The lower line of Figs. 4.4 and 4.5 represents a cut along the whole of the Galactic Plane for the same component. The top line of these figures represents the total emission at 408 MHz and as can be seen the thermal contribution is the minor, yet still significant component at this frequency. Also, it is interesting to note that the relationship between the net 60 μm and thermal radio emission derived from the inner Galactic Plane appears to apply well to the Cygnus complex which is situated at $l \sim 80°$ and is a fairly nearby feature.

In Section 2.3 we described three different models of the HI-associated dust emission at 60 μm. We used the second model which assumed that 'standard' dust grains are immersed in a varying interstellar radiation field for subsequent work determining the relation between the residual 60 μm and thermal radio emission. Model C, which we have called the 'small grain' model, assumed that the HI-associated dust emission at 60 μm was one fifth of that at 100 μm. To see how sensitive the thermal–non-thermal separation technique is to the assumed grain model at 408 MHz we carried out, for a small area of sky only, the same procedure but taking the 'small grain' model for the HI-associated dust emission. The method of determining the net 60 μm intensity–11 cm brightness temperature relation was discussed in Section 3.3. The lower envelopes of seven plots of the thermal 11 cm against residual 60 μm emission covering the longitude range $53° \geq l \geq 11°$ were determined. The average gradient was found to be $(4.7 \pm 1.2) \times 10^{-6}\,\mathrm{mK\,(Jy\,sr^{-1})^{-1}}$ which is within one standard deviation of the average slope found in Section 3.3 using the 'standard grain' model. The residual 60 μm brightness intensity for the small grain model should therefore be scaled by $2.5 \times 10^{-7}\,\mathrm{K\,(Jy\,sr^{-1})^{-1}}$ in order to obtain the estimated 408 MHz thermal component assuming everywhere is optically thin. After convolution to $51'$ we can compare the two models. In Fig. 4.6 is shown a cut along the Galactic Plane of the 408 MHz thermal emission. The top, dashed line was derived using the standard grain model of HI-associated dust emission and the lower, solid line from the small grain model. When compared with the total 408 MHz temperatures (top line of Fig. 4.2) the differences between the two models are relatively small especially away from peaks in the emission.

The thermal emission at 408 MHz predicted from the standard grain model residual 60 μm emission with corrections for optically thick sources is now subtracted from the total emission to give the distribution of the non-thermal emission. In order to facilitate the study of the large scale distribution of this emission we have also subtracted the contributions from catalogued SNRs which lie within $\sim 2°$ of the inner Galactic Plane. The method employed is similar to that used when making corrections to the estimates of emission from optically thick sources. The Catalogue of Galactic Supernova Remnants compiled by Green (1987) gives the galactic co-ordinates, angular size, flux spectral index (α) and flux at 1 GHz (S(1GHz)) of each SNR. All objects except for W50 have an angular diameter less than the $51'$ resolution of the 408 MHz survey and so we have approximated them to point sources.

Source name	Position l	b	Fluxes (Jy) S(408MHz)	S(5GHz)	S^{corr}(408MHz) (Jy)	T(0) (K)
W51	49.4	−0.3	22.7	37.2	25.1	19.7
	49.5	−0.4	53.2	114.9	94.4	74.0
W43	30.5	−0.3	7.1	6.5	1.3	1.0
	30.8	−0.0	60.6	86.5	50.5	39.6
M17	15.0	−0.7	313.4	478.3	301.1	236.1
RCW	351.1	+0.7	49.8	47.9	11.7	9.2
127	351.2	+0.7	18.9	22.5	10.0	7.8
	351.2	+0.5	17.2	20.9	9.7	7.6
	351.4	+0.7	119.8	158.0	83.2	65.2
G333.6	333.1	−0.4	26.7	42.1	27.4	21.5
−0.2	333.1	−0.0	3.1	3.5	1.4	1.1
	333.2	−0.1	7.3	12.3	8.5	6.7
	333.3	+0.1	1.7	2.8	1.9	1.5
	333.3	−0.4	13.3	34.2	30.6	24.0
	333.6	−0.1	16.6	15.0	2.7	2.1
	333.6	−0.2	23.2	84.4	85.2	66.8
RCW	305.1	+0.1	15.0	14.2	3.2	2.5
74	305.2	+0.0	27.7	28.0	8.3	6.5
	305.2	+0.2	37.2	52.0	29.6	23.2
	305.3	+0.1	6.3	9.2	5.5	4.3
	305.4	+0.2	23.5	39.4	27.1	21.3
	305.6	+0.0	16.7	17.8	6.2	4.9
RCW	291.3	−0.7	19.6	97.4	105.5	82.7
57	291.6	−0.5	137.2	172.1	83.9	65.8
CARINA	287.4	−0.6	141.2	* 125.0	19.4	15.2
	287.6	−0.6	120.3	* 103.0	12.0	9.4

Table 4.3: Optically thick sources. Fluxes are listed in Shaver and Goss (1970) except for entries marked * which were taken by Shaver and Goss from Gardner and Morimoto (1968). See text for explanation of S^{corr} and $T(0)$.

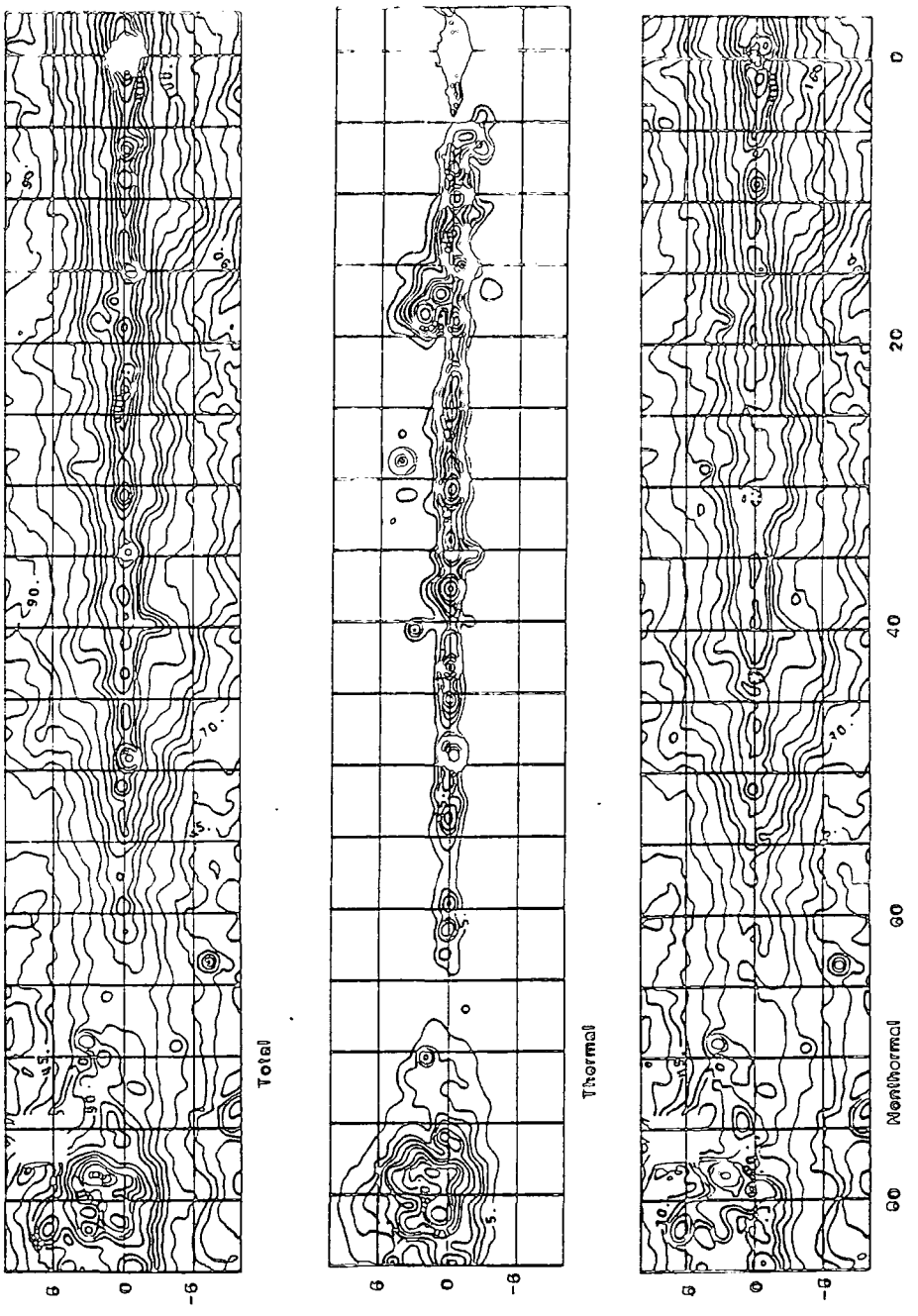

Figure 4.2: Contour maps of the 408 MHz emission from the Galactic disc in the first quadrant of galactic longitude showing the thermal and non-thermal separation. Upper map: the total brightness temperatures observed by Haslam *et al.* (1982). Middle map: the thermal component deduced from the 60 μm band IRAS data as detailed in the text. Lower map: the non-thermal (synchrotron) component with known supernova remnants close to the plane removed. Contour levels for the total and non-thermal maps are from 20 to 50 K in steps of 5 K, from 50 to 100 K in steps of 10 K, from 100 to 200 K in steps of 20 K, from 200 to 400 K in steps of 50 K and then in steps of 100 K. Contour levels for the thermal map are from 5 to 20 K in steps of 5 K, from 20 to 60 K in steps of 10 K, from 60 to 100 K in steps of 20 K, from 100 to 200 K in steps of 40 K and then in steps of 100 K.

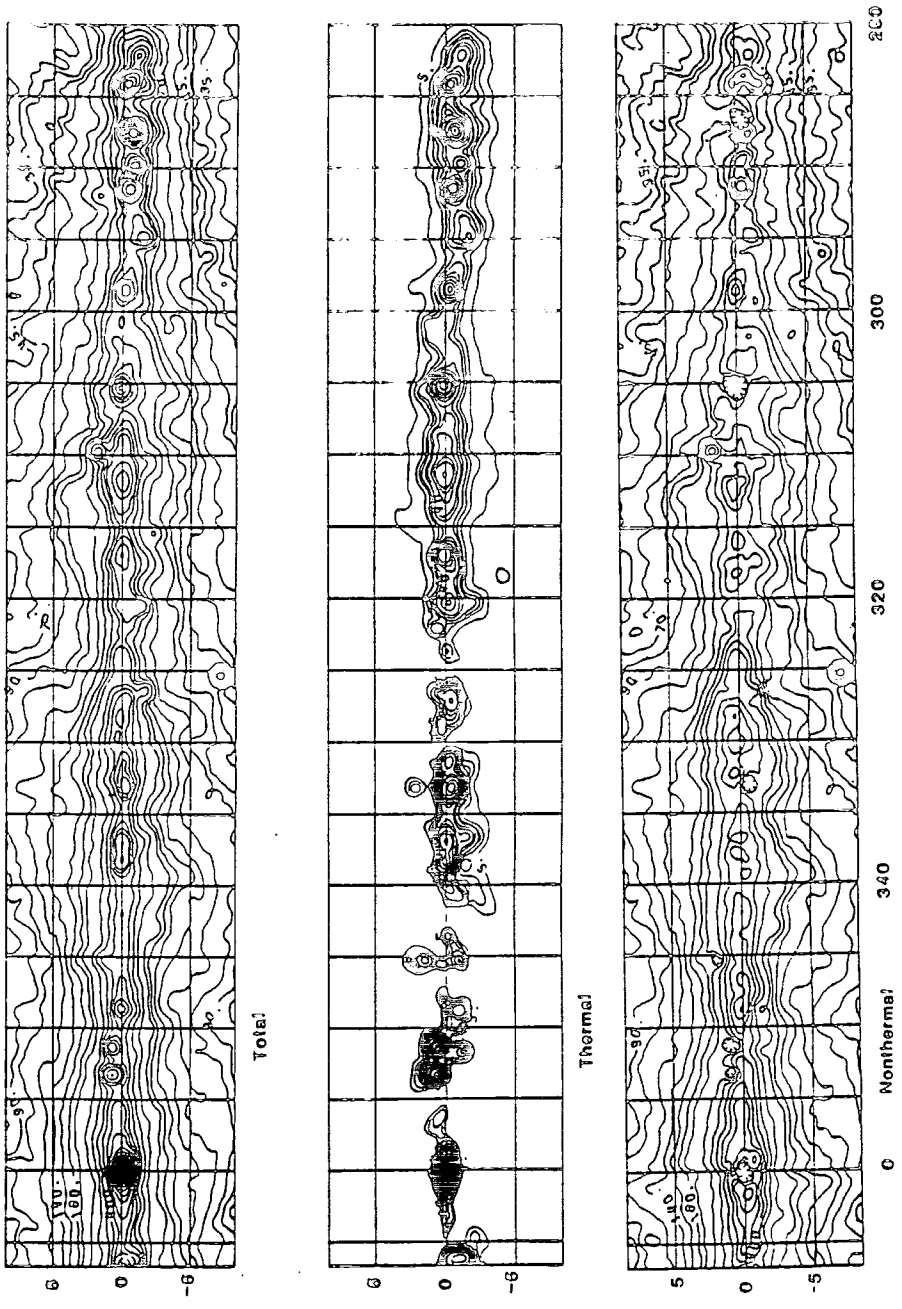

Figure 4.3: As for Fig. 4.2 but for the fourth quadrant.

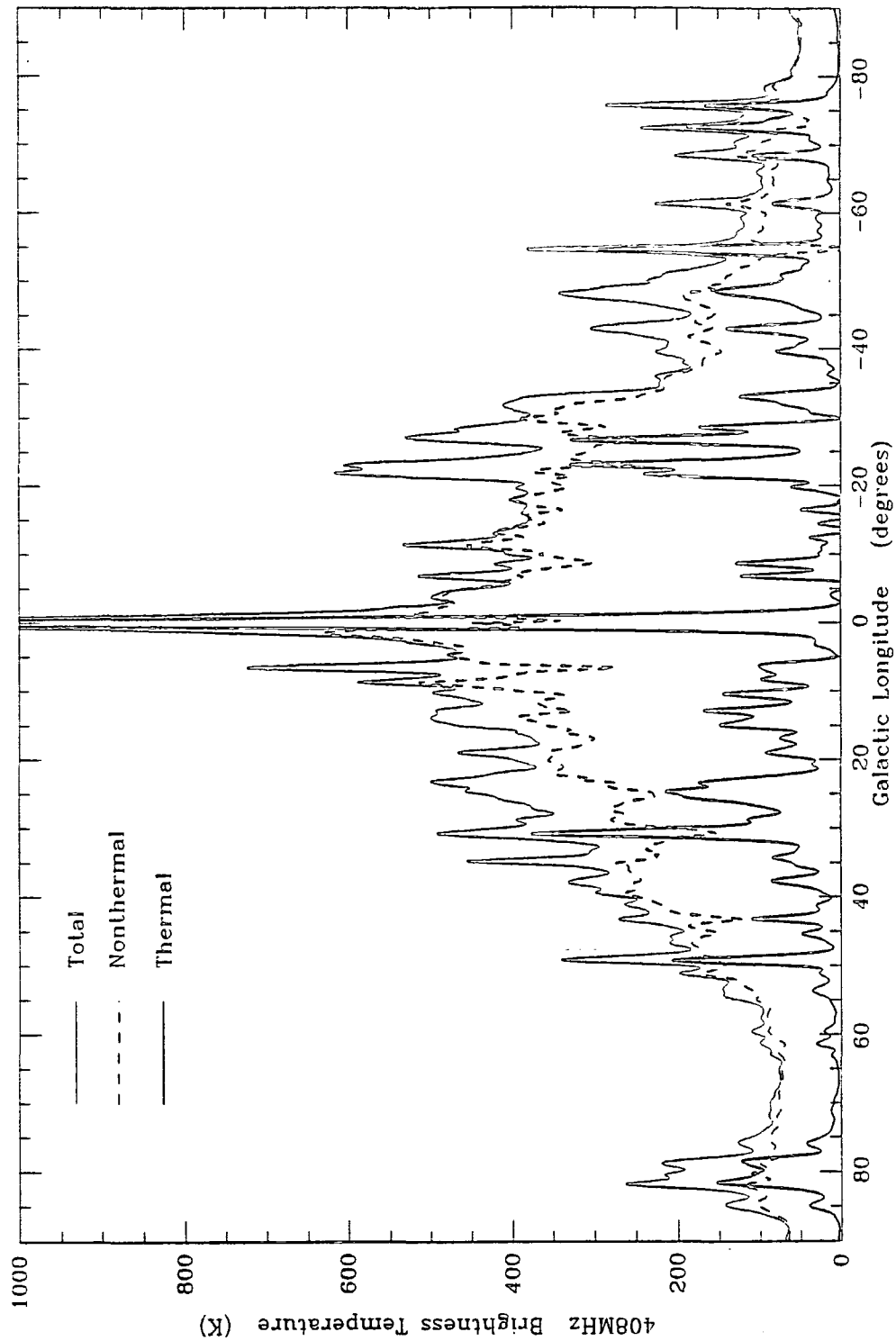

Figure 4.4: Cut along $b = 0°$ for the inner Galaxy of the 408 MHz emission with thermal–non-thermal separation. Top, solid line: total emission; dashed line: non-thermal emission; lower, solid line: thermal emission.

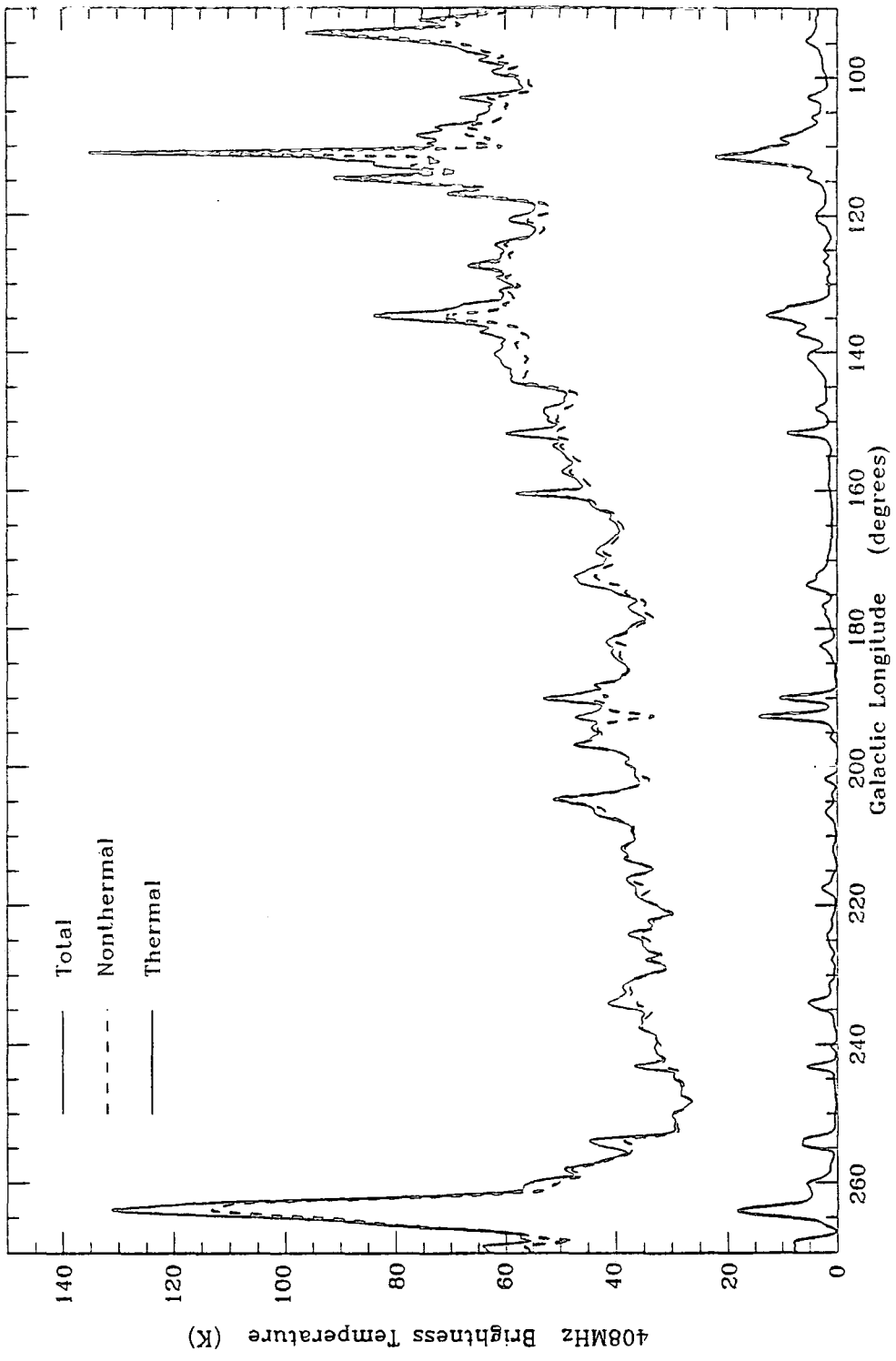

Figure 4.5: As for Fig. 4.4 but for the outer Galactic Plane.

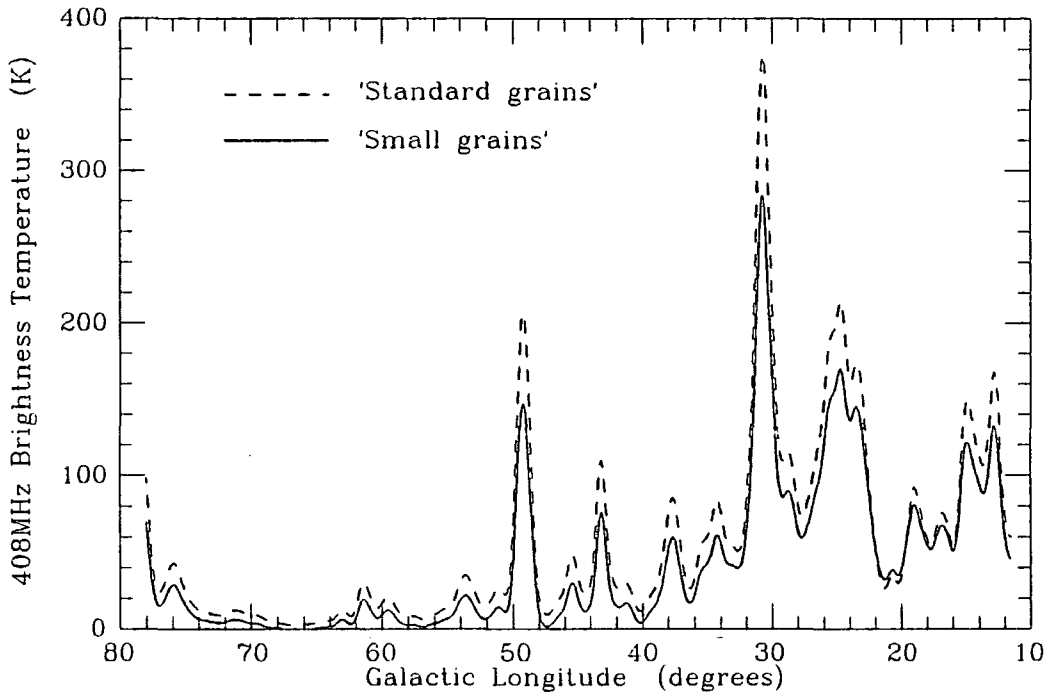

Figure 4.6: Cut along $b = 0°$ of the 408 MHz thermal emission derived using the 'standard grain' model of the HI-associated emission (dashed line) and the 'small grain' model (solid line).

Hence the temperature distribution of each SNR can be represented as a gaussian of half power width $51'$ and peak temperature $T(0)$ given by:

$$\left[\frac{T(0)}{\mathrm{K}}\right] = 0.131(0.408)^{-(\alpha+2)}\left[\frac{S(1\,\mathrm{GHz})}{\mathrm{Jy}}\right] \tag{4.6}$$

The source W50, which has dimensions $120' \times 60'$, was approximated to an elliptical gaussian. Table 4.4 gives a list of the SNR positions, 408 MHz flux and $T(0)$ for each SNR in the catalogue within the inner half of the Galaxy and less than $\sim 2°$ from the plane. Maps were generated of the modelled brightness temperatures of the SNRs which could be subtracted directly from the total 408 MHz non-thermal emission. The residual emission is shown in the lower maps of Figs. 4.2 and 4.3. In Figs. 4.4 and 4.5 the middle, dashed line represents the non-thermal emission along $b = 0°$ with SNRs subtracted. Some of the SNRs seem to have an overestimated spectral index or 1 GHz flux since on subtraction a local minimum remains. An example of this can be seen in Fig. 4.4 for the SNR at $6.4 - 0.1$. Immediately to the left of this minimum in brightness temperature there is a peak in the non-thermal emission. This is due to the large, extended source at $8.7 - 0.2$ which is one of the SNR candidates which we picked out from the 11 and 6 cm surveys. A contour map of the emission at 6 cm was given in Fig. 4.1 in the last section.

An interpretation of the non-thermal distribution at 408 MHz in terms of cosmic ray electrons and magnetic field is given in Chapter 5 but next we compare the relative merits of this method of thermal–non-thermal separation with those of the traditional, radio spectral index approach.

4.3 Comparison of the thermal–non-thermal separation with the spectral index method

The spectral index method of separating the Galactic radio thermal and non-thermal emission involves the use of two radio continuum surveys at different frequencies, covering a common area of sky and having the same angular resolution. The spectral index of each component is assumed to be constant, the thermal having a brightness temperature spectral index, α_{th}, of 2.0 or 2.1. The higher value includes an approximation to the frequency dependence of the Gaunt factor, a term appearing in the calculation of thermal bremsstrahlung emissivity. The non-thermal component has a larger index, α_{nth}, typically in the range 2.6 to 3.1 depending on the choice of the author. The value of α_{th} assumes that the Galaxy is optically thin at both frequencies which is normally true away from very bright thermal sources of emission and provided that the observations are not at too low a frequency. With these assumed values of α_{th} and α_{nth} it is possible in principle to find the relative proportions of thermal and non-thermal emission for each line of sight.

Mezger (1978) gives a peak brightness temperature profile along the Galactic Plane of the thermal emission from diffuse ionized gas at 1390 MHz which is a composite of two distributions derived by Westerhout (1958) and Mathewson *et al.* (1962) using the spectral index technique. We can obtain a similar profile by scaling from our 408 MHz thermal

Name	Position l	b	Flux at 408 MHz (Jy)	Peak T_b at 51′ resolution
MSH11-61A	290.1	−0.8	70.5	55.3
MSH11-62	291.0	−0.1	20.9	16.4
MSH11-54	292.0	+1.8	17.9	14.0
	293.8	+0.6	8.6	6.7
	296.1	−0.5	11.5	9.0
1156-62	296.8	−0.3	15.7	12.3
	298.5	−0.3	7.2	5.6
	298.6	0.0	5.2	4.1
	302.3	+0.7	8.6	6.7
Kes17	304.6	+0.1	21.9	17.2
	308.7	0.0	17.2	13.5
	309.2	−0.6	10.0	7.9
	309.8	0.0	26.6	20.9
	311.5	−0.3	6.3	4.9
	312.4	−0.4	56.6	44.4
	315.4	−0.3	14.3	11.2
MSH14-57	316.3	0.0	36.6	28.7
MSH15-52	320.4	−1.2	91.6	71.8
	321.9	−0.3	17.0	13.3
Kes24	322.3	−1.2	13.4	10.5
	323.5	+0.1	4.2	3.4
MSH15-56	326.3	−1.8	214.7	168.4
Kes27	327.4	+0.4	59.9	47.0
	328.0	+0.3	4.9	3.9
MSH15-57	328.4	+0.2	17.9	14.1
	330.2	+1.0	9.2	7.2
	332.0	+0.2	15.7	12.3
RCW103	332.4	−0.4	43.8	34.4
MSH16-51	332.4	+0.1	39.1	30.7
	335.2	+0.1	28.2	22.1
	336.7	+0.5	9.4	7.4
CTB33	337.0	−0.1	26.6	20.9
	337.2	−0.7	3.7	2.9
Kes40	337.3	+1.0	24.8	19.5
Kes41	337.8	−0.1	25.0	19.6

Table 4.4: Positions, 408 MHz fluxes and peak brightness temperatures for SNRs in the inner half of the Galaxy and $\lesssim 2°$ from the Galactic Plane derived from data given in Green's Catalogue of Galactic Supernova remnants (1987). (Continued on next page.)

Name	Position l	b	Flux at 408 MHz (Jy)	Peak T_b at 51′ resolution
	338.1	+0.4	1.9	1.5
	338.3	0.0	13.1	10.3
	338.5	+0.1	35.3	27.7
	340.4	+0.4	8.6	6.7
	340.6	+0.3	7.2	5.6
	341.9	−0.3	5.3	4.2
	342.0	−0.2	5.0	3.9
	344.7	−0.1	4.7	3.7
	346.6	−0.2	15.7	12.3
CTB37A	348.5	+0.1	85.1	66.7
CTB37B	348.7	+0.3	31.4	24.6
	349.7	+0.2	31.3	24.6
	350.0	−1.8	47.0	36.8
	350.1	−0.3	11.2	8.8
	351.2	+0.1	8.6	6.7
	352.7	−0.1	10.3	8.1
	355.9	−2.5	12.5	9.8
MSH17-39	357.7	−0.1	53.0	41.5
	357.7	+0.3	17.2	13.5
	359.1	−0.5	21.5	16.8
SagA East	0.0	0.0	204.9	160.7
	1.9	+0.3	1.1	0.9
Milne 56	5.4	−1.2	38.3	30.0
W28	6.4	−0.1	458.0	359.2
	9.8	+0.6	6.3	4.9
	10.0	−0.3	2.6	2.0
	11.2	−0.3	36.0	28.3
	11.4	−0.1	8.6	6.7
	12.0	−0.1	5.6	4.4
	15.9	+0.2	8.6	6.7
Kes67	18.8	+0.3	42.9	33.7
	18.9	−1.1	57.3	44.9
	20.2	−0.2	10.0	7.8
	21.5	−0.9	7.7	6.0
Kes69	21.8	−0.6	119.9	94.0

Table 4.4: *contd.* Positions, 408 MHz fluxes and peak brightness temperatures of SNRs. (Continued on next page.)

Name	Position l	b	Flux at 408 MHz (Jy)	Peak T_b at 51′ resolution
	22.7	−0.2	54.8	43.0
W41	23.3	−0.3	93.9	73.7
	23.6	+0.3	10.5	8.2
	24.7	+0.6	23.9	18.8
	24.7	−0.6	11.0	8.6
Kes73	27.4	0.0	9.4	7.3
	27.8	+0.6	39.3	30.8
Kes75	29.7	−0.3	18.7	14.7
	30.7	+1.0	8.6	6.7
3C391	31.9	0.0	41.1	32.2
Kes78	32.8	−0.1	14.4	11.3
	33.2	−0.6	7.5	5.9
Kes79	33.6	+0.1	34.0	27.0
W44	34.7	−0.4	333.1	261.2
3C396	39.2	−0.3	29.7	23.3
W50	39.7	−2.0	149.7	42.4
Flo	40.5	−0.5	17.2	13.5
3C397	41.1	−0.3	29.7	23.3
W49B	43.3	−0.2	59.5	46.7
HC30	46.8	−0.3	21.9	17.2
W51	49.2	−0.7	200.2	157.0
	54.1	+0.3	0.6	0.4
HC40	54.4	−0.3	42.3	33.2
4C21.53	57.2	+0.8	2.8	2.2
DA495	65.7	+1.2	10.3	8.1
	73.9	+0.9	11.8	9.2
CTB87	74.9	+1.2	11.2	8.8
	84.2	−0.8	17.2	13.5

Table 4.4: *contd.* Positions, 408 MHz fluxes and peak brightness temperatures of SNRs.

component prediction using a spectral index of 2.1. By drawing a lower envelope through the minima in the profile we can compare directly the temperatures of the two profiles. We find that our deduced thermal emission is consistently lower, having temperatures only 25–50% of those given by Mezger. This suggests that we have underestimated and/or the spectral index method has overestimated the diffuse thermal component.

At the edge of the low density HII regions it might be expected that the temperature of the dust would be lower than that nearer the centre and hence the fraction of the total IR emission detected in the IRAS 60 μm band would decrease. Assuming a λ^{-2} emissivity law for dust grains, the fraction of the total IR emission in the 60 μm band from dust at 20 K is only about 28% of that at 30 K. Therefore, the radio to 60 μm emission ratio for regions of lower dust temperature will be higher and scaling the residual 60 μm brightness intensities by the average ratio will underestimate the thermal radio emission . It would seem from this argument that correlation of the radio with the total IR emission would have been a better approach. The total IR emission could be estimated using both the 60 and 100 μm bands. However, as we have seen in previous sections the ratio of the 60 to 100 μm intensity throughout the Galactic disc seems fairly constant suggesting that following this alternative approach would make little difference to our results. However, although it appears that the temperature towards the edges of the ELD HII regions does not decrease much it must be borne in mind that the postulated small grains, line emission or averaging along the line of sight may all conspire to conceal it.

We can examine the thermal–non-thermal separation of Westerhout (1958) in more detail in order to illustrate some of the problems associated with the spectral index approach. The separation was of the 1390 MHz survey of the Galactic disc between $l \simeq 352.3°$ and 88.3° made with the 25 m telescope at Dwingeloo with a 34′ beam. The low frequency survey was that of Hill *et al.* (1958) made with the Mills Cross at 85.5 MHz at a resolution 50′. It is important for this method of separation that the temperatures are absolutely determined for both of the surveys. For the 85.5 MHz survey the absolute temperatures were assumed to be known but at 1390 MHz they were given with respect to an unknown base-level. To determine this base-level, temperatures from a 900 MHz survey by Denisse *et al.* (1955; 1957) in positions well away from the plane were extrapolated to 1390 MHz. For the extrapolation, they assumed that the points were far enough from the Plane to have no thermal contribution to the temperature and they assumed a non-thermal spectral index of 2.70 which was a mean of values determined earlier by several authors. Having thus found the base-level of the 1390 MHz survey the spectral index between 85.5 and 1390 MHz was checked at the highest latitudes measured at the lower frequency. It was discovered to be on average only 2.60. A non-thermal index of 2.70 could be obtained if the temperature scale of the 85.5 MHz survey was multiplied by 1.32 or that of the 1390 MHz survey was multiplied by 0.75. Rather than alter either of the temperature scales, however, Westerhout decided to perform the separation with an assumed non-thermal spectral index of 2.6. Despite all of these careful examinations of the base-levels and scales, later observations of Cas A revealed that the 1390 MHz temperature scale needed to be multiplied by a correction factor of 0.81 (Altenhoff *et al.*, 1960). The thermal emission from the diffuse ionized gas which Mezger (1978) presents used the thermal component of the emission derived from the Westerhout

	Brightness temperature (K)		
l	Westerhout	Mathewson *et al.*	Stockert
38.8°	10.9	10.5	8.5
36.3°	12.0	12.0	8.7
24.8°	18.7	17.2	16.6

Table 4.5: Comparison of 1390 MHz temperatures for three different longitudes at $b = 0°$ derived from three different radio continuum surveys.

survey after this correction factor had been applied.

The uncertainties in the temperatures of radio continuum surveys can be illustrated further if we compare the brightness temperatures found for identical positions in different surveys made at similar resolution and frequency. We compare three surveys; Westerhout's 1390 MHz survey at 34′ resolution, the Mathewson *et al.* (1962) survey at 1440 MHz and resolution 50′ and the Stockert 1420 MHz survey (Reich, 1982, Reich and Reich, 1986) made at a resolution of 35′. For three points along the Galactic Plane where Westerhout's lower envelope of the 1390 MHz temperature profile is identical to the total temperature, we calculated what the corresponding temperatures would be from the Stockert survey by subtracting a 2.8 K extragalactic background and scaling from 1420 to 1390 MHz with a spectral index 2.7. Similarly, the absolute 1440 MHz survey temperatures for the same points were scaled appropriately to the same resolution and frequency as the Westerhout survey. The base-level and 0.81 scale correction factor were included in the Westerhout temperatures. The values are shown for three galactic longitudes in Table 4.5. If we assume that the most recent measurements, those of the Stockert survey, are correct then the spectral index for the total emission deduced from earlier surveys is too flat and the fraction of the emission inferred to be thermal is too high. The most obvious sources of the discrepancies between the surveys are in the determination of the absolute temperature and scale and are major sources of uncertainty in the spectral index method.

Reich and Reich have used the Stockert survey together with the 408 MHz survey of Haslam *et al.* (1982) to separate the thermal and non-thermal emission at 1420 MHz along the Galactic Plane between 50° and 10° in longitude. The spectral index of the total emission is everywhere > 2.6 and so if the same non-thermal spectral index was adopted here as was used by Westerhout there would be no predicted thermal emission at all. Reich and Reich chose a non-thermal spectral index of 3.1 which they argue is in accord with earlier observations at frequencies between 1.4 and 15.5GHz and with recent models of cosmic ray origin and propagation. The thermal component of the 1420 MHz brightness temperatures along the Galactic Plane are shown in Fig. 4.7 together with those predicted from the 60 μm band emission. The two are generally at the same level, with our estimates having larger excursions from the mean. This is to be expected since our derived thermal component is not constrained to be less than the total 1420 MHz emission as is the Reich and Reich estimation. Therefore, if our separation is correct, it seems that the non-thermal

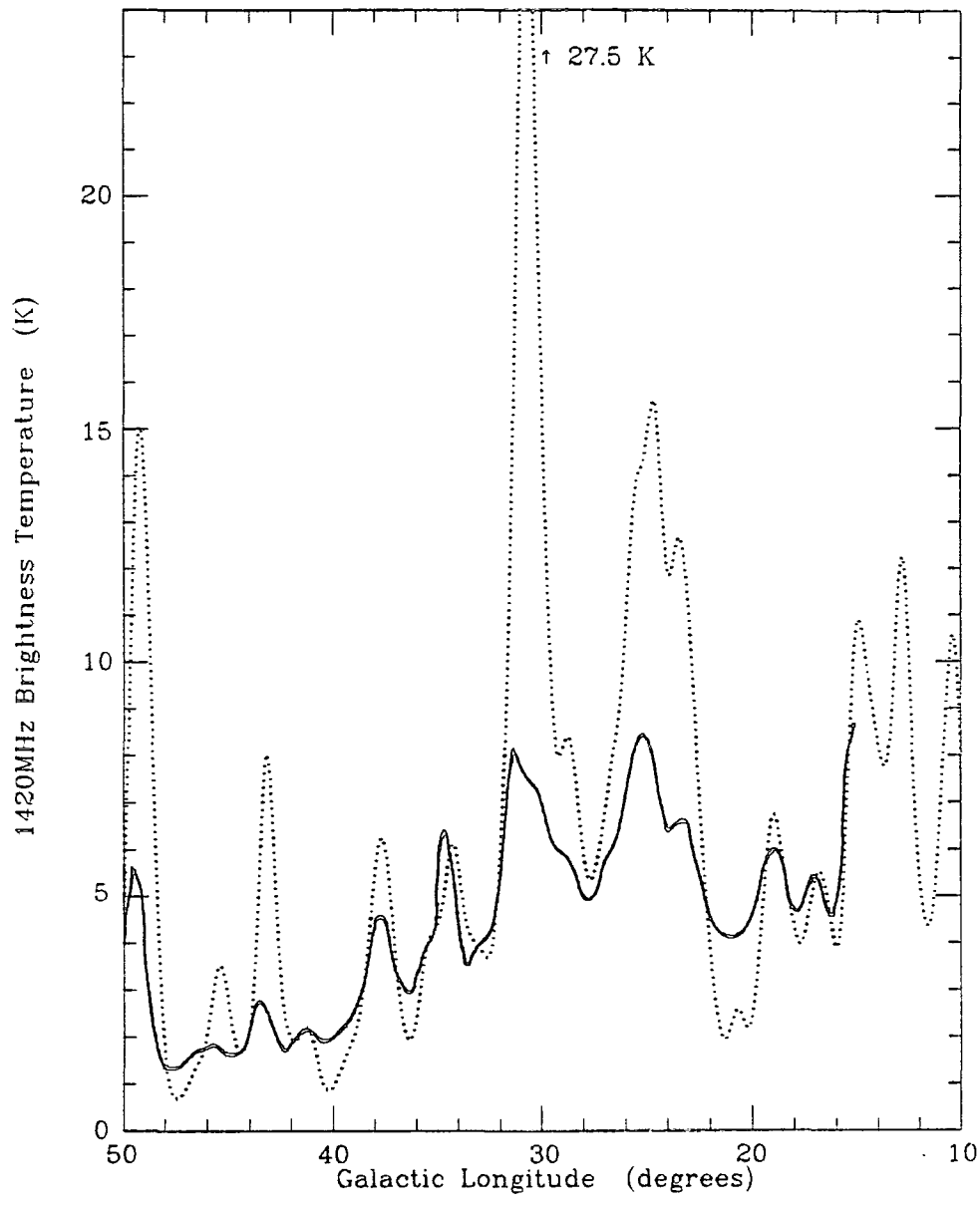

Figure 4.7: Estimations of the thermal component of the 1420 MHz radio continuum emission along a part of the Galactic Plane. The solid line is that estimated by Reich and Reich from the Stockert survey, assuming a non-thermal spectral index of 3.1. The dotted line is scaled from the residual 60 μm band emission.

emission does have a steep spectrum between 408 and 1420 MHz. The non-thermal spectral index between 85.5 and 1390 MHz and 408 and 1420 MHz are reconciled if the spectrum steepens considerably above 408 MHz implying that the 85.5 to 408 MHz spectral index is much less than 2.6.

Chapter 5

Modelling the synchrotron emission of the Galaxy.

5.1 Introduction

In the last chapter we presented the results of the subtraction of the thermal emission at 408 MHz from the Galactic Plane within the latitude range $|b| \leq 8\frac{1}{3}^{\circ}$. In this chapter we shall continue the work of previous authors in trying to model the synchrotron emission from the Galaxy and hopefully gain further insight into the structure of the Galaxy, in particular the nature of its magnetic field. We will take the proximity of the brightness temperatures predicted by a given model to the non-thermal 408 MHz emission deduced by the separation method described in previous chapters (henceforth called the 'observed' non-thermal emission) as an indication of the feasibility of the model. Obviously it will not be possible to construct a model that reproduces every detail of the 'observed' emission but only the large scale distribution. In fact the 'observed' distribution itself has a few shortcomings which arise mainly from the thermal subtraction procedure. We have already pointed out in the last chapter that for one or two of the SNRs subtracted, the emission was over-estimated leaving a local minimum on the contour maps (Figs. 4.2, 4.3). Other local minima are due to over-subtraction of brightness temperatures from the central parts of bright HII regions. Our attempts at allowing for optical depth effects at 408 MHz reduced but did not remove completely the local minima. On the contour maps these minima were blanked out to avoid confusion with genuine, unsubtracted sources.

In Fig. 5.1 our best estimate of the observed 408 MHz non-thermal emission from the Galaxy along $b = 0^{\circ}$ is displayed. It is the large scale features of this emission that we aspire to reproduce from model predictions of brightness temperature along the Galactic Plane. The extragalactic contribution to the non-thermal emission, which at 408 MHz amounts to ~ 6 K (Lawson *et al.*, 1987) has been subtracted. Also, several local minima produced by over-estimations of the temperatures of some sources discussed above have been omitted to give a clearer picture of the large scale variation of the emission. Upward pointing arrows marked 'HII' or 'SNR' indicate the positions of these. Minima at $l \sim$

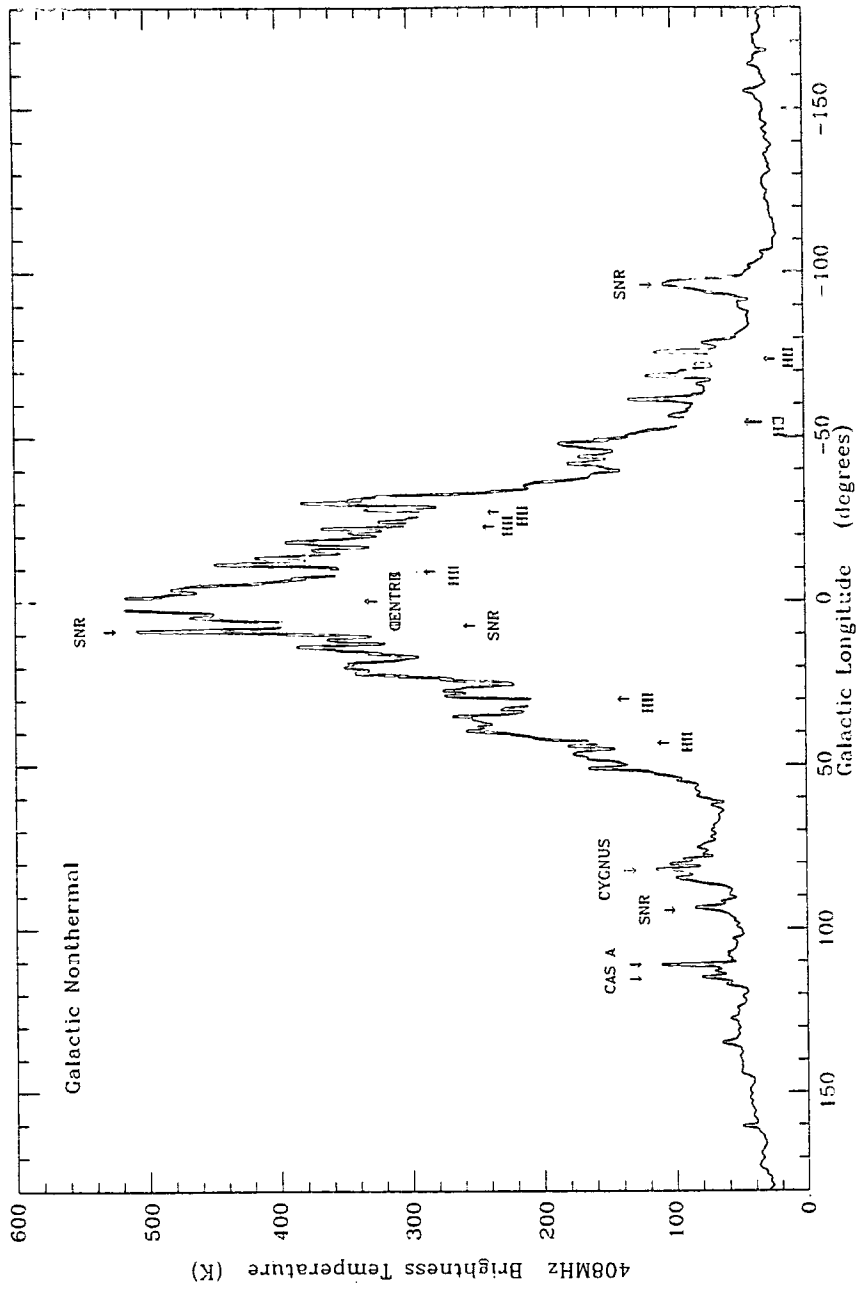

Figure 5.1: Profile along the Galactic Plane showing the best estimate of the non-thermal (synchrotron) emission at 408 MHz, the derivation of which was described in Chapter 4. Here, a 6 K extragalactic background has been subtracted also. Local minima produced by over-estimations of the emission from a few sources have been blanked out and the upward pointing, labelled arrows show the positions and nature of these sources. The positions of a few unsubtracted SNRs also are marked (downward pointing arrows) as are the spikes caused by the side lobes of Cas A, and the position of the Cygnus complex.

287°(−73°), 305°(−55°), 334°(−26°) and 31° are caused by the Carina Nebula, RCW 74, G333.6 − 0.2 and W43 respectively all of which were corrected for optical thickness. The minima at $l \sim 338°(-22°), 351°(-9°)$ and 43° were also due to strong thermal sources but no correction to the thermal subtraction was made in these directions. The flux of the SNR at 6.4 − 0.1 was also over-estimated, perhaps because an incorrect spectral index for the source was assumed. The range of directions within ~ 2° of the Galactic Centre has also been omitted because, as mentioned in earlier chapters, it is a special region with different properties to the rest of the Galaxy. Some discrete sources are also indicated in Fig. 5.1. No SNRs were subtracted from the 408 MHz survey in the outer parts of the Galaxy and hence there remain peaks at $l \sim 264°$ (Vela) and at $l \sim 94°$ (CTB104A). Two spikes at $l \sim 115°$ and 111° are caused by side lobes of Cas A. The peak at $l \sim 9°$ is due to one of our SNR candidates (see Section 4.1). Around $l \sim 80°$ there is a small amount of residual emission from the Cygnus complex.

The non-thermal or synchrotron emission from the Galaxy is produced by electrons moving at relativistic velocities in the Galactic magnetic field. The brightness temperature, T_b, along a particular line of sight through the Galaxy at a frequency ν is given by the equation:

$$\left[\frac{T_b(\nu)}{\mathrm{K}}\right] = 6.168 \times 10^4 \left[\frac{\nu}{\mathrm{MHz}}\right]^{\frac{-(\gamma+3)}{2}} \int_s \left[\frac{N_e(s)}{\mathrm{m^{-2}sr^{-1}s^{-1}GeV^{-1}}}\right] \left[\frac{H_\perp(s)}{\mu\mathrm{G}}\right]^{\frac{\gamma+1}{2}} \left[\frac{ds}{\mathrm{kpc}}\right] \quad (5.1)$$

the derivation of which can be found in e.g. Kearsey (1983), Pacholczyk (1970). Here, s is the distance along the line of sight and $H_\perp(s)$ is the magnitude of the component of the magnetic field perpendicular to the line of sight at distance s. The high energy cosmic ray (CR) electrons which are accelerated by the magnetic field are assumed to have a power-law differential flux distribution:

$$\text{Flux} = N_e(s) E^{-\gamma}\, dE\ \mathrm{m^{-2}sr^{-1}s^{-1}} \quad (5.2)$$

in an energy range dE between E and $E + dE$. The γ appearing in both Equation 5.1 and 5.2 is the spectral index of the differential energy spectrum of the CR electrons and $N_e(s)$ represents the flux of CR electrons per GeV at 1 GeV. It can be seen, therefore, that the synchrotron emission observed from the Galaxy depends on the electron flux density, the Galactic magnetic field and their variation with position along the line of sight and hence their variation with position in the Galaxy.

5.2 Previous work: the unfolding method

Observations of the radio continuum emission from the Galactic Plane have revealed that on the large scale the level of emission increases towards lower longitudes in a stepwise fashion. This can be seen in Fig. 5.1. In his analysis of Galactic synchrotron emission Mills (1959) suggested that these steps could be a consequence of the spiral structure of the Galaxy and that the peaks not accounted for by discrete sources could be in directions which are tangential to spiral arms. Since 1959 the observed radio continuum has been expounded by

many authors in terms of spiral structure and a fairly extensive review of this was presented by Kearsey (1983). Here we will describe some of the more recent interpretations of the distribution of Galactic synchrotron emission which we hope to employ and develop further in this chapter.

Two main approaches have been adopted in analysing the Galactic synchrotron emission. The first is an unfolding technique which takes the observed two dimensional distribution of emission over the sky and by making certain assumptions about the symmetry of the problem deduces the emissivity as a function of position in the Galaxy using an iterative procedure. The second approach is from the other direction in that a model of the spiral arm pattern and variation of emissivity over the Galaxy is constructed first and then the predicted emission from this model is compared with observation. This second method is the one we will use here although the former is regarded as being complementary and some results of the unfolding method will be invoked.

In 1981, Phillipps *et al.* studied the distribution of Galactic synchrotron emission using the unfolding technique which is described fully together with the results obtained and conclusions drawn in two papers henceforth referred to as PKOHSI and PKOHSII. The data used was the same all-sky radio continuum survey at 408 MHz by Haslam *et al.* (1982) which we have used in the present work. We first outline the analysis of PKOHSI whose study was confined to the Galactic Plane.

The lower envelope of the Galactic Plane profile was used rather than the full profile as the former exhibits more clearly the step-like features without confusion by discrete sources. In addition, a 6 K extragalactic background level was removed and 20% of the remaining emission was attributed to the extended thermal emission following Hirabayashi (1974). An expression for the brightness temperature of synchrotron radiation was given in Equation 5.1. PKOHSI defined the emissivity $\epsilon(\nu)$ from an emitting region whose line of sight length is S as $T_b(\nu)/S$. Therefore, $\epsilon(\nu) \propto H_\perp^{(\gamma+1)/2}$. It was assumed that there are two components to the magnetic field, a regular component with magnitude H_{reg} and with direction along the spiral arms of the Galaxy, and an irregular component of magnitude H_{irreg} and which on the large scale ($\gtrsim 100$ pc) is assumed to be isotropic. The ratio of the two components were taken to be constant even on compression in spiral arms. There has to be an irregular component of the magnetic field if the regular component lies along spiral arms. An absence of irregular field would imply that in the directions which are tangential to an arm there would be no magnetic field component perpendicular to the line of sight. This is incompatible with observations.

The emissivity was assumed to take the form of a product of two components, one depending only on the galactocentric radius and the other determined by the assumed spiral pattern. The Galactic Plane was divided into sixty logarithmic spiral sections and by unfolding the brightness temperatures along the plane the emissivity of each of these spiral sections was deduced. The emissivity variation with position in the plane was then determined from the assumed variation of emissivity with galactocentric radius. In the outer Galaxy, where no unfolding could be performed, the emissivities had to be extrapolated from the inner Galaxy. Of course there was no unique solution and PKOHSI investigated the effects of changing the form of the radial emissivity function, the relative magnitudes

of the regular and irregular magnetic field components and the inner and outer extent of the spiral pattern. In addition, the pitch of the logarithmic spiral sections was a free parameter although independent observations suggested that the pitch angle is about 12°. The assumption of smooth logarithmic spiral arms is undoubtedly unrealistic as the authors admitted. It is highly likely that the arms will tend to deviate from the best fitted smooth arms and indeed may not even be logarithmic spirals. PKOHSI therefore cautioned against making comparisons of the predicted width and enhancement of arm emissivities deduced from the unfolding with theoretical predictions from density wave theory since the arm widths they deduced will be smeared out somewhat.

The merit of the unfolded emissivity deduced from a given set of assumed parameters was assessed by how well the observed brightness temperatures were reproduced. A measure of the suitability of the derived pitch of the spiral arms was how pronounced the features in the azimuthal emissivity variation were.

From their analysis PKOHSI made the following conclusions about the structure of the Galaxy and its spiral pattern.

1. As expected, it seems that to have a predominantly regular magnetic field is incompatible with the observations. A totally irregular magnetic field can be used for the inner Galaxy but no satisfactory extrapolation can be made to the outer parts of the Galaxy. The most satisfactory combination tried was that with equal regular and irregular components. Given that this is the case and making the assumption that the local CR electron density is $80\,E^{-2.6}\mathrm{m}^{-2}\mathrm{s}^{-1}\mathrm{sr}^{-1}\mathrm{GeV}^{-1}$ (Meyer, 1974), then the magnitude of either component in the solar neighbourhood is between 2.7 and 3.4 μG which is within the range of estimates made from independent observations. (See Section 5.9 for a discussion of the magnetic field strength in the solar neighbourhood.)

2. Three radial functions of emissivity were assayed and in the inner Galaxy they were found to represent the data equally well once the best scale length for each had been determined. The three forms are $R^{-1.9}$, $\exp(-R/3.9\mathrm{kpc})$ and $\exp(-(R/7.8\mathrm{kpc})^2)$ where R is the galactocentric radius. In order to reproduce the temperatures in the outer Galaxy, the extrapolation had to be extended to 16 and 20 kpc respectively for the power law and exponential forms. The gaussian form falls off too rapidly to produce the required level of emissivity even with extrapolation out to an indefinite radius. The authors suggested that this indicates that the decrease in emissivity flattens out in the outer Galaxy or that another arm exists beyond the solar circle which could not be deduced from the unfolding.

3. The inner extent for which the spiral pattern is applicable seems to be at a radius of about 3.6 kpc and there appears to be an asymmetry of emission about the centre which could be due to a bar-like structure.

4. Concerning the spiral arms themselves, it appears that 12° is indeed the optimum pitch angle and that the spiral pattern has a two-fold symmetry in the sense that there are two deep minima separating higher emissivity regions. These may consist of pairs of arms or a multiple structure but in any case, three arms could be easily distinguished

which coincide with arms delineated by the positions of HII regions mapped out by Georgelin and Georgelin (1976). Lack of resolution due to the smearing out effect mentioned earlier inhibits further distinction of individual arms.

The main development in PKOHSII was to extend the unfolding method to three dimensions in order to study the variation of emissivity with height above the Galactic Plane. In addition, the effect of allowing for the regularization of some of the isotropic magnetic field component on compression by a shock front was explored. This involved making further assumptions about conditions in the ISM in order to obtain the variation of compression over the Galactic Plane. However, it was discovered that the resultant emissivity distribution and the predicted brightness temperatures along the plane were almost identical with those of PKOHSI. With the added confidence that the emissivity variation in the Galactic Plane deduced in PKOHSI was a good representation, the authors proceeded to study the emission away from the plane.

In order to do this PKOHSII assumed that the emissivity in three dimensions can be expressed as:

$$\epsilon(R,\theta,z) = \epsilon(R,\theta) f(\frac{z}{z_o(R,\theta)}) \tag{5.3}$$

with z being the height above the plane and θ an angle measured in the plane about the Galactic Centre. Also, $z_o = 1$ at the Sun and $f(z/z_o) \simeq 1$ along the Galactic ridge. The form of $f(z/z_o)$ was assumed initially to be symmetrical about the Galactic Plane and to have the same form at all positions within the Galaxy but with a varying scale factor. The latitude profiles with which predicted temperatures could be compared were constructed by drawing the lower envelope of a superposition of the brightness temperatures from either side of the plane at a given galactic longitude. This was to reduce as far as possible the excess emission over the general spiral structure from local features such as loops and spurs or discrete sources.

The general policy for deducing the emissivity was to use an unfolding procedure for one latitude profile in or close to the anticentre direction to obtain the general form of $f(z/z_o)$. Then, using the emissivity variation in the Galactic Plane deduced in PKOHSI and the assumed form of z_o, temperatures were predicted for latitude cuts at other longitudes which then could be compared with the profiles constructed from the observations. However, it was discovered that the profiles in the second quadrant were wider than for the other three quadrants which made it impossible to reproduce all latitude cuts with this adopted procedure. It was decided to concentrate just on fitting those latitude profiles lying in the 1st, 3rd and 4th quadrants and to find the form of $f(z/z_o)$ at $l = 210°$ instead of in the anticentre direction.

The most physically realistic and successful model which PKOHSII investigated (Model 3D3) has $z_o = \exp((R-10)/8\text{kpc})$ so that the scale factor of the emission doubles between 4 and 10 kpc and again between 10 and 16 kpc from the Galactic Centre. This is in line with the variation of the scale height of the gas in the Galaxy. Also, in an arm region the compression factor reduces with increasing z according to the results of calculations by Brindle *et al.* (1987) of the demodulation of spiral arms with height above the plane in the spiral shock model. Hence at $z \sim 0.5$ kpc the arm and interarm regions merge smoothly.

The function $f(z/z_o)$ falls off very rapidly at first to ~ 1.1 kpc and then has a long tail linearly decreasing with increasing z out to 16.7 kpc. The HWHM of f at $R = 10$ kpc is 0.85 kpc in an interarm region. The linear, non-spherical halo was constructed such that the observed pole temperature (i.e. at $b = \pm 90°$) would be reproduced. The emissivity of the model halo is about a tenth of that of the thin disc.

So far the unfolding procedure of one particular group of authors has been discussed in detail mainly because some of their results will be used in the model developed in the present work. However it is worth mentioning a contemporary study of the same data that was undertaken by Beuermann, Kanbach and Berkhuijsen (1985). The method adopted here was to assume from the beginning that there exists a thin disc and a thick disc of diffuse synchrotron emission and by considering two longitudinal profiles of brightness temperature along the inner Galactic Plane the emissivity of each disc could be simultaneously deduced. Both discs were assumed to possess spiral structure and the Galactic Plane was divided into logarithmic spiral sections as in PKOHSI but this time the pitch angle taken was 13°. The unfolding procedure considered both sides of the Sun–Galactic-Centre line separately unlike PKOHSI. Beyond the solar circle the emissivities had to be extrapolated and it was assumed that the form of the radial fall off was exponential extending to between 16 and 20 kpc. The variation with height above the plane was assumed to be of the form:

$$\epsilon(z) = \epsilon_{thick}\mathrm{sech}^a(\frac{z}{z_o}) + \epsilon_{thin}\mathrm{sech}^b(\frac{z}{z_o}) \qquad (5.4)$$

Regarding the magnetic field, Beuermann *et al.* took the direction of the regular component to lie along the spiral arms and the isotropic component preferentially had the same magnitude as the aligned field which is in accord with the best model of PKOHSI.

The unfolding technique was an iterative procedure making some initial estimates of the equivalent thickness, the maximum galactocentric radius of emission, the absolute emissivity at the Sun ($R_\odot = 10$ kpc) and the scale length of the emissivity for both thick and thin discs. Improvements on these parameters were made until a satisfactory reproduction was obtained fron the unfolded emissivities of the observed brightness temperatures of selected latitude profiles and the anticentre distribution. It wad found that the radial variation of the emissivity between 4 and 10 kpc could be approximated sufficiently well by exponential functions having scale lengths 3.3 and 3.9 kpc for the thin and thick disc respectively. This is to be compared with 3.9 kpc deduced for the total non-thermal emission by PKOHSI. The thick disc was found to contribute 90% of the power at 408 MHz from diffuse sources and its equivalent thickness increased from 2.3 to 6.3 kpc between galactocentric radii 4 and 16 kpc. The corresponding widths for the thin disc were 0.25 and 0.61 kpc. The spiral structure deduced from the unfolding was evident in both discs and a pattern consisting of two pairs of arms could be discerned. The arm–interarm emissivity contrast was ~ 4 for equal regular and isotropic magnetic field components.

The main difference between the model of Beuermann *et al.* and that of PKOHSI and II is that the former assumes that there is a thick disk whereas the latter invokes an extended Galactic halo. The results and conclusions of the two studies are broadly similar and the discrepancies between the two can be regarded as indicating the level of uncertainty involved in the unfolding method.

5.3 Previous work: the modelling method

We next turn our attention to the second approach of interpretation of the synchrotron emission from the Galaxy, namely that of modelling the emissivity variation and then comparing the predicted brightness temperatures with those observed. In particular, a summary of the work initially developed by French (1977) and later modified by Kearsey (1983) will be given. It is this study which we hope to further in the present work having the advantage of an improved estimate of the non-thermal emission at 408 MHz. Also, we can exploit relevant observations and calculations which have appeared more recently in the literature. Much of the work done by French (1977) is also described by French and Osborne (1976) and Brindle *et al.* (1978). The data which French used to compare the predicted brightness temperatures against were in the form of an all-sky composite survey at 150 MHz compiled by Landecker and Wielebinski (1970). The highest resolution was 2.2°. Kearsey was able to take advantage of the all-sky map of Haslam *et al.* (1982) at 408 MHz with its much higher resolution (HPBW 51′).

The brightness temperature due to the synchrotron emission at a frequency ν along a particular line of sight was given in Equation 5.1, and Equation 5.2 shows the assumed form of the variation of electron flux with CR electron energy. The spectral index of the differential electron energy spectrum, γ, appears in both equations. If the magnetic field strength in the solar neighbourhood is $\sim 3\,\mu$G then the synchrotron emission at frequencies from $\sim$ 100 to $\sim$400 MHz is emitted by electrons of energy in the range 1–10 GeV. From the local electron spectrum of Meyer (1974) therefore, the value of γ for this range of energy is 2.6 and the observed local value of N_e, which also appears in Equations 5.1 and 5.2 is $80^{+70}_{-30}\,\mathrm{m^{-2}s^{-1}sr^{-1}GeV^{-1}}$. Throughout the calculations of French and Kearsey these values of γ and $N_e(R_\odot)$ are used and γ is assumed to be the same over the whole Galaxy even though the field strength is likely to vary.

The extragalactic background was taken by French to be 50 K at 150 MHz and by Kearsey to be 6 K at 408 MHz. Both authors took these values from the estimates of Bridle (1967) who assumed that there is the ubiquitous 3 K relic black-body emission from the Big Bang and a uniform contribution from the combined emission of all other galaxies. The thermal contributions of the Galactic emission is assumed in both cases to be a fixed percentage of the total. According to Hirabayashi (1974) this percentage is 7% at 150 MHz and 20% at 408 MHz.

The basic model of French for the synchotron emission from the Galaxy assumes that most radio emission emanates from a disc of 1 kpc width and 30 kpc diameter. The Sun is situated at a radius of 10 kpc from the Galactic Centre and half way between the faces of the disc. This disc is constituted of stars, dust and gas. Beyond the disc there exists a halo which was assumed to have the form of a cylinder centred on the Galactic Centre and having a radius of 15 kpc. The halo of Kearsey was chosen to be spherical instead but had the same diameter and positioning as the cylinder model.

Within the disc the gas, dust and stars are concentrated within arms which spiral out from the Galactic Centre region. The spiral density wave theory is one of the leading theories used to explain the maintenance of such a structure. Much of the pioneering work

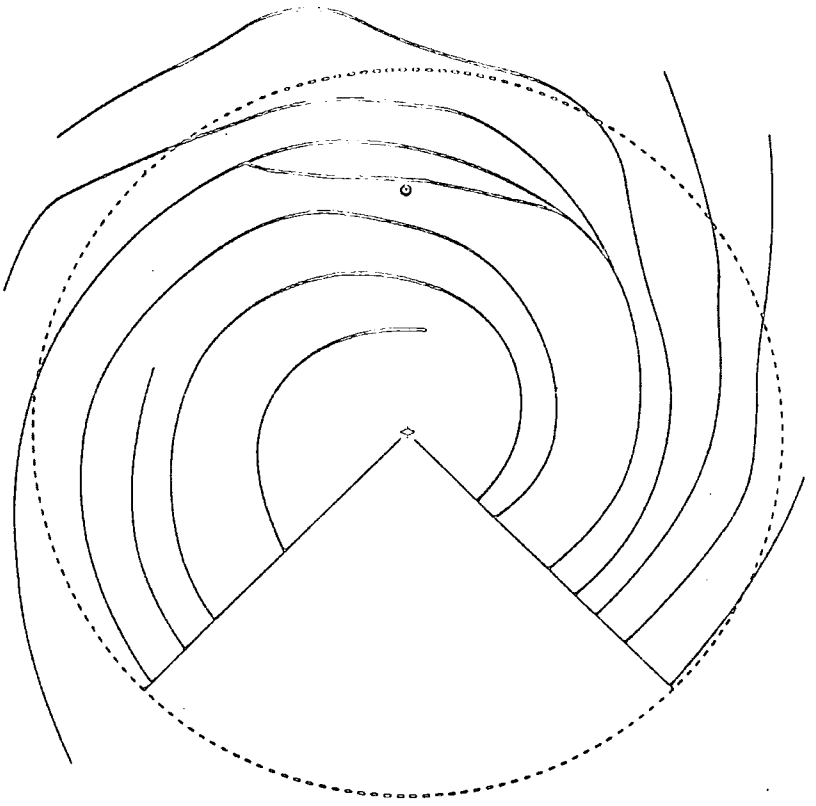

Figure 5.2: The arm pattern used by French (1977). (Taken from Kearsey, 1983.)

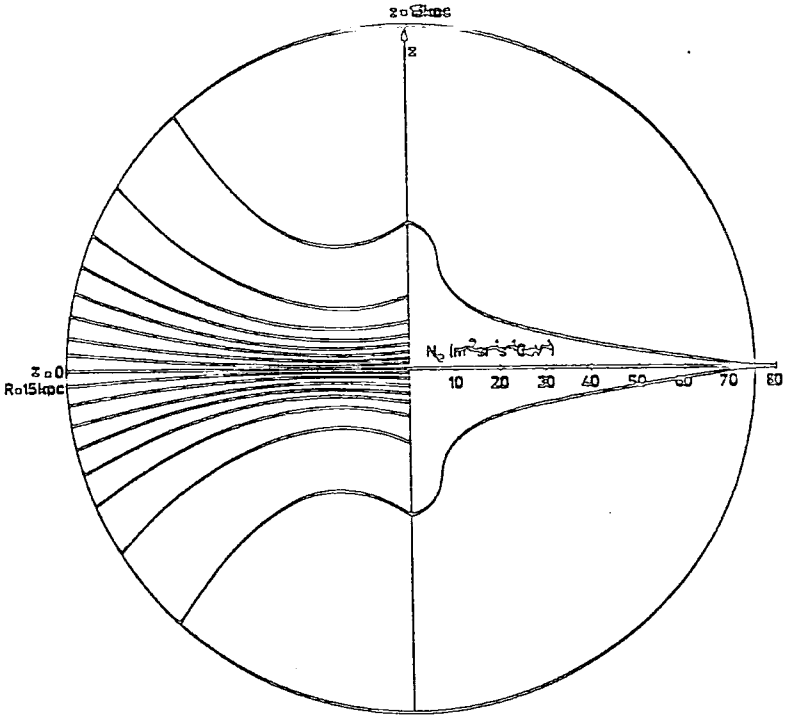

Figure 5.3: Distribution of electron flux density out of the plane as a result of the variation of $w(R)$. The left-hand side shows lines of constant flux density as a function of R and z. The right-hand side shows the profile of flux density for $R = 0$. (Taken from Kearsey, 1983.)

on this hypothesis was performed by Lin and Shu (1964, 1966) and Lin, Yuan and Shu (1969). It was proposed that density waves sweep through the Galaxy which in the non-linear case (Roberts, 1969) causes shock formation within the dust, gas and stars. French assumed that the Galactic magnetic field is 'frozen' into the gas which implies that it too is compressed in the shock fronts. This being the case, then the positions of spiral arms deduced from the observed distribution of the interstellar gas will also indicate the form of the synchrotron spiral structure. French constructed a picture of the spiral arms by combining the structure inferred from the positions of compact HII regions by Georgelin and Georgelin (1976) within the solar circle and the results of Verschuur (1973) who mapped the HI distribution in the outer Galaxy. This composite pattern is shown in Fig. 5.2. There is not much information available for the far side of the Galaxy and within ~ 4 kpc of the Galactic Centre the structure appears to become confused. For these reasons French made no attempt at modelling the Galaxy within the longitude range $30° > l > 330°$. The local arm was placed 0.5 kpc from the Sun in the anticentre direction so the Sun is situated in an interarm region.

Various models of the electron distribution were assayed but French found the best results were obtained if it was assumed that within the plane the electron flux density does not change over the Galaxy. Thus the value of N_e could be assigned the locally measured value of $80^{+70}_{-30}\mathrm{m^{-2}s^{-1}sr^{-1}GeV^{-1}}$ for all galactocentric radii between 4 and 15 kpc. The assumption of constancy of electron flux density implies that there is no variation between the arm and interarm regions and that the electrons must diffuse rapidly compared with the rotation velocity of the density waves. The variation of N_e out of the plane which was found to reproduce most nearly the 150 MHz data has the following form:

$$N_e(R,z) = N_o \left[1 - 0.35548\left(\frac{z}{w(R)}\right) + 0.04733\left(\frac{z}{w(R)}\right)^2 - 0.002127\left(\frac{z}{w(R)}\right)^3\right] \quad (5.5)$$

Here z is the height above the plane in kpc and N_o is the value of N_e in the plane i.e. $80\,\mathrm{m^{-2}s^{-1}sr^{-1}GeV^{-1}}$. The scale height of the electrons, $w(R)$, was assumed to have the same form as that observed for the gas even though the actual width of the CR electron distribution is much larger than that of the gas. Therefore, $w(R)$ is expressed as:

$$w(R) = 0.591 - 0.0652R + 0.0106R^2 \quad (5.6)$$

This variation ensures that the electron distribution becomes much wider in the outer Galaxy. The form of the electron flux density is illustrated in Fig. 5.3. At the solar radius $w(R_\odot) = 1$ and the full width of the electron distribution is 21.7 kpc.

The magnetic field was assumed to be comprised of two components. The first is the regular component whose direction lies along the spiral arms parallel to the Galactic Plane. Where there are two adjacent arms the direction of the field was assumed to vary in a linear fashion between the two different orientations. The other, irregular component was assumed to be such that along any particular line of sight the overall distribution of orientations is isotropic.

Equation 5.1 can be rewritten:

$$T_b(\nu) = 6.168 \times 10^4 \nu^{-2.8} \int_s N_e(s) \left(H_{\perp reg}(s) + H_{\perp irreg}(s)\right)^{1.8} ds \tag{5.7}$$

where it has been assumed that $\gamma = 2.6$. The units of the various quantities are the same as those in Equation 5.1. French showed that Equation 5.7 can be approximated adequately by:

$$T_b \simeq 6.168 \times 10^4 \nu^{-2.8} \int_s \left(N_e H_{\perp reg}^{1.8} + N_e H_{\perp irreg}^{1.8}\right) ds \tag{5.8}$$

Further, it was supposed that the ratio of the regular to irregular field is constant over the Galaxy in the interarm regions but that in the arms the irregular component undergoes a certain degree of alignment along the direction of the arm, the extent of which depends on the compression in the arm. Taking these suppositions into account, French calculated the effective component of the irregular field perpendicular to the line of sight in terms of the regular component, the compression ratio and the ratio, F, of the regular to irregular field in the uncompressed state. Thus the above equation was rewritten:

$$T_b(\nu) = 6.168 \times 10^4 \nu^{-2.8} \int_s (N_e(s) \left[\rho_c(s) H_{reg}(s) \sin\theta\right]^{1.8} + 0.6861 N_e(s) \left[\frac{\rho_c(s) H_{reg}}{F}\right]^{1.8} Y(s)) ds \tag{5.9}$$

where

$$Y(s) = \left[1 - 0.477 \left(\frac{\rho_c^2 - 1}{\rho_c^2}\right) \cos^2\theta\right]. \tag{5.10}$$

Here, ρ_c is the ratio of the density of the gas at a certain point to the density it would have in the uncompressed state. An approximation to the variation of ρ_c across a spiral arm as predicted from spiral density wave theory was made and in addition French performed some rough calculations of how this variation is demodulated with increasing distance from the plane. Thus:

$$\rho(a, z) = \left[4.1 f(z) \exp\left(\frac{-13.7a}{A}\right) + 0.7\right] / 0.7 \tag{5.11}$$

where

$$f(z) = \begin{cases} 1 + 0.7715z - 17.0z^2 + 22.914z^3 & z < 0.5\,\text{kpc} \\ 0 & z \geq 0.5\,\text{kpc} \end{cases} \tag{5.12}$$

Here, a is the distance of the point at (R, z) under consideration from the shock of the nearest arm and A is the shortest distance between adjacent arms passing through (R, z).

In Equations 5.9 and 5.10 θ is the angle that the regular magnetic field direction at the point under consideration makes with the line of sight direction. $H_{reg}(s)$ is the magnitude of the regular magnetic field at a distance s along the line of sight. The precise form of H_{reg} assumed by French was:

$$H_{reg}(R) = H_o \left[1 - \exp\left(\frac{-R^2}{4}\right)\right] \exp\left(\frac{-R^2}{R_o^2}\right) \tag{5.13}$$

with R being the galactocentric radius measured in kpc. This is a modified form of the field variation proposed by Theilheim and Langhoff (1968). H_{reg} is a function of R only, has a maximum at about 4 kpc, and is zero at the Galactic Centre in line with predictions of the dynamo theory of magnetic fields. The form of the field within $R \simeq 4$ kpc was not very important to French as he was not making any predictions of T_b for $30° > l > 330°$. The value of R_o, the scale length of the magnetic field was a free parameter and therefore was chosen later in the normalizing procedure. H_o is a constant and because Equation 5.13 must satisfy the observed result that $H_{reg} = 3\mu$G at $R_\odot$ then H_o was determined by the value of R_o. In addition to R_o, the ratio of the regular to irregular field components, F, is a free parameter and both were chosen such that the temperatures predicted at $l = 180°$ and 310° were identical to the observed values in these two directions.

The predicted longitude profile for $b = 0°$ and a few latitude profiles of T_b at 150 MHz from French's best model are shown in Fig 5.4. The predictions have been convolved to the resolution of the 150 MHz survey. The dotted lines represent the observations and solid lines the predictions. The lower and upper solid lines in the latitude cuts are the predicted temperatures before and after adding the estimated spur emission respectively. Estimates of the extragalactic background, the Galactic thermal emission, spurs and point sources have been subtracted from the observed $b = 0°$ profile at 150 MHz which is then compared with the predicted synchrotron emission temperatures. On the other hand, for the latitude cuts the estimations of the background, thermal emission and spurs have been added to the predicted temperatures and so predictions are compared with the total observed emission at 150 MHz. The modelled longitude profile shows a broad similarity with the observations although the detailed positions and shapes of peaks are not terribly representative of those observed. For the latitude cuts predictions are in general quite good but the addition of estimations of spur emission seems to have an adverse effect on the quality of the fit to the observations.

On inheriting the problem of explaining the synchrotron emission, Kearsey tried not only to reproduce more closely the peaks in the directions tangential to spiral arms but also to extend predictions to cover the central region of the Galaxy. Beginning where French left off, Kearsey investigated a series of models for the synchrotron emission each successive model improving on the previous one. As mentioned earlier the higher resolution survey at 408 MHz was used for assessing the suitability of each model. Since much of the software developed by Kearsey to perform the integrations along the line of sight and subsequent convolution of the resulting brightness temperatures is used, with modifications, in the present work, the numerical techniques he adopted to make the modelling tractable by computer are now described.

For the integration along a particular line of sight expressed by Equation 5.9, the integrand was evaluated at regular intervals of $\Delta s = \frac{0.015}{cosb}$ kpc where b is the galactic latitude of the point under consideration. Thus, for a given galactic longitude, as the latitude varies the evaluation points are all directly above or below a fixed point in the plane. This is advantageous since some of the quantities which have to be determined in the integrand are not functions of z, e.g. H_{reg}, and so the value calculated at a point in the plane will be the same for all points along a line normal to the plane at that position. A step size of 15 pc

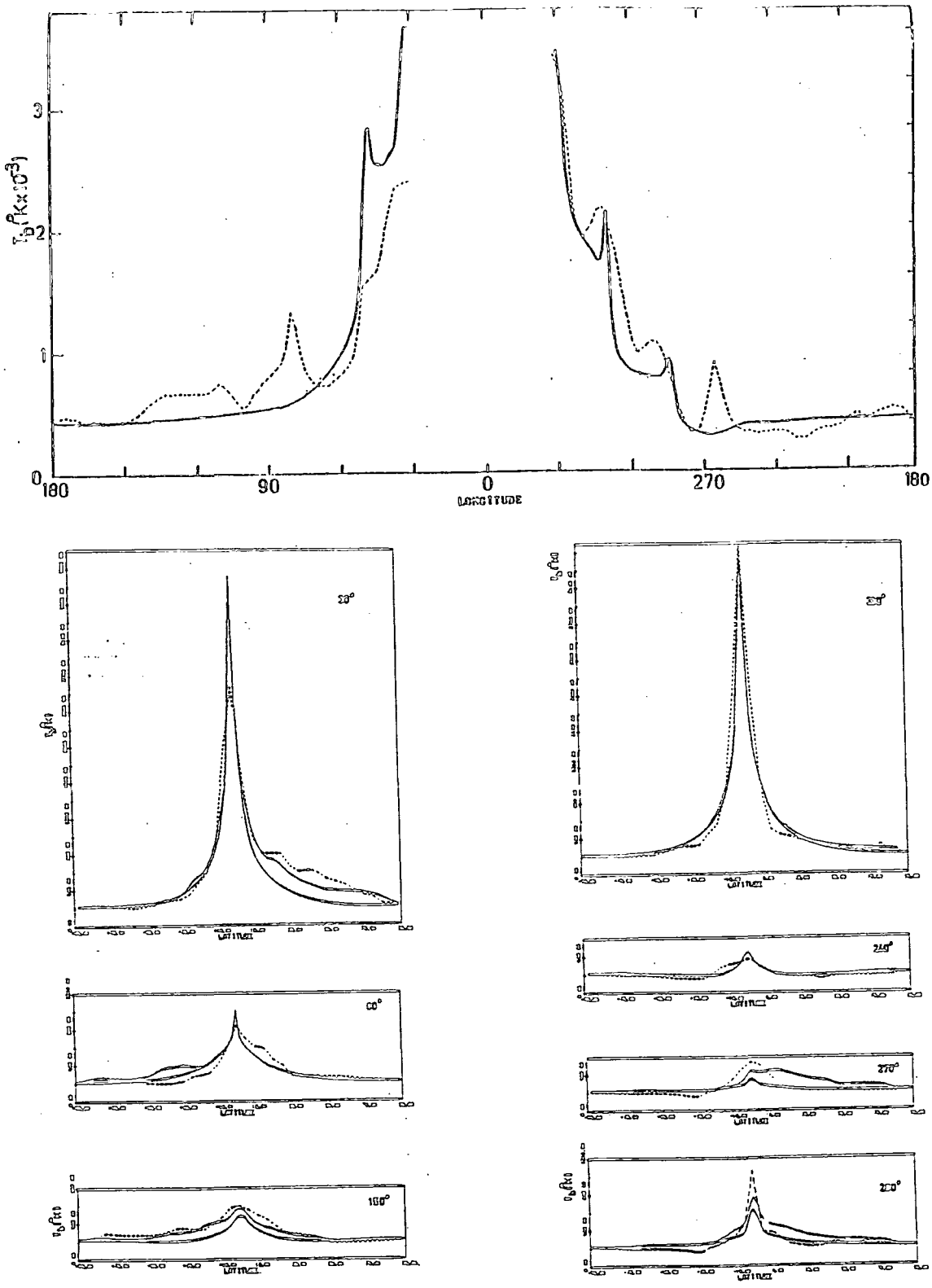

Figure 5.4: Comparison of the 150 MHz temperatures predicted by French's best model (solid line) with those observed (dashed line). The top diagram is a profile along $b = 0°$ and the rest are a few representative cuts across the plane. (Taken from Kearsey, 1983).

within the plane is smaller than the features in the model and so the numerical integration with the use of Simpson's formula should provide a good approximation. However, for increasing latitudes the step size becomes larger and so a poorer estimation of the integral may be expected. Kearsey pointed out however that at larger distances from the plane the modelled quantities tend to smoother distributions and so provided the calculation is not performed at too high a latitude the numerical integration should still give acceptable results.

Before the integrand can be calculated it is necessary to fix both F and R_o by means of a normalization procedure. Two points along the plane are chosen, one at $l = 180°$ and the other near the Galactic Centre but preferably not at an emission peak because then the whole procedure would depend on the chosen model for the variation of compression across an arm and not so much on the variation of quantities on a Galaxy-wide scale. R_o and F are not calculated explicitly but rather the quantities R_o^2 and RATIO$= \frac{F^{1.8}}{0.6861}$. At both longitudes in turn, the value of RATIO required for the integration to produce the exact observed temperature for a given R_o^2 is found for several values of R_o^2. Thus two curves can be drawn of RATIO *vs* R_o^2, one for each longitude. The values of the two parameters where these two lines cross are those which will yield the exact temperatures observed at both longitudes simultaneously and will produce normalized temperatures for other positions in the sky.

Another quantity to be calculated in the integrand is the compression factor which in turn depends on the distances of the point under consideration to the nearest arms. It is necessary therefore to be able to define the spiral arm pattern in a reasonably efficient way for computation. The locus of each spiral arm was defined by giving its position in a polar co-ordinate system about the Galactic Centre, the angle, ϕ, being measured clockwise about the line from the Galactic Centre to the Sun. The value of R, the galactocentric radius of the arm is input in steps of $\Delta\phi = 15°$ and a Chebyshev interpolation is performed on the whole arm. The coefficients of the interpolation are calculated for each arm in turn and are then input into the main, temperature calculating program together with the values of RATIO and R_o^2. The compression factor, ρ_c, at a point now can be calculated since the perpendicular distances from the point to the two nearest arms can be found. Although initially Kearsey added the compressions from both arms, in subsequent models he discovered it was preferable to take the maximum value of ρ_c.

Another computational economy measure employed was to calculate temperatures for positive latitudes only since in the model the temperature distribution is assumed symmetrical about the Galactic plane. Having calculated the temperatures at 408 MHz for a given region of sky on a $1° \times 1°$ grid, Kearsey then increased the temperatures by 23.5% to account for the thermal emission and then added another 6 K for the extragalactic contribution. Before the brightness temperatures were compared with observations they were convolved to the $51'$ resolution of the 408 MHz all-sky survey.

Fig. 5.5 shows the $b = 0°$ profile of the observed brightness temperatures (dashed line) at 408 MHz together with the temperatures predicted using a model almost identical to French's best model. It differs only in the compression factor which is taken to have the

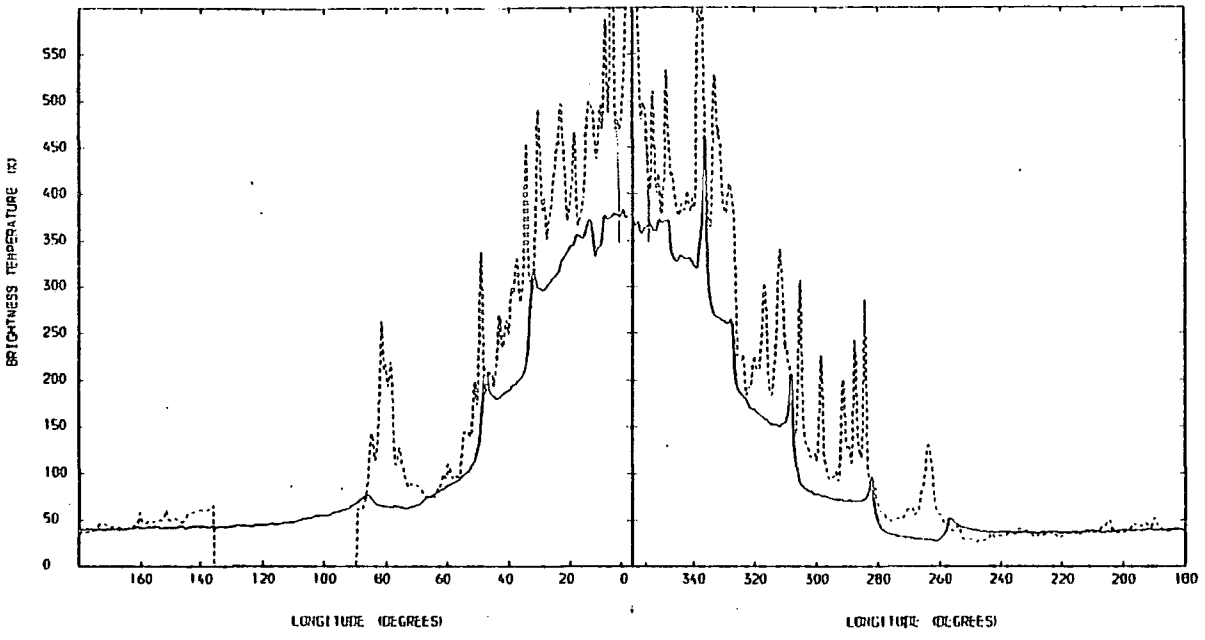

Figure 5.5: Profile of 408 MHz emission along the Galactic Plane as predicted by Kearsey's Model 0 which is almost identical to French's best model for fitting the emission at 150 MHz. The 408 MHz observations of Haslam *et al.* are shown for comparison (dashed line). (Taken from Kearsey, 1983.)

form:

$$\rho_c = \left[4.1 \exp\left(\frac{-4a}{0.5}\right) + 0.7\right] / 0.7 \tag{5.14}$$

rather than that in Equation 5.11. The above form implies a constant width of ~ 0.5 kpc which Kearsey felt was more representative of the results of density wave theory. Also, predictions have been generated right across the central region of the Galaxy. To do this the arms were extended and joined across the sector behind the Galactic Centre which, as can be seen in Fig. 5.2, French had made no attempt to model. Temperatures of 380 and 40 K, representative of the observed temperatures at 408 MHz, were assigned to $l = 0°$ and 180° respectively to normalize the model. In actual fact the temperature at $l = 0°$ is ~ 2000 K but is a special region and so the value, more typical of the plateau on either side of the centre between $|l| \simeq 15°$ and 35°, was adopted instead. In order to reproduce these temperatures simultaneously the required values of R_o^2 and RATIO were 135 kpc^2 and 0.8053 respectively which implies that $F = H_{reg}/H_{irreg} = 0.91$ in an uncompressed region. As can be seen in Fig. 5.5 the predicted profile fits the observed emission in a broad sense but the detailed features observed are not reproduced very well. In the central region the predicted temperatures are too low and elsewhere several of the peaks are not quite coincident with those observed and the troughs of emission behind the peaks are often too deep.

Kearsey found that by moving the path of arms he could control the position at which predicted peaks appeared in the profile and the height of that peak increased with decreasing arm curvature as the line of sight length through the arm increases. Over the ten models

that he developed Kearsey altered the spiral pattern considerably in order to improve the fit and the final pattern is shown in Fig. 5.6. Perhaps the most obvious change is in the central region. There is a partial ellipse, into which spiral arms smoothly merge. The semi-major and -minor axes of the complete ellipse would be 5 and 4 kpc respectively. Antecedent models had incorporated a complete ellipse in an attempt to produce the variation in emission in the longitude range $30° \geq l \geq 325°$, particularly the tangents at $l \simeq 25°$ and 328°. The later inclusion of the broken bar and removal of parts of the ellipse was done in the hope of simulating the asymmetries in the observed profile. In the very central region the lower envelope of the emission is biased towards the northern side of the Galaxy whereas overall in the range $30° \geq l \geq 325°$ the reverse is true. As can be seen in Fig. 5.7 Kearsey's scheme has met with partial success but the fit to the longitude range $15° \geq l \geq 355°$ is still not entirely satisfactory.

Away from the central region the spiral pattern of Model 10 basically consists of two multiple arm structures. The positions of the arms inward from the Sun have been moved in order to relocate the peaks in the predicted profile. The local arm has been moved, truncated and re-extended finally resting at 0.5 kpc beyond the Sun as it was in French's preferred model. Its outward extent was reduced to produce a minimum in the predicted emission corresponding to that seen at $l \simeq 240°$. Only one arm has been removed completely, this being the one which is most distant from the Galactic Centre in the anticentre direction in Fig. 5.2. An additional small section or 'feather' arm has been included to enhance the predicted emission in the $l = 30°$ to 45° region.

When Kearsey introduced an ellipse into the spiral pattern the field was also given elliptical symmetry having the modified form:

$$H_{reg} = H_o \exp\left(\frac{-R^2}{R_o^2}\right)\left[1 - \overline{\exp}\left(-R^2\left(\cos^2\left(\frac{123-\phi}{8}\right) + \sin^2\left(\frac{123-\phi}{4}\right)\right)\right)\right] \quad (5.15)$$

which tends towards the original form (Equation 5.13) at large R. As mentioned before, ϕ is the angle clockwise from the Galactic Centre to Sun line and the angle that the semi-major axis makes with this line is 123°.

The form of the compression across a spiral arm also was altered in favour of a smoother variation. It had been observed that in external spiral galaxies the emission tends to wander somewhat about the main locus of an arm which could well have a broadening effect on the compression over the arm. Kearsey pointed out that if the dynamics of the gas clouds were important rather than the intercloud medium this also could have a front broadening effect. The modified variation for the compression then was taken to be gaussian with $\sigma = 1/6$ kpc:

$$\rho_c = \max\left[C_R \exp\left(-18d_{in}^2\right), C_R \exp\left(-18d_{out}^2\right)\right]/0.7 + 1.0$$

$$C_R = \begin{cases} 1.98 & R < 10\,\text{kpc} \\ (15.0 - R)0.396 & 15 > R > 10\,\text{kpc} \end{cases} \quad (5.16)$$

Here d_{in} and d_{out} are the perpendicular distances of a point to the nearest arm towards and away from the Galactic Centre respectively. The maximum compression ratio is 3.8:1 compared with 6.9:1 for the form in Equation 5.11

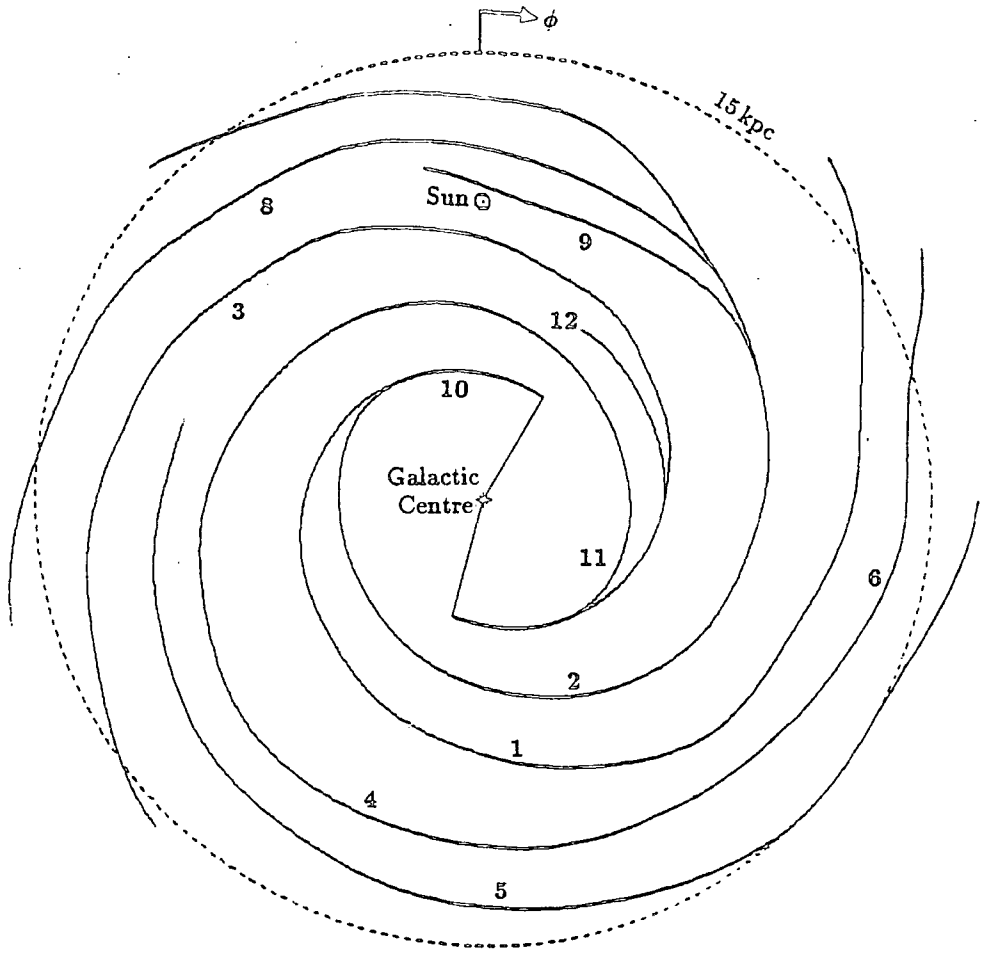

Figure 5.6: Final spiral arm pattern (Model 10) of Kearsey (1983).

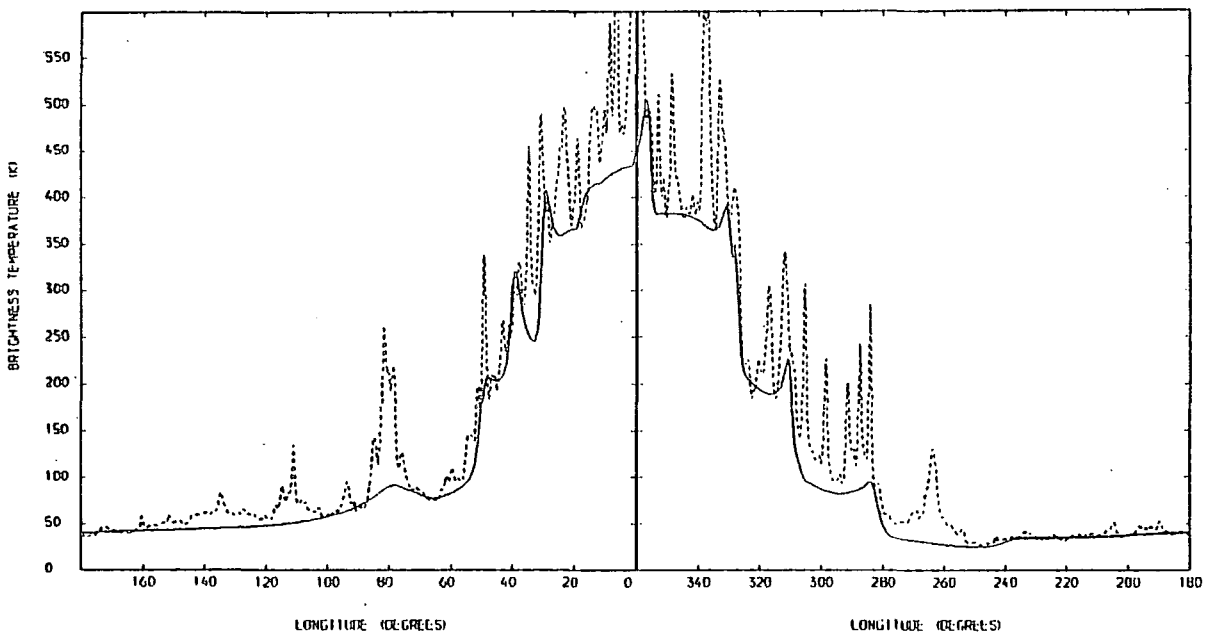

Figure 5.7: Predicted longitude profile along the Galactic Plane at 408 MHz for Kearsey's best model (Model 10). (Taken from Kearsey, 1983.)

Having made all these alterations the values of R_o^2 and RATIO required to obtain normalized temperatures was 139 kpc^2 and 0.73 respectively. In addition to the $b = 0°$ longitude profile, Kearsey compared contour maps and latitude cuts of observed and modelled distributions. A few latitude cuts are shown in Fig. 5.8 for $|b| < 60°$ where dashed lines are observed and solid lines predicted temperatures. Generally the fit to the observations is quite good. One of the most obvious discrepancies, however, is seen in the cuts at $l = 320°$, 310°, 300° and to a lesser extent for $l = 20°$, 10°, 0°, 350°, 340° and 330° where the modelled profile is too narrow at the base of the central peak. Another run of the modelling procedure was made therefore with an electron distribution such that $w(R)$ in Equation 5.5 was kept constant at 0.5 which improved latitude cuts at $l = 60°$, 320°, 310° and 300° at the expense of a degrading of the general fit at high latitudes. The pole temperature observed is 20 K and the model with variable $w(R)$ predicts 17 K. For constant $w(R)$ however the temperature drops to $\sim$ 12 K. Kearsey interpreted the narrower ridge in the fourth quadrant in terms of arm tapering with increasing distance from the Galactic Centre.

5.4 Comparisons of models with the 'observed' non-thermal distribution

As mentioned in Section 5.1 we will be referring to the non-thermal distribution of Galactic emission deduced using the infrared–thermal radio correlation as the 'observed' non-thermal (or synchrotron) emission. This will facilitate discussion of comparisons of it with the results of further developments of models using Kearsey's method. First however, it will be instructive to compare the estimations of the thermal emission at 408 MHz derived from the IR–radio correlation with that of Kearsey's final model which was taken to have temperatures 23.5% as large as those of the synchrotron component. The two estimates for the Galactic Plane are shown in Fig. 5.9. It can be seen that there is considerable disparity between the two distributions. The modelled emission is in general more than twice as large as the scaled infra-red estimate in the outer Galaxy in the longitude range $280° \geq l \geq 70°$ and at $l \simeq 80°$ the model makes no estimate of the emission from the Cygnus complex whereas the scaled IR has a substantial contribution here. In the inner Galaxy the scaled IR does not exhibit the same rapid increase in the underlying level of emission towards the central region as does the model. Instead, the diffuse thermal emission of the scaled IR remains fairly small throughout the plane having a local minimum near the Galactic Centre.

There are coincident peaks in the thermal emission of the two estimates at $l \sim 80°$, 50°, 310° and 280° but other peaks in the model distribution at $l \sim 40°$, 30°, 355°, 330° and 325° are slightly offset from any peak appearing in the scaled IR. Another very noticeable difference between the two estimations is over the longitude range 360°–340° where the general level of the scaled IR emission is substantially lower than the model prediction. The same occurs to a lesser extent at $l \simeq 325°$. The scaled IR distribution has many more features due to individual HII complexes and they are not constrained to coincide with peaks in the synchrotron distribution which necessarily is the case for the model distribution.

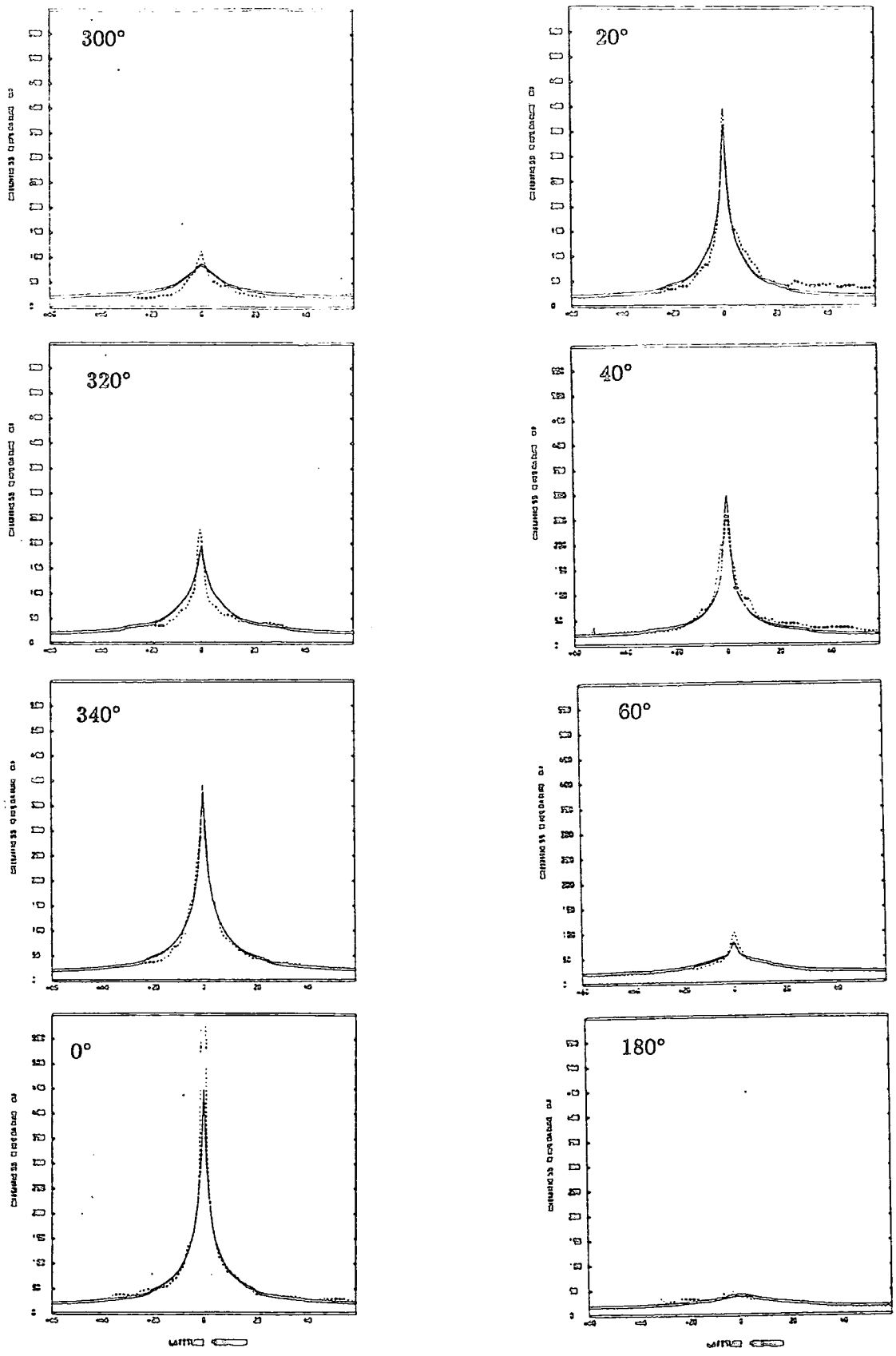

Figure 5.8: Predicted latitude profiles of Kearsey's best model (solid line) compared with the total observed at 408 MHz (dashed line). (Taken from Kearsey, 1983.)

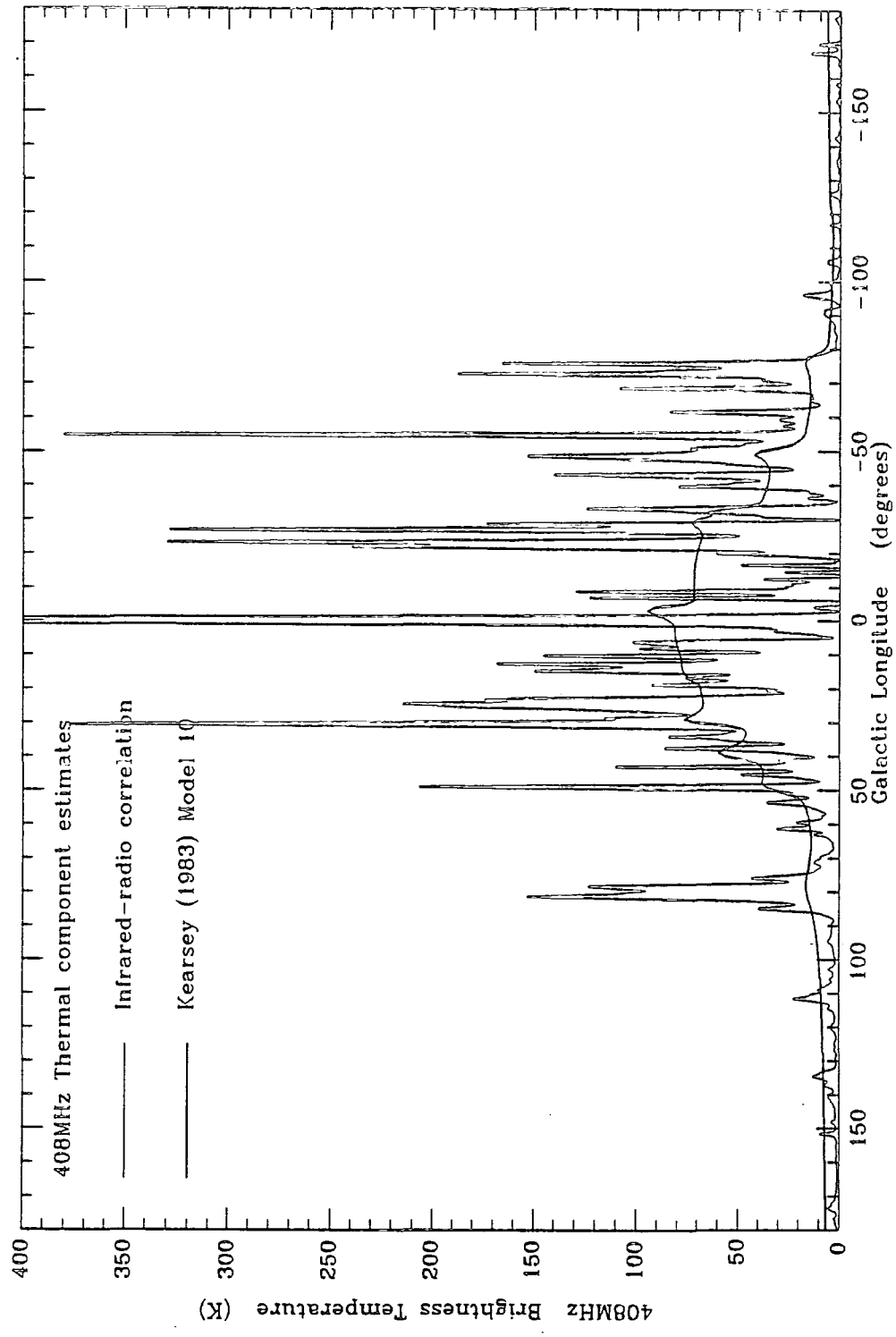

Figure 5.9: A comparison between the profiles along the Galactic Plane of the thermal radio continuum brightness temperatures at 408 MHz estimated by Kearsey (1983) (thick solid line) and the present work (thin solid line). The former assumes that the temperatures are $23\frac{1}{2}\%$ as large as the synchrotron emission at 408 MHz and the latter was derived from the IRAS 60 μm band–thermal radio continuum emission correlation discussed in previous chapters of this thesis.

By comparing models of synchrotron emission with the 'observed' synchrotron emission, therefore, we should reduce any confusion between thermal sources and true features of synchrotron spiral structure in the Galaxy.

In Fig. 5.10 we compare the 'observed' synchrotron emission along the Galactic Plane with that predicted by the final model of Kearsey which was described in the previous section. Since we are comparing the model against a different distribution of temperatures, a renormalization of the model is required. Normalization points were taken at $l = 0°$ and 180° having 'observed' temperatures 300 and 34 K respectively instead of 380 and 40 K used by Kearsey for the total 408 MHz emission. Fig 5.11 shows a graph of the variation of the parameters RATIO *vs* R_o^2 for the two longitudes with their values at the intersection point being 0.63 and 196 kpc^2 respectively. This is to be compared with values 0.73 and 139 kpc^2 found by Kearsey when modelling the total emission. The longer scale length required reflects the higher level of the 'observed' synchrotron emission relative to the scaled IR in the outer Galaxy than assumed for the thermal and non-thermal components in Kearsey's models.

By comparing Fig. 5.1 with Fig. 5.7 we can see that subtracting the scaled thermal temperatures from the total emission along the Galactic Plane has removed to a large extent the asymmetry that existed about the central longitudes in the range $20° \gtrsim l \gtrsim 340°$. Evidently this will influence the course which any modifications to the existing models will follow. The fit of the model at the moment to the 'observed' temperatures along the Galactic Plane are quite good for $180° \geq l \geq 60°$ and $270° \geq l \geq 80°$. In the inner Galaxy, however, the peak at $l = 28°$ is too high in the model whereas there is no peak at all to coincide with that 'observed' at $l \simeq 20°$. The distribution in the central region $20° \gtrsim l \gtrsim 330°$ is very poorly represented by the model although some of the discrepancy perhaps could be attributed to a conservative choice of normalization temperature at $l = 0°$. In general it appears that the peaks in the model are too sharp followed by troughs which are excessively deep. Clearly therefore there remains some scope for improvement of the model of the synchrotron emission and we will discuss the modifications made in the remainder of this chapter.

5.5 The spiral arm pattern

5.5.1 Changes to Kearsey's pattern

In this section we will discuss changes that we have made to Kearsey's final model of the pattern of spiral arms which seem to enhance the similarity of the predicted temperatures to the 'observed' non-thermal emission at 408 MHz. The spiral pattern, after alterations have been made, is shown in Fig. 5.12 and should be compared with Fig. 5.6 of the last section. In both figures there is a number assigned to each arm and these will aid description of the changes. Also, both figures show the sense in which the angle ϕ is measured about the Galactic Centre. The most obvious distinction between the patterns in Figs. 5.12 and 5.6 lies in the central region. We have dispensed with the broken bar and reinstated a complete ellipse. The motivation for this is partly the diminution of the asymmetry about

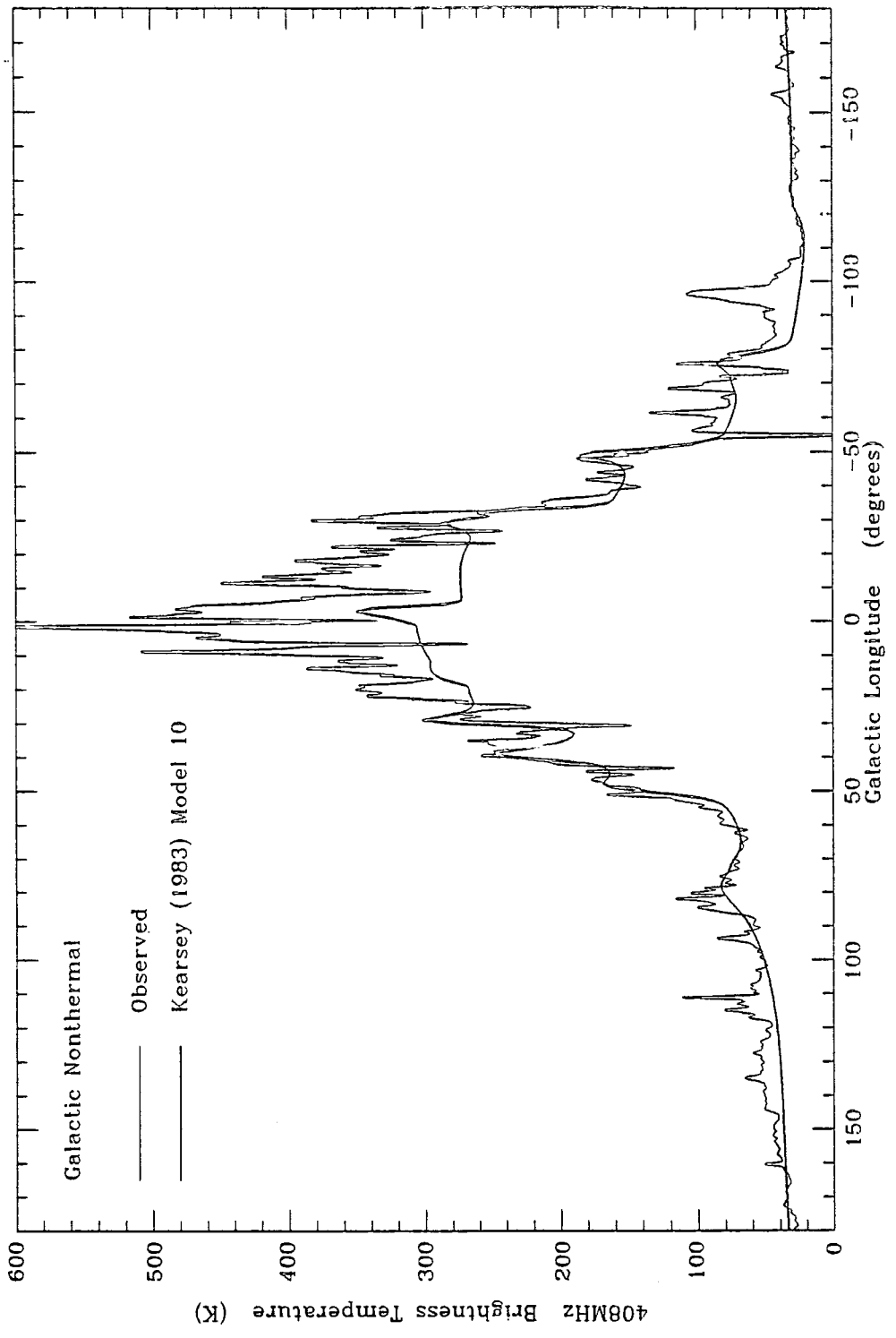

Figure 5.10: Profiles along the Galactic Plane comparing the 'observed' synchrotron emission at 408 MHz with the temperatures predicted by the final model of Kearsey (1983). The model has been normalized to the 'observed' synchrotron emission at $l = 0°$ and 180°.

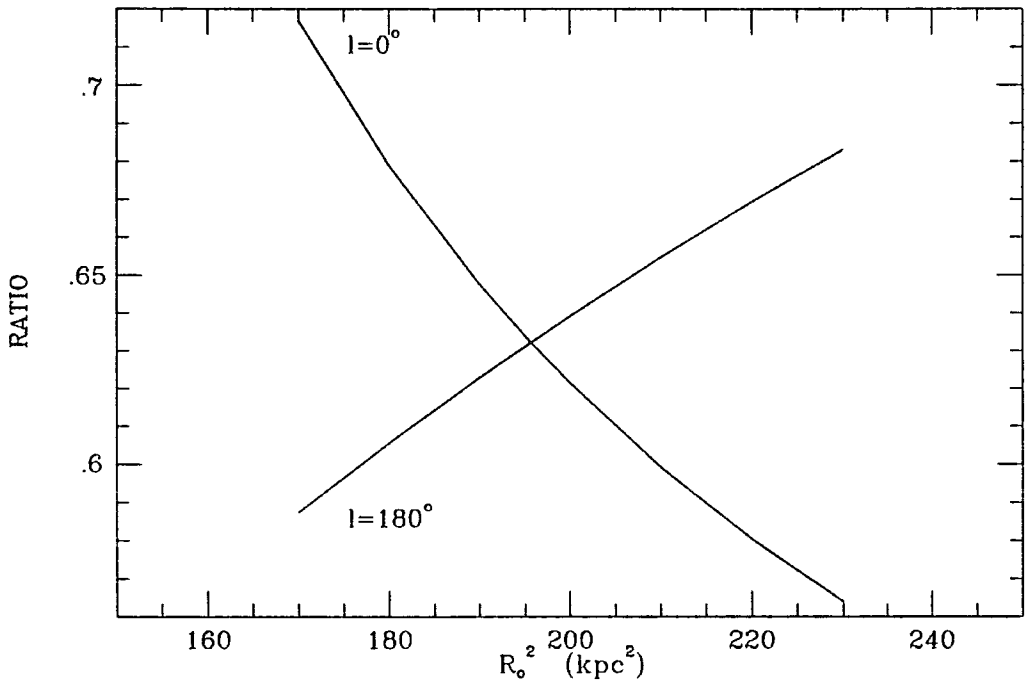

Figure 5.11: The variation of values of the free parameters RATIO and R_o^2 in Kearsey's final model required to reproduce the 'observed' synchrotron emission in the normalization directions $l = 0°$ and 180°. The point of intersection of the two curves, where the 'observed' temperatures are reproduced for both directions simultaneously, occurs at RATIO=0.63 and $R_o^2 = 196\,\mathrm{kpc}^2$.

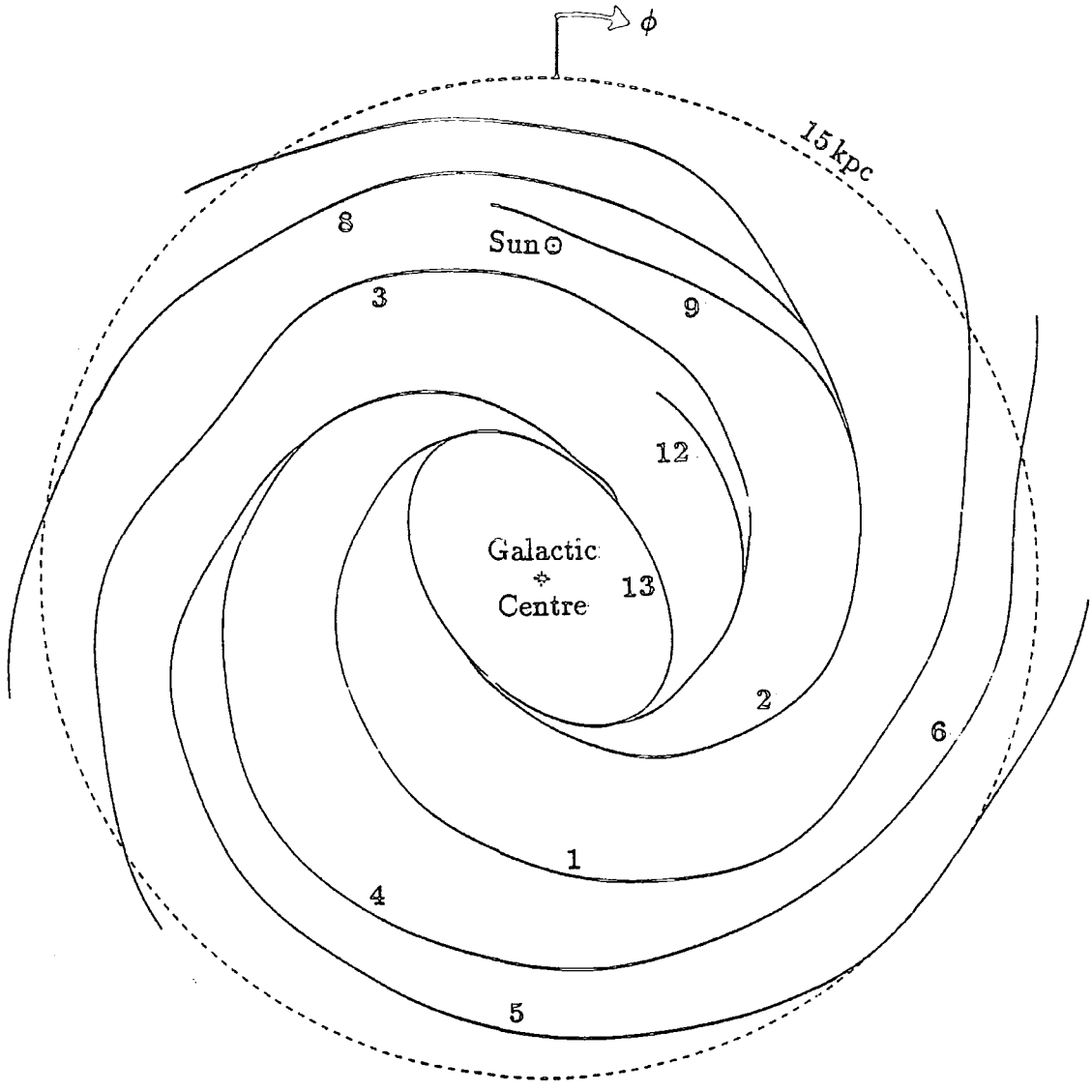

Figure 5.12: The spiral arm pattern adopted in modelling the 'observed' synchrotron emission. Differences between this pattern and that finally used by Kearsey can be seen by comparing this figure with Fig. 5.6.

the Galactic Centre which was remarked upon in the last section. It can be attributed to the very small levels of thermal emission which were subtracted from the total in the range $360° \geq l \geq 340°$ compared with larger levels in the corresponding range on the northern side of the Galaxy. Phillipps *et al.* (1981) (PKOHSI) discovered an apparent asymmetry in the emissivity about the Galactic Centre for $R < 3.6\,\mathrm{kpc}$ which could, on the face of it, imply the presence of a bar. However, they pointed out that in the centre of the Galaxy the lower envelope taken for the unfolding may in fact include a component from discrete sources which in this region could be so abundant that their emission merges together. In this case the underlying synchrotron emission may well be more symmetrical than it seems at first. Our thermal–non-thermal separation supports this line of argument and suggests that the removal of the bar is in order. The retention and completion of an ellipse however provides a means of engineering a peak at $l = 20°$ which is seen in the 'observed' profile in Fig. 5.10. To this end the ellipse has a semi-major axis 5 kpc and semi-minor axis 3.2 kpc with the major axis at an angle $\phi = 140°$ to the Sun-Centre line. Thus the line of sight in the plane at $l = 20°$ is a tangent to the ellipse at a distance of about 3.8 kpc from the Galactic Centre. By using such an orientation it is hoped to reproduce the peak which appears on the other side of the Galactic Centre at $l \simeq 330°$ as well.

To eliminate the peak at $l = 30°$ in the predicted profile of Fig. 5.10, which now appears unnecessary, the arm labelled '4' in both Fig. 5.6 and 5.12 was re-routed to join the ellipse at $\phi = 45°$ in such a manner that no line of sight is tangential to it in the first quadrant. Likewise arm '2' is now forced to follow a similar path. This change will not have any striking effect on the form of the predicted temperatures since for the portion of arm '2' which is altered neither the old or new curves have a tangent which is in the direction of the Sun. Changing the path of arm '2' merely improves the symmetry of the overall pattern. Arms '1' and '3' are both diverted slightly so that they merge smoothly with the ellipse. The last alteration made to the pattern is to arm '5' which previously stopped abruptly at $\phi = 300°$. Now the arm is brought round to run into arm '4' at the point where the line of sight at longitude 310° is tangential to arm '4'. This will at most produce an enhancement to the peak in this direction but joining in arm '5' at this point prevents the creation of another, separate peak in the predicted temperature profile. This final change also improves the symmetry of the spiral pattern.

The overall pattern in Fig. 5.12 is now more like two pairs of arms rather than having two multiple arm structures as in Fig. 5.6. Obviously it is easier to make out more detailed structure in the locations nearest to the Sun and it is envisaged that arms '1', '4' and '5' which pass behind the Galactic Centre would also have small feather arms attached.

The positions of all the arms and the ellipse in Fig 5.12 are tabulated in Table 5.1. Each arm is given a number corresponding to those on Fig 5.12 and ϕ_o represents the angle at one end of the arm with $\Delta\phi$ being its angular extent. The column of figures below these parameters is the distance of the arm from the Galactic Centre and is given at angles:

$$\phi_n = (\phi_o - 15n)° \quad \text{where} \quad n = 0, 1, 2, \ldots, 24.$$

ARM	1	2	3	4	5	6	8	9	12	13
ϕ_o	330	225	150	45	300	135	45	65	90	140
$\Delta\phi$	285	270	285	270	210	75	150	75	60	360
	4.89	3.21	4.89	3.21	8.10	12.40	10.95	10.15	6.05	5.00
	5.25	3.42	5.25	3.50	8.95	12.90	11.06	10.35	6.15	4.77
	5.45	3.70	5.40	3.70	10.00	13.65	11.30	10.05	6.25	4.29
	5.65	4.20	5.75	4.32	11.40	14.20	11.80	9.95	6.45	3.81
	6.00	4.95	6.05	5.20	12.00	14.80	12.45	10.25	6.60	3.47
	6.35	6.00	6.45	6.30	12.60	16.95	12.80	11.30		3.27
	6.65	7.00	6.80	7.28	12.90		13.20			3.20
	7.00	8.00	7.25	8.10	13.25		14.00			3.27
	7.55	8.95	7.75	8.65	13.70		14.50			3.47
	8.05	9.40	8.10	9.30	14.05		15.40			3.81
	8.60	9.85	8.80	9.80	14.55		16.35			4.29
	9.30	10.35	9.45	10.40	15.00					4.77
$R(\phi)$	10.10	10.95	10.22	11.00	15.00					5.00
	10.90	12.05	10.68	11.25	15.60					4.77
	11.10	13.20	10.68	11.40	16.55					4.29
	11.60	13.50	11.45	11.65						3.81
	12.40	14.10	12.95	11.90						3.47
	13.10	14.65	13.70	12.05						3.27
	14.65	15.75	14.55	12.40						3.20
	16.30		15.55							3.27
										3.47
										3.81
										4.29
										4.77
										5.00

Table 5.1: Positions of arms corresponding to Fig 5.12

Since a number of substantial changes have been made to the spiral arm pattern within the solar circle, it is necessary to recalculate the parameters R_o^2 and RATIO for two normalization directions. As before, one point is taken at $l = 180°$ having temperature 34 K. The other however is now at $l = 10°$ with temperature 300 K, thus reducing the influence of the Galactic Centre on the normalization. The new values of the parameters are $175\,\mathrm{kpc}^2$ and 0.60 which implies that the ratio of the uniform to random magnetic field is 0.61. The predictions of the temperatures along the Galactic Plane were recalculated using these parameters and the new spiral arm pattern but keeping all other aspects of the model identical to that described in Section 5.3. The results are shown in Fig. 5.13.

As can be seen the peak which appeared at $l = 30°$ in Fig. 5.10 has been successfully eliminated and now there is an additional peak at $l = 20°$. The model predicts a plateau of 300 K over the range $10° \geq l \geq 335°$ which is not at all in line with the 'observed' behaviour in this region. Also, the peak at $l \simeq 330°$ is not exactly in coincidence with the actual maximum seen. Obviously this could be remedied by further manipulation of the ellipse.

This exercise has demonstrated that it is possible to model the 'observed' distribution of local maxima in the synchrotron emission by means of careful positioning of a number of spiral arms. However, it appears that within the central $\sim 4\,\mathrm{kpc}$ of the Galaxy it is very difficult to reproduce the 'observed' emission just with a system of arms and a ring, ellipse or bar. The form of the temperature variation over the central few tens of degrees in galactic longitude may be better explained in terms of conditions unique to the Galactic Centre leading to different distributions of, for example, electron density or magnetic field strength there. We will explore this possibility in the next section, but in the remainder of this section our empirically derived spiral pattern of Fig. 5.12 will be compared with those derived from other observations and with the expectations of theory.

5.5.2 Observation and theory of Galactic spiral structure

In calculating the synchrotron emission from the Galaxy we are really concerned with the structure of the magnetic field. However, the Galaxy-wide distribution determined from measurements is not very well known. Also, in the model it has been assumed throughout that the magnetic field is 'frozen' into the gas since the gas is partially ionized and so the field is compressed with it. Given that this is the case then the observed structure of the gas should tell us about the structure of the magnetic field also. This is not to say that the gas distribution is known in great detail either but the multitude of attempts at mapping spiral structure can be compared with the pattern we have used here. Observations of nearby external spiral galaxies at optical wavelengths have revealed an abundance of different patterns of spiral arms ranging from grand-design or two-arm spiral galaxies such as M51, to galaxies with much less spiral structure such as M33. Determining the morphology possessed by the Galaxy is considerably more difficult because of our internal position. Observations at optical wavelengths can only reveal information about the relatively local structure because of obscuration of light by dust lying along a line of sight. Therefore most of the studies of the global distribution of gas have been concentrated at longer wavelengths which can penetrate the ISM.

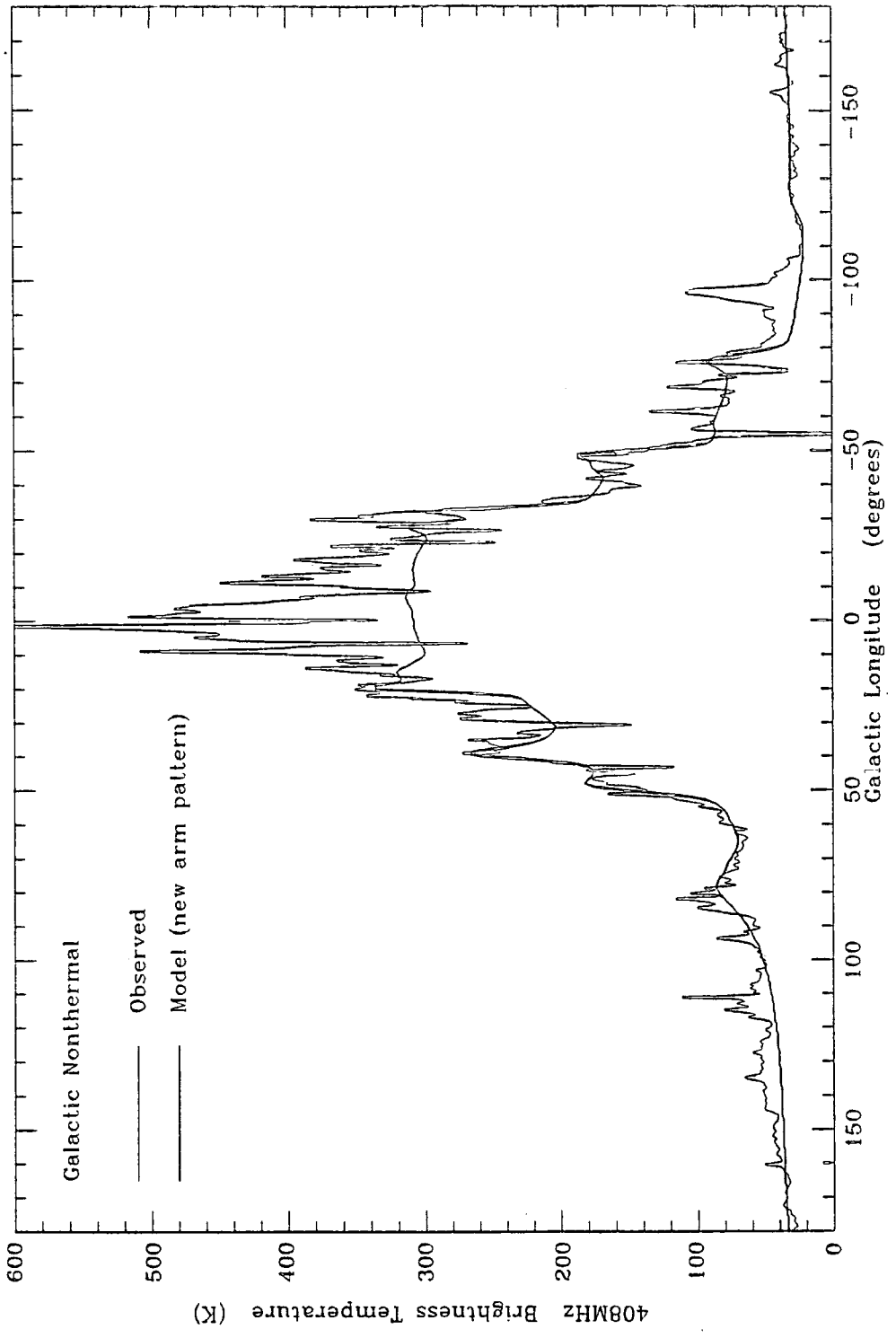

Figure 5.13: A comparison of predicted 408 MHz synchrotron emission along the Galactic Plane (thick solid line) with that 'observed' (thin solid line). The model used is identical to that responsible for the profile shown in Fig. 5.10 except that the spiral arm pattern shown in Fig. 5.6 has been replaced with our modified pattern presented in Fig. 5.12.

The three main tracers of gas structure which have been employed are the 21 cm emission of HI gas, the recombination lines of HII regions and the 2.6 mm ^{12}CO line associated with molecular hydrogen. In 21 cm line surveys a profile of the intensity of radiation against frequency shift from the central frequency is measured at each sampling point. The Doppler shift can be translated into line of sight velocity which has components from the peculiar velocity of the gas and its motion about the Galactic Centre relative to the Sun. These velocity profiles can then be used to find a mean rotation curve *i.e.* the variation of the rotation velocity of gas with galactocentric radius assuming that the motion is all in circular orbits and is axisymmetric. As well as velocity information, the velocity profiles also contain information about the variation of spin temperature and density of the HI gas. In order to extract this, a certain set of assumptions must be made. The first studies of the distribution of the HI gas in the Galaxy (*e.g.* Schmidt, 1957 and Westerhout, 1957) assumed that the gas was optically thin with a constant spin temperature and that the motion of the gas was in a circular orbit following the previously determined rotation curve. Thus, all variations in the intensity were interpreted as density structure and indeed a system of arms was apparent from the analysis. Further studies described by Weaver (1974) looked for curves and loops in the $T_b(l,v)$ diagram of the Berkeley 21 cm survey but still assumed circular rotation. However, as Burton (1971, 1972) pointed out, there is evidence for significant non-circular motion of HI gas with deviations from the mean rotation curve of the order of $\pm 10\,\mathrm{kms}^{-1}$ which is a few percent of the circular rotation velocity. Burton showed that it was possible to model measured velocity profiles of 21 cm surveys adequately by assuming that the density of the gas is everywhere constant and that intensity variations are due to streaming motions of the gas. However, if the density is taken as the sole cause of intensity variations then the contrast between the arms and interarms in the derived spiral structure is unrealistically high. It was clear then, that although density variations are certainly present in the Galaxy, the effect of non-circular motions of the gas on the observed profiles is much stronger. Later attempts at unravelling the information in 21 cm line surveys have taken a modelling approach. The observed brightness temperatures as a function of longitude and velocity ($T_b(l,v)$) are reconstructed using models of density and kinematic variations which invoke density wave theory. Simonson (1976) followed this method and constructed a spiral pattern consisting of two arms with small pitch angle originating 4 kpc from the Galactic Centre with a multiple arm structure of larger pitch angle beyond the solar circle. Such approaches therefore assume that the Galaxy has a spiral structure rather than proving that it does.

The well-known study by Georgelin and Georgelin (1976) of the distribution of bright HII regions in the Galaxy involved distance determination using observations at optical and radio wavelengths. The optical measurements allowed a more direct way of finding the distance to the HII region but were confined only to within 9 kpc of the Sun. Distances measured from radio recombination lines are determined kinematically and hence there is a distance ambiguity but the problems of attribution of streaming motions to density variations are not incurred. In cases where there were optical or 21 cm absorption measurements as well as radio recombination line observations it was possible to determine whether the HII region is at the 'near' or 'far' distance. The spiral pattern that Georgelin and Georgelin

obtained was four armed, had a pitch angle of $\sim 12°$ and the Sun was situated in a spur from one of the major arms. The positions of the line of sight tangents to the arms coincided with maxima in 11 cm radio continuum data and there was also reasonable agreement with the models from the HI 21 cm emission of Kerr (1969) and Weaver (1970).

Studies of structure from CO line emission surveys are affected by the same sort of problem as the HI surveys. The use of molecular clouds as a tracer of spiral structure is a relatively new approach and there has been some argument about their suitability for this. Cohen *et al.* (1980) claimed that molecular clouds are very good tracers of spiral arms following their analysis of surveys made in the first and second quadrants. They identified features in the CO data with spiral arms that are apparent in the 21 cm surveys and noted a higher contrast of intensity between arms and interarms than in HI measurements. A similar CO survey made in the fourth quadrant has been studied by Cohen *et al.* (1985) and Grabelsky *et al.* (1987) and has shown that the Carina arm can be clearly distinguished. They deduced that the arm-interarm contrast is about 13:1 in CO. However Solomon, Sanders and Rivolo (1985) concluded from another CO survey of the north side of the Galaxy that it is only the warm molecular clouds that are the spiral tracers and that the cold clouds have a more widespread distribution.

Fig. 5.14 shows a collection of some of the spiral structures for the Galaxy that have been deduced from the tracers HI, HII and CO. Our final pattern is also shown again for comparison and as can be seen it still shows some similarity with that of Georgelin and Georgelin from which it has evolved. It is hoped that this short and by no means exhaustive review has given the impression that resolving the pattern of the arms of the Galaxy is difficult and a detailed and complete picture is still not available despite a tremendous amount of work by many people.

We have already alluded to spiral density waves as being a theoretical explanation of spiral structure in galaxies. Some of the earliest work on this was by Lin and Shu (1964, 1966) and Lin, Yuan and Shu (1969). The theory proposes that there exists density waves moving through the disc of the Galaxy. The disc is assumed to be thin and to possess already a spiral distribution of matter. Consequently, the gravitational field was found to have spiral perturbations and using the rotation curve of Schmidt (1965) it was possible to solve equations of motion of gas and stars which move across these gravitational perturbations in their passage around the Galaxy. In these initial papers the equations were simplified by assuming that the spiral structure had a very small pitch angle and that perturbations in the gravitational field were small to enable linearization of the equations. The distribution of stars and gas found by solving these equations was also spiral and by equating this to the initial state then a dispersion relation for the density waves was obtained. This dispersion relation predicts that there are two galactocentric radii for which the rotation of gas and stars is circular and are referred to as the Lindblad resonances. In Our Galaxy the 4 kpc ring has been identified with the inner resonance. The corotation radius is the galactocentric radius at which the spiral density wave pattern and the stars and gas both rotate at the same angular velocity. For the Galaxy it is believed that this would occur at a galactocentric radius of 16–18 kpc for a pattern speed of 11–13 $\mathrm{km\,s^{-1}\,kpc^{-1}}$ in a two-armed spiral density wave pattern.

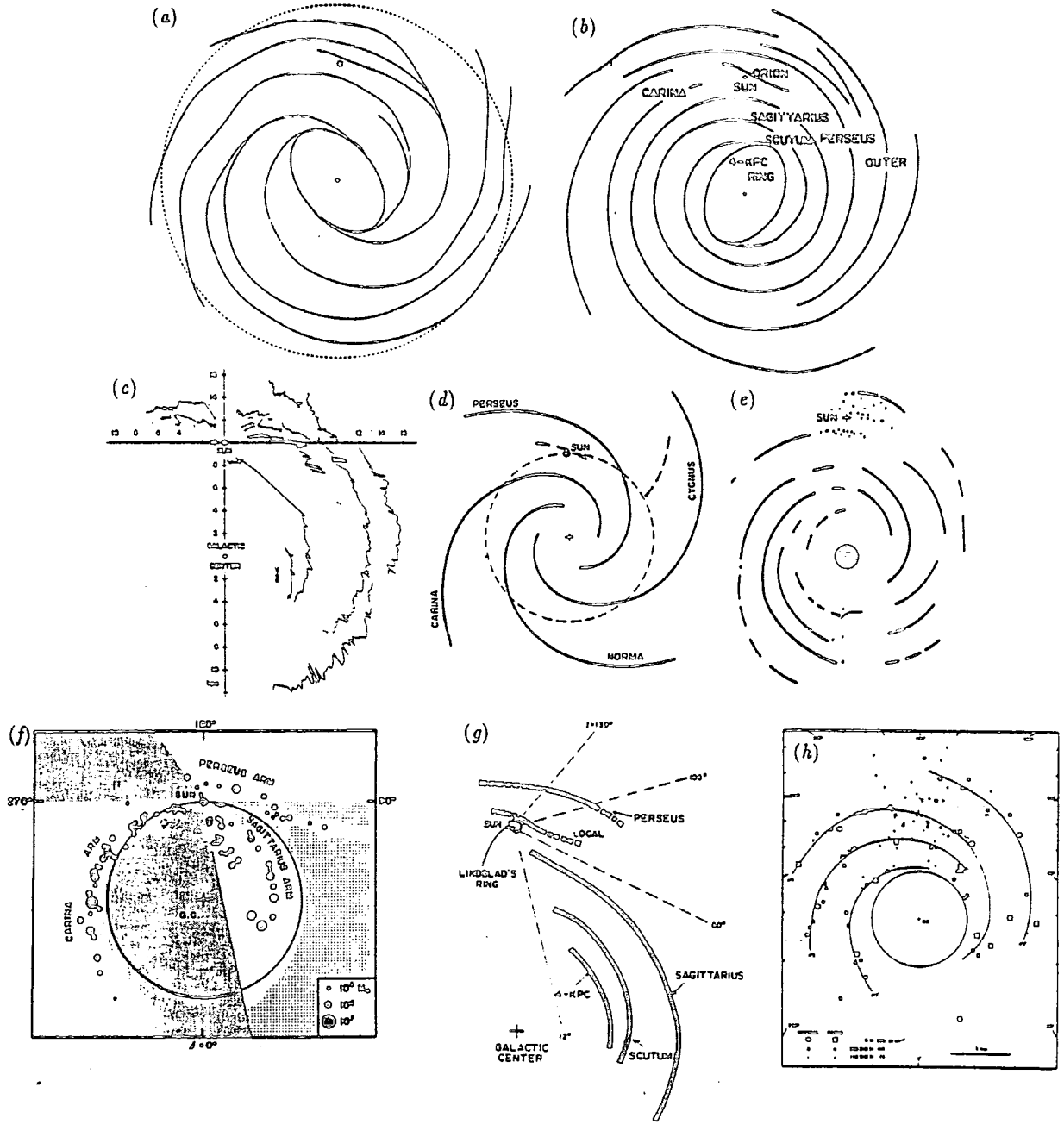

Figure 5.14: A collection of some of the spiral structures which have been proposed for the Galaxy following analyses of observations of HI, HII or ^{12}CO. For comparison we show again in (*a*) the pattern used in our model of the Galactic synchrotron emission. (*b*) Simonson (1976) (HI), (*c*) Weaver (1974) (HI), (*d*) Blitz (taken from Bok, 1983) (CO and HI), (*e*) Robinson *et al.* (taken from Bok, 1983) (CO), (*f*) Cohen *et al.* (1985) (CO), (*g*) Cohen *et al.* (1980) (CO), (*h*) Georgelin & Georgelin (1976) (HII).

One problem with the theory was that for the small perturbation necessary to keep the equations linear, the resulting spiral pattern of stars and gas would not be very large and certainly not as well defined as observed in some spiral galaxies. To progress any further, therefore, it was clear that the nonlinear solutions of the equations of motion must be used. This was first tackled by Roberts (1969) who assumed that the gravitational perturbations were due to the stars only and then solved the nonlinear equations for the gas only. The random speeds of the gas were expected to be much lower than those of the stars and hence the gas should react more violently to any gravitational perturbation. Solutions were in the form of a set of almost circular, concentric stream tubes and in each tube the gas encountered a shock in two positions along the tube. Collectively they formed a two-armed spiral shock arrangement in which gas is compressed forming dust lanes. It was proposed that the compression could precipitate star formation. Roberts and Yuan (1970) found that incorporating the magnetic field into the two-armed spiral shock model (TASS) was possible and the magnetic field direction lay nearly parallel to that of the spiral arms.

The early publications on the theory assumed that the gas had only two phases; dense clouds with temperatures of only 20–200 K surrounded by a diffuse medium with higher temperature of the order of 10^4 K (Field, Goldsmith and Habing, 1969). However Mckee and Ostriker (1977) suggested that the ISM could be better described as a three phase medium. The cool, dense clouds of the two phase model is supposed to be surrounded by a warmer ($\sim 10^4$ K), less dense envelope within which the gas is partly ionized. This warm gas acts as an interface between the cold clouds and a very hot diffuse plasma intercloud medium with temperature $\sim 10^6$ K. This new model appeared at first sight to be incompatible with density wave theory as it was supposed that the plasma had the largest filling factor and would therefore determine the dynamics of the gas. The sound speed of the plasma however is too large to form strong shocks on encountering density waves and hence would suggest that neither star formation triggering nor dust lane production would occur (Cox and Smith, 1974). Another problem with density wave theory was explaining how the pattern was maintained. It was pointed out by Toomre (1977) that these proposed density waves would break up within a few rotations of the Galaxy. A few possible, but perhaps rather contrived solutions to these problems were proposed. Explanations of the former problem included the suggestion that it was the warm phase of the three component medium which dictated the effective sound speed of the gas (Schmidt-Kaler and Weigandt, 1980). Another explanation supposed that in the interarm regions the filling factor of the plasma was quite small unlike that in the arms (Reinhardt and Schmidt-Kaler, 1979). Mechanisms for spiral arm maintenance have invoked the existence of bars in the Galactic nucleus (Lin, 1970) or the gravitational effects of nearby galaxies (Toomre, 1981).

Another mechanism for the production of spiral patterns that has been suggested is 'stochastic self-propagating star formation' which was a development by Gerola and Seiden (1978) of an idea proposed by Mueller and Arnett (1976). Shock waves from supernova explosions of massive stars in the Galaxy compress neighbouring gas and thus trigger star formation. The new massive stars are now available to repeat the process which is therefore self-propagating. Aggregates of stars are produced by this method and the differential galactic rotation draws them out into arm structures not unlike features seen in spiral

galaxies. In the original model of Mueller and Arnett, however, these features did not persist for great lengths of time. One of the refinements made by Gerola and Seiden was to assume that the probability of a supernova event triggering star formation in the surrounding ISM was less than unity. Results showed that spiral arm patterns similar to those observed in galaxies would form and they depended exclusively on the assumed galactic rotation curve. Individual features still would have only a short lifetime but the continual regeneration gave the appearance of a spiral pattern which rotated rigidly for several rotation periods. Although this theory seems to side step the problems of producing a strong shock in a three phase ISM that were incurred in the density wave theory and produces a pattern of relative longevity it has been pointed out by Roberts and Hausman (1984) that some of the ordered structure evolving from the model may be a consequence of the modelling procedure rather than physical properties.

In 1980, Cowie realized that it is possible to treat the ISM as a fluid of clouds over timescales longer than 10^7 years and deduce the dynamics of such a fluid assuming that the pressure is $\rho < v^2 >$ where ρ is the average mass density and $< v^2 >$ is the mass averaged square velocity dispersion of the clouds. In a sequel to this paper the following year the dynamics of such a fluid were explored in relation to density wave theory. It was shown that in the inner arms of a spiral galaxy, cooling of the 'cloud gas' leading to instability and subsequent formation of large bound complexes provided a mechanism for the production of giant molecular clouds.

Levinson and Roberts (1981) and Roberts and Hausman (1984) again assumed that the dense clouds of the ISM dictate the dynamics of the medium. However, instead of treating the clouds as a fluid, each cloud was a particle in a N-body system orbiting the galactic centre and undergoing collisions with other clouds. The collisions were assumed inelastic and clouds were supposed to experience an increase in velocity from nearby SNRs. Provision was made within the model for protostars to form and, after a suitable length of time, for SN explosions to occur following cloud collisions or SNR interaction. It was found on introduction of a spiral gravitational perturbation and assuming that collisions between clouds is the dominant star formation mechanism that galactic shocks formed and the clouds concentrated in spiral arms. The results appeared to be almost independent of the collisional mean free path and clouds tended to accumulate into large complexes within the arms due to their inelastic collisions. Once the spiral patterns for these collision-dominated star formation models had been established then they appeared to be stable for the remainder of the simulation. For one simulation the emphasis was laid on the triggering of star formation from interactions with SNR *i.e.* a stochastic self-propagating star formation model and it was found that any spiral arms which formed were ephemeral. Roberts and Hausman pointed out that this particulate method of dealing with clouds gave a better picture of structure on a small scale than could be produced with the cloud fluid of Cowie (1980, 1981). It would appear, therefore, that the model of Roberts and Hausman could resolve some of the problems of density wave theory. By treating the gas as cloud particles, spiral shocks and cloud complexes, which could be identified with GMCs, can form. Additionally, the cloud-cloud collision dominated cases seem to produce spiral patterns that persist for at least 10^9 years.

The spiral arm patterns displayed in a paper by Bok (1983), which were taken from Blitz and Robinson *et al.*, and that of Georgelin and Georgelin (1976) all have four major arms. The pattern suggested in the present work and which is shown in Fig. 5.14 together with these other three, has two pairs of arms with several branches and spurs. The two-armed mode of density wave theory is the fundamental and therefore predominant mode but higher modes are not incompatible with the theory (Miller, 1976; Lin and Bertin, 1985). It has been suggested that the formation of branches and spurs and feathers could be the result of nonlinear responses to spiral gravitational perturbation (Shu, Milione and Roberts, 1973). The simulations of Gerola and Seiden using the stochastic self-propagating star formation scenario are capable of producing multiple arm spiral patterns also.

5.6 The magnetic field

5.6.1 Observations and theory

The measurement of magnetic fields in the Galaxy or external galaxies is difficult but a number of approaches are available to determine the direction and intensity of fields. A full description of these and the theory behind them can be found in reviews by Sofue *et al.* (1986) and Heiles *et al.* (1987). Optical polarization measurements provide information about the orientation of the field. In the majority of cases the field of external spiral galaxies seems to be aligned parallel to the spiral arms (see Sofue *et al.*, 1986). At radio frequencies several techniques exist which enable not only the directions of magnetic fields but also magnitudes to be determined. The direction of the field component perpendicular to the line of sight can be determined from polarization measurements of the radio synchrotron emission after due allowance is made for Faraday rotation of linearly polarized light passing through a magneto-ionic plasma. The angle of rotation ϕ_F at wavelength λ is given by the expression:

$$\phi_F = RM\lambda^2 \,(\mathrm{rad}) \tag{5.17}$$

where RM is the rotation measure given by:

$$RM = 0.81 \int n_e B_{\|} \, dl \tag{5.18}$$

Here n_e and $B_{\|}$ are the thermal electron density and magnetic field parallel to the line of sight along the path length l between the source of polarized emission and the observer. The determination of the dispersion measure of pulsars which is proportional to $\int n_e \, dl$ has been used together with these rotation measurements to find directly the mean magnetic field parallel to the line of sight, weighted according to the electron density, in the local solar neighbourhood. No such direct method can be used however for the determination of fields in external galaxies as no pulsar dispersion measures are available and allowances have to be made for the rotation measure due to the foreground intergalactic medium and interstellar medium of our Galaxy. Without a measurement of n_e for the galaxy, assumptions must be made in order to estimate the magnetic field. However, a method proposed by Tosa and Fujimoto (1978) has been used extensively to determine the global

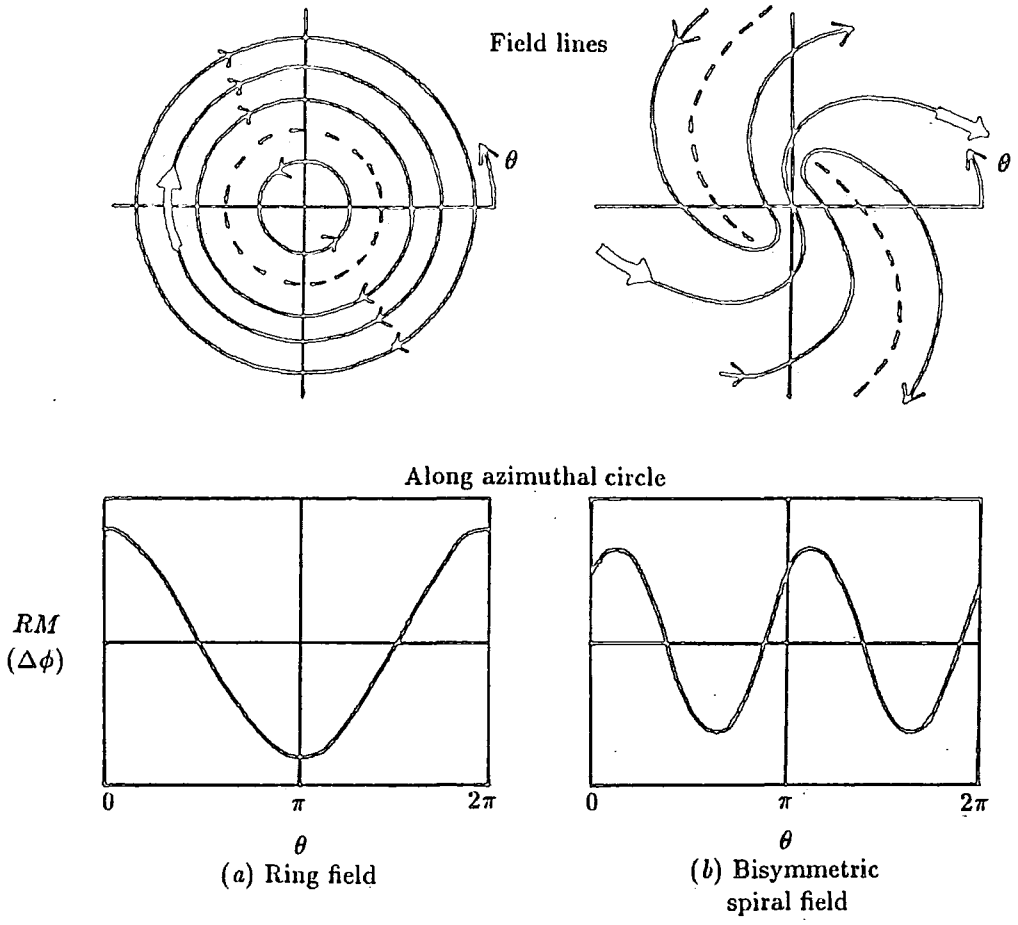

(a) Ring field

(b) Bisymmetric spiral field

Figure 5.15: (*a*).The ring and bisymmetric magnetic field configurations in disk galaxies. (*b*).Variations of RM against azimuthal angle θ along a circle. Taken from Sofue *et al.* (1986).

distribution of the magnetic field in the plane of spiral galaxies using the spatial variation of the rotation measure, due to the galaxy only, across its disc. The two configurations normally considered are a ring field and bisymmetric spiral (BSS) field (see Fig. 5.15). For the former the variation of the rotation measure with azimuthal angle along a circle about the galactic centre is single-sinusoidal whereas for the latter it is double-sinusoidal. So far two galaxies, M51 and M81, have been discovered to have clear bisymmetric field distributions. The best example is M81 which has recently been studied by Krause *et al.* (1989). Two examples of ring fields in galaxies also have been found to date, in M31 (Beck, 1982) and IC342 (Sofue *et al.*, 1985).

The configuration of the magnetic field in our Galaxy remains somewhat controversial. Attempts at its determination usually involve the analysis of the rotation measures of QSOs, radio galaxies and pulsars. Three groups examining measurements inside the solar circle found that the direction of the field in the Sagittarius arm is opposite to that in the local, Orion arm and have inferred that a field reversal exists between these two arms (Thomson

and Nelson, 1980; Simard-Normandin and Kronberg, 1979; Simard-Normandin and Kronberg, 1980; Sofue and Fujimoto, 1983). Sofue and Fujimoto also found that the direction of the field seems to follow the spiral arms which were deduced by Georgelin and Georgelin (1976). All of these observations have been interpreted as an indication of a BSS pattern of magnetic field in our Galaxy. However, Vallée (1983), in an analysis of rotation measures in the direction of the Perseus arm found no field reversal between it and the Orion arm and in the Perseus arm the field direction appears to be in an azimuthal direction suggesting to the author that the field may be better represented by a circular pattern.

It would seem from the available observations to date that the structure of the magnetic field is related to the gas spiral arms. As mentioned in the previous section, Roberts and Yuan (1970) incorporated a ring magnetic field into density wave theory. Both the gas stream lines and field lines are considered to be closed and parallel to each other and the gas is subject to a spirally perturbed gravitational field. As a result of compression in the shock fronts produced, the magnetic field inside the arms was found to be enhanced and lie almost along the spiral arm. In BSS fields spiral gaseous arms also would form but whether they can be identified with those arms formed by density wave theory is unclear (Sofue *et al.*, 1986).

Most models for generating magnetic fields in spiral galaxies invoke a turbulent dynamo model which was first proposed by Parker (1971). In the disc of a galaxy the helical turbulence of interstellar gas coupled with the differential rotation of gas about the centre of the disc generates and amplifies a large scale magnetic field. Dynamo models usually assume a flat disc galaxy (Parker, 1971) or an oblate spheroid (White, 1977, 1978) and the eigenfunctions to the induction equations correspond to different modes of excitation of the dynamo. In the first models *e.g.* by White, only the first mode was considered which is axisymmetric and the resulting field consists of a toroidal component in the plane of the galaxy and a much weaker poloidal component. The next higher mode is the bisymmetric case whose field depends on the azimuth as well as radial distance from the galactic centre and height above the plane (Sofue, 1987; Ruzmaikin *et al.*, 1988). Chiba and Tosa (1989) have studied the global distribution of bisymmetric spiral ($m = 1$) modes generated by the galactic dynamo and have found that they grow more slowly than axisymmetric modes ($m = 0$) with eigenfunctions restricted to narrow radial ranges in the disc. This is in accord with the observation that many galaxies seem to have field distributions comprising of a mixture of modes. However, it is difficult to explain within the framework of standard dynamo theory the apparent dominance of a BSS mode seen in some galaxies and also the coherence of such modes over the whole of the disc. The dynamo model requires an initial field to exist and it has been suggested (*e.g.* Ruzmaikin *et al.*, 1988) that this could be provided by ejected fields from supernova explosions. Other authors have claimed that there is a predominance of the BSS configuration seen in local spiral galaxies and the fact that the structure contains open field lines, is strongly suggestive of a primordial origin of the magnetic field. The field is trapped in the protogalaxy and wound up and maintained by a dynamo mechanism (Fujimoto, 1987, Sofue *et al.*, 1986).

5.6.2 Changes to the model

In the model of synchrotron emission of the Galaxy at 408 MHz described in the last section from which the profile in Fig. 5.13 was obtained the regular field component has been assumed to lie along spiral arms and parallel to the Galactic Plane. The radial decrease in the uncompressed state was constructed to fall off as $\exp(-R^2/R_o^2)$ at large R and to have zero magnitude at the centre. No provision was made for the possibility of field reversals which are predicted in bisymmetric spiral and some axisymmetric field models (Ruzmaikin, 1985). Since the reversals and hence lines of null field are likely to occur in interarm regions where the compression factor of the field is low, the presence or absence of field reversals should not make much difference to the integrated synchrotron emission along a line of sight.

It seems that the radial variation of the field used to obtain predicted temperatures in the plane for Fig. 5.13 is satisfactory for larger radii but fails to reproduce the high'observed' temperatures in the longitude range $20° \gtrsim l \gtrsim 330°$. This suggests that the variation becomes much steeper towards the centre of the Galaxy. In the normalization procedure we could have used say, $l = 0°$, $T_b = 370\,\mathrm{K}$ in an attempt to improve the fit of the predicted central longitudes but this would be to the detriment of the fit at mid-longitudes. It is apparent therefore that to obtain a more satisfactory fit overall to the 'observed' temperatures we will have to modify the form of the radial variation of the field. By experiment it was found that a new variation of the form:

$$H_{reg} = H_o(1 - \exp(-2R^2)) \left[\exp(-\left(\frac{R}{R_o}\right)^2) + \exp(-\left(\frac{R}{R_1}\right)^4)\right] \qquad (5.19)$$

possesses the properties required. This is to be compared with the old form of the radial variation:

$$H_{reg} = H_o \left(1 - \exp\left(\frac{-R^2}{4}\right)\right) \exp\left(-\left(\frac{R}{R_o}\right)^2\right) \qquad (5.20)$$

These two functions are plotted in Fig. 5.16 with H_o in both set so that $H_{reg\odot} = 3\,\mu\mathrm{G}$. Both functions have zero field at $R = 0$, but in Equation 5.19 the first term ensures that the peak is much closer to the centre than before. In Fig. 5.16 the peak in the modified function has moved in to $\sim 1.3\,\mathrm{kpc}$ from $\sim 4\,\mathrm{kpc}$. The new form has a much higher, sharper peak, the maximum value is $\sim 9.7\,\mu\mathrm{G}$ instead of the previous $\sim 4.8\,\mu\mathrm{G}$. The fall off of the field is very rapid at first due to the introduction in the second term of Equation 5.19 of an additional $\exp(-(R/R_1)^4)$. Beyond about 4.5 kpc the two distributions behave in the same way, each being dominated by $\exp(-(R/R_o)^2)$ in the second term of the expressions.

The new form of the field has introduced a third free parameter into the calculations of the synchrotron emission and a new method of normalizing the predictions has been adopted to determine all three, R_1, R_o and RATIO . First, the old form of $H_{reg}(R)$ (Equation 5.20) is used to normalize to $T_b = 34\,\mathrm{K}$ at $l = 180°$ and $T_b = 300\,\mathrm{K}$ at $l = 10°$ as before. This yields a value of R_o =13.2 kpc, which is virtually the same as that obtained in the previous section since the only difference is the removal of the elliptical symmetry in the form of H_{reg}. The next step is to replace Equation 5.20 with Equation 5.19 in the calculations and renormalize

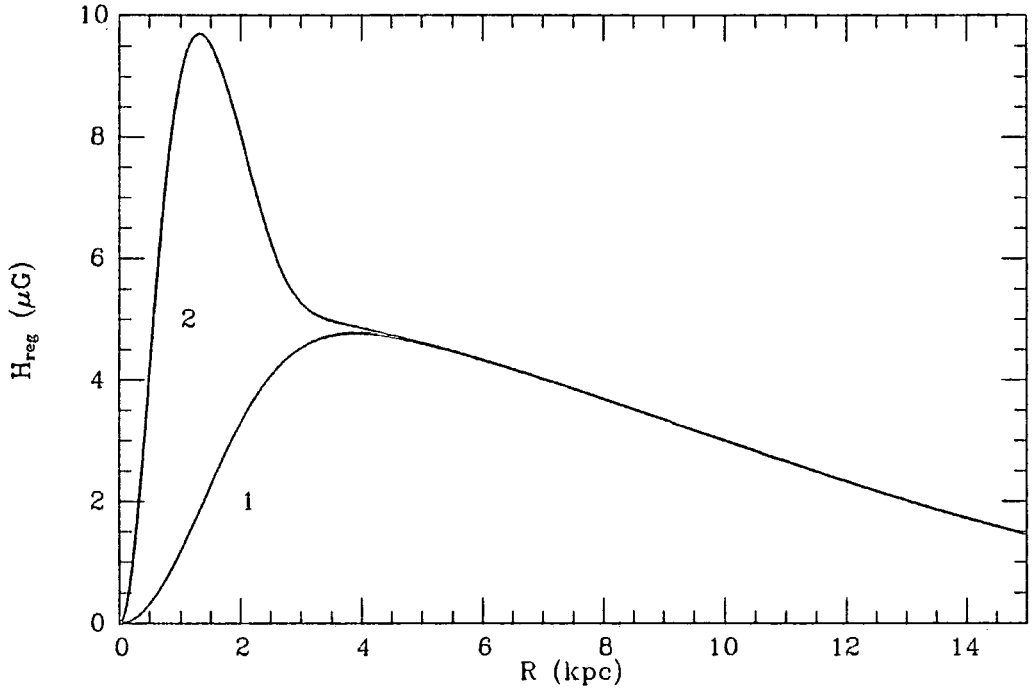

Figure 5.16: Radial variations of the magnitude of the regular component of the magnetic field, H_{reg}. (1) Used by Kearsey (1983) (Equation 5.20). (2) The modified form used in the present work (Equation 5.19). Both variations have been normalized so that $H_{reg\odot} = 3\,\mu$G.

having this time set R_o =13.2 kpc and determining the values of R_1 and RATIO which will produce $T_b = 34\,\mathrm{K}$ at $l = 180°$ & $T_b = 370\,\mathrm{K}$ at $l = 10°$. With everything else in the calculations of synchrotron brightness temperature being identical to that in the previous section and from which we predicted the plane profile in Fig. 5.13, the normalization values are R_o =13.2 kpc, R_1 =2.07 kpc and RATIO =0.60, hence $H_{reg}/H_{irreg} = 0.61$. The Galactic Plane profile which is obtained with our new form for H_{reg} is shown in Fig. 5.17 and it can be seen that there is a significant improvement in the fit of the predicted temperature to those observed over the central longitudes. The value of R_1 used in Fig. 5.16 is 2.25 rather than 2.07 kpc because we have anticipated the value obtained for our final model which has other changes introduced, described in succeeding sections, and which each alter the normalization values by a small amount.

It is important to note that the variation of H_{reg} we have used is not necessarily the true variation of the Galactic magnetic field with galactocentric radius. The synchrotron emissivity is approximately proportional to $N_o H^2$ (see previous sections) and in the model used in this work it was assumed that N_o, the value of N_e in the Galactic Plane (Equation 5.5), is independent of the galactocentric radius with all variations attributed to the magnetic field only. In fact this is probably not the case. For example, Bloemen *et al.* (1986) have deduced from a study of the distribution of diffuse Galactic γ-rays that the radial variation of CR electron density with galactocentric radius can be approximated by an exponential function of scale length 4–11 kpc for $R \geq 3\,\mathrm{kpc}$. An analysis of the γ-ray data from the COSB satellite by Bhat *et al.* (1986) revealed that there is an energy dependent radial gradient for cosmic-ray electrons. For electrons of energy $\sim 5\,\mathrm{GeV}$, which emit the majority of their energy at frequencies around 408 MHz, the CR intensity would fall off as $\sim \exp(-R/14\,\mathrm{kpc})$. Approximating our modified form of H_{reg} to $\exp(-R/12.2\,\mathrm{kpc})$ for $R \simeq 4$–12 kpc and using the result from Bhat *et al.* then the true scale length of the field would be $\sim 22\,\mathrm{kpc}$ which represents an extremely slow fall off of field strength with increasing galactocentric radius.

The usual assumption made when trying to determine the magnetic field strength from synchrotron emissivity without any knowledge of the electron flux density is that equipartition exists between the energy density of CRs and the magnetic field. If this were the case in the Galaxy then:

$$H_{eq}^2 \propto N_{eq} \tag{5.21}$$

(Sofue *et al.*, 1986), which would imply that the emissivity:

$$\epsilon \propto H_{eq}^4 \tag{5.22}$$

If we take the approximate exponential scale length of 12.2 kpc for H_{reg} in the region $R = 4$–12 kpc then $\epsilon \propto \exp(-R/6.1\mathrm{kpc})$ which implies that the scale lengths for the electron flux density and magnetic field, assuming equipartition is valid, are ~ 12 and 24 kpc respectively, neither of which are far removed from the corresponding 14 and 22 kpc derived above.

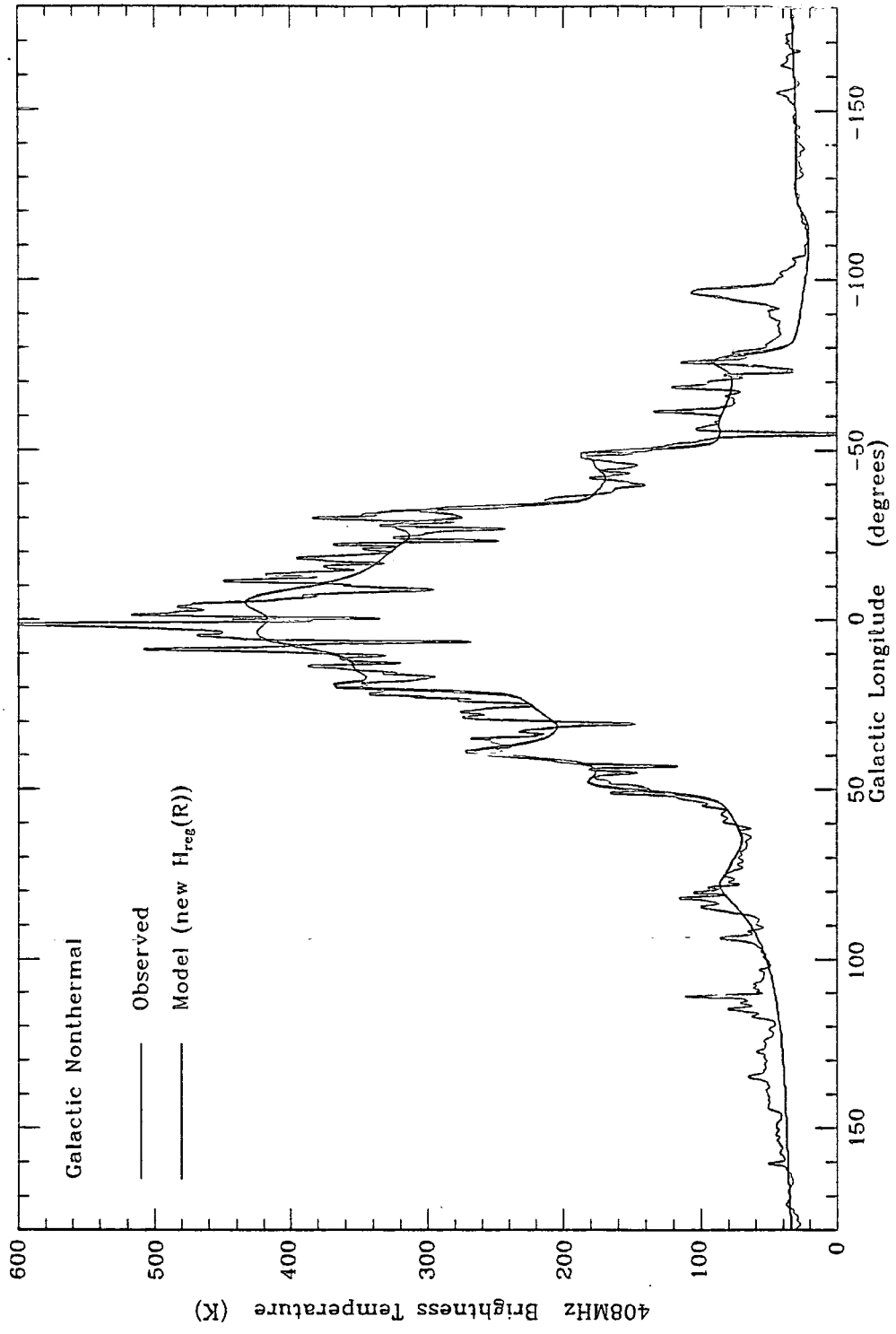

Figure 5.17: A comparison of predicted 408 MHz synchrotron emission along the Galactic Plane (thick solid line) with that 'observed' (thin solid line). The model used is identical to that responsible for the profile shown in Fig. 5.13 except that the form of $H_{reg}(R)$ is given in Equation 5.19, presented as curve (2) in Fig. 5.16.

Considering the distribution in Equation 5.19 in more detail then:

$$H_{eq} \propto \exp\left(\frac{-R^4}{X^4}\right) \quad X \simeq 2.68\,\mathrm{kpc}, \quad N_{eq} \propto \exp\left(\frac{-R^4}{Y^4}\right) \quad Y \simeq 2.25\,\mathrm{kpc}, \quad 1.5 \lesssim R \lesssim 3\,\mathrm{kpc}$$
$$H_{eq} \propto \exp\left(\frac{-R^2}{X^2}\right) \quad X \simeq 18.7\,\mathrm{kpc}, \quad N_{eq} \propto \exp\left(\frac{-R^2}{Y^2}\right) \quad Y \simeq 13.2\,\mathrm{kpc} \quad 15 \gtrsim R \gtrsim 3\,\mathrm{kpc}.$$

There is no obvious reason why equipartition should occur in galaxies but it is one way of making estimates about the field in the absence of measurements of the CR flux densities especially in external galaxies and values obtained are usually not too far removed from those obtained for our Galaxy by independent methods (*e.g.* M31, Beck, 1982).

5.6.3 Comparison with other field determinations

We can compare our empirically determined form of the variation of H_{reg} with R along the Galactic Plane with forms proposed or deduced by other authors. Fig. 5.18 shows a compilation of a few of these together with our own. The curve of White (1977) was predicted from turbulent dynamo theory modelling the Galactic disc as an oblate spheroid and adopting the rotation curve of Mihalas (1968). Two forms are shown from the work of Sánchez-Saavedra and Battaner (1987) who found steady-state solutions of magnetohydrodynamic equations which depended upon a free parameter, k, which is the ratio between the pressure at the centre of the Galaxy and a minimum critical pressure required to prevent imaginary solutions to the magnetic fields being obtained. The actual curves from which the distribution shown in Fig. 5.18 were obtained are for the uniform and random components and so we present the uniform component only, assuming that $H_{reg}/H_{irreg} \simeq 0.6$ and $H^2_{total} = H^2_{reg} + H^2_{irreg}$. By drawing together the results of the unfolding of the 408 MHz emission by Phillipps *et al.* (1981) (PKOHSI, see section 5.2) and the variation of the CR electron density with R deduced by Bloemen *et al.* (1986), Heiles (1987) also estimated that the magnetic field should fall off very slowly from the centre of the Galaxy:

$$H \propto \exp\left(\frac{-R}{20\mathrm{kpc}}\right) \quad R \gtrsim 3\,\mathrm{kpc} \tag{5.23}$$

The curve drawn in Fig. 5.18 which represents this has been normalized to $3\,\mu$G at $R_\odot$.

All of the distributions in Fig. 5.18 show a gentle fall off with R at larger radii with the exception perhaps of that of White (1977). The theoretical models of White and Sánchez-Saavedra and Battaner predict a very steep increase of regular field towards the Galactic Centre. These values towards the Galactic Centre seem unrealistically large and may be difficult to reconcile with the 'observed' synchrotron emission.

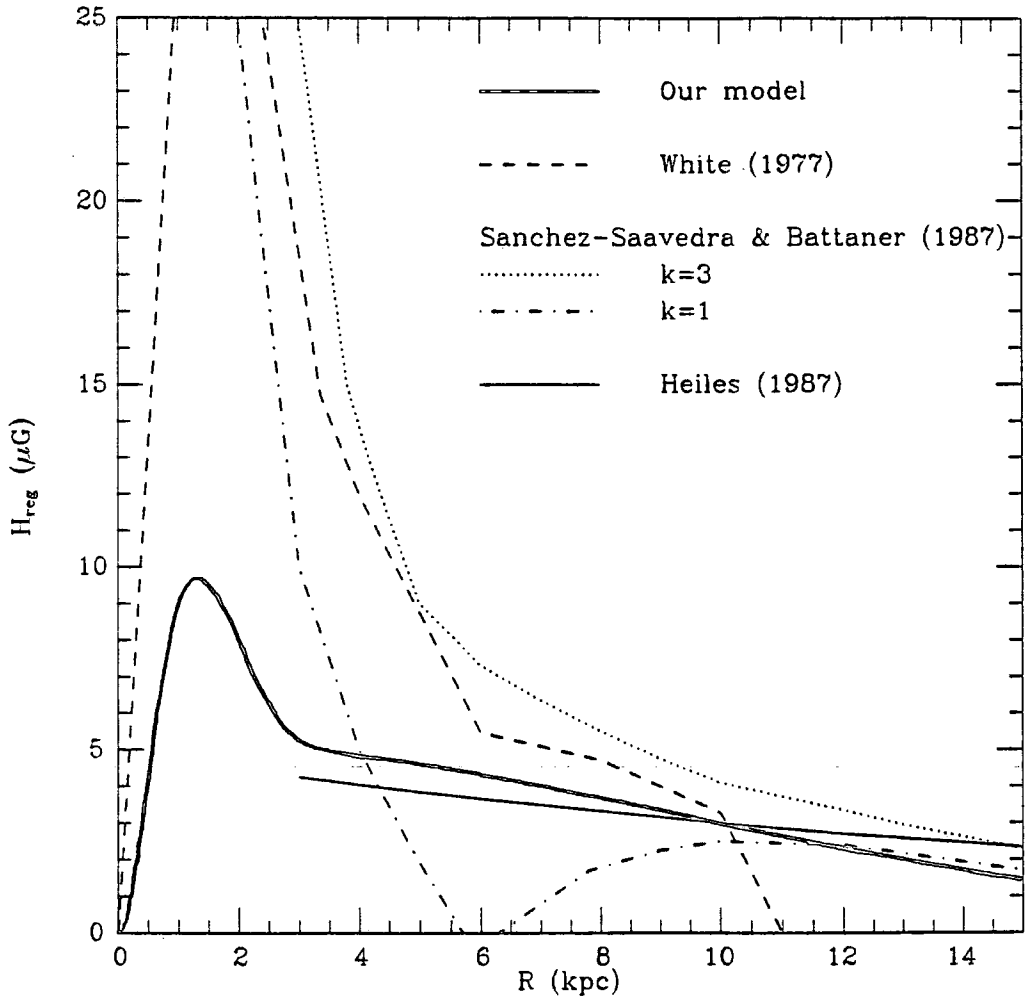

Figure 5.18: A comparison of our modified form of H_{reg} (Equation 5.19) with variations with R deduced by other authors either theoretically (White, 1977; Sánchez-Saavedra and Battaner, 1987) or from observations (Heiles, 1987). See text for further details of individual curves.

5.7 Variations with height above the plane

5.7.1 Models of the electron distribution

So far we have only been concerned with the emission along the Galactic Plane and in this section the 408 MHz brightness temperatures away from the plane will be considered. It has been assumed that the variation of H_{reg} is independent of z and all variations in that direction are included in the electron density and the demodulation of the compression factor, ρ_c, in a spiral arm. The assumed independence of H_{reg} with z need not be the case in reality, and it is quite likely that both the field and the electron flux density vary with height above the plane. Assigning all the z-dependence to a single variable facilitates calculations and is one extreme of the spectrum of possible combinations of the two.

In all, three different variations of electron flux density with height have been input into the model and assessed for their suitability:

1. The variation deduced by French (1977) which best fit observations at 150 MHz. This was discussed in Section 5.3 and the polynomials for $N_e(z/w(R))$ and variation of the scaling factor $w(R)$ were given in Equations 5.5 and 5.6. Fig. 5.3 is a representation of the electron density over the Galaxy.

2. The same form of N_e was used as above but $w(R)$ was assumed to be constant at 0.5. This was the final change made by Kearsey (1983) as we have mentioned in Section 5.3.

3. In Section 5.2 we described the work of Phillipps *et al.* (1981a, 1981b) (PKOHSI, PKOHSII). They unfolded the 408 MHz brightness temperatures and in PKOHSII deduced the variation of emissivity with height above the plane including the same compression demodulation above the spiral arms as is incorporated in the present model (see Section 5.3, Equation 5.12). This same form of the emissivity variation can be attributed to that of the electron flux density since we have assumed that H_{reg} does not vary with height above the plane.

In Fig. 5.19 the forms of the variation of N_e with z which are equivalent to the variations of $\epsilon(z)$, are shown for each of these three cases in an interarm region (*i.e.* $\rho_c = 1$). A summary of the polynomials used are as follows:

$$\text{(i).} \quad N_e\left(\tfrac{z}{w(R)}\right) = \begin{cases} 80\left(1 - 0.35528\left(\tfrac{z}{w(R)}\right) + \right. & \\ \left. 0.04733\left(\tfrac{z}{w(R)}\right)^2 - 0.002127\left(\tfrac{z}{w(R)}\right)^3\right) & \tfrac{z}{w(R)} \leq 10.85\,\text{kpc} \\ 0 & \tfrac{z}{w(R)} > 10.85\,\text{kpc} \end{cases}$$

where $$w(R) = 0.591 - 0.0652R + 0.0106R^2 \qquad (5.24)$$

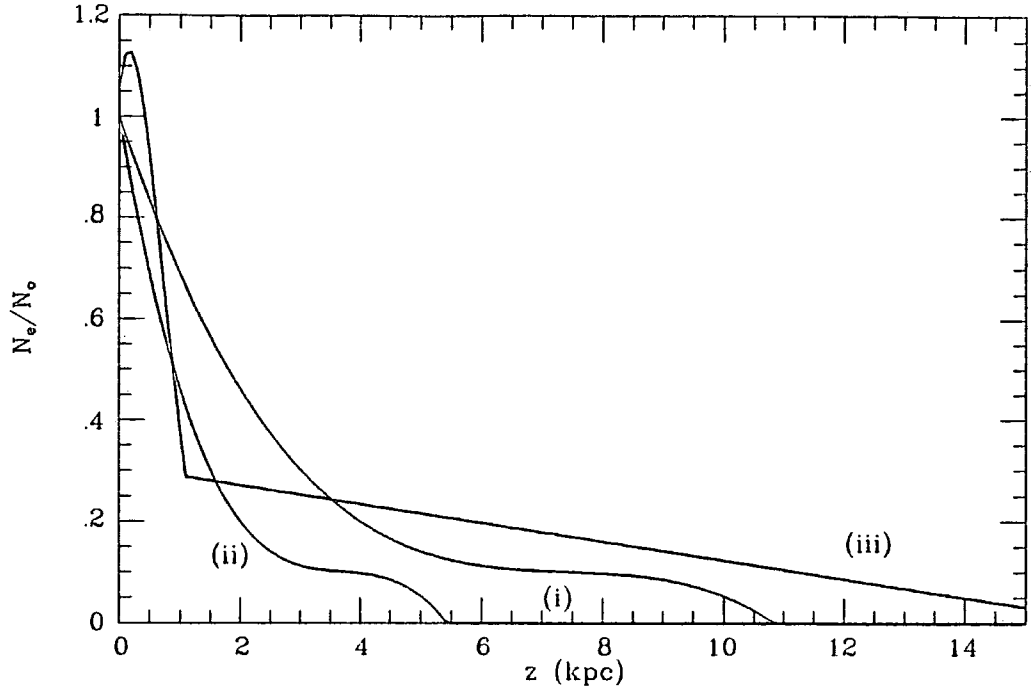

Figure 5.19: Illustration of the three variations of the electron flux density, or equivalently the emissivity, with height above the plane which we have assessed for suitability in modelling the 408 MHz synchrotron emission in the Galactic disc. Each curve represents the variation at the solar galactocentric radius and in a region where the gas is uncompressed. The curves (i), (ii) and (iii) are expressed mathematically in Equations 5.24, 5.25 and 5.26 respectively.

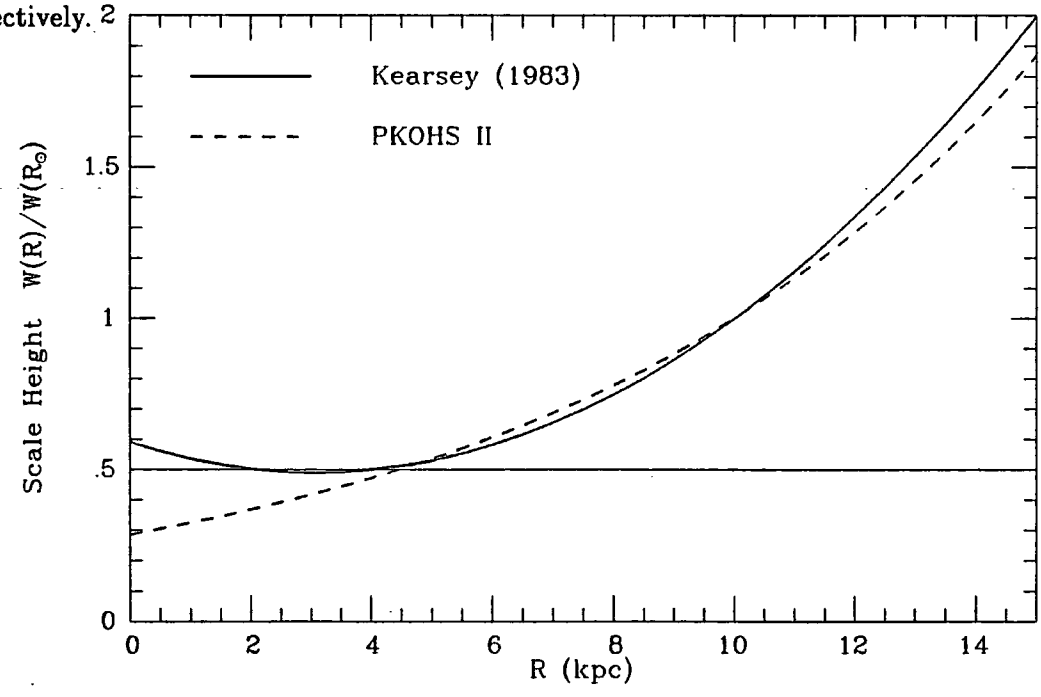

Figure 5.20: Variations of the scale factor of the electron distribution with galactocentric radius. The thick solid curve corresponds to the expression for $w(R)$ in Equation 5.24 (case (i)), a constant scale height of 0.5 kpc is used for electron distribution (ii) and the dashed line is the form assumed by PKOHSII (distribution (iii), Equation 5.26).

$$\text{(ii).} \qquad N_e\left(\tfrac{z}{0.5}\right) = \begin{cases} 80\left(1 - 0.35528\left(\tfrac{z}{0.5}\right) + \right. \\ \left. 0.04733\left(\tfrac{z}{0.5}\right)^2 - 0.002127\left(\tfrac{z}{0.5}\right)^3\right) & \tfrac{z}{0.5} \leq 10.85\,\text{kpc} \\ 0 & \tfrac{z}{0.5} > 10.85\,\text{kpc} \end{cases} \tag{5.25}$$

$$\text{(iii).} \quad N_e\left(\tfrac{z}{z_o}\right) = \begin{cases} 80\left(1.063 + 0.9344\left(\tfrac{z}{z_o}\right) - 3.551\left(\tfrac{z}{z_o}\right)^2 + \right. \\ 2.645\left(\tfrac{z}{z_o}\right)^3 - 0.8192\left(\tfrac{z}{z_o}\right)^4 + \\ \left. 0.1134\left(\tfrac{z}{z_o}\right)^5 - 0.00579\left(\tfrac{z}{z_o}\right)^6\right) & \tfrac{z}{z_o} \leq 1.1\,\text{kpc} \\ 80\left(0.30788 - 0.018436\left(\tfrac{z}{z_o}\right)\right) & 16.7 \geq \tfrac{z}{z_o} \geq 1.1\,\text{kpc} \\ 0 & \tfrac{z}{z_o} \geq 16.7\,\text{kpc} \end{cases} \tag{5.26}$$

where $$z_o = \exp\left(\tfrac{R-10}{8\text{kpc}}\right)$$

Curves in Fig. 5.19 represent these polynomials for the local solar neighbourhood *i.e.* z_o and $w(R) = 1$, and the functions are relative to the value along the Galactic Plane, *i.e.* N_e/N_o. The forms of $w(R)$ and z_o are both displayed in Fig. 5.20. As can be seen there is little difference between the two except close to the Galactic Centre and in fact we used $w(R)$ both for case (i) and (iii) when actually calculating the synchrotron emission. In addition, the boundary to the spherical halo over-rode any extension of the functions beyond a 15 kpc radius from the Galactic Centre.

For cases (i) and (ii) the fall-off is steady and fairly gradual which is a contrast to that of case (iii) which has a rapid fall-off from the plane out to about 1.1 kpc followed by a large halo whose emissivity decreases linearly and very slowly. The peak in the distribution is at $z = 0.15$ kpc rather than $z = 0$ but as PKOHSII pointed out this is introduced in the polynomial approximation to a fairly flat distribution in the true emissivity out to about 0.3 kpc.

All the functions in Fig. 5.19 are equal or very close to unity at $z = 0$ and so for any of the electron distributions the Galactic Plane profile will look like that in Fig. 5.17. In Fig. 5.21 a series of latitude profiles for $|b| \leq 10°$ are shown. For each longitude the 'observed' synchrotron emission is drawn together with the predicted profiles for each electron flux density variation. The modelled profiles are all symmetrical about the Galactic Plane and so cannot be expected to reproduce the effects of the warping in the outer Galaxy which causes a shift of the peak temperatures away from $b = 0°$ in the second and third quadrants. As pointed out by PKOHSII, at $l \simeq 30°$ and 330° the temperatures are enhanced by Loop I and so none of the predictions produce a particularly good fit in these directions. Discrete sources which are obvious in the 'observed' profiles are due to Tycho's SNR at $l = 120°$, Puppis A SNR at 260° and a radio galaxy at 310°.

All three cases separately produce a reasonable representation of the 'observed' profile except for a few longitudes *e.g.* $l = 30°$ and 330° where the observed emission is enhanced

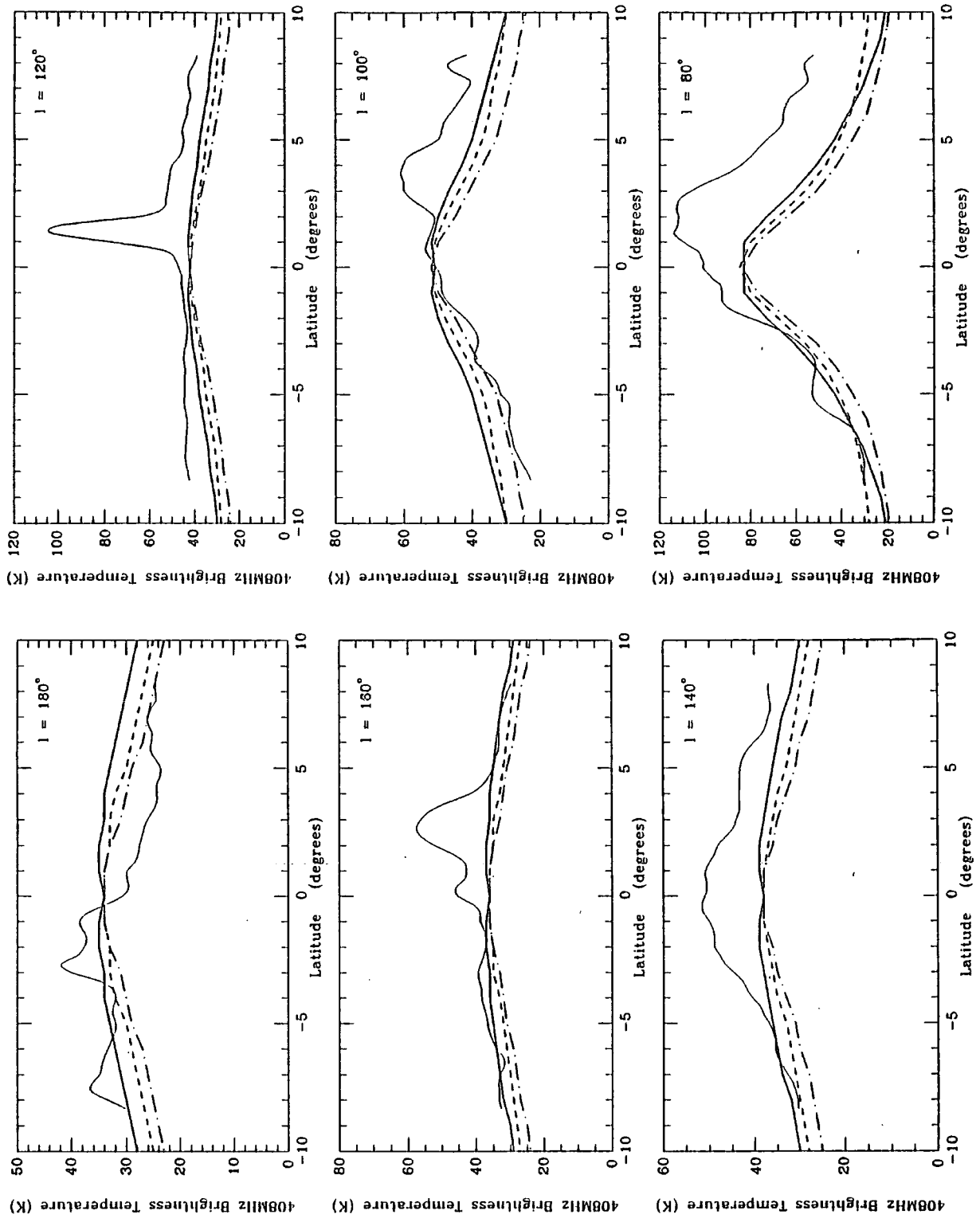

Figure 5.21: Latitude cuts across the Galactic Plane at regular intervals in longitude showing the 'observed' synchrotron emission at 408 MHz (thin, solid line) and the profile predicted by the model when using the electron distributions: (i) Equation 5.24 (dashed line), (ii) Equation 5.25 (dot-dashed line) and (iii) Equation 5.26 (thick, solid line). All parameters used in the model other than N_e are identical to that used to produce the profile along the plane shown in Fig 5.17. (Continued on next page.)

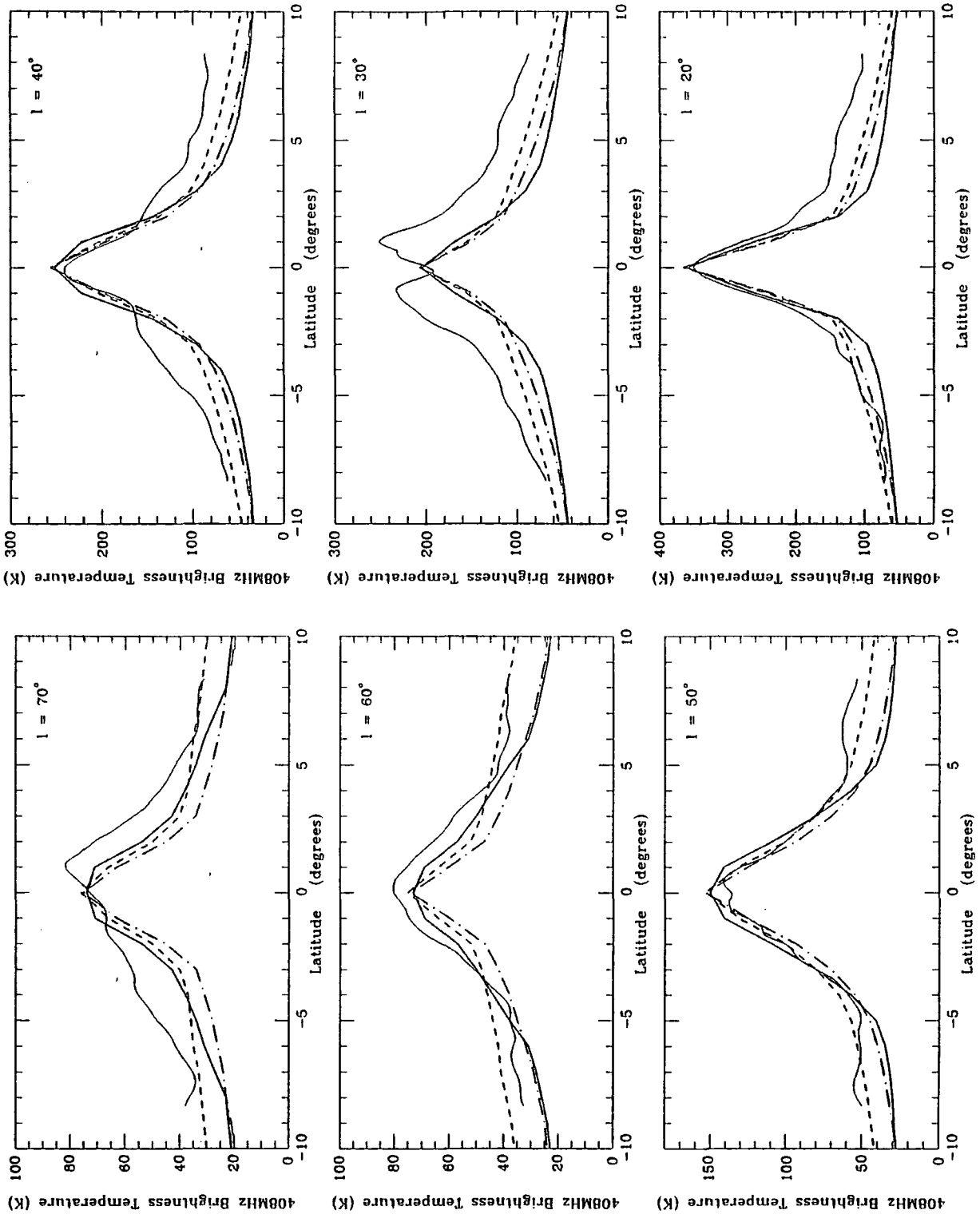

Figure 5.21: *contd.* (Continued on next page.)

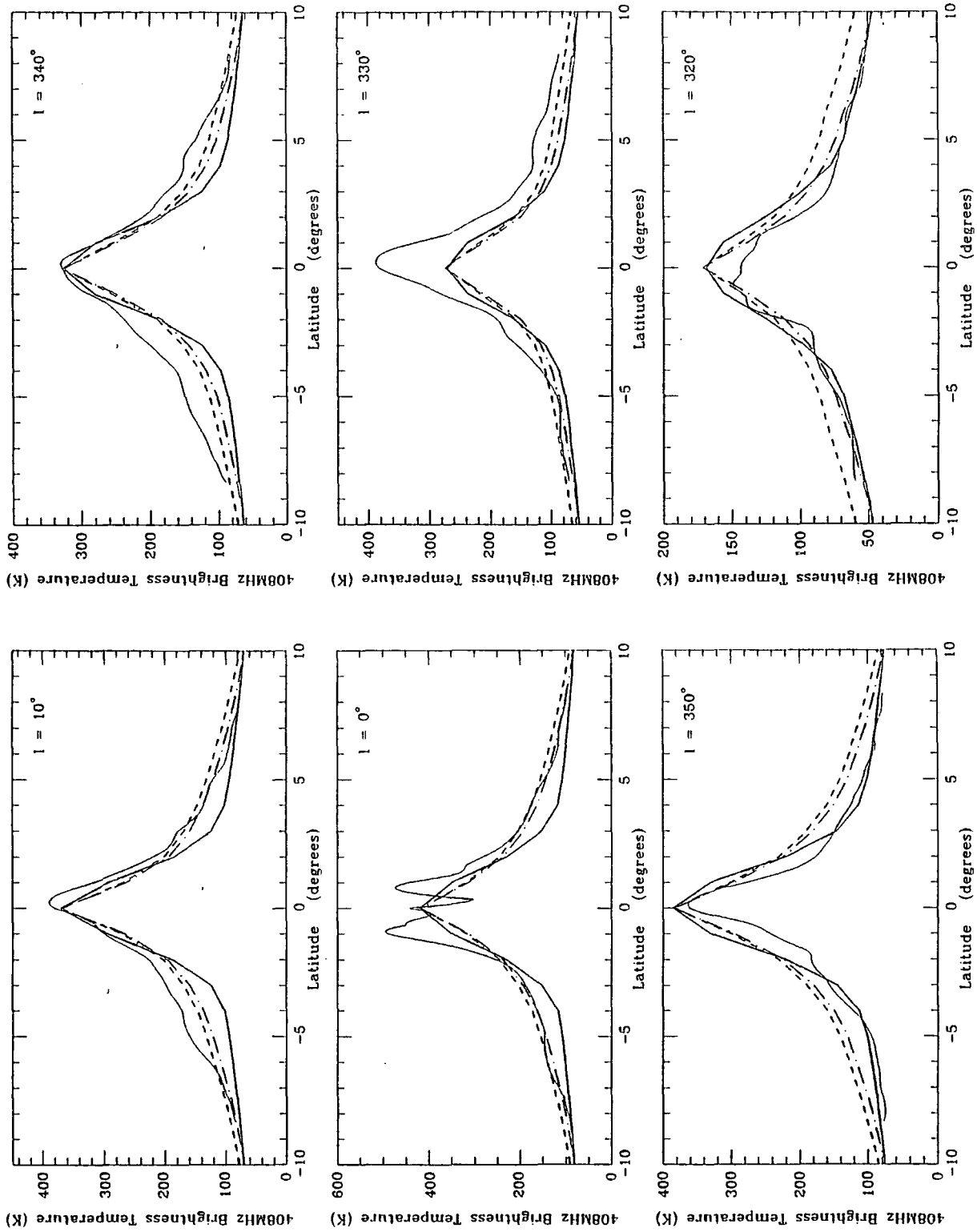

Figure 5.21: *contd.* (Continued on next page.)

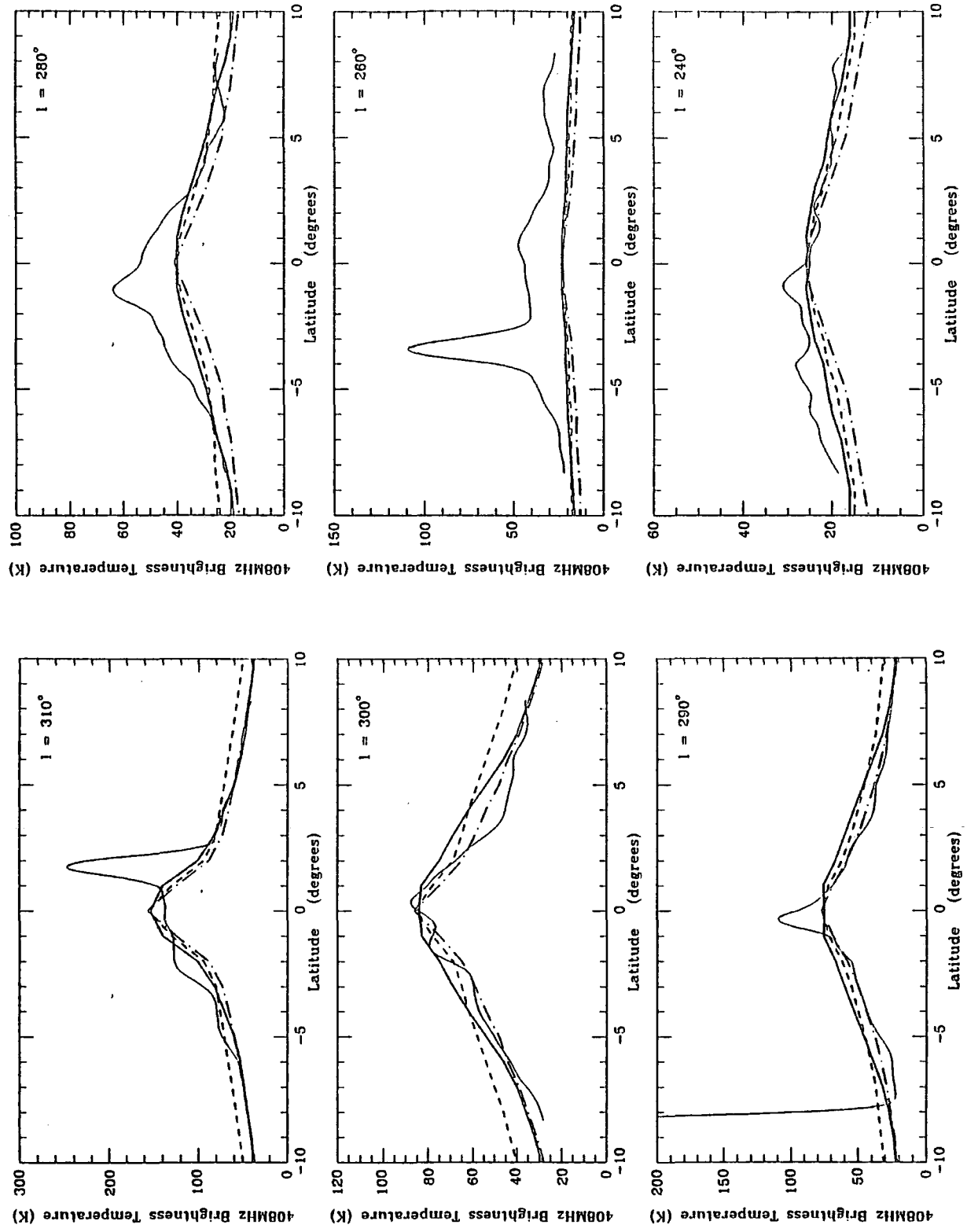

Figure 5.21: *contd.* (Continued on next page.)

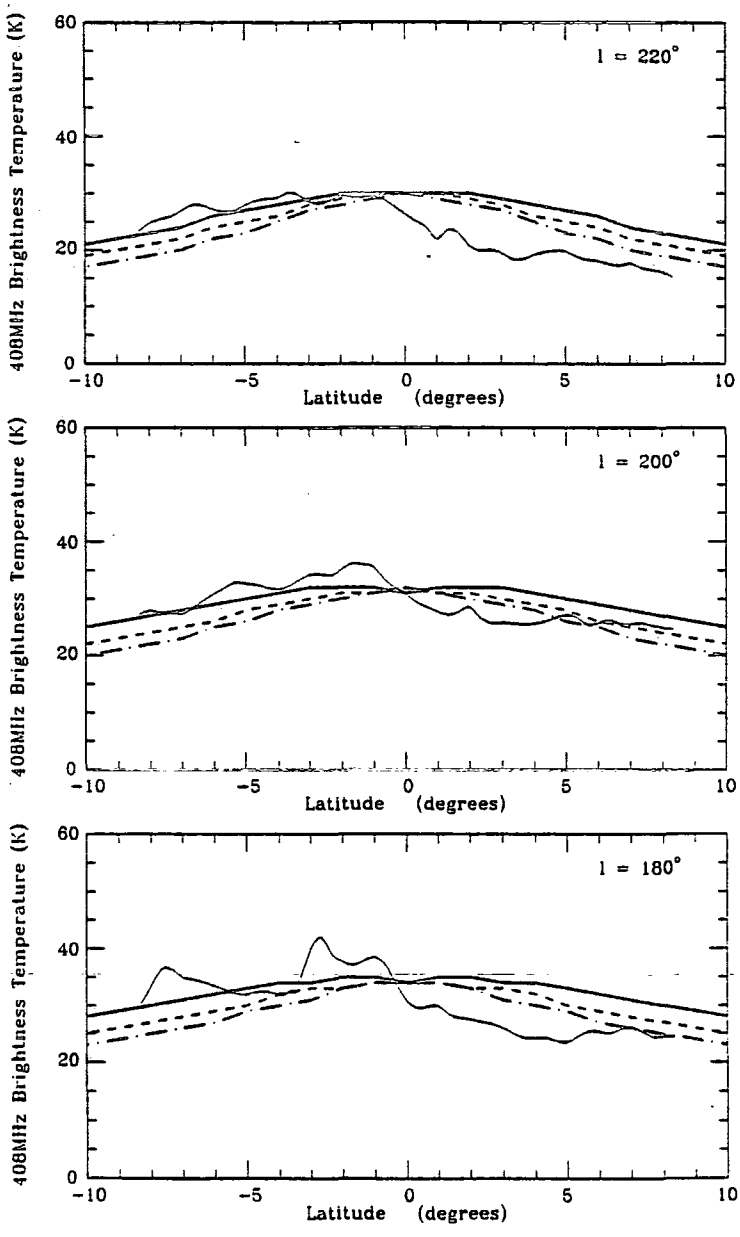

Figure 5.21: *contd.*

by contributions from Loop I and therefore the predictions fall short of the 'observed' brightness temperatures. It is difficult to assess which of the models produces the closest fit to the 'observations' overall as each case has its own strengths and weaknesses over different ranges of l and b. Case (i) is perhaps the worst fit overall since for many of the profiles the peak about the plane is too sharp and then the fall-off at higher latitudes too gradual. This behaviour is clearly seen at $l = 310°$. However at $l = 10°, 0°, 50°$ and for negative latitudes at $l = 20°$ and $80°$ the predictions fit the 'observations' quite well. These longitudes are all in the first quadrant. For case (ii) the predictions often fall away too rapidly from the Galactic Plane in the second and third quadrants which reflects the narrow scale factor $w = 0.5$ assumed over the whole Galaxy. Longitudes where the fit is quite good are in the inner Galaxy at $l = 290°$, $310°$, $320°$, $0°$, $10°$ and $50°$ and for negative latitudes at $l = 20°$ and $100°$. A general feature of case (iii) latitude cuts is the broader, flatter peak about the plane for $|b| \lesssim 2°$ which is most obvious for the inner two quadrants and is closest to the shape of the 'observed' profiles in this region. However, the initial fall-off over mid-latitudes is often too steep in the longitude range $70° \geq l \geq 330°$. The fit is good for $l = 240°$, $280°$, $310°$, $320°$ and $160°$ and for negative b at $l = 180°$, $200°$, $220°$ and $80°$. At $l = 50°$ the fit is good within $5°$ of the plane. The variation of the scale height of the electron flux density has been chosen to have roughly the same variation as that of the gas. The latitude profiles of case (iii) could perhaps be improved upon if it was assumed that in the inner Galaxy the scale height of N_e does not decrease so rapidly with decreasing R as the gaseous disc.

Another way of comparing the merits of the three electron distributions is to see how near each prediction is to the 'observed' pole temperature. PKOHSII observed that the pole temperatures at 408 MHz was 14.2 K and 12.5 K at the north and south Galactic poles respectively having subtracted a 6 K extragalactic background. Noting however that in an area of $\sim 2°$ diameter about the north pole the temperature seems to be slightly higher than the general level of temperatures in that region they decided to compare the model predictions with the lower temperature of 12.5 K at the south Galactic pole. Predictions of the pole temperature require a knowledge of the perpendicular distances to the nearest arms on either side of the Sun along the Sun–Galactic Centre line. These distances have been estimated from the spiral arm pattern of Fig. 5.12. The arm outward from the Galactic Centre was estimated to be 0.6 kpc from the Sun and the arm inward towards the Galactic Centre to be 1.2 kpc from the Sun. The constant, RATIO is also required for which we assumed a value 0.692 for all three cases of the variation of N_e (again anticipating the results of a final normalization which will be discussed in Section 5.8). The values of the pole temperature obtained are:

Case	Pole temperature (K)
(i)	11.7
(ii)	5.9
(iii)	12.3
observed	12.5

Case (ii), having the much smaller scale height, predicts a very low pole temperature. Case (i) with twice the scale height of (i) is much closer to the observed value. However

the inclusion of the large extended halo in case (iii) seems to produce the pole temperature nearest to that observed. Of course, a change in the assumed value of RATIO would alter all the predicted pole temperatures but they would still be in the same order of increasing temperature (ii), (i), then (iii). The agreement of case (iii) with the observed pole temperatures is not unexpected since PKOHSII chose the behaviour of the halo to reproduce observations at the poles at 408 MHz. In the unfolding of the 408 MHz brightness temperatures into a thick and thin disc of emission by Beuermann *et al.* (1985) (see Section 5.2) they obtained a predicted pole temperature of only 8.6 K. However they argued that the value of the emissivity at the Sun should really be larger than they found because the Sun is situated in a local arm feature not incorporated into the unfolding. Adopting the best value of the emissivity in the solar neighbourhood from independent estimates they found that their two disc model now predicted a pole temperature very close to that observed. The equivalent width of the thick disc was 3.6 kpc but this was assuming that the spiral structure was present at all heights above the plane within the disc. If, as was supposed by PKOHSII and in the present work, that demodulation of the compression in an arm occurs with increasing z, then the width of the disc of Beuermann *et al.* would have to be greater in order to produce the correct pole temperature.

5.7.2 Observation and theory of galactic halos

Other observational evidence for a thick disc or halo in the Galaxy comes from comparisons of the rotation measures of extragalactic radio sources and pulsars (see *e.g.* Sofue *et al.*, 1986). The rotation measure for pulsars is smaller than that for extragalactic sources which indicates the presence of Galactic magnetic fields beyond ~ 500 pc from the plane which is about the limit of the extent of the pulsar z-distribution. Radio halos and thick discs have been observed in several edge-on spiral galaxies. One such galaxy which has received a fair amount of attention is NGC891. A multi-frequency study of this galaxy by Allen *et al.* (1978) revealed that there are two distinct components, a thin disc and a thicker disc and emission was detected at 21 cm as far as 6 kpc above the plane. Equipartition between the magnetic field and cosmic rays (see Section 5.6) imply that the field decreases from 10 to 5 μG between 0 and 4 kpc from the plane of the Galaxy with the particle density falling to a quarter of its value in the plane. Klein *et al.* (1984) studied five galaxies at 10.7 GHz and found that they had full widths of between 2.15 and 4.83 kpc. Because of the lack of linear polarization measurements of the extended emission away from the plane in edge-on galaxies and our own Galaxy, the detailed configuration of the magnetic field in galactic halos has not yet been very well determined.

Theoretically, a halo magnetic field is required in dynamo models of bisymmetric spiral field configurations in order to maintain the disc field in a steady state. A primordial origin of magnetic field necessarily implies that there will be a poloidal field component in a galaxy which could be concentrated in the central region by accretion (Sofue, 1987, Fujimoto, 1987). In addition to the magnetic field and CRs, the Galactic halo contains a hot, diffuse, gaseous component and observational evidence suggests that this also extends to several kpc above the Galactic Plane (Savage, 1987). All three components will naturally

influence each other and may or may not be in an equilibrium state. Mechanisms other than dynamo processes which may contribute to the formation and structure of a galactic halo include Parker instabilities (*e.g.* Mouschovias, 1975) and supernova driven winds (Klein, 1989).

Of the three forms of N_e investigated in this section, the third case taken from PKOHSII seems to be the most suitable. Advantages over the other two are its plateau of emissivity about the Galactic Plane and its two components in the form of a thin disc and a halo. The fit of the latitude cuts seems to be reasonably good for a larger range of longitudes than the other two forms of N_e. Therefore we will use case (iii) for further investigations which are described in subsequent sections of this chapter.

5.8 Spiral arm widths

Roberts and Yuan (1970) incorporated the magnetic field into density wave theory and studied the effect it had on the dynamics of the gas. They found that the addition of a magnetic field was compatible with the two armed spiral shock pattern for the gas developed by Roberts (1969). Roberts and Yuan investigated the effect of the magnetic field which lies parallel to the direction of the spiral arms on the variation of gas compression across a shock and found that the shock was not as strong as models with no magnetic field. In modelling the synchrotron emission at 150MHz, French (1977) approximated the variation of this gas compression across a shock by an exponential function:

$$\rho_c = \left(5.9 f(z) \exp\left(\frac{-13.7a}{A}\right) + 1.0\right) \tag{5.27}$$

where $f(z)$ is the demodulation of this compression with height above the plane given in Equation 5.12 of Section 5.3. Here a is the distance from the peak compression of the nearest inner arm and A is the distance between arms.

In Kearsey's later models the gas compression was altered to a smoother gaussian function since he considered the peaks produced in the synchrotron temperature distribution to be too spiked. Thus the assumed form of ρ_c was changed to:

$$\begin{aligned} \rho_c &= C_R\, f(z) \exp(-18a^2) + 1.0 \\ C_R &= \begin{cases} 2.8 & R \leq 10\,\mathrm{kpc} \\ 0.57(15 - R) & 15 \geq R \geq 10\,\mathrm{kpc} \end{cases} \end{aligned} \tag{5.28}$$

where a is the distance of the nearest arm, inner or outer. The maximum compression is now 3.8:1 instead of 6.9:1 as in the density wave model, and $\sigma = \frac{1}{6}$ kpc. Kearsey pointed out that this second form of the gas compression across an arm may be more suitable if the particles in the shock were gas clouds rather than individual atoms as was assumed in the earlier versions of density wave theory including that by Roberts and Yuan (1970).

In this section we will investigate this idea further and try to see whether Kearsey's altered form for the compression is reasonable in the light of more recent theoretical work on the dynamics of the interstellar medium. We turn to the work of Roberts and Hausman

(1984) who modelled the ISM in spiral galaxies. We have already mentioned this paper in Section 5.5. Briefly, N-body simulations of a system of 'cloud' particles orbiting about the Galactic Centre in a spirally perturbed gravitational potential were performed. The clouds experienced dissipative collisions and velocity boosting from expanding SNRs both of which triggered off star-formation. The results of the modelling showed that galactic shocks formed with clouds accumulating in spiral arms. In all models the global distributions appeared to be largely independent of the collisional mean free path of the clouds and except for cases dominated by sequential star-formation, a steady state was reached lasting at least 10^9 years. The width of cloud density enhancements across an arm were typically in the range 800–1100 pc. The variation of number density of clouds with spiral phase at a galactocentric radius of 8 kpc is reproduced from Roberts and Hausman (1984) in Fig. 5.22. This particular variant is from a model which lays equal emphasis on the collision and SNR velocity boosting mechanisms for star formation, the collisional mean free path is 200 pc and the number of cloud particles in the simulation was 10 000. The time elapsed is 600 Myr after the beginning of the simulation by which time a steady state has been reached. This profile is typical of all models and is fairly symmetrical about 200° phase. We assume that the width, in phase, of the arm is the number of degrees between the first points either side of the peak where the density is equal to the average cloud density and take this to be equivalent to 1 kpc in distance. Next, a gaussian function set on a unit d.c. level is fitted to the profile. The gaussian function has a peak value of 2.5, implying that the maximum compression is 3.5:1, and $\sigma = 0.2$ kpc. Therefore, ρ_c is assumed to have the form:

$$\begin{aligned} \rho_c = & \quad C_R\, f(z) \exp(-12.5a^2) + 1.0 \\ C_R = & \begin{cases} 2.5 & R < 10\,\text{kpc} \\ (15 - R)0.5 & 15 \geq R \geq 10\,\text{kpc} \end{cases} \end{aligned} \tag{5.29}$$

and is shown superimposed upon the profile of Roberts and Hausman (1984) in Fig. 5.22. The density wave theory variation of ρ_c, the variation used by Kearsey and that derived here from Roberts and Hausman are all shown together in Fig. 5.23. We have assumed that $A = 1.7$ kpc in Equation 5.27 for the purposes of this diagram. The two gaussian variations differ only in that the one derived here is slightly broader and has a slightly lower peak value.

The new expression for ρ_c was incorporated into the calculations of synchrotron emission and Fig. 5.24 shows the resulting Galactic Plane profile obtained. There is little difference between this profile and that shown in Fig. 5.17 except that the peaks are slightly lower and smoother, for example, those at $l \simeq 315°(-45°)$ and 20°. Likewise there is little difference between the latitude cuts in Fig. 5.21 (case (iii)) and those with the new ρ_c shown in Fig. 5.25 except for slightly lower peak values in some of the cuts. With all other aspects of the model being the same as that used for Fig. 5.17, the new values of R_o, R_1 and RATIO found in the normalization are 13.2 kpc, 2.25 kpc and 0.692 respectively, which implies $H_{reg}/H_{irreg} = 0.66$ when $\rho_c = 1$.

The model which predicts the brightness temperatures along the plane shown in Fig. 5.24 and the latitude cuts in Fig. 5.25 will be regarded as our final and best representation of

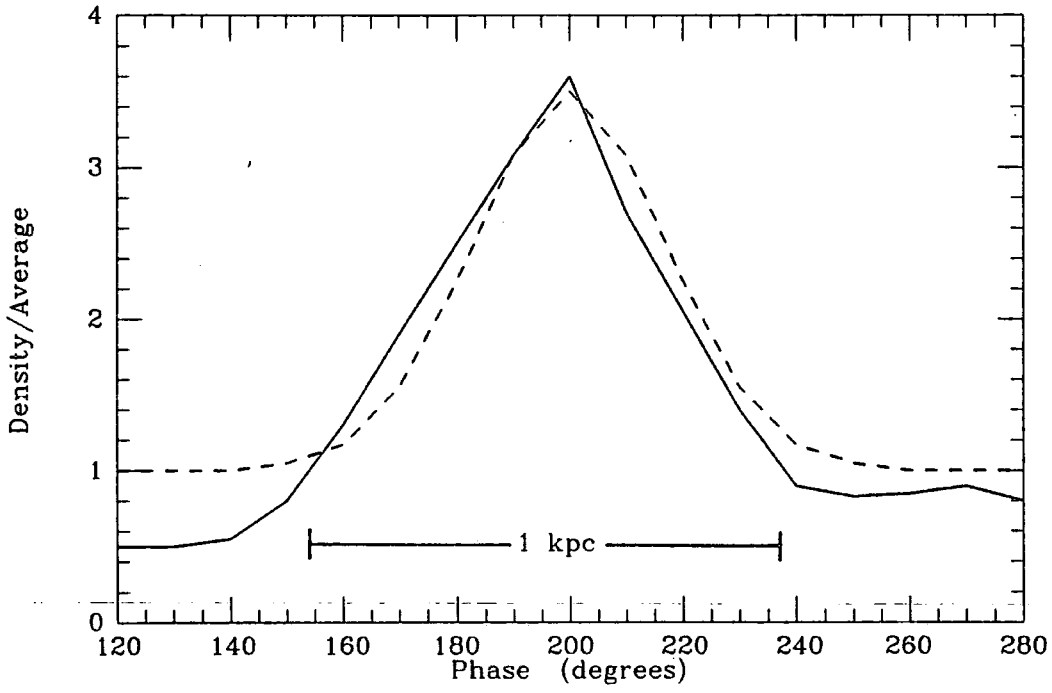

Figure 5.22: The solid line shows a typical gas cloud density variation with phase across a spiral arm at 8 kpc from the Galactic Centre obtained at the end of a N-body simulation by Roberts and Hausman (1984) of a system of 'cloud' particles orbiting the Galactic Centre in a spirally perturbed gravitational potential. The density of clouds is expressed relative to the average and marked underneath the curve is the full width of the arm amounting to a linear distance of 1 kpc. The dashed line is a gaussian fit to the simulated variation and has $\sigma = 0.2$ kpc.

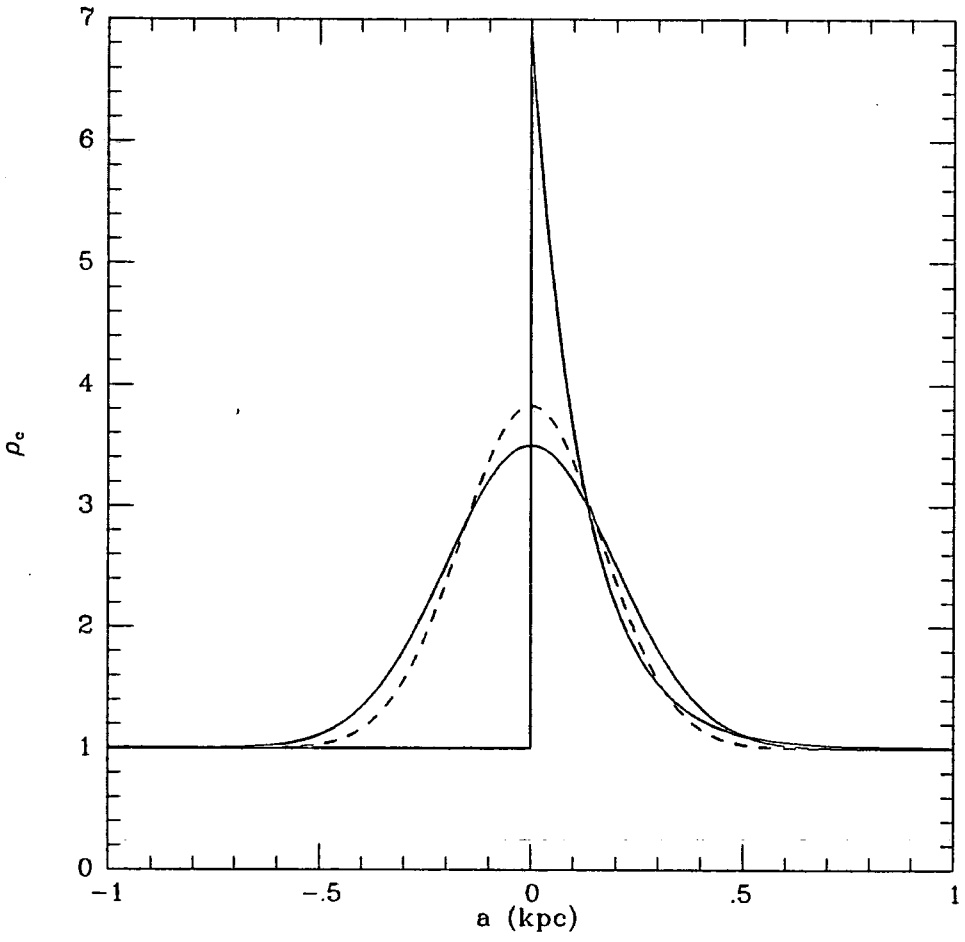

Figure 5.23: Variation of gas compression factor, ρ_c, across a spiral arm against distance from the maximum compression. The spiked distribution is that predicted by density wave theory and a represents the perpendicular distance to the nearest arm inwards to the Galactic Centre. The maximum compression factor is 6.9:1. The narrower gaussian distribution (dashed line) is that adopted by Kearsey (1983) having $\sigma = \frac{1}{6}$ kpc and maximum compression 3.8:1. The broader gaussian (solid line) is the fit to the typical cloud density variation across an arm generated in N-body simulations by Roberts and Hausman (1984), has $\sigma = \frac{1}{5}$ kpc and maximum compression 3.5:1.

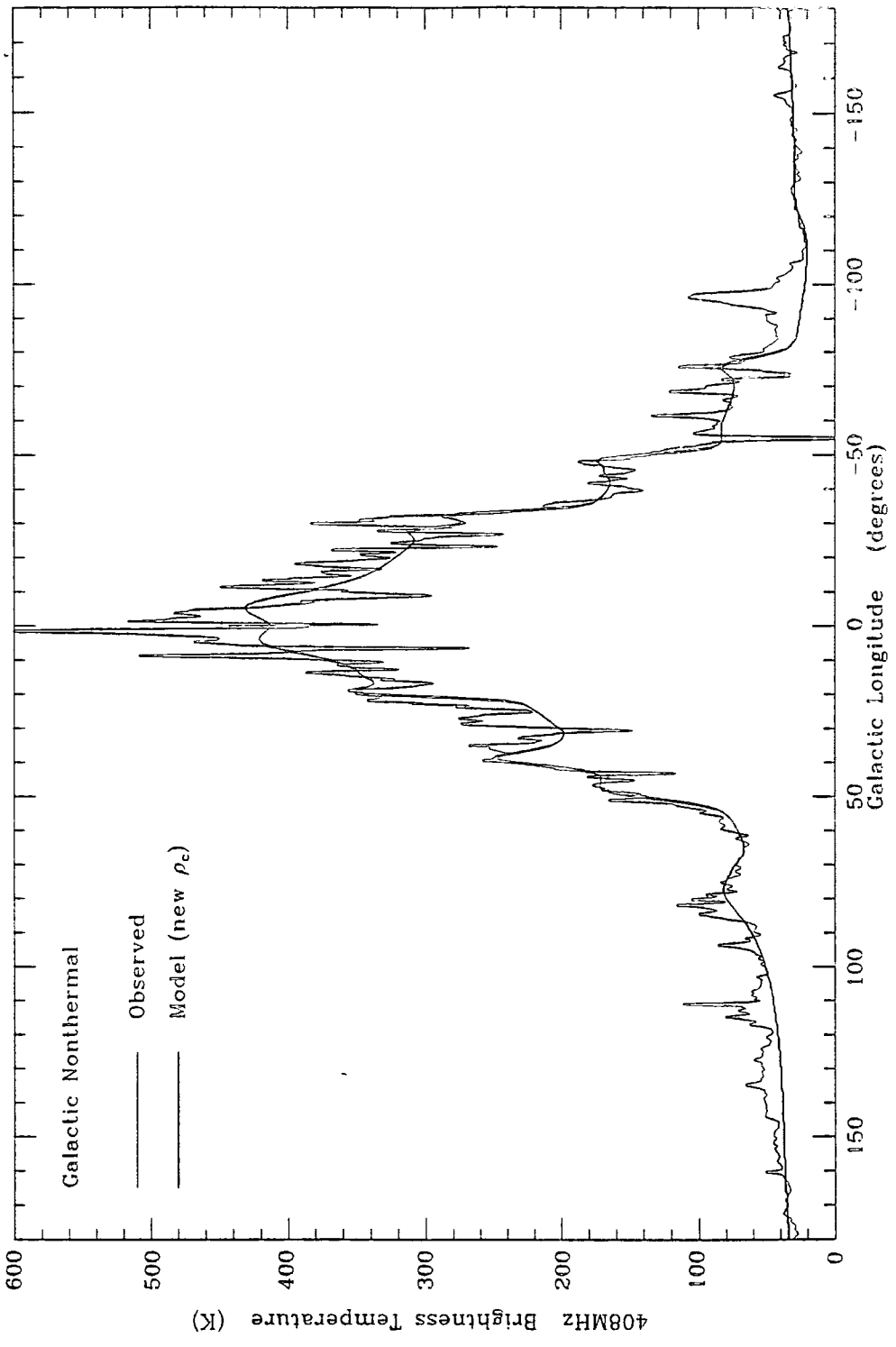

Figure 5.24: A comparison of predicted 408 MHz synchrotron emission along the Galactic Plane (thick, solid line) with that 'observed' (thin, solid line). The model used differs from that used to produce the profile in Fig. 5.17 in the assumed emissivity variation with height above the plane and variation of gas compression across a spiral arm, neither of which have made very significant changes to the to the predicted profile. The model used to predict this Galactic Plane profile is our final and best representation of the 'observed' emission.

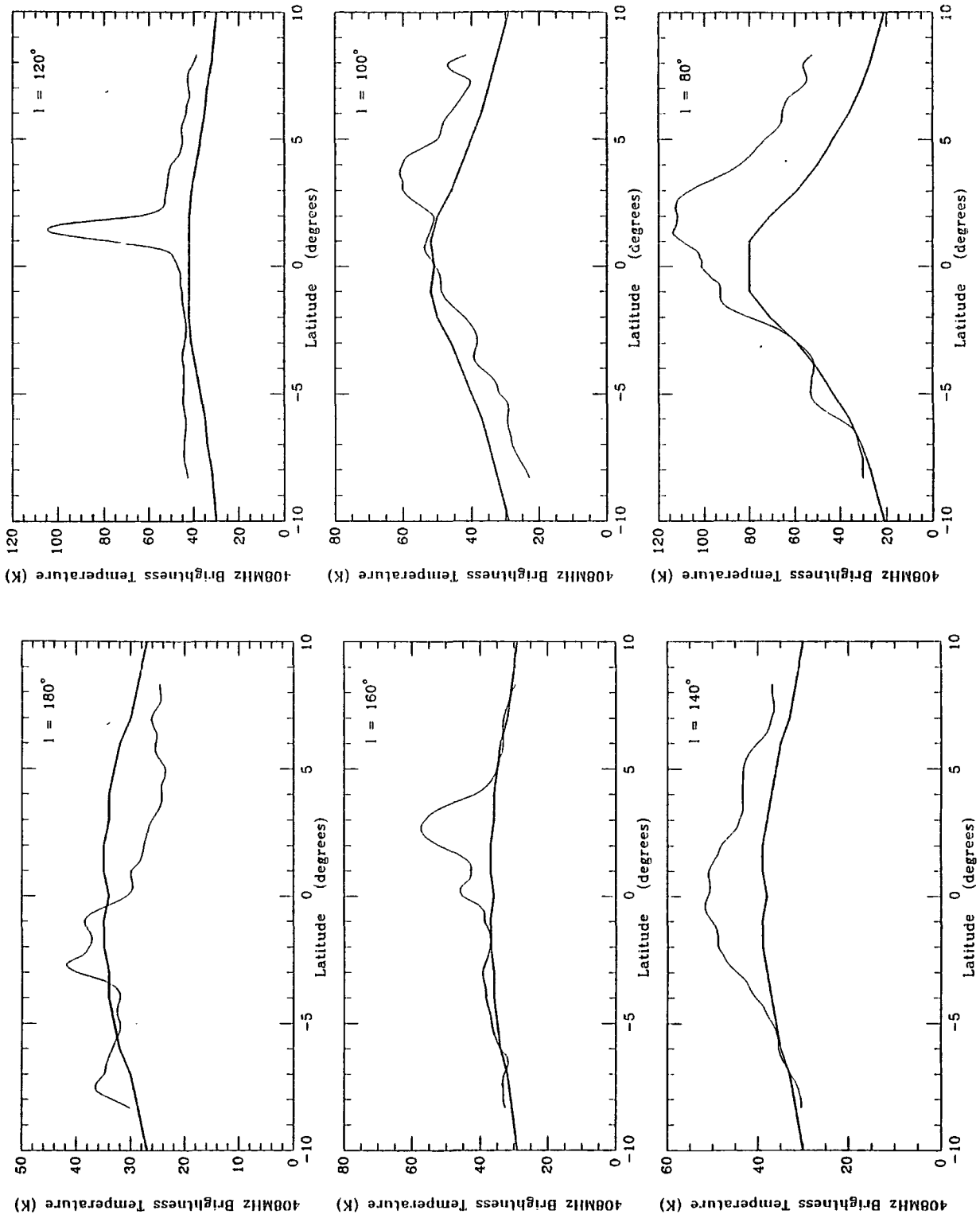

Figure 5.25: Latitude cuts across the Galactic Plane at regular intervals in longitude showing the 'observed' synchrotron emission at 408 MHz (thin line) and that predicted by our final model (thick line).

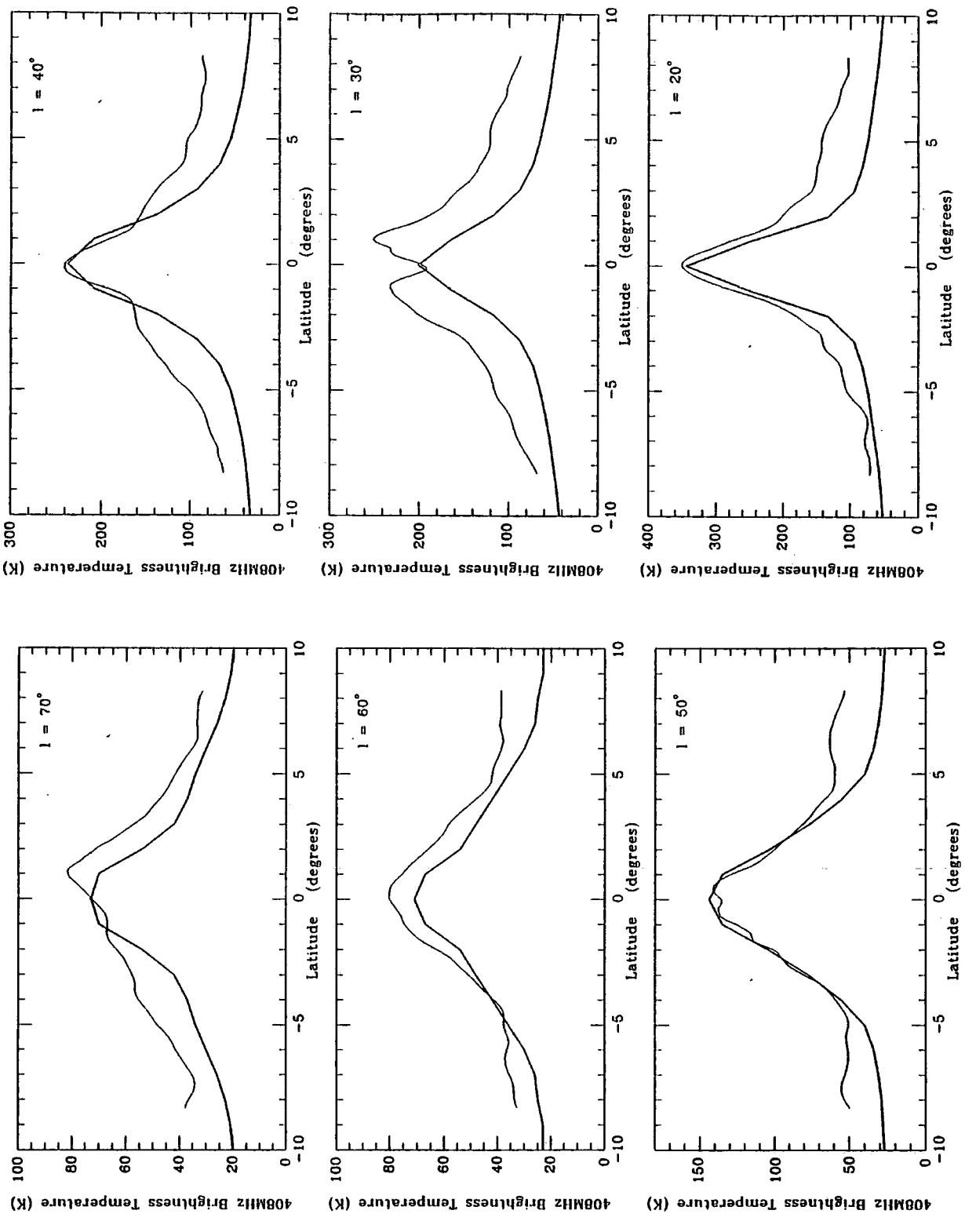

Figure 5.25: *contd.* (Continued on next page.)

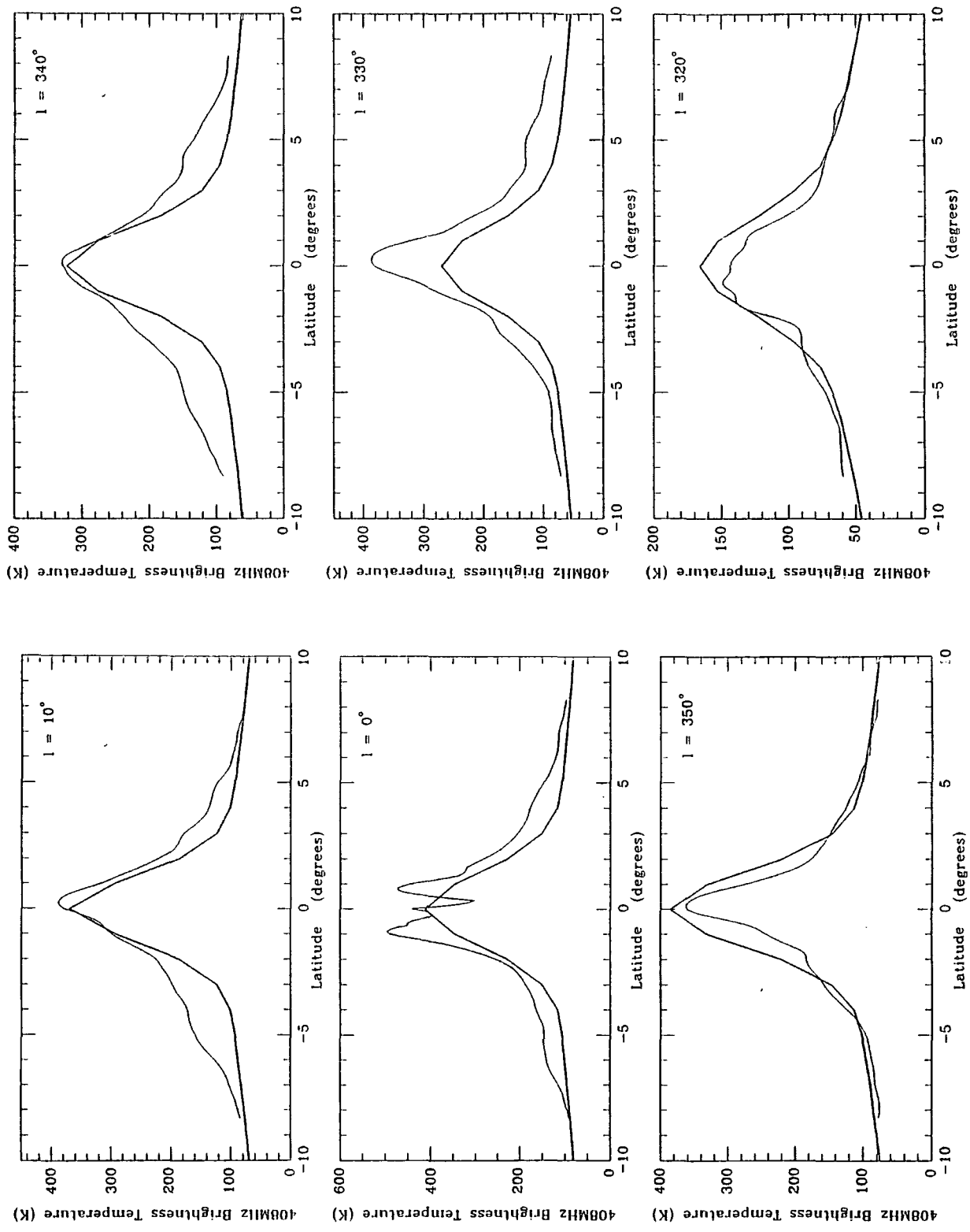

Figure 5.25: *contd.* (Continued on next page.)

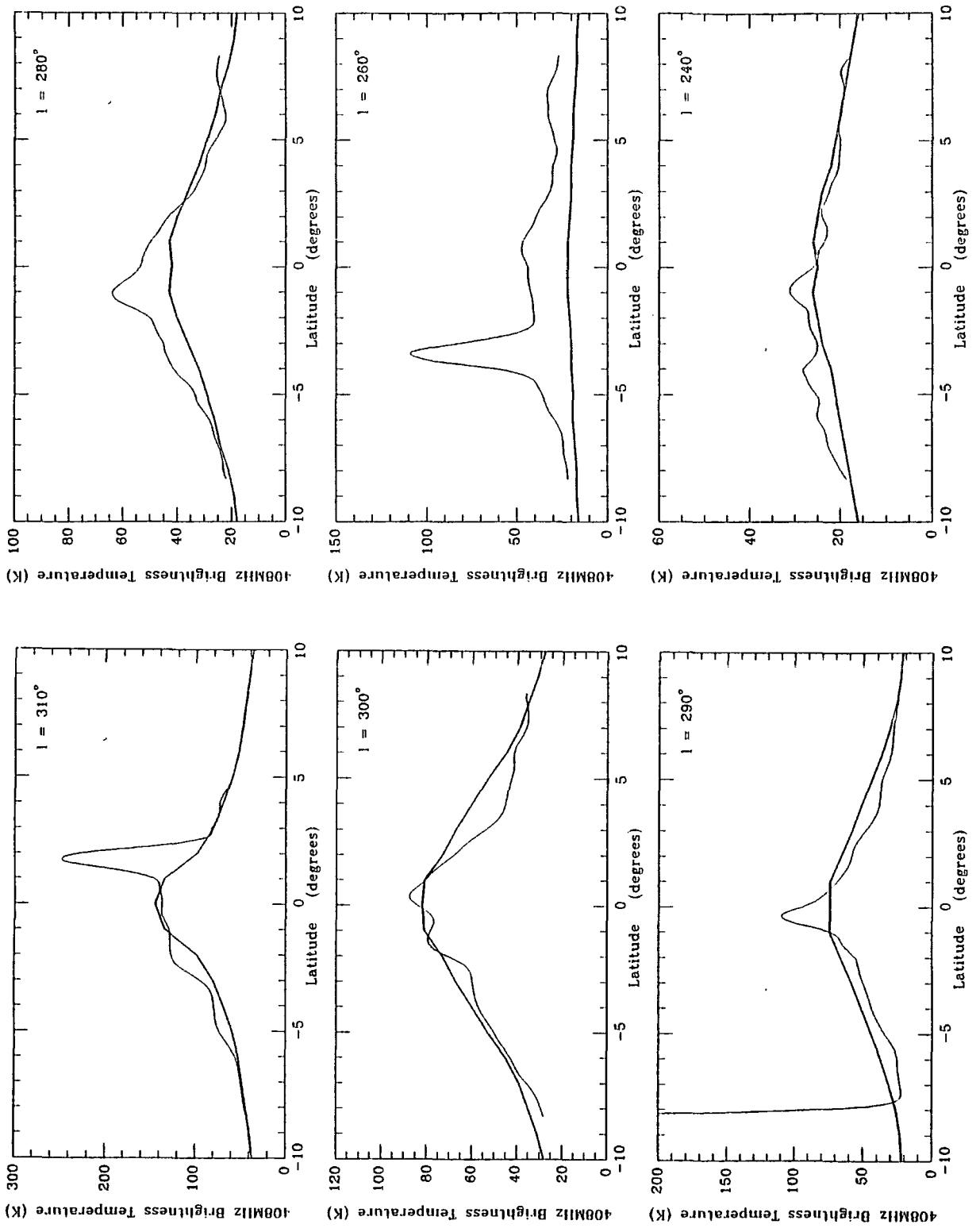

Figure 5.25: *contd.* (Continued on next page.)

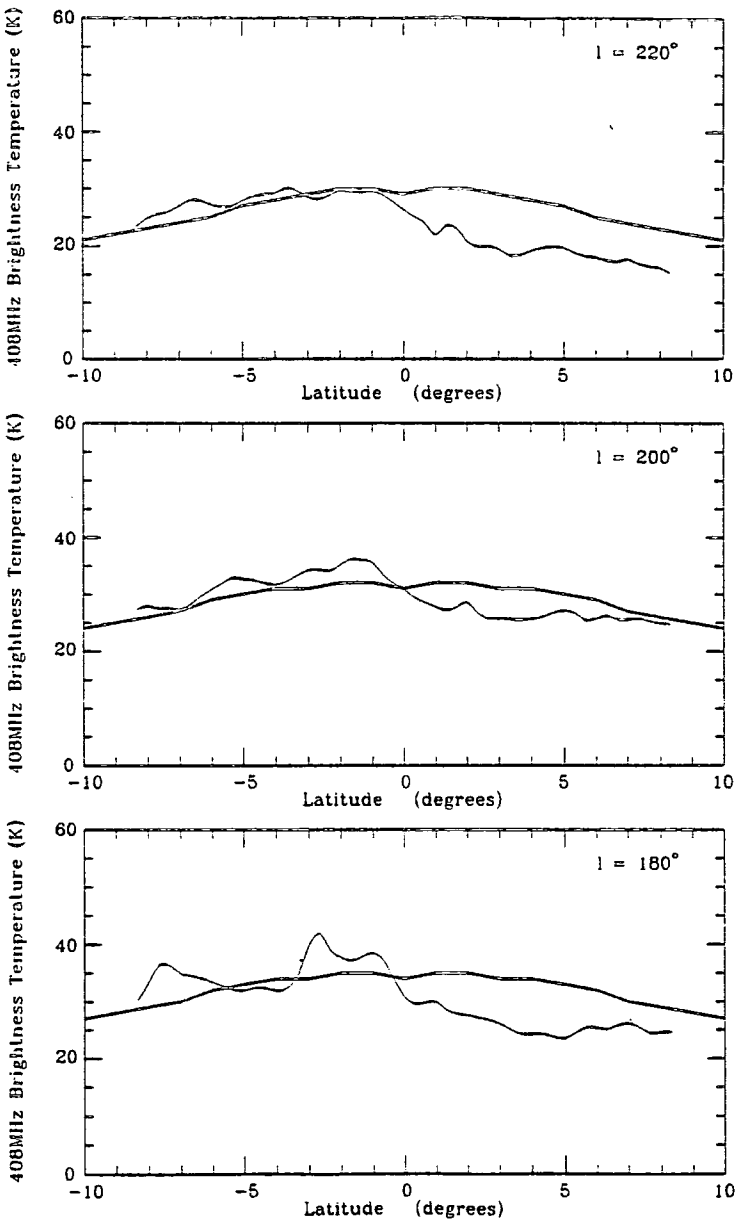

Figure 5.25: *contd.*

the 'observed' emission. As we have mentioned before this model is not unique in that combinations of different values or variations of the parameters involved could produce very similar brightness temperatures. Obviously more improvements could be made to this model and a few suggestions for doing this will be discussed in the final section of this chapter. Table 5.2 is a summary of the properties of our final model and Fig. 5.26 shows contour maps of the predicted synchrotron emission along the plane for $|b| \leq 10°$ together with the 'observed' synchrotron emission for $|b| \leq 8.33°$ for comparison. Any alterations to the model made in the remaining sections of this chapter are purely exploratory and will not be incorporated into the final model.

5.9 The local magnetic field

Throughout the modelling of the synchrotron brightness temperatures at 408 MHz we have assumed that the uniform component of the local magnetic field has a magnitude of $3\,\mu$G. The distance to the nearest spiral arm, the local Orion arm, is about 0.6 kpc measured from the diagram in Fig. 5.12. This implies that there is negligible compression of the gas and hence the magnetic field in the solar neighbourhood (see Figs. 5.22 and 5.23). Therefore, using the value of RATIO deduced from the normalization (see Table 5.2) we can infer that for a solar neighbourhood regular magnetic field strength of $3\,\mu$G, the irregular field strength is $4.5\,\mu$G. The value of $3\,\mu$G adopted for the regular component was the value derived by PKOHSI in the unfolding along the Galactic Plane and assuming that the field has roughly equally strong regular and irregular magnetic field components.

Most other determinations of the magnitude of the field have been made using rotation measures (RMs), mainly of pulsars. Manchester (1972) was the first to use RMs for this purpose and from a small sample of 19 pulsars deduced the local uniform component of the magnetic field to be $3.5 \pm 0.5\mu$G. Analysis of a larger sample of 38 pulsars in 1974 and including a $\cos b$ weighting to the RMs led Manchester to revise this value down to $2.2 \pm 0.4\mu$G. Thomson and Nelson (1980) used 48 pulsars all within 3 kpc of the Sun and analysed RMs by three methods each with a different degree of sophistication. A straightforward, least squares fit implied that the magnetic field strength was $1.5 \pm 0.2\mu$G. However, the authors regarded this as unrealistic and tried to improve the analysis first by taking into account the z-variation of the uniform field which yielded a value of $2.4 \pm 0.4\mu$G. By incorporating field reversals in the local solar neighbourhood as well, a value of $3.5 \pm 0.5\mu$G was obtained. They also estimated the irregular field strength to be between 4 and $14\,\mu$G. In a review of the subject, Heiles (1987) pointed out that the most simple case considered by Thomson and Nelson (1980) gave a uniform magnetic field strength of the same order as the analyses by Manchester and Taylor (1977) and Inoue and Tabara (1981) ($\sim 1.6\mu$G) done on a smaller sample of pulsars with maximum distance only 2 kpc from the Sun. Lyne and Smith (1989) have used the RMs and dispersion measures (DMs) of pulsars in the second and third quadrants or less than 1 kpc inside the solar circle to deduce that the local regular magnetic field strength is between 2–3 μG and directed towards $l \simeq 90°$. The pulsars used by Lyne and Smith are part of a larger set of 185, some of which are much further inside the solar circle and the analysis of the RMs and DMs of these more distant

Quantity	Equation/Description/Value	Eqn.	Sectn.
Dimensions of Galaxy	disk: radius 15 kpc thickness 1 kpc halo: radius 15 kpc (spherical) spiral arm pattern – see Fig. 5.12		5.3 5.5
Brightness temperature	$T_b(\nu) = 6.168 \times 10^4 \nu^{-2.8} \int_0 \underbrace{N_e(s)\,[\rho_c(s) H_{reg}(s) \sin\theta]^{1.8}}_{\text{regular}} +$ $\underbrace{0.6861 N_e \left[\frac{\rho_c H_{reg}}{F}\right]^{1.8}}_{\text{irregular}} Y(s)\, ds$ T_b(K), ν(MHz), s(kpc), N_e(m^{-2}s^{-1}sr^{-1}GeV^{-1}), H_{reg}(μG)	5.9	5.3
Irregular field realignment in arms	$Y(s) = 1 - 0.477 \left(\frac{\rho_c^2 - 1}{\rho_c^2}\right) \cos^2\theta$	5.10	5.3
Gas compression factor across an arm	$\rho_c = CR\, f(z) \exp(-12.5 a^2) + 1$ $CR = \begin{cases} 2.5 & R \le 10\,\text{kpc} \\ (15 - R)0.5 & 15 \ge R \ge 10\,\text{kpc} \end{cases}$	5.29	5.8
Compression demodulation with z	$f(z) = \begin{cases} 1 + 0.7715z - 17.0z^2 + 22.914z^3 & z \le 0.5\,\text{kpc} \\ 0 & z > 0.5\,\text{kpc} \end{cases}$	5.12	5.3
Flux of electrons Spectral index: Energy Frequency	Flux $= N_e(s) E^{-\gamma}\, dE$ $N_{e\odot} = 80\,\text{m}^{-2}\text{s}^{-1}\text{sr}^{-1}\text{GeV}^{-1}$ $\gamma = 2.6$ $\alpha = (\gamma + 3)/2 = 2.8$	5.2	5.1 5.3 5.3
Electron flux density	$N_e(\frac{z}{z_o}) = 80 \times \begin{cases} 1.063 + 0.9344(\frac{z}{z_o}) - 3.551(\frac{z}{z_o})^2 + 2.645(\frac{z}{z_o})^3 - 0.8192(\frac{z}{z_o})^4 + 0.1134(\frac{z}{z_o})^5 - 0.00579(\frac{z}{z_o})^6 & \frac{z}{z_o} \le 1.1 \\ 0.30788 - 0.018436(\frac{z}{z_o}) & 1.1 \le \frac{z}{z_o} \le 16.7 \\ 0 & \frac{z}{z_o} \ge 16.7 \end{cases}$ $z_o = 0.591 - 0.0652R + 0.0106R^2$	5.26 5.24	5.7 5.7
Regular field	$H_{reg}(R) = H_o(1 - \exp(-2R^2))(\exp - \left(\frac{R}{R_o}\right)^2 + \exp - \left(\frac{R}{R_1}\right)^4)$ $H_{reg\odot} = 3\,\mu\text{G}$	5.19	5.6 5.9
Normalization parameter	scale lengths: R_o =13.2 kpc R_1 =2.25 kpc RATIO =0.692 $\Rightarrow F = \frac{H_{reg}}{H_{irreg}} = (0.6861\text{RATIO})^{1/1.8} = 0.66$ $H_o = 5.33\,\mu\text{G}$		5.6 5.8
Pole temperature	12.3 K		5.7

Table 5.2: Summary of details of final model for predicting synchrotron emission of the Galaxy at 408 MHz

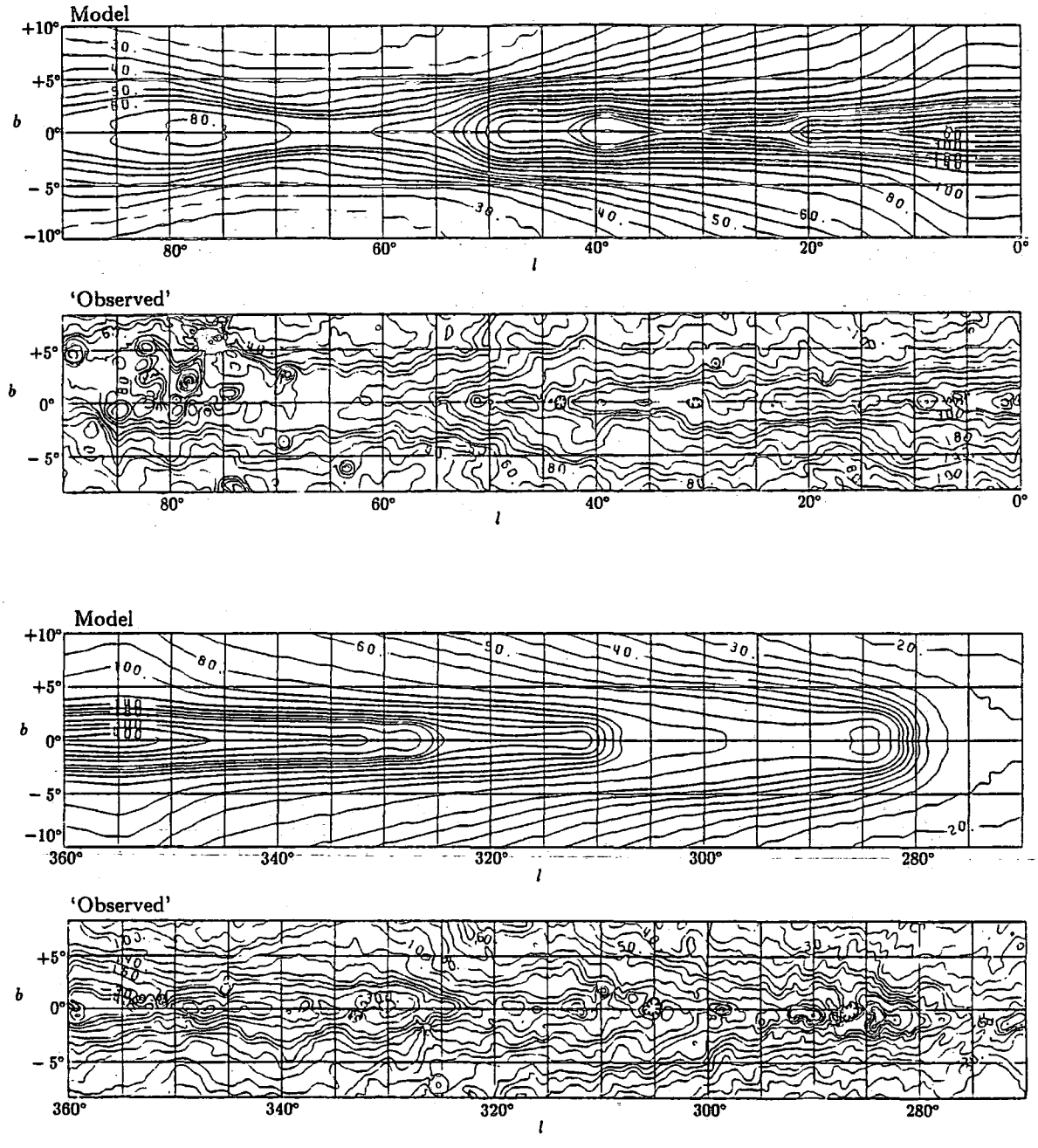

Figure 5.26: Contour maps of the synchrotron emission at 408 MHz along the Galactic Plane for $|b| \leq 10°$ predicted by our final model. (See Table 5.2 for a summary of the model parameters). For comparison similar contour maps for $|b| \leq 8\frac{1}{3}°$ of the 'observed' synchrotron emission at 408 MHz are shown also. Contour levels for all maps: from 10 to 60 K in steps of 5 K, from 60 to 100 K in steps of 10 K, from 100 to 200 K in steps of 20 K, from 200 to 400 K in steps of 50 K and then in steps of 100 K. (Continued on next page.)

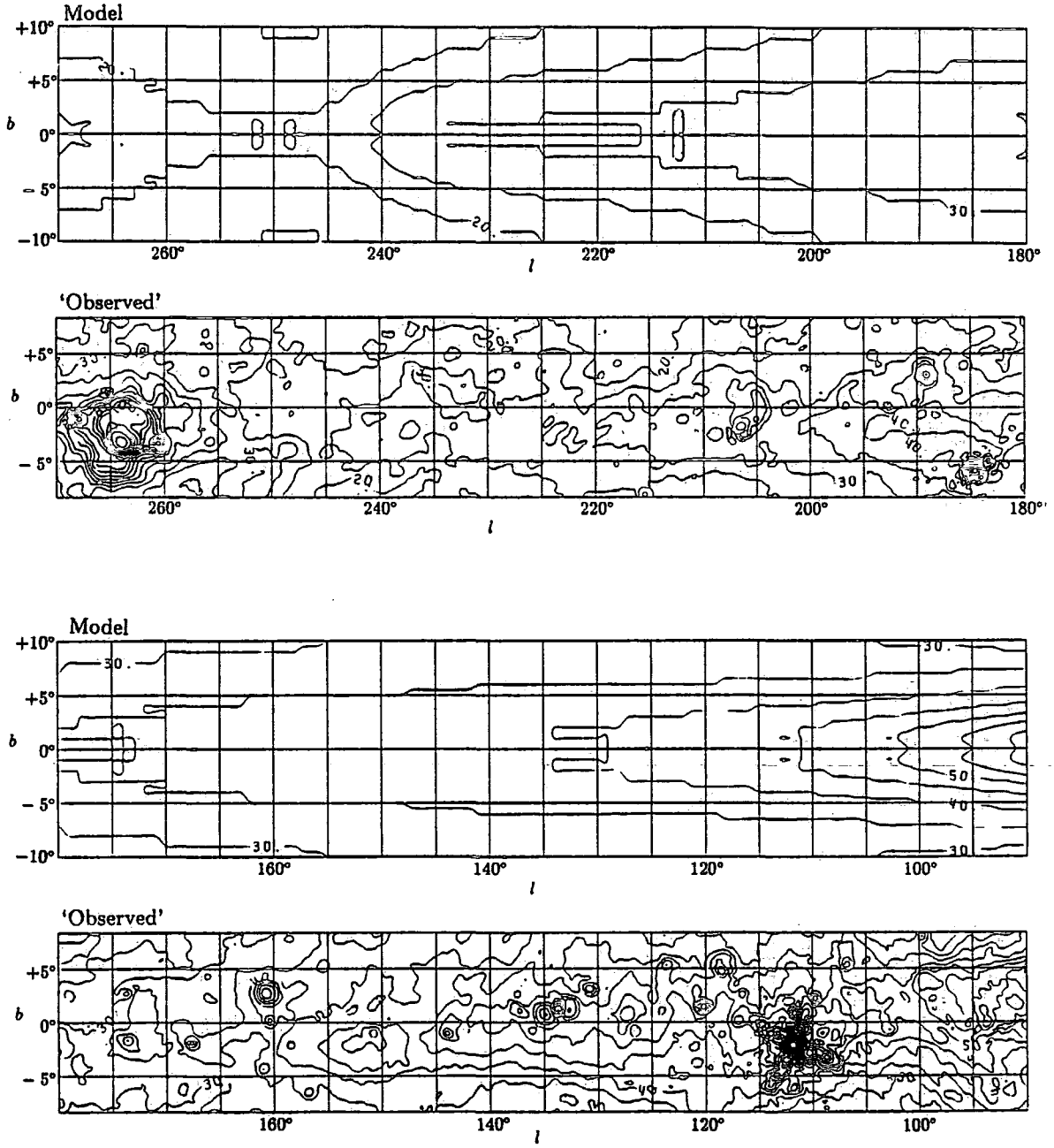

Figure 5.26: *contd.*

pulsars suggests that a field reversal occurs and that the field strength is larger at smaller galactocentric radii. Variations of RMs between pulsars which are very close to each other show that irregular field structure is on the scale of $\sim 100\,\mathrm{pc}$.

Despite these very recent results supporting our assumption of a value above $2\,\mu\mathrm{G}$, in this section we shall suppose that the local uniform field strength is really as low as $1.6\,\mu\mathrm{G}$ and investigate what effect this has on the predicted Galactic synchrotron brightness temperatures. A change in the assumed $H_{reg\,\odot}$ necessitates renormalization as was described in Section 5.6. The values of R_o, R_1 and RATIO thus obtained are 14.6 kpc, 2.65 kpc and 0.149 respectively. This implies that $F = H_{reg}/H_{irreg} = 0.28$ giving for $H_{reg\,\odot} = 1.6\,\mu\mathrm{G}$ values of $H_{irreg\,\odot} = 5.7\,\mu\mathrm{G}$ and $H_{tot\,\odot} = 5.9\mu\mathrm{G}$. The pole temperature that these new parameters predict is 12.5 K, exactly the same as the observed temperature. A longitude profile with the smaller uniform field component is shown in Fig. 5.27. The most noticeable difference between this figure and Fig. 5.24 is the sharper, higher peaks in the former. This can be explained by the fact that there is an increased proportion of the emission from the irregular component and along a tangent to an arm this component is the sole contributor to the synchrotron emission as the regular component lies along the direction of the line of sight. The increased value of R_1 has produced a broader peak about the Galactic Centre and the lower temperatures within 20° of $l = 0°$ are a poorer fit to those 'observed' than before. A way of improving the predictions and still retaining $H_{reg\,\odot} = 1.6\,\mu\mathrm{G}$ might be to reduce the value of C_R and broaden the variation of the compression factor (see Section 5.8 and Table 5.2 therein) which should lower and smooth the peaks but then the model would not agree so well with the results of the simulations performed by Roberts and Hausman (1984).

5.10 A comparison with M81

In 1975, Roberts, Roberts and Shu used results of density wave theory to categorize spiral galaxies in terms of two parameters. The first is the ratio of the mass and a characteristic dimension, the second is the degree of mass concentration in the galactic centre. In density wave theory this second parameter determines the pitch angle, i, of the spiral arms, *i.e.* how tightly wound the spiral pattern is. The two parameters taken together, according to theory, provides the velocity of the gas perpendicular to the spiral arms, $\omega_{\perp o}$. This dictates the shock strength and therefore the development of an arm. The two quantities i and $\omega_{\perp o}$ were calculated using the observed rotation curves of 24 nearby galaxies at half the radius of the observed galactic disc. The Hubble Type of a spiral galaxy is a classification of the optical appearance of the spiral pattern. For galaxies without central bars the structure is designated Sa for a tightly wound system and Sc for an open morphology. The Luminosity Class is a system introduced by van den Bergh (1960a, 1960b) which also classifies galaxies in terms of the intrinsic luminosity and correlated development of the arms. A Luminosity Class I refers to a bright galaxy with well-developed arms of high compression. Galaxies become increasingly fainter and arms broader and less well-developed with increasing numeral up to Class V for faint dwarf galaxies. Both Hubble Type and Luminosity Class therefore are observable properties of galaxies and Roberts, Roberts and Shu found that there was a good correlation between these and the theoretically derived quantities when they plotted i

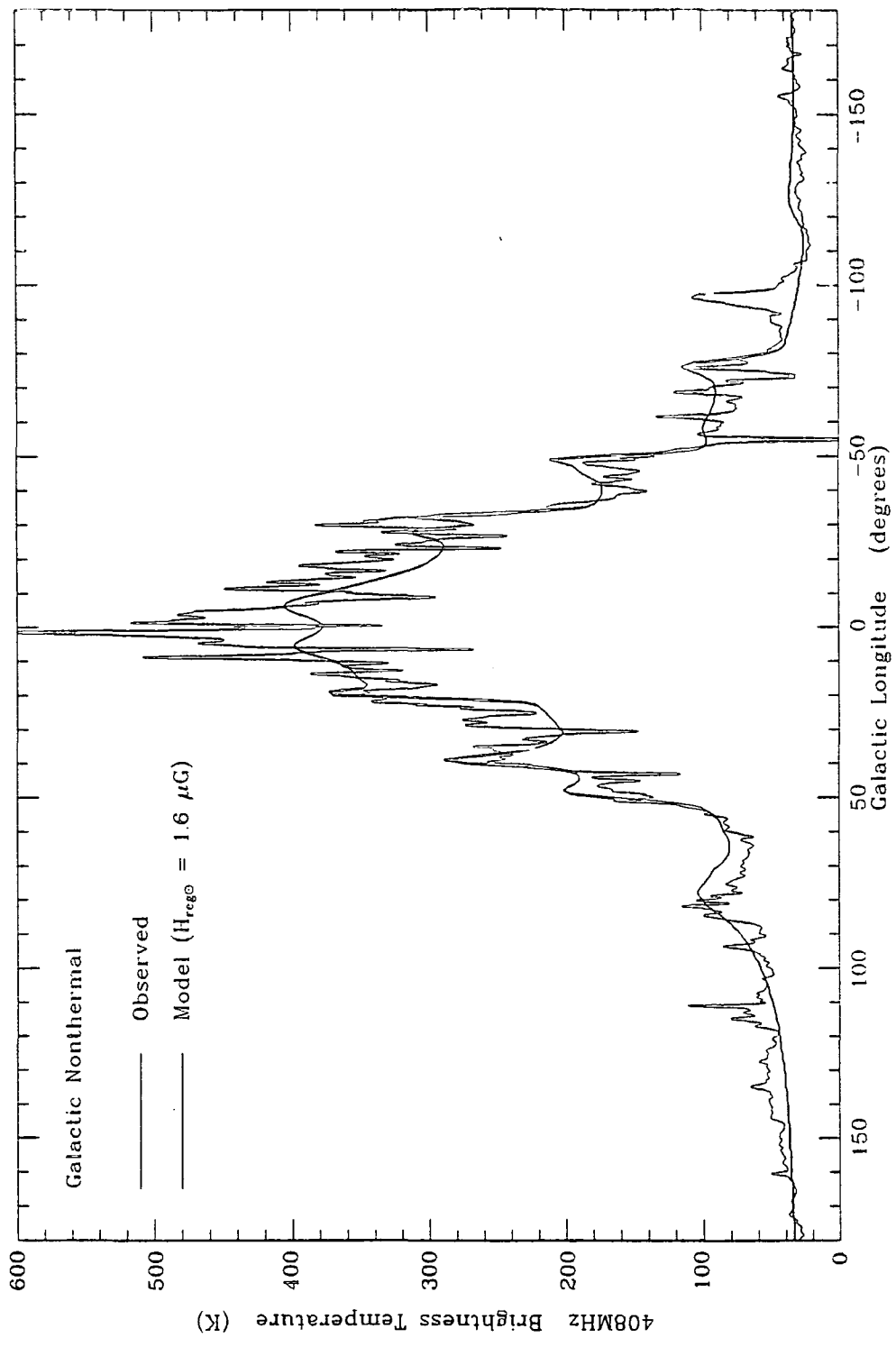

Figure 5.27: A comparison of the predicted 408 MHz synchrotron emission along the Galactic Plane (thick line) with that 'observed' (thin line). The model used is the same as the final model which predicts the profile shown in fig. 5.24 except that the local regular magnetic field strength has been changed from 3 to 1.6 μG.

against Hubble Type and more especially $\omega_{\perp o}$ against Luminosity Class. These correlations therefore are an indication of the consistency of density wave theory with the observable properties of spiral galaxies.

Obviously it is difficult to determine the Hubble Type and Luminosity Class of our own Galaxy because of our internal viewpoint. However, an estimation of the classification is SbcII. Observations of the spiral arms suggest that they are quite loosely wound having a pitch angle of about 12° in the solar neighbourhood (Georgelin and Georgelin, 1976) and this then puts the Hubble Type between Sb and Sc. A Luminosity Class II (Beck and Reich, 1985) suggests that the Galaxy has intermediate luminosity and spiral arms which are broader and of lower compression than those of a grand design such as M51 (ScI) or M101 (ScI) but narrower and better defined than for example, M33 (ScII–III). Of the nearby galaxies which have been studied quite extensively at radio wavelengths, M81 with classification SbI–II (Roberts, Roberts and Shu, 1975) is fairly close to that of our own Galaxy. M81 may therefore be a suitable spiral galaxy to use as a comparison with properties of the model for the Milky Way which we have developed throughout this chapter. In addition to having a similar classification to the Galaxy, the normal to the disc of M81 is 59° to the line of sight and so the spiral pattern should be observable. It is only within the last few years however that radio observations of M81 have been made with sufficiently high resolution to be able to distinguish separate spiral arms.

In 1986, Bash and Kaufman reported on the results of observations of radio continuum emission from M81 at 6 and 20 cm made with the Very Large Array (VLA) Telescope. The resolution was sufficient to discern two major spiral arms of non-thermal radio emission whose morphology was fairly patchy having width of the order of 1–2 kpc in the plane of the sky. This observation led Bash and Kaufman to the conclusion that either the scale height of the shocked gas in an arm is much larger than that adopted for the HI and the apparent breadth of the arms is the effect of looking at an angle to the plane or that the arms really are much wider than would be predicted by the classical hydrodynamic calculations of density wave theory. The latter explanation for the wide spiral arms seen in M81 supports the cloud-particle density wave model of Roberts and Hausman (1984) which we have discussed in previous sections.

Earlier observations of the total and linearly polarized radio continuum at 6.3 and 2.8 cm of M81 by Beck *et al.* (1985) with the Effelsberg 100 m telescope determined some average properties of the magnetic field in the main spiral arms. Using assumptions of equipartition of energy they estimated that the average total magnetic field strength is $7.5 \pm 1.5\,\mu$G. The average degree of polarization found was $14 \pm 6\,\%$ which implies that the average uniform field is $3 \pm 1.5\,\mu$G with the ratio of the uniform to random components being 0.44 ± 0.15. Beck *et al.* also noted that in the western spiral arm of M81 the degree of polarization appears to be very high with a maximum value of $\sim 60\%$.

A very recent study by Krause *et al.* (1989) combines the 6.3 cm observations of M81 by Beck *et al.* (1985) with new high resolution measurements with the VLA at 20 cm. The angular resolution of the 20 cm data is equivalent to 0.7 kpc × 1.1 kpc along the major and minor axes in the plane of the galaxy. They also noted that the widths of the two major arms are too large to agree with classical density wave theory and that the enhancement in

the arm is also too low to be consistent with compression in a strong shock. The uniform field seems to lie along the optical spiral arms and the mean pitch angle is $18° \pm 6°$, slightly larger than the $\sim 12°$ of the Galaxy. The azimuthal rotation measure is double-periodic and so the field configuration is a bisymmetric spiral, possibly maintained by a turbulent dynamo mechanism. Unfortunately, the reversal of the magnetic field across neutral lines cannot be seen because the resolution is not good enough.

One surprising result of the linear polarization measurements is that there is a high degree of polarization at 20 cm in the interarm regions having a value of $47 \pm 3\%$ in the south-west and $17 \pm 4\%$ in the north-east interarm regions. The value of the ratio of the uniform to random field strength in the south-west interarm is about twice that for an average over the spiral arms of M81. However, the total field is still smaller in the interarm. This result is the reverse of what might be expected and certainly the opposite trend to that assumed in our models of the magnetic field in the Milky Way where we suppose that there is a partial alignment of irregular field within an arm. Krause *et al.* suggested two explanations of these findings; the $\alpha\omega$-dynamo is more efficient in the interarm region or the uniform field created by dynamo action is not as disrupted in an interarm region compared with an arm region where there is a much higher frequency of SN explosions causing turbulence. They also suggested that tidal effects from the nearby galaxy M82 could reduce the ordering of the magnetic field in the north-east interarm region of M81 below that found in the south-west interarm region.

In our model of the Galaxy, the uniform magnetic field lies along the directions of arms and parallel to the plane and is assumed to be compressed in proportion to the gas in spiral arms because the field is 'frozen' into the gas. The irregular field is assumed to be isotropic and the component lying normal to the arm and parallel to the plane is not compressed (*e.g.* PKOHSII) which means that the random field now has a slight bias along the direction of the arm. French (1977) found that a good approximation to the effective irregular field strength along a line of sight is:

$$H_{eff} = \rho_c Y^{\frac{1}{1.8}} \frac{H_{reg}}{F}$$

$$\text{where } Y = \left[1 - 0.477 \left(1 - \frac{1}{\rho_c^2}\right) \cos^2\theta\right] \qquad (5.30)$$

cf. Equations 5.9 and 5.10. H_{reg} is the uncompressed uniform field strength at a given radius, F is the ratio of uncompressed regular to irregular field and θ is the angle between the line of sight and the arm direction. When viewing in directions parallel to but at different distances from an arm ($\theta = 0°$), Y decreases from unity outside the arm to 0.562 inside the arm when the gas reaches the maximum compression of $\rho_c = 3.5$. Perpendicular to the arm in the plane ($\theta = 90°$) Y is always 1. Therefore in the plane of the Galaxy at $R = R_\odot$ the effective irregular field strength along the arm is $11.6\,\mu$G and perpendicular to the arm is $15.9\,\mu$G when $F = 0.66$. The first two columns of Table 5.3 summarize the magnitudes and ratios of components of the magnetic field for our model of the Milky Way and the observed values for M81.

To see what effect the aligning of the isotropic field parallel to spiral arms has on

Parameter	1. M81 observation		Galaxy model									
			2. Alignment & compression			3. No Alignment		4. Disordering & compression		5. Disordering & no compression		
	Arm[3]	Interarm[4]	Arm[5]		Interarm	Arm[5]	Interarm	Arm[5]	Interarm	Arm[5]	Interarm
F					0.66		0.70		0.81		0.41
ρ_{cmax}			3.5		1.0	3.5	1.0	3.5	1.0	1.0	1.0
			$\theta = 0°$	$\theta = 90°$							
Y			0.562	1.0	1.0	1.0	1.0	0.69[7]	1.0[7]	0.69[7]	1.0[7]
B_u/B_r[1]	0.44 ± 0.15	1.0 ± 0.1	0.91[6]	0.66	0.66	0.70	0.70	0.39	0.81	0.20	0.41
$B_u(R_\odot)\,\mu$ G	3.0 ± 1.5	4.5 ± 1.0	10.5		3.0	10.5	3.0	7.2	3.0	2.1	3.0
$B_r(R_\odot)\,\mu$G	7.0 ± 1.5	4 ± 1	11.6[6]	15.9	4.5	15.0	4.3	18.8	3.7	10.6	7.3
$B_t(R_\odot)\,\mu$G[2]	7.5 ± 1.5	6 ± 1	15.6[6]	19.1	5.4	18.3	5.2	20.1	4.8	10.8	7.9

Table 5.3: Comparisons of field strengths for M81 and models of the Milky Way

[1] B_u/B_r =ratio of uniform (regular) to random (irregular) field.

[2] $B_t = (B_u^2 + B_r^2)^{1/2}$ =total field strength.

[3] Average over $3 < R < 6$ kpc which covers mainly spiral arms. From Beck *et al.* (1985) at 6 cm.

[4] From Krause *et al.* (1989) at 20 cm for SW interarm region.

[5] Values for positions of peak gas compression.

[6] For B_r read H_{eff}.

[7] For Y read Y'.

the overall synchrotron brightness temperatures predicted by the model of the Galaxy, we remove the factor Y from Equation 5.9 and then recalculate the brightness temperatures along the Galactic Plane at 408 MHz. We have to renormalize the temperatures which yields new values of the free parameters but apart from that all other parameters in the calculations are identical to those summarized in Table 5.2. The new values of R_o, R_1 and RATIO required are 14.1 kpc, 2.9 kpc and 0.77 ($\Rightarrow F = 0.70$). The resulting longitude plot along the plane is shown in Fig. 5.28. As might be expected, the peaks in the emission from directions whose lines of sight are tangential to an arm are over-estimated. Before, the partial realignment of the random field reduced the component of the field lying perpendicular to the line of sight and hence decreased the synchrotron emission, but now no such reduction takes place. The field strengths at the solar circle for this case assuming uniform compression of the isotropic component are shown in the third column of Table 5.3. The irregular field strength in the non-aligned case is about 30% larger than the effective irregular field when viewing along a tangent to a spiral arm in the aligned case.

Next we try to model the behaviour observed in M81 where the interarm regions have a higher uniform to irregular field ratio than in the arm. An approximation to this apparent state of affairs in M81 might be to assume that:

$$\text{uniform field :} \qquad B_u = \rho_c Y' H_{reg} \tag{5.31}$$

$$\text{random field :} \qquad B_r = \rho_c \tfrac{1}{Y'} \tfrac{H_{reg}}{F} \tag{5.32}$$

$$\text{where :} \quad Y' = 1 - 0.34\left(1 - \tfrac{1}{\rho_c^2}\right) \tag{5.33}$$

This implies that:

$$B_u/B_r = FY'^2$$

and so if:

$$\rho_c = 1 \quad \text{then } Y' = 1 \quad \text{and } B_u/B_r = F$$
$$\rho_c = 3.5 \quad \text{then } Y' = 0.69 \quad \text{and } B_u/B_r = F/2.1$$

This proposed model takes no account of any alignment of the magnetic field on compression in an arm but assumes that the effect is swamped by a disordering mechanism which increases with increasing compression. This sort of behaviour may be expected if SNRs were the disturbing influence of the uniform magnetic field. The amended form of Equation 5.9 now is:

$$T_b(\nu) = 6.168\times10^4\nu^{-2.8}\int_s\left(N_e(s)\left[\rho_c(s)Y'(s)H_{reg}(s)\sin\theta\right]^{1.8} + 0.6861N_e(s)\left[\frac{\rho_c(s)H_{reg}(s)}{Y'F}\right]^{1.8}\right)ds \tag{5.34}$$

Fig. 5.29 shows the form of Y'^2 and $Y^{-\frac{1}{1.8}}(cos\theta = 1)$ with varying distance from positions of maximum of compression in an arm and are proportional to the ratio B_u/B_r for the cases when the uniform field is disordered in an arm and when the random field is aligned in an arm respectively.

The new values of R_o, R_1 and RATIO required are 14.2 kpc, 3.0 kpc and 1.0 which implies $F = 0.81$ and the field components at the maximum of gas compression and in the

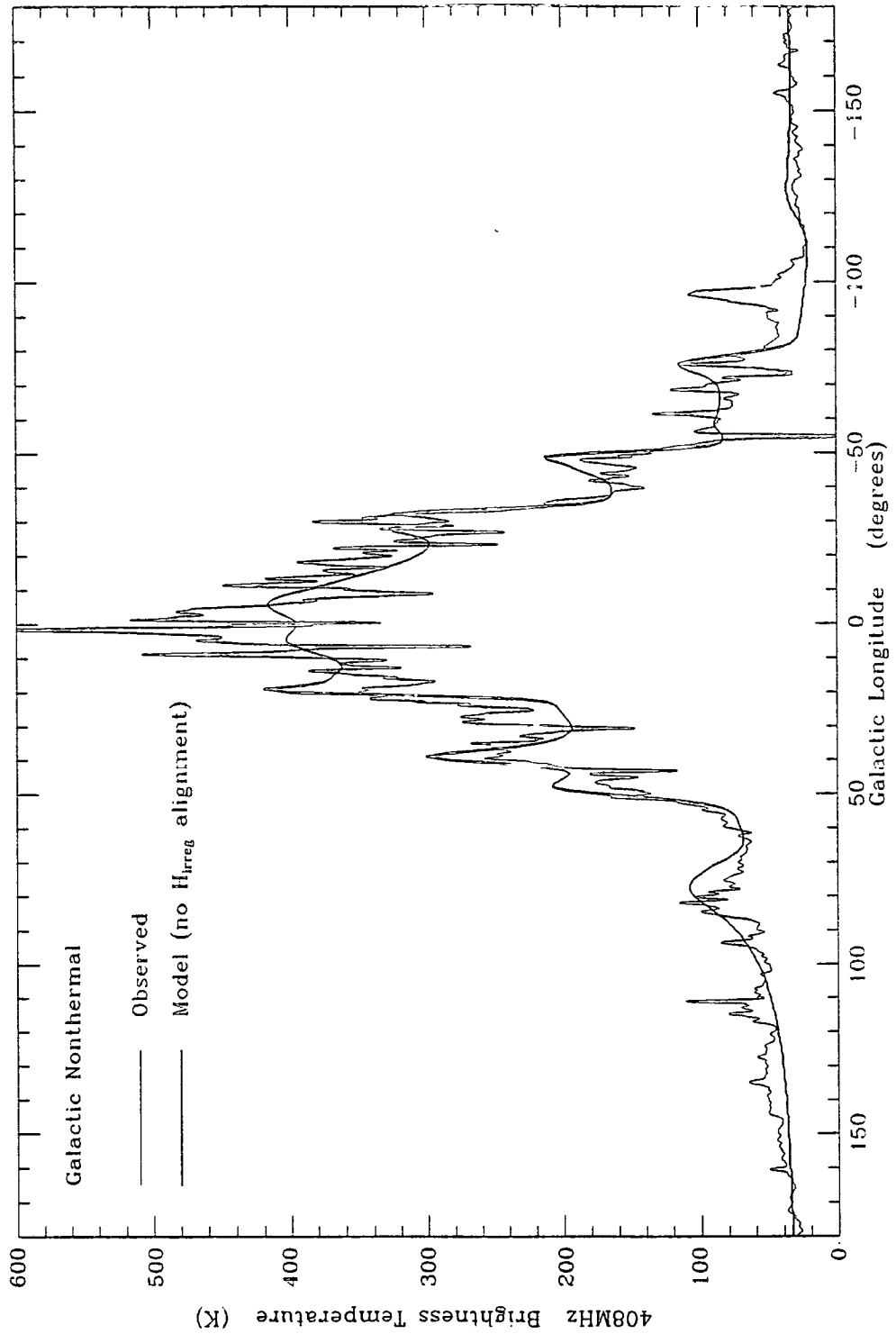

Figure 5.28: A comparison of the predicted 408 MHz synchrotron emission along the Galactic Plane (thick line) with that 'observed' (thin line). The model used is the same as the final model whose parameters are summarized in Table 5.2 except that the alignment factor, Y, has been omitted.

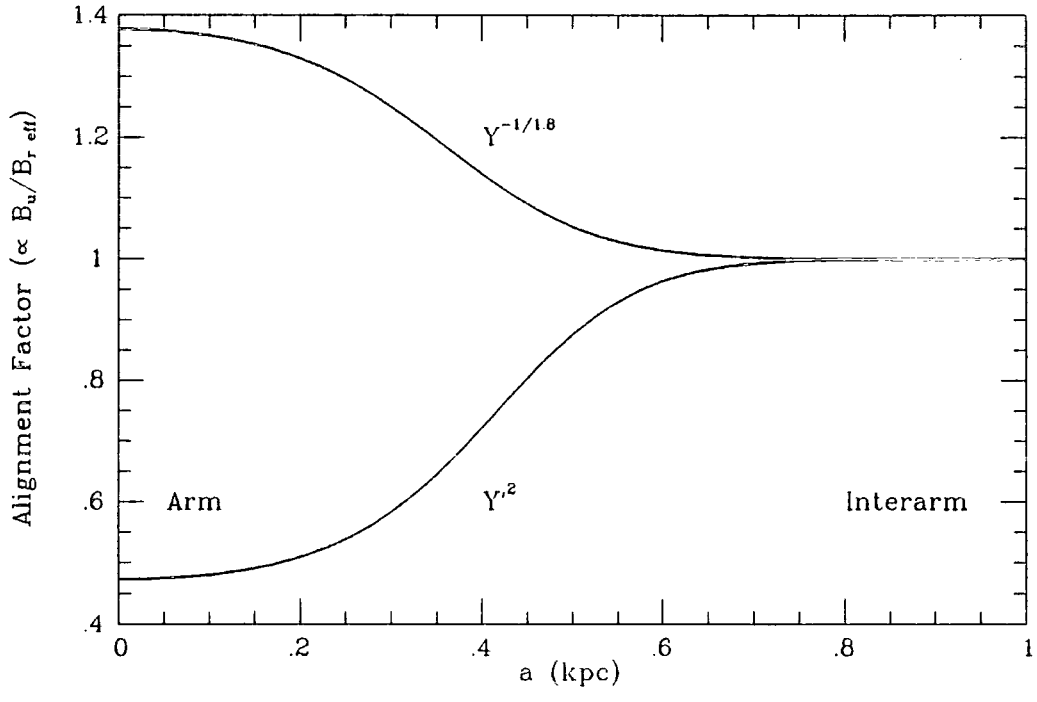

Figure 5.29: The variation of Y'^2 and $Y^{-\frac{1}{1.8}}$ $(\cos\theta = 1)$ with perpendicular distance from a position of maximum gas compression. The former is proportional to the ratio of the regular to irregular field for the case when the uniform field is disordered in an arm.The latter is proportional to the ratio of the regular to effective irregular field when looking along a tangent to the path of an arm and field alignment takes place in the arm.

interarm region at $R_\odot$ are shown in Column 4 of Table 5.3. The irregular field at maximum compression rises to a very high value of $20\,\mu$G which naturally is reflected in the large predicted brightness temperatures at 408 MHz along the Galactic Plane (see Fig. 5.30). The general level of the background emission is good but the peaks are much too high. One way of reducing the height of the peaks would be to assume that the compression of the magnetic field across an arm is not as great as was previously supposed. The extreme case we could take is when the magnetic field is not coupled to the gas and suffers no compression in an arm. The compression dependent disturbances of the uniform component however are still effective. R_o, R_1 and RATIO for this case become 15.9 kpc, 2.4 kpc and 0.30 and hence $F = 0.41$. Column 5 of Table 5.3 has the corresponding field strengths for this model. As can be seen the uniform component is smaller within an arm than in the interarm. This was observed for M81 as shown in Column 1 of the table. In the plane profile of Fig. 5.31 the predicted brightness temperatures in the peaks have come down significantly and are reasonable approximations to the peaks in the 'observed' emission on the whole. The general level of emission, however, is not a very good fit to that 'observed'. The large scale length required to reproduce the level in the outer Galaxy means that the predictions are too high in the mid-longitude range $100° \gtrsim |l| \gtrsim 30°$.

To summarize, M81 is believed to have a similar Hubble Type and Luminosity Class to the Galaxy. The morphology of the spiral arms in M81 seems to be in general agreement with the cloud-particle density wave model of Roberts and Hausman (1984) which we have used in our modelling of the Milky Way. Krause *et al.* (1989) have found that the uniform to random field strength within the interarm regions of M81 is higher than in the arms. Also, at a recent meeting (IAU Symposium No. 140, Heidelberg), Beck reported the observation of a large degree of field alignment in the interarm regions of M51, the other galaxy which has been shown to have a BSS field distribution. This suggests that the phenomenon may not be peculiar just to M81. Preliminary investigations including this behaviour within the framework of the model of our Galaxy indicate that with sufficient fine tuning of the parameters Y', ρ_c and perhaps H_{reg}, an adequate fit to the 'observations' could be obtained. The falsification or otherwise of the different models investigated however, is difficult with the limited observational data available at the present time for M81 or the Galaxy.

5.11 Possible future developments of the model

At the end of Section 5.8 we summarized the parameters of a model which we feel reproduces the 'observed' synchrotron emission of the Galaxy at 408 MHz satisfactorily. We do not claim that this model is unique in producing a good fit to the data but the assumed parameters and their variations are reasonable in the light of present theories and observations. There are several refinements and further investigations which perhaps could be undertaken in the future and will be briefly described here.

1. **Inclusion of the Galactic warp.** In all the modelling we have done, the predicted synchrotron emission was always assumed to be symmetrical about the $b = 0°$ line. It is well established that the centre of the HI disc of the Galaxy deviates from this line

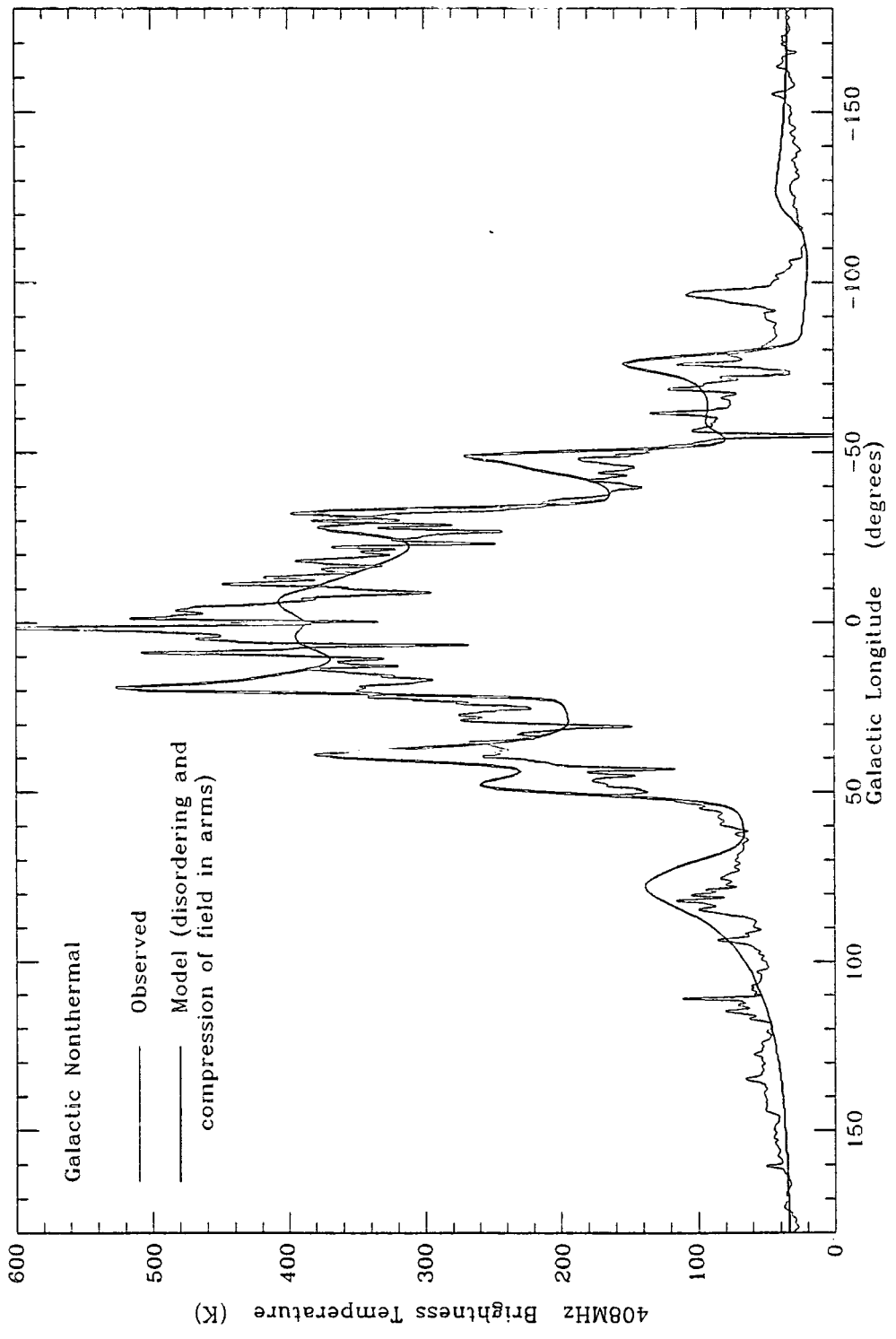

Figure 5.30: A comparison of predicted 408 MHz synchrotron emission along the Galactic Plane (thick line) with that 'observed' (thin line). The model used is an attempt to simulate a disordering of magnetic field in the spiral arms by inclusion of a factor Y' into the line of sight integration (Equations 5.31–5.34). All other parameters used are the same as those of our final model (see Table 5.2).

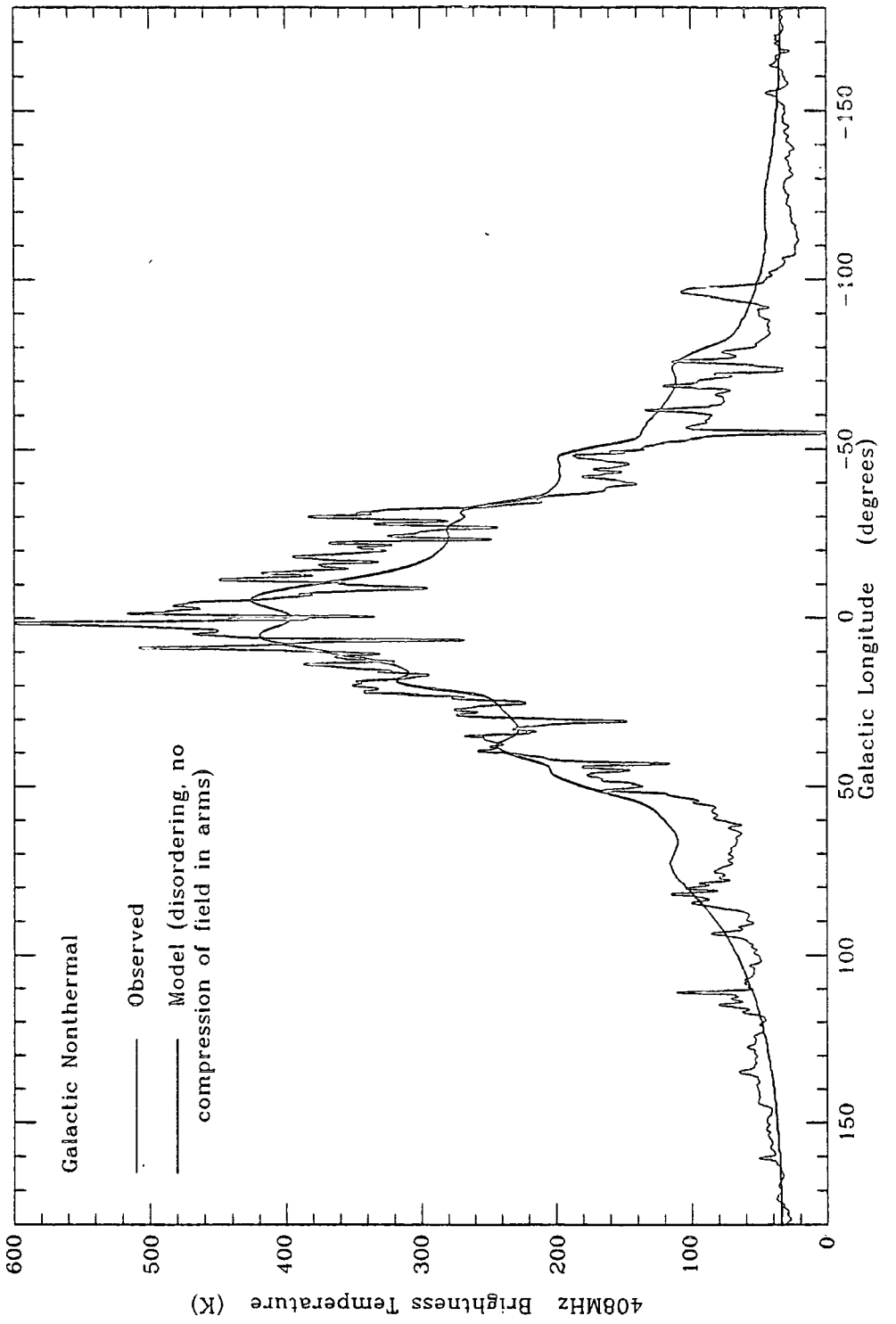

Figure 5.31: Comparison of predicted 408 MHz synchrotron emission along the Galactic Plane (thick line) with that 'observed' (thin line). As for the model which produced the profile shown in Fig. 5.30, disordering of the magnetic field occurs in spiral arms but this time the field is not compressed with the gas.

by as much as 850 pc in the outer parts of the Galaxy, lying above $b = 0°$ in the second quadrant and below in the third (*e.g.* Henderson, Jackson and Kerr, 1982). It is quite likely that the radio disc has similar deviations from $b = 0°$ and their inclusion in the modelling may well improve fits to latitude profiles in the outer Galaxy, although incorporation of a Galactic warp into the models by PKOHSII suggest that the change to our predictions will be small.

2. **Spectral index, α.** The calculation of the synchrotron brightness temperatures depend on the spectral index, α, where $T_b(\nu) \propto \nu^{-\alpha}$ and throughout this work we have taken a value of 2.8 as did Kearsey. The assumption of a constant spectral index for the Galaxy seems to be a reasonable approximation to first order. Lawson *et al.* (1987) studied spatial variations in the spectral index between 38 and 1420 MHz in the northern hemisphere and found that contrary to earlier low resolution studies the variations are predominantly connected with the radio loops and not the Galactic halo. (Earlier papers, *e.g.* Bridle, 1967 reported that the spectrum steepened with increasing latitude). Likewise Reich and Reich (1988) found little evidence for a variation of α with z between 408 and 1420 MHz for the inner Galaxy at least. However they did conclude that the non-thermal spectral index could be as high as 3.1. Perhaps a further line of investigation would be to see what effect assuming a higher spectral index would make to the overall calculations of the synchrotron brightness temperatures. If α was assumed to be 3.0 then the power of the magnetic field would be 2.0 and the step between Equations 5.7 and 5.8 would be exact.

3. **Radio loops.** A refinement to the model which could prove more difficult to effect satisfactorily is the inclusion of Galactic radio loops. French (1977) attempted to do this but found the results were unsatisfactory and even detrimental to the general fit of the model. Both Lawson *et al.* (1987) and Reich and Reich (1988) noted that the majority of spectral index variations above the plane are due to the loops and this could be difficult to model.

4. **Electron flux density.** As mentioned in Section 5.7 the fit of the variation of the electron flux density with height above the plane taken from PKOHSII could be improved especially by reducing the rate of fall-off of the electron flux over mid-latitudes in the inner Galaxy.

5. **Magnetic field compression.** A study of the variation of interstellar magnetic field strength with gas density led Troland and Heiles (1986) to conclude that the field does not appear to increase over gas density ranges 0.1 to $\sim 100\,\mathrm{cm}^{-3}$ and that all measurements of fields made in gas of density within this range do not exceed 10–20 μG. The densities of gas that we are considering are unlikely to be outside this range yet in our calculations, except for some in Section 5.10, we took the magnetic field compression to be in proportion to the gas compression in line with theory of gas compressed by a shock wave normal to the field. As Heiles (1987) points out, it is possible to explain these observations of Troland and Heiles if the density

increases by streaming of gas at low density along field lines. However, he claims that there is substantial evidence for the presence of shocks and the few measurements that exist of fields associated with expanding shells show that the field is slightly stronger than that for arbitrarily chosen positions. Whether this extends to large scale shock fronts associated with spiral arms is unclear. However, the fact that we see peaks in the directions of the tangents to arms implies that either the isotropic field component increases in the arm due to some disordering mechanism, thus increasing the perpendicular field component (see previous section) and/or the field is compressed at least to some extent with the gas. Future work, therefore might involve further consideration of this problem.

Chapter 6

Conclusions

6.1 Summary

In this thesis we have strengthened the case for the proposition of Haslam and Osborne (1987) that a significant proportion of the emission from the Galactic disc at far infrared wavelengths originates in regions of ionized hydrogen. The striking resemblance of the detailed morphology of Galactic emission detected in the IRAS 60 μm band to that of high frequency radio continuum at a similar angular resolution is a manifestation of this, as is the high correlation coefficients obtained for plots of 60 μm intensity against 11 or 6 cm brightness temperature. The correlation exists not only for the bright compact HII regions along the Galactic Plane but also for the more extended, low density regions.

By contrast, non-thermal sources of emission appearing in radio continuum surveys have very low levels of IR emission. On the small scale this has enabled us to produce a list of new supernova remnant candidates, picked out from the 11 cm Effelsberg survey and the 6 cm Parkes survey. Each candidate has little or no corresponding 60 μm emission and it is not listed in current supernova remnant catalogues. A more important consequence of the strong 60 μm–thermal radio continuum emission correlation from the standpoint of the present work is that on the larger scale the 60 μm emission enables the identification of the thermal component of the radio continuum which can be subtracted from the total thus leaving a clearer view of the synchrotron emission close to the Galactic Plane. This we have done for the all-sky survey of Haslam *et al.* (1982) at 408 MHz. At this frequency the non-thermal emission dominates but the thermal emission makes a significant contribution which has to be removed if the synchrotron emission is to be modelled in detail along the Galactic Plane.

Preliminary preparation of the IRAS 60 μm band Galactic Plane maps involved subtraction of the zodiacal light contamination and also the contribution of the HI-associated dust to the Galactic FIR emission. To predict the latter we use a model assuming a mixture of silicate and graphite grains in radiative equilibrium with the ambient interstellar radiation field together with the three dimensional distribution of HI gas. While this produces impressive fits to the observed Galactic 60 μm emission at galactic latitudes $\gtrsim 5°$, where we would expect little contribution from HII-associated dust, the variation of 60 to 100 μm

colour temperatures along the plane does not show the same high, near constant values as that of the total observed emission. This necessarily implies a decreasing 60 to 100 μm ratio with decreasing galactic longitude for the HII-associated emission. From these results we can either conclude, as have a number of other authors, that there exists an additional population of small grains not in equilibrium with their local interstellar radiation field or that the HI predictions and therefore those of the HII-associated emission are correct in which case we have the problem of explaining the apparently decreasing colour temperatures of the latter with increasing proximity to the Galactic Centre. We have put forward one suggestion which proposes that a significant fraction of 100 μm emission from HII regions is in fact from OIII line emission and that the [OIII/O] abundance increases with decreasing distance from the Galactic Centre. In reality both small grains and line emission could be contributing to the far infrared emission. We have performed a thermal–non-thermal separation of the 408 MHz emission for a restricted range of longitudes to quantify the effect of an additional population of small grains and to gain some idea of the uncertainty in the estimation of the 408 MHz thermal emission. We find that the 'small grain' variant of the HI-associated dust emission at 60 μm leads to a reduction in thermal radio brightness temperatures on those from the 'standard grain' variant of about 25%. However, because the thermal is the smaller component at 408 MHz the uncertainty in the non-thermal component at 408 MHz due to uncertainties in the grain model is less than 10%.

Regarding the determination of the linear relationship between the residual or HII-associated 60 μm emission and the thermal radio continuum emission at 6 and 11 cm we find no systematic variation with galactic longitude. For the longitude range $76° \geq l \geq 359°$ and $|b| \leq 1\frac{1}{2}°$ we find an average residual 60 μm to 11 cm intensity ratio of 700 ± 200 and for longitude range $40° \geq l \geq 280°$ over the same range of galactic latitude the average 60 μm to 6 cm intensity ratio is 810 ± 250. We have used this mean 60 μm:11 cm value to scale the residual 60 μm emission from the whole of the Galactic Plane and for $|b| \leq 8\frac{1}{3}°$ to a frequency of 408 MHz assuming a thermal radio spectral index of 0.1 ($S_\nu \propto \nu^{-0.1}$). The validity of the application of the scaling factor beyond the range covered by the 11 cm survey and into the outer Galaxy is implied from the good fit of the scaled IR to the observed 408 MHz (predominantly thermal) emission from the local Cygnus complex which was just outside of the 11 cm survey area.

As a by-product of the thermal–non-thermal separation procedure we have been able to use the 60 μm band emission to estimate various quantities for the Galaxy as a whole. We find a value of 4 ± 2 for the infrared excess (IRE) for HII regions which is in good agreement with theoretically derived values. The 60 μm luminosity of the Galaxy associated with ionized hydrogen beyond r kpc from the centre ($r = R_\odot/10$) is estimated to be $1.2 \times 10^{23}\, r^2$ W Hz^{-1}. The ionized gas has a total mass of $\sim 10^9 K^{-0.5}\, r^2\, M_\odot$ where K is the clumping factor of HII regions. We have been able to make rough estimates of the total far infrared luminosity and radio power of the Galaxy and find that the ratio of these is compatible with the tight correlation between these quantities which has been observed for other disc galaxies. On comparison of our thermal–non-thermal separation with those of other authors who used the spectral index technique, we find that our estimate of the thermal emission is consistently lower than earlier estimates but is in reasonable agreement

with the more recent results of Reich and Reich (1988). Discrepancies between distributions derived using the same spectral index method with different radio surveys highlight the difficulties encountered when applying the technique. Our new separation method has enabled us to circumvent these problems.

Having separated the components of the emission at 408 MHz we are left with a clearer picture of the non-thermal contribution. We have tried to improve upon the model of the Galactic synchrotron emission of Kearsey (1983) and have used our separated non-thermal component as a standard against which we can assess the suitability of the model predictions. For the purposes of the modelling we refer to our separated non-thermal component as the 'observed' synchrotron emission at 408 MHz.

To obtain a reasonable fit to the 'observed' peaks and steps in the synchrotron emission close to the plane, we have constructed a pattern of spiral arms which has two pairs of arms emanating from a central ellipse. To produce an acceptable fit to the underlying increase of synchrotron emission with decreasing galactocentric radius in the Galactic Plane we have constructed a function for the synchrotron emissivity which is zero at the Galactic Centre, rises sharply to a peak at $\sim$ 1.3 kpc and falls off slowly beyond $\sim$ 3 kpc from the centre. Using the scale length of the cosmic ray electron flux density which has been derived by Bhat *et al.* (1986) from an analysis of γ-ray data, we find that the Galactic magnetic field must have a very long scale length of $\sim$ 22 kpc. This is in agreement with the scalelength derived if we assume that equipartition exists in the Galaxy between the energy density of cosmic rays and magnetic field.

We find that the emissivity variation with height above the plane deduced by Phillipps *et al.* (1981b) can be successfully incorporated into our model, producing generally good fits to 'observed' cuts across the plane and also predicting a pole temperature close to the actual value. The distribution of Phillipps *et al.* assumes a thick disc of emission of half-width $\sim$ 1 kpc surrounded by an extended halo of low luminosity stretching out to about 16 kpc from the plane.

We have modelled the variation of Galactic magnetic field across a spiral arm as a gaussian function with $\sigma = 0.2$ kpc and the maximum compression of the field in an arm is 3.5:1. Not only does this predict peaks in the Galactic Plane profile of the synchrotron emission at 408 MHz which are of the correct height and width but also is compatible with the results of Roberts and Hausman's (1984) N-body simulations of spiral arm formation which treat individual gas clouds as the unit particle rather than individual atoms.

A ratio of regular to irregular field in interarm regions of 0.66 is required when we assume partial realignment of the irregular component on compression within the arms. The regular field component in the local solar neighbourhood is assumed to have a value of 3 μG and a reduction of this value to as low as 1.6 μG, which has been claimed by some authors, would be difficult to accommodate within the model.

Recent observations of M81 and M51, the former being a galaxy of similar Luminosity Class and Hubble Type to our own, show that a higher degree of alignment of field exists in interarm regions than in the arms. Preliminary investigations including this behaviour in our model of the Galaxy indicate that it may be possible with suitable adjustments of other parameters to obtain a reasonable fit to the 'observed' synchrotron emission at 408 MHz.

6.2 Future work

1. The Cygnus complex

The Cygnus complex lies close to the Galactic Plane at a longitude of $\sim 78°$. It is believed to lie in a spiral arm beyond the solar circle and is about $1\frac{1}{2}$–2 kpc distant from the Sun. The majority of the sources in the complex are HII regions and therefore the radio continuum emission is predominantly thermal. As mentioned earlier our estimation of the thermal radio continuum emission at 408 MHz from the Cygnus complex seems to fit remarkably well to the observed emission even though it lies outside of the range of the 11 cm survey which was used to find the appropriate scaling factor of the HII-associated 60 μm emission.

Further study of the IR–radio correlation in the Cygnus complex could be made using the 11 cm map of Wendker (1970) with 11′ resolution. A more careful and accurate subtraction of the zodiacal light contribution from the IRAS maps would be possible using the recently acquired all-sky distribution of zodiacal light, described by Boulanger and Pérault (1988) in which dependence on parameters such as solar elongation and time are included. An estimation of the HI contribution to the FIR using both 'standard' and 'small' grain models (Section 2.3) would give some idea of the uncertainties in the contribution of this component. Using both 60 and 100 μm band residual intensities would enable a pixel by pixel estimation of the total FIR emission and so variations in the IR to radio ratio over the complex could be interpreted in terms of variations in the infrared excess.

2. Low frequency radio absorption

At high radio frequencies the optical depth of the Galaxy is generally $\ll 1$ and the total brightness temperature along a given line of sight is just the sum of the thermal and non-thermal components. However, at low frequencies (< 100 MHz), regions of ionized gas absorb background emission in addition to emitting thermal emission. Thus at low galactic latitudes where the majority of the HII is situated, along a particular line of sight the brightness temperature depends not only on the strength of thermal and non-thermal sources but also on their relative positions. Therefore, the study of low frequency radio continuum surveys should in theory reveal information about the three dimensional structure of the Galactic disc and indeed distances to discrete compact HII regions have been estimated in the past. An extension of this would be to study the three dimensional distribution of thermal and synchrotron sources on a larger scale. Our derived non-thermal and thermal components at 408 MHz could be used together with the model of spiral structure of the Galaxy to predict brightness temperatures in the plane at low frequencies. Such predictions would be compared with observations. It may be possible to determine whether the thermal and non-thermal spiral arms are in general coincident or displaced from each other.

Initially, the 29.9 MHz survey by Jones and Findlay (1974) could be used. This is similar in resolution to the 408 MHz data and covers the Galactic Plane from 30° down to 225° in longitude. In the near future however, the new 34.5 MHz survey made by Sastry *et al.* using the decametre wave radio telescope at Gauribidamur, India should become available. The resolution of this survey is slightly better than that of the 29.9 MHz survey. The advantage

of using measurements at these frequencies rather than at even lower frequencies, apart from higher resolution, is that the absorption is not complete and so still provides information on the conditions in inner parts of the Galaxy.

3. Modelling the synchrotron emission of the Galaxy at 408 MHz

At the end of Chapter 5 we gave a list of possible future developments of our model for the synchrotron emission of the Galaxy. Among these were: inclusion of the Galactic warp, investigating the effect on the predicted temperatures of assuming a higher non-thermal spectral index, modelling the Galactic radio loops and improving the form of the emissivity variation with height above the plane.

References

Allen, R.J., Baldwin, J.E. & Sancisi, R., 1978. *Astr. Astrophys.*, 62, 397.

Altenhoff, W.J., Downes, D., Good, L., Maxwell, A. & Rinehart, R., 1970. *Astr. Astrophys. Suppl.*, 1, 319.

Altenhoff, W.J., Downes, D., Pauls, T., & Schraml., J, 1979. *Astr. Astrophys. Suppl.*, 35, 23.

Altenhoff, W., Mezger, P.G., Strassl, H., Wendker, H. & Westerhout, G., 1960. *Veröff Univ. Sternw. Bonn* No.59.

Bash, F.N. & Kaufman, M., 1986. *Astrophys. J.*, 310, 621.

Beck, R., 1982. *Astr. Astrophys.*, 106, 121.

Beck, R., & Golla, G., 1988. *Astr. Astrophys.*, 191, L9.

Beck, R., Klein, U. & Krause., M., 1985. *Astr. Astrophys.*, 152, 237.

Beck, R. & Reich, W., 1985. In: *The Milky Way Galaxy, IAU Symp. No.* 106, p.239, eds. van Woerden, H., Allen, R.J. & Burton, W.B., Reidel, Dordrecht.

Beuermann, K., Kanbach, G., & Berkhuijsen, E.M., 1985. *Astr. Astrophys.*, 153, 17.

Bhat, C.L., Mayer, C.J., Rogers, M.J., Wolfendale, A.W. & Zan, M.A., 1986. *J. Phys. G: Nucl. Phys.*, 12, 1087.

Bloemen, J.B.G.M., Strong, A.W., Blitz, L., Cohen, R.S., Dame, T.M., Grabelsky, D.A., Hermsen, W., Lebrun, F., Mayer- Hasselwander, H.A. & Thaddeus, P., 1986. *Astr. Astrophys.*, 154, 25.

Bok, B.J., 1983. *Astrophys. J.*, 273, 411.

Boulanger, F., Beichman, C., Désert, F.X., Helou, G., Pérault, M. & Ryter, C., 1988. *Astrophys. J.*, 332, 328.

Boulanger, F., Baud, B., van Albada, G.D., 1985. *Astr. Astrophys.*, 144, L9.

Boulanger, F. & Pérault, M., 1988. *Astrophys. J.*, 330, 964.

Braun, R., 1987. *Astr. Astrophys.*, 171, 233.

Braun, R. & Strom, R.G., 1986a. *Astr. Astrophys.*, 164, 193.

Braun, R. & Strom, R.G., 1986b. *Astr. Astrophys.*, 164, 208.

Bridle, A.H., 1967. *Mon. Not. R. astr. Soc.*, 136, 219.

Brindle, C., French, D.K., Osborne, J.L., 1978. *Mon. Not. R. astr. Soc.*, 184, 283.

Burton, W.B., 1970. *Astr. Astrophys.*, 10, 76.

Burton, W.B., 1971. *Astr. Astrophys.*, 10, 76.

Burton, W.B., 1972. *Astr. Astrophys.*, 19, 51.

Burton, W.B., 1976. *Ann. Rev. Astr. Astrophys.*, 14, 275.

Burton, W.B. & Gordon, M.A., 1978. *Astr. Astrophys.*, 63, 7.

Burton, W.B., Deul, E.R., Walker, H.J. & Jongeneelen, A.A.W., 1986. In: *Light on Dark Matter*, p.357, ed. Israel, F.F., Reidel, Dordrecht.

Caux, E., Serra, G., Gispert, R., Puget, J.L., Ryter, C., Coron, N., 1984. *Astr. Astrophys.*, 137, 1.

Caux, E., Puget, J.L., Serra, G., Gispert, R., Ryter, C., 1985. *Astr. Astrophys.*, 144, 37.

Chiba, M. & Tosa, M., 1989. *Mon. Not. R. astr. Soc.*, 238, 621.
Chlewicki, G. & Laureijs, R.J., 1988. *Astr. Astrophys.*, 207, L11.
Clark, D.H. & Caswell, J.L., 1976. *Mon. Not. R. astr. Soc.*, 174, 274.
Cohen, R.S., Cong, H., Dame, T.M. & Thaddeus, P., 1980. *Astrophys. J.*, 239, L53.
Cohen, R.S., Grabelsky, D.A., Alvarez, H., Bronfman, L.May, J. & Thaddeus, P., 1985. *Astrophys. J.*, 290, L15.
Cowie, L.L., 1980. *Astrophys. J.*, 236, 868.
Cowie, L.L., 1981. *Astrophys. J.*, 245, 66.
Cox, D.P. & Smith, B.W., 1974. *Astrophys. J.*, 189, L105.
Cox, M.J., Eales, S.A.E., Alexander, P. & Fitt, A.J., 1988. *Mon. Not. R. astr. Soc.*, 235, 1227.
Cox, P., Krügel, E. & Mezger, P.G., 1986. *Astr. Astrophys.*, 155, 380.
Cox, P. & Mezger, P.G., 1987. In: *Comets to Cosmology, 3rd IRAS Symp.*, p.97, ed. Lawrence, A., Springer-Verlag, Berlin.
Denisse, J-F., Leroux, E. & Steinberg, J-L., 1955. *Comptes Rendus*, 240, 278.
Denisse, J-F., Lequeux, J. & Leroux, E., 1957. *Comptes Rendus*, 244, 3030.
Devereux, N.A. & Eales, S.A.E., 1989, preprint.
Dickey, J.M. & Salpeter, E.E., 1984. *Astrophys. J.*, 284, 461.
Downes, D., Wilson, T.W., Bieging, J. & Wink, J., 1980. *Astr. Astrophys. Suppl.* 40, 379.
Draine, B.T. & Anderson, N., 1985. *Astrophys. J.*, 292, 494.
Draine, B.T. & Lee, H.M., 1984. *Astrophys. J.*, 285, 89.
Drapatz, S., 1979. *Astr. Astrophys.* 75, 26.
Duley, W.W., 1973. *Astrophys. Space Sci.*, 23, 43.
Duric, N., Bourneuf, E. & Gregory, P.C., 1988. *Astr. J.*, 96, 81.
Dwek, E., Dinerstein, H.L., Gillett, F.C., Hauser, M.G. & Rice, W.L., 1987a *Astrophys. J.*, 315, 571.
Dwek, E., Petre, R., Szymkowiak, A. & Rice, W.L., 1987b. *Astrophys. J.*, 320, L27.
Field, G.B., Goldsmith, D.W. & Habing, H.J., 1969. *Astrophys. J.*, 158, 173.
Fitt, A.J., Alexander, P. & Cox, M.J., 1988. *Mon. Not. R. astr. Soc.*, 233, 907.
French, D.K. & Osborne, J.L., 1976. *Mon. Not. R. astr. Soc.*, 174, 267.
French, D.K., 1977. *PhD thesis*, University of Durham.
Fujimoto, M., 1987. In: *Interstellar Magnetic Fields.*, p.23, eds. Beck, R. & Gräve, R., Springer-Verlag.
Fürst, E., Handa, T., Reich, W., Reich, P. & Sofue, Y., 1987a. *Astr. Astrophys. Suppl.*, 69, 403.
Fürst, E., Reich, W. & Sofue, Y., 1987b. *Astr. Astrophys. Suppl.*, 71, 63.
Gardner, F.F. & Morimoto, M., 1968. *Aust. J. Phys.*, 21, 881.
Gavazzi, G., Cocito, A. & Vettolani, G., 1986. *Astrophys. J.*, 305, L15.
Georgelin, Y.M. & Georgelin, Y.P., 1976. *Astr. Astrophys.*, 49, 57.
Gerola, H. & Seiden, P.E., 1978. *Astrophys. J.*, 223, 129.
Gispert, R., Puget, J.L. & Serra, G., 1982. *Astr. Astrophys.* 106, 293.
Gosachinskiĭ, I.V., 1985. *Sov. Astron.*, 29, 128.

Grabelsky, D.A., Cohen, R.S., Bronfman, L., May, J., & Thaddeus, P., 1985. *Astrophys. J.*, 290, L15.
Green, D.A., 1984. *Mon. Not. R. astr. Soc.*, 209, 499.
Green, D.A., 1985. *Mon. Not. R. astr. Soc.*, 216, 691.
Green, D.A., 1988. *Astrophys. Space Sci.*, 148, 3.
Greenberg, J.M. & Hong, S.S., 1974. In: *Galactic and Radio Astronomy, IAU Symp. No.* 60, p.155, ed. Kerr, F. & Simonson, S.C., Reidel, Dordrecht.
Güsten & Mezger, P.G., 1983. *Vistas in Astronomy*, 26, 159.
Harding, D.S. & Harding, A.K., 1982. *Astrophys. J.*, 257, 603.
Harwit, M., Houck, J.R. & Stacey, G.J., 1986. *Nature*, 319, 646.
Haslam, C.G.T. & Osborne, J.L., 1987. *Nature*, 327, 211.
Haslam, C.G.T., Salter, C.J., Stoffel, H. & Wilson, W.E., 1982. *Astr. Astrophys. Suppl.*, 20, 37.
Hauser, M.G., Gillett, F.C., Low, F.J., Gautier, T.N., Beichman, C.A., Neugerbauer, G., Aumann, H.H., Baud, B., Boggess, N., Emerson, J.P., Houck, J.R., Soifer, B.T., Walker, R.G., 1984. *Astrophys. J.*, 278, L15.
Hauser, M.G., Silverberg, R.F., Stier, M.T., Kelsall, T., Gezari, D.Y., Dwek, E., Walser, D., Mather, J.C. & Cheung, L.H., 1984. *Astrophys. J.*, 285, 74.
Haynes, R.F., Caswell, J.L, & Simons, L.W.J., 1978. *Aust. J. Phys. Astrophys. Suppl.*, 45, 1.
Heiles, C., 1987. In: *Interstellar Processes*, p.171, eds. Hollenbach, D.J. & Thronson, H.A., Reidel, Dordrecht.
Heiles, C. & Cleary, M.N., 1979. *Aust. J. Phys. Astrophys. Suppl.*, 47, 1.
Heiles, C. & Habing, H.J., 1974. *Astr. Astrophys. Suppl.*, 14, 1.
Helou, G., Soifer, B.T. & Rowan-Robinson, M., 1985. *Astrophys. J.*, 298, L7.
Henderson, A.P., Jackson, P.D. & Kerr, F.J., 1982. *Astrophys. J.*, 263, 116.
Hill, E.R., Slee, O.B. & Mills, B.Y., 1958. *Aust. J. Phys.*, 11, 530.
Hirabayashi, H., 1974. *Publ. Astron. Soc. Japan*, 26, 263.
Hummel, E., 1986. *Astr. Astrophys.*, 160, L4.
Hummel, E., Davies, R.D., Wolstencroft, R.D., van der Hulst, J.M. & Pedlar, A., 1988. *Astr. Astrophys.*, 199, 91.
Inoue, M. & Tabara, H. ,1981. *Publ. Astr. Soc. Japan.*, 33, 603.
IRAS Catalogs and Atlases, Explanatory Supplement, 1985. Eds Beichman, C.A., Neugebauer, G., Habing, H.J., Clegg, P.E. & Chester, T.J., JPL D-1855, Jet Propulsion Laboratory, Pasadena.
Jones, B.B. & Findlay, E.A., 1974. *Aust. J. Phys.*, 27, 687.
de Jong, T., Klein, U., Wielebinski, R. & Wunderlich, E., 1985. *Astr. Astrophys.*, 147, L6.
Kearsey, S., 1983. *PhD thesis*, University of Durham.
Kerr, F.J., 1969. *Ann. Rev. Astr. Astrophys.*, 7, 39.
Klein, U., 1989. In: *Magnetic Fields in Galaxies*, Workshop held in Postdam, GDR to be published in *Geophysical and Astrophysical Fluid Dynamics.*
Klein, U., Wielebinski, R. & Beck, R., 1984. *Astr. Astrophys.*, 133, 19.
Krause, M., Beck, R. & Hummel, E., 1989. *Astr. Astrophys.*, in press.

Kulkarni, S.R. & Heiles, C., 1987. In: *Interstellar Processes*, p.87, eds. Thronson, H. & Hollenbach, D., Reidel, Dordrecht.
Landecker, T.L. & Wielebinski, R., 1970. *Aust. J. Phys. Astrophys. Suppl.*, 16, 1.
Laureijs, R.J., Chlewicki, G. & Clark, F.O., 1988. *Astr. Astrophys.*, 192, L13.
Lawson, K.D., Mayer, C.J., Osborne, J.L. & Parkinson, M.L., 1987. *Mon. Not. R. astr. Soc.*, 225, 307.
Levinson, F.H. & Roberts, W.W., 1981. *Astrophys. J.*, 245, 465.
Lin, C.C., 1970. In: *Galactic Astronomy*, 2, eds. Gordon & Breach.
Lin, C.C. & Shu, F.H., 1964. *Astrophys. J.*, 140, 646.
Lin, C.C. & Shu, F.H., 1966. *Proc. Nat. Acad. Sci.*, 55, 229.
Lin, C.C. & Bertin, G., 1985. In: *The Milky Way Galaxy., IAU Symp. No.* 106, p.513, eds. Woerden, H.V., Allen, R.J. & Burton, W.B., Reidel, Dordrecht.
Li, Ti Pei, Riley, P.A. & Wolfendale, A.W., 1983. *Mon. Not. R. astr. Soc.*, 203, 87.
Lizst, H.S., 1985. In: *The Milky Way, IAU Symp. No.* 106, p.283, eds. van Woerden, H., Allen, R.J., Burton, W.B., Reidel, Dordrecht.
Lockman, F.J., 1979. *Astrophys. J.*, 232, 761.
Lonsdale, C.J., Good, J. & Rice, W., 1985. *Catalogued Galaxies and Quasars Observed in the IRAS Survey*, Jet Propulsion Laboratory.
Low, F.J., Beintema, D.A., Gautier, T.N., Gillett, F.C., Beichman, C.A. Neugerbauer, G., Young, E., Aumann, H.H., Boggess, N., Emerson, J.P., Habing, H.J., Hauser, M.G., Houck, J.R., Rowan-Robinson, M., Soifer, B.T., Walker, R.G. & Wesselius, P.R., 1984. *Astrophys. J.*, 278, L19.
Low, F.J., Kurtz, R.F., Poteet, W.M. & Nishimura, T., 1977. *Astrophys. J.*, 214, L115.
Lin, C.C., Yuan, C. & Shu, F.H., 1969. *Astrophys. J.*, 155, 721.
Lyne, A.G. & Smith, F.G., 1989. *Mon. Not. R. astr. Soc.* 237, 533.
Maihara, T., Oda, N., & Okuda, H., 1979. *Astrophys. J.*, 227, L129.
Manchester, R.N., 1972. *Astrophys. J.*, 172, 43.
Manchester, R.N., 1974. *Astrophys. J.*, 188, 637.
Manchester, R.N. & Taylor, J.H., 1977. In: *Pulsars*, W.H.Freeman, San Francisco.
Marsden, P.L., Gillett, F.C., Jennings, R.E., Emerson, J.P., de Jong, T. & Olnon, F.M., 1984. *Astrophys. J.*, 278, L29.
Mathis, J.S., 1986. *Astrophys. J.*, 301, 423.
Mathis, J.S., Mezger, P.G. & Panagia, N., 1983. *Astr. Astrophys.*, 128, 212.
Mathis, J.S., Rumpl, W. & Nordsieck, K.H., 1977. *Astrophys. J.*, 217, 425.
Matthewson, D.S., Healey, J.R. & Rome, J.M., 1962. *Aust. J. Phys.*, 15, 354 and 369.
McKee, C.F. & Ostriker, J.P., 1977. *Astrophys. J.*, 218, 148.
Meyer, P., 1974. In: *Origin of cosmic rays*, p.233, eds. Osborne, J.L. & Wolfendale, A.W., D.Reidel, Dordrecht.
Mezger, P.G., 1978. *Astr. Astrophys.*, 70, 565.
Mezger, P.G. & Henderson, A.P., 1967. *Astrophys. J.*, 147, 471.
Mezger, P.G., Mathis, J.S. & Panagia, N., 1982. *Astr. Astrophys.*, 105, 372.
Mezger, P.G., & Smith, L.F., 1975. In: *Proc. of the 3rd European Astronomy Meeting, Tbilisi*, p.369, ed. Kharadze, E.K., Acad. Sci. Georgian SSR.

Mihalas, D., 1968. In: *Galactic Astronomy*, Freeman & Co., San Francisco and London.
Miller, R.H., 1976. *Astrophys. J.*, 207, 408.
Mills, B.Y., 1959. *Publ. Astron. Soc. Pacific*, 71, 267.
Milne, D.K., 1971. In: *The Crab Nebula, IAU Symp. No.* 46, p.248, eds. Davies, R.D. & Smith, F.G., Reidel, Dordrecht.
Mouschovias, T.C., 1975. *Astr. Astrophys.*, 40, 191.
Mueller, M.W. & Arnett, W.D., 1976. *Astrophys. J.*, 210, 670.
Mufson, S.L., McCullough, M.L., Dickel, J.R., Petre, R., White, R. & Chevalier, R., 1986. *Astr. J.*, 92, 1349.
de Muizon, M. & Rouan, D., 1985. *Astr. Astrophys.*, 143, 160.
Myers, P.C., Dame, T.M., Thaddeus, P., Cohen, R.S., Silverberg, R.F., Dwek, E., Hauser, M.G., 1986. *Astrophys. J.*, 301, 398.
Nishimura, T., Low, F.J. & Kurtz, R.F., 1980. *Astrophys. J.*, 239, L101.
Odegard, N., 1986. *Astr. J.*, 92, 1372.
Pacholczyk, A.G., 1970. In: *Radio astrophysics. Non-thermal processes in galactic and extragalactic sources*, eds. Burbidge, G. & Burbidge, M., W.H.Freeman and Co., San Francisco.
Pajot, F., Boissé, P., Gispert, R., Lamarre, J.M., Puget, J.L., Serra, G., 1986. *Astr. Astrophys.*, 157, 393.
Panagia, N., 1978. In: *Infrared Astronomy*, p.115, eds. Setti, G. & Fazio, G., Reidel, Dordrecht.
Parker, E.N., 1971. *Astrophys. J.*, 163, 255.
Pauliny-Toth, I.I.K. & Shakeshaft, J.R., 1962. *Mon. Not. R. astr. Soc.*, 124, 61.
Pérault, M., Boulanger, F., Puget, J.L., Falgarone, E., 1987, preprint.
Persson, C.J.L. & Helou, G., 1987. *Astrophys. J.*, 314, 513.
Phillipps, S., Kearsey, S., Osborne, J.L., Haslam, C.G.T., & Stoffel, H., 1981a. *Astr. Astrophys.*, 98, 286. (PKOHSI)
Phillipps, S., Kearsey, S., Osborne, J.L., Haslam, C.G.T., & Stoffel, H., 1981b. *Astr. Astrophys.*, 103, 405. (PKOHSII)
Pipher, J.L., 1973. In: *Interstellar Dust and Related Topics, IAU Symp. No.* 52, p.559, eds. Greenberg, J. & van der Hulst, Dordrecht, Reidel.
Puget, J.L., Léger, A. & Boulanger, F., 1985. *Astr. Astrophys.*, 142, L19.
Purcell, E.M., 1976. *Astrophys. J.*, 206, 685.
Reich, W., 1982. *Astr. Astrophys. Suppl.*, 48, 219.
Reich, P. & Reich, W., 1986. *Astr. Astrophys. Suppl.*, 63, 205.
Reich, P. & Reich, W., 1988. *Astr. Astrophys.*, 196, 211.
Reich, W., Fürst, E., Altenhoff, W.J., Reich, P. & Junkes, N., 1985. *Astr. Astrophys.*, 151, L10.
Reich, W., Fürst, E., Reich, P. & Junkes, N., 1988. In: *Supernova Remnants and the Interstellar Medium., IAU Colloq., No.* 106, 293.
Reich, W., Fürst, E., Steffen, P., Reif, K. & Haslam, C.G.T., 1984. *Astr. Astrophys. Suppl.*, 58, 197.
Reinhardt, M. & Schmidt-Kaler, T., 1979. *Astrophys. Space Sci.*, 66, 121.

Reynolds, R.J., 1984. *Astrophys. J.*, 282, 191.
Reynolds, R.J., 1985. *Astrophys. J.*, 298, L27.
Rieke, G.H., Lebofsky, M.J. & Low, F.J., 1985. *Astr. J.*, 90, 900.
Roberts, W.W., 1969. *Astrophys. J.*, 158, 123.
Roberts, W.W. & Yuan, C., 1970. *Astrophys. J.*, 161, 877.
Roberts, W.W., Roberts, M.S. & Shu, F.H., 1975. *Astrophys. J.*, 196, 381.
Roberts, W.W., & Hausman, M.A., 1984. *Astrophys. J.*, 277, 744.
Rowan-Robinson, M., 1986. *Mon. Not. R. astr. Soc.*, 219, 737.
Ruzmaikin, A.A., Sokoloff, D. & Shukurov, A.M., 1985. *Astr. Astrophys.*, 148, 335.
Ruzmaikin, A.A., Sokoloff, D. & Shukurov, A.M., 1988. *Nature*, 336, 24.
Ryter, C. & Puget, J.L., 1977. *Astrophys. J.*, 215, 775.
Ryter, C., Puget, J.L. & Pérault, M., 1987. *Astr. Astrophys.*, 186, 312.
Sánchez-Saavedra, M.L. & Battaner, E., 1987. In: *Interstellar Magnetic Fields*, p.128, eds. Beck, R. & Gräve, Springer-Verlag, Berlin.
Sanders, D.B., Clemens, D.P., Scoville, N.Z., Solomon, P.M., 1986. *Astrophys. J. Suppl. Ser.*, 60, 1.
Sanders, D.B. & Mirabel, I.F., 1985. *Astrophys. J.*, 298, L31.
Savage, B.D., 1987. In: *Interstellar Processes*, p.123, eds. Hollenbach, D.J. & Thronson, H.A., Reidel, Dordrecht.
Schmidt, M., 1957. *Bull. astr. Inst. Neth.*, 13, 247.
Schmidt, M., 1965. In: *Galactic Structure, Stars and Stellar Systems*, 5, 513, eds. Blaaw, A. & Schmidt ,M.
Schmidt-Kaler, T. & Wiegandt, R., 1980. *Astr. Astrophys.*, 89, 67.
Schraml, J. & Mezger, P.G., 1969. *Astrophys. J.*, 156, 269.
Shaver, P.A. & Goss, W.M., 1970. *Aust. J. Phys. Astrophys. Suppl.*, 14, 133.
Shu, F.H., Milione, V. & Roberts, W.W., 1973. *Astrophys. J.*, 183, 819.
Simard-Normandin, M. & Kronberg, P.P., 1979. *Nature*, 279, 115.
Simard-Normandin, M. & Kronberg, P.P., 1980. *Astrophys. J.*, 242, 74.
Simonson, S.C., 1976. *Astr. Astrophys.*, 46, 261.
Sodroski, T.J., Dwek, E., Hauser, M.G. & Kerr, F.J., 1987. *Astrophys. J.*, 322, 101.
Sofue, Y., 1987. In: *Interstellar Magnetic Fields*, eds. Beck, R. & Gräve, R., Springer-Verlag, Berlin.
Sofue, Y. & Fujimoto, M., 1983. *Astrophys. J.*, 265, 722.
Sofue, Y., Klein, U., Beck, R. & Wielebinski, R., 1985. *Astr. Astrophys.*, 144, 257.
Sofue, Y, Fujimoto, M. & Wielebinski, R., 1986. *Ann. Rev. Astr. Astrophys.*, 24, 459.
Solomon, P.M., Sanders, D.B., & Rivolo, A.R., 1985. *Astrophys. J.*, 292, L19.
Strong, A.W., 1975. *J. Phys. A: Math. Gen.*, 8, 617.
Strong, A.W., Riley, P.A., Osborne, J.L., Murray, J.D., 1982. *Mon. Not. R. astr. Soc.*, 201, 495.
Swarup, G. & Subrahmanya, C.R., 1976. In: *Radioastronomy and Cosmology, IAU Symp. No.* 74, p.125, ed. Jauncey, D.L., Reidel, Dordrecht.
Tereby, S. & Fich, M., 1986. *Astrophys. J.*, 309, L73.
Theilheim, K.O. & Langhoff, W., 1968. *J.Phys.A.*, 1, 694.

Thomson, R.C. & Nelson, A.H., 1980. *Mon. Not. R. astr. Soc.*, 191, 863.
Toomre, A., 1977. *Ann. Rev. Astr. Astrophys.*, 15, 478.
Toomre, A., 1981. In: *The Structure and Evolution of Normal Galaxies.*, eds. Fall, S.M. & Lynden- Bell, D., C.U.P., Cambridge.
Tosa, M. & Fujimoto, M., 1978. *Publ. Astron. Soc. Japan*, 30, 315.
Tosatti, E. & Bassani, F., 1970. *Nuovo Cimento*, 65B, 161.
Troland, T.H., & Heiles, C., 1986. *Astrophys. J.*, 301, 339.
Vallée, J.P., 1983. *Astr. Astrophys.*, 123, 85.
Vallée, J.P., 1983. *Astr. Astrophys.*, 124, 147.
van den Bergh, S., 1960a. *Astrophys. J.*, 131, 215.
van den Bergh, S., 1960b. *Astrophys. J.*, 131,558.
Verschuur, G.L., 1973. *Astr. Astrophys.*, 27, 73.
Völk, H.J., 1989. *Astr. Astrophys.*, in press.
Wall, J.V. & Cooke, D.J., 1975. *Mon. Not. R. astr. Soc.*, 171, 9.
Walterbos, R.A.M., & Schwering, P.B.W., 1987. *Astr. Astrophys.*, 180, 27.
Weaver, H., 1970. *IAU Symp. No.* 38, p.126. D.Reidel, Dordrecht.
Weaver, H., 1974. In: *Galactic Radio Astronomy, IAU Symp. No.* 6, p.573, eds. Kerr, F.J. & Simonson, S.C. D.Reidel, Dordrecht.
Weaver, H. & Williams, D.R.W., 1973. *Astr. Astrophys. Suppl.*, 8, 1.
Weiland, J.L., Blitz, L., Dwek, E., Hauser, M.G. Magnani, L. & Rickard, L.J., 1986. *Astrophys. J.*, 306, L101.
Wendker, H.J., 1970. *Astr. Astrophys.*, 4, 378.
Westerhout, G., 1957. *Bull. astr. Inst. Neth.*, 13, 201.
Westerhout, G., 1958. *Bull. astr. Inst. Neth.*, 14, 215.
White, M.P., 1977. *PhD thesis*, University of Durham.
White, M.P., 1978. *Astrn. Nachr.*, 299, 209.
Worrall, D.M., 1977. *PhD thesis*, University of Durham.
Wunderlich, E. & Klein, U., 1988. *Astr. Astrophys.*, 206, 47.
Wunderlich, E., Klein, U. & Wielebinski, R., 1987. *Astr. Astrophys. Suppl.*, 69, 487.

Acknowledgements

My supervisor, Dr. J.L. Osborne is thanked for his guidance, patience and encouragement throughout the course of my studies over the past three years. I am grateful to Prof. A.W. Wolfendale both for the use of the facilities of the Department of Physics at Durham University and for his interest in and advice regarding my research. I would like to thank Dr. C.G.T. Haslam for his assistance, provision of radio continuum data and hospitality on my visits to the Max-Planck-Institute für Radioastronomie in Bonn. Discussions with Dr. R. Beck, Dr. P. Cox and Prof. P.G. Mezger, also at the Max-Planck-Institut, were of great value.

I acknowledge SERC for my Research Studentship and the IPMAF team at the Rutherford Appleton Laboratory for providing the IRAS data and software. The use of the computing facilities at Durham University have proved invaluable, especially the local Starlink node, whose manager Mr. A.P. Lotts is thanked both for the general running of the cluster and for assistance in solving computing problems that I have encountered.

The friendship and help received from many other members of and visitors to the Physics Department at Durham is greatly appreciated and I commend Tony Banday, Margaret Chipchase, Neasa Foley, Iain MacLaren, Mike Parkinson, Ken Richardson and David Wilkinson for putting up with me.

Finally, thanks to my family and friends who have given me every support and encouragement in my academic pursuits, especially to my parents to whom I would like to dedicate this thesis.